Hydrodynamics of a
Monolithic Stirrer Reactor

PROEFSCHRIFT

ter verkrijging van de graad van doctor
aan de Technische Universiteit Delft,
op gezag van de Rector Magnificus prof. ir. K.C.A.M. Luyben,
voorzitter van het College voor Promoties,
in het openbaar te verdedigen op
dinsdag 25 januari 2011 om 15.00 uur
door

Hercules Petrus KRITZINGER

Master of Science in Mechanical Engineering,
Universiteit Stellenbosch,
geboren te Ceres, Zuid-Afrika

Dit proefschrift is goedgekeurd door de promotoren:

Prof. dr. ir. C.R. Kleijn
Prof. dr. ir. H.E.A van den Akker

Samenstelling promotiecommissie:

Rector Magnificus	voorzitter
Prof. dr. ir. C.R. Kleijn	Technische Universiteit Delft, promotor
Prof. dr. ir. H.E.A. van den Akker	Technische Universiteit Delft, promotor
Prof. dr. J.A Moulijn	Technische Universiteit Delft
Prof. dr. ir. M.T. Kreutzer	Technische Universiteit Delft
Prof. dr. ir. A.I. Stankiewicz	Technische Universiteit Delft
Prof. dr. ir. J.A.M. Kuipers	Technische Universiteit Eindhoven
Prof. dr. G.J. Heynderickx	Universiteit Gent

Vir Carien, Peter en Anke

Contents

Chapter 1

Introduction

1.1 Project description

The monolithic stirrer reactor (MSR) is a novel concept for heterogeneously catalyzed reactors and is presented as an alternative device to slurry reactors. It uses a modified stirrer on which structured catalyst supports (monoliths) are fixed to form permeable blades. The monoliths consist of small square parallel channels on which a layer of catalytic material can be applied. The stirrer now has both a catalytic and a mixing function. The main advantage of this reactor type is the ease of the catalyst handling, since the catalyst is easily separated from the reaction mixture and can be re-used.

The goal of this work is to study the hydrodynamic operation of the MSR and develop models for its design. In particular, to evaluate the two main functions of the stirrer (i) mixing of the bulk fluid, and (ii) pumping fluid through the monolith to allow the catalytic reaction to take place.

A hydrodynamic study is not sufficient to operate a chemical reactor - skills from diverse backgrounds are required. Therefore this work forms one of the two parts of the design project "Development of Monolithic Stirrer Reactors: Operational Characteristics and Scale-up Methods". The process development and reactor engineering were performed by Ingrid Hoek of Reactor and Catalysis Engineering Department (R&CE) at Delft University of Technology. The result of that study has been published earlier as "Towards the Catalytic Application of a Monolithic Stirrer Reactor" (Hoek, 2004).

1
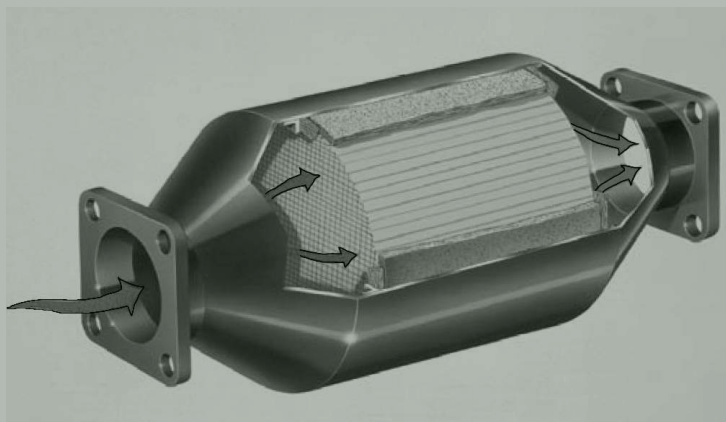
Figure 1.1: *Catalytic converter with monolith in situ. Reproduced with permission from Johnson Matthey.*

1.2 Background

1.2.1 Monoliths and catalysis

Monoliths are an example of structured catalyst support. Monoliths consist of a large number of small ($\sim 1mm$), parallel channels or cells, with a constant cross-section. Different cell shapes are available, with square, triangular and hexagonal the most common. Some monoliths are manufactured from the active catalyst material, but most often they are manufactured by extrusion from metal (aluminum) or ceramic (corderiete) material. The catalytic active material is then applied in a thin layer as a washcoat to the monolith surface.

Monoliths have been widely applied for catalytic converters in automotive exhausts (see figure 1.1) and other pollution control devices (Villermaux & Schweich, 2004). Heck *et al.* (2001) reviewed monoliths more generally as supports for catalytic gas phase reactions. Examples of processes where monoliths are used include: ozone destruction in aircraft air-conditioning systems; as diesel oxidation catalyst to convert liquid particles (soluble organic fraction), and gaseous CO and HC (hydrocarbons) in the exhausts of heavy-duty trucks, buses and passenger cars; catalytic combustion for gas turbines and steam-reforming of hydrocarbons. The success of the monolith as catalyst support has led to research on a number of other applications.

Other in-depth reviews on the application of monoliths include that of Koltsakis & Stamatelos (1997) on the use of monoliths in the automotive industry, those by Kapteijn *et al.* (1999) and Roy *et al.* (2004) on monoliths in multiphase applications, as well as a paper by Giroux *et al.* (2005) who evaluated monoliths for hydrogen production in fuel cell applications.

Monoliths, or structured catalysts in general, have a number of advantages compared to slurry type catalysts: easy separation of the catalyst from the reaction mixture, lower pressure drop, and simpler scale-up. Hydrodynamics in a structured catalyst can be controlled more easily. In addition, the structure of the monolith is adjustable in terms of channel diameter, shape, and length, to the demands of the specific process (Hoek, 2004).

The use of monoliths on the stirrer has one unique feature when compared to other monolith applications mentioned in literature: fluid can flow either through or around the monolith. One of the key issues in this investigation is the quantification of this 'flow split' through and around the monolith.

1.2.2 Stirred tank reactors

It would not be unfair to describe stirred tank reactors as ancient technology. Descriptions by Agricola (1556) in his book "De Re Metallica" (On the Nature of Metals) show stirring devices being used in the mining industry. Much of the descriptions reference older work like the *Naturalis Historia* of Pliny the Elder from 77 AD (Wikipedia, 2009). Yet, they are also very modern equipment and provide a large part of mechanical agitation for mixing processes. As such, there exists a vast body of scientific literature on the operation and design of these devices. Despite this large research effort, work continues to improve the design e.g., by using novel reactor shapes or stirrer configurations.

The stirrer is used to provide mechanical energy required to mix or blend the reactants in such a way that the desired reaction or transfer process occurs at the desired rate. When using a stirred tank reactor (STR) for heterogeneous catalysis, the catalyst are usually added to the reactants in the form of fine particles or powder. In most cases a portion of the energy is now also used to keep the catalyst particles in suspension inside the reactor.

Previous experimental and numerical analyses of the STR are not directly applicable to investigation of the MSR. The monolithic stirrer is much larger, with volumetric blades, when compared to standard stirrers e.g., propeller, pitch bladed turbine or a disc turbine. However, earlier studies serve as a guide on how to approach the investigation of the MSR. In general the hydrodynamic operation of STR's are characterized by (i) mixing efficiency, (ii) power consumption, and (iii) flow field characteristics. The Kramers Laboratory of Delft University of Technology has a long history in STR research. Kramers *et al.* (1958), after whom the laboratory was named, presented conductivity experiments on the mixing times in a number of different stirred tanks. Later Van't Riet & Smith (1973) visualized the trailing vortex structure behind the blades of a Rushton disc turbine. Derksen & Van den Akker (1999) performed a numerical study of the flow and turbulence in a STR using large-eddy simulations. Hartmann *et al.* (2004) extended the LES simulations with an additional sub-grid scale model, and compared the results with a RANS calculation using the Shear-stress transport k-ω turbulence model (Menter, 1994), and LDA experiments.

1.2.3   Monolithic stirrer reactor

The problems related to using a slurry catalyst, i.e., separation of the catalyst from the reaction mixture, attrition and agglomeration of catalyst particles and safety in case of a runaway reaction, can be reduced significantly if the catalyst is immobilized. Fixing the catalyst to a monolith structure (either by washcoating or impregnation) is one solution. However, by fixing the catalyst, some other means of contacting the reaction mixture and the catalyst must be devised.

Carmody (1964) presented a reactor where catalyst pellets were placed in baskets fixed to the stirrer. The reactor was used for laboratory experiments of kinetics with minimal external mass transfer limitations. A number of subsequent studies, based on this concept, have been reviewed by Choudhary & Doraiswamy (1972). Liakopoulos *et al.* (2001) used spinning baskets filled with monolith pieces and (Spee, 1999) coated the stirrer blades with catalyst.

Bennet *et al.* (1991) performed an extensive study of reaction kinetics and reaction for monolith reactors. The reaction kinetics was studied in a stirred reactor with two stirrers: (i) a basket stirrer with small pieces of monolith and (ii) a monolith block attached directly to the shaft of the stirrer. Operating parameters were selected to ensure that the reaction was not limited by the external mass transfer. Another set of experiments was performed to evaluate the actual mass transfer correlations for heat and mass transfer in monoliths. In this experiment the monolith was installed in a tubular reactor. The coefficients in the equations differed significantly from earlier publications (Hawthorn, 1974; Votruba *et al.*, 1975).

A monolith stirrer reactor, i.e., a reactor with a stirrer with monolith blocks fixed to the shaft, was tested by Edvinsson-Albers *et al.* (1998) and shown to work for low viscosity fluids. The hydrodynamics were studied by measuring power draw for monoliths with different densities, and for different sized monoliths. These results confirmed that liquid flows through the monolith channels. A model was proposed for the liquid flow rate through the monolith and the model was used to correlate the mass transfer rates with the earlier model of Bennet *et al.* (1991).

Prior to Edvinsson-Albers *et al.* (1998), the basket stirrer with catalyst (or catalytic stirrer) was used primarily in the investigation of reaction kinetics with limited to no external mass transfer limitations. The flow rate of liquid through the monolith or catalyst was not as important as the overall conversion. With the proposal to employ a monolithic stirrer reactor for production, the operating characteristics of the reactor (and also the flow rate through the monolith) becomes more important. Following the proposal of Edvinsson-Albers *et al.* (1998) a collaborative research project was initiated with the title: "Development of Monolithic Stirrer Reactors: Operational Characteristics and Scale-up Methods". The participants were the group of Prof. Harry van den Akker (*Kramers Laboratorium voor Fysische Technologie*) and the group of Prof. Jacob Moulijn (Reactor & Catalysis Engineering). The investigators focused on illustrating the catalytic applicability of the new reactor, as reported by Hoek (2004), and the study of the single-phase hydrodynamic operation of the reactor, as reported in this manuscript.

1.2.4 Computational Fluid Dynamics

"Computational fluid dynamics is the analysis of systems involving fluid flow, heat transfer and associated phenomena such as chemical reactions by means of computer based simulation" (Versteeg & Malalasekera, 1995). A computational fluid dynamics (CFD) analysis starts with a problem statement in which the domain of interest (geometry) is defined and the relevant physics identified. The Navier-Stokes equations form the common starting point as the set of differential equations which describe the physics of the problem. Additional equations can also be required for multi-phase flows, for turbulence, heat transfer and/or species transport. The domain is discretized by dividing it into a number of computational units (elements or cells). Applying the governing differential equations in each cell leads to a system of algebraic equations. Due to the non-linearity of the differential equations numerical solutions methods are required to obtain a solution. A number of techniques can be used to solve the differential equations: finite-elements, finite-difference and finite-volume methods. Other methods for obtaining solutions include Lattice-Boltzmann methods, spectral methods and direct simulation Monte-Carlo methods. The present investigation uses the 'work-horse' of the industry, that is the finite-volume method. Details of CFD are given in several textbooks: Roach (1976) wrote one of the first books on the topic and includes a short history of CFD; Patankar (1980) is the standard reference for finite-volume methods; more recent books are by Versteeg & Malalasekera (1995) and Ferziger & Perić (2002). Information is available online at major CFD code vendors, several research institutes and at `www.cfd-online.com`. The latter is currently the best starting point on the internet.

The success of CFD in academic and industrial application is due to several advantages over physical experiments. In principle the CFD approach yields a virtual model with the experimenter (user) having total control of all parameters. This reduces reliance on expensive physical testing and prototyping. It can be used to investigate equipment and processes where physical experiments are dangerous, e.g., testing equipment above design limits. The virtual model removes the need for scaling, e.g., when studying flow around a ship hull or pollutant dispersion in a city. In comparison to a physical experiment, the numerical experiment gives access to an almost unlimited level of detail, thereby providing better insight in the physics.

Despite the advantages, several issues remain in using CFD. The equations describing the physics may contain approximations, e.g., for the modeling of turbulence, or dispersed multiphase phenomena, which are necessary to make solutions feasible. The discretization (mesh) results in a discrete set of equations which is again an approximation of the continuous case. Iterative solutions are required to solve the set of equations and the level of convergence will determine the accuracy of the solution. Successful application of CFD requires a person skilled and experienced in both numerical methods and in fluid dynamics (Versteeg & Malalasekera, 1995).

Despite the growing availability of CFD codes (whether commercial, research or open source) the operator will remain the critical component. An unfortunate example was presented by Verdier (2004) who benchmarked two CFD codes in solving laminar flow past a 2-dimensional cylinder in plane flow. The conclusion states "There is apparently no hope for Fluent to get even a rough idea of this coefficient, no matter how long we wait or how refined the mesh is." As indicated by the response from Fluent (included in the paper), this statement was unjustifiable due to a number of modeling errors. Several large initiatives have been launched to address the issue of credible CFD results. These include a number of extensive publications on the topics of code verification and validation (Jasak, 1996; AIAA, 1998; Roach, 1998; Oberkampf & Trucano, 2002), as well as more practical advice in the form of best practice guidelines (Casey & Wintergerste, 2000; Menter, 2002; WS Atkins Consultants, 2002).

The commercial code selected for the research, Fluent, is considered to be verified and validated against a large range of industrial flow problems. However, it was noted that user experience is as important. A research laboratory provides a good environment in which to 'develop and improve' user knowledge. In particular, the *Kramers Laboratorium voor Fysische Technologie*, has been actively involved in CFD for more than two decades – both in application, code development and fundamental research. Applied research in the laboratory includes: stirred tanks, cyclones, static mixers, bubble columns, CVD reactors, microreactors, and crystallizers. Code development and more fundamental research areas include: rarefied gas flows, multi-phase flow, and Lattice-Boltzmann code.

1.3   Organization of the thesis

An experimental and numerical investigation of liquid flow through and around monoliths is the topic of *Chapter 2*. The focus is on a monolith in a channel flow - where the flow conditions can be carefully controlled - to evaluate pressure drop correlations from literature and to test the CFD modeling approach. For the latter the flow field around the monolith was measured with LDA and used to validate the CFD study. A method for measuring the monolith flow, or the monolith channel velocities, is described.

In *Chapter 3* we develop a model for the monolith flow rate in the case where flow can go either through or around the monolith. This model is an idealization because in the MSR the flow around the monolith is expected to be very different from that in a straight channel. However, it is an attempt to capture the physics of the process and is expected to be functional, with some modification, also in the case of the MSR.

Chapter 4 describes the experimental work performed to analyze a prototype MSR. The global flow field in the reactor is characterized. We evaluate the power draw and mixing times to calculate the mixing efficiency of the stirrer. The amount of flow through the monolith is calculated and compared to experiments.

Simulation of the prototype MSR is the subject of *Chapter 5*. The case of a solid stirrer blade is used to test the numerical modeling without the added simplification of a porous monolith. In this we evaluate different strategies to model (i) the stirrer movement, (ii) turbulence modeling, and (iii) the effect of having a free liquid surface on top of the reactor. Subsequently we look at monolithic stirrer blades and compare results to the experiments in Chapter 4.

Design for industrial application requires predictive models for the operation of the equipment. In *Chapter 5* an attempt is made to evaluate the impact of a number of parameters on the hydrodynamic operation of the MSR. In this we concentrate on stirrer design, e.g., number of monoliths, size of monolith compared to stirrer, size of stirrer compared to tank size, and the vertical and angular spacing of monoliths. This is accomplished by using the simplified engineering models for channel flows.

The conclusions of our investigation are presented in *Chapter 6*, together with some recommendations for possible extensions.

Chapter 2

Flow through and around a monolith

2.1 Introduction

Flow through monolith structures has been investigated since the late 1960's when they were introduced for air pollution control - mainly in automotive exhausts. The pressure drop and flow distribution can be considered as the most important hydrodynamic parameters. Pressure drop is directly related to the operating cost of the monolith reactor. The flow distribution, or flow uniformity, through the monolith affects the conversion efficiency and catalyst utilization. Design goals include a minimum pressure drop with a maximum flow uniformity.

In the application of monoliths as stirrer blades, the flow through the monolith is not confined by an external duct, pipe or converter body. As a result, fluid may either pass through the channels or flow around the monolith. This is the main difference to other applications of monoliths. This chapter aims to characterize the flow through and around a monolith in a duct flow. A secondary objective is to compare results with CFD simulations of the monolith that are to be used in subsequent work on the MSR.

Because CFD contains the complete flow and pressure field in the solution, it offers more detailed insight into the flow when compared to experimental measurements. However, fully resolving the monolith channels in simulations of large systems, where the monolith is only a small component, is not yet practical with existing computing hardware. It is common practice to model the monolith as a momentum sink, similar to models for flow through porous media. The loss coefficients required to model the monolith are derived from the pressure drop over the monolith.
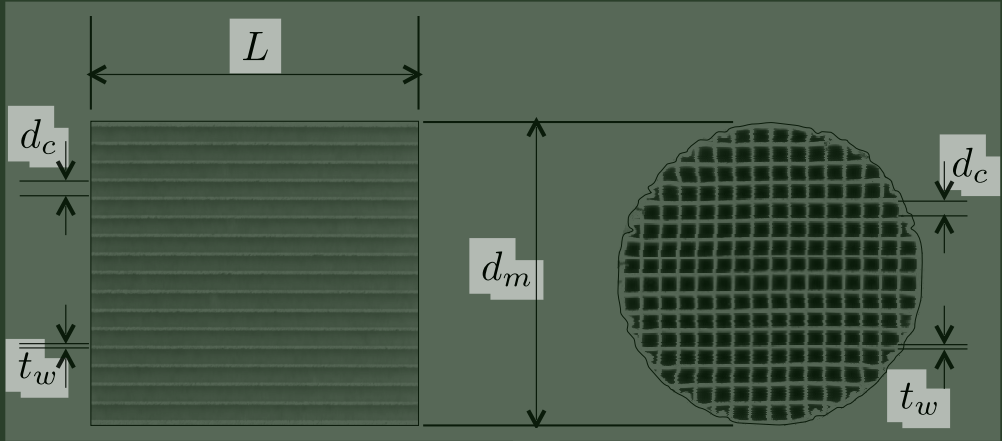
Figure 2.1: *Scanned image of an uncoated 200cpsi monolith (not to full size). Important geometric features are labeled on the image.* Left: *Vertical section through the monolith.* Right: *Front view of the monolith showing square channels and structure of the walls.*

Section 2.2 reviews the available literature on monolith flow. The focus is on experimental and numerical studies applicable to the present research. This is followed in section 2.3 by a description of the experimental study performed with a monolith placed in a square duct. CFD simulations of the experiments are described in section 2.4. Results are presented in 2 parts: Section 2.5.1 presents the monolith pressure drop characteristics and compares the experiments and CFD of the flow field around the monolith; section 2.5.2 focuses on the flow through the monolith. The chapter ends with a summary of the main findings.

2.2   Literature review

2.2.1   Monolith structure

As described in the previous chapter, monoliths are manufactured from a variety of materials and with different physical properties as required by the application. In general a monolith is a single structure with many parallel channels, also called cells, separated from each other by walls. The channels are often rectangular, but triangular, hexagonal and higher order polygons are also manufactured. Further additions can include internal fins, bumps on the wall or interconnected channels (perforated walls). The monoliths used in this study were manufactured from corderiete with square channels (supplied by Corning Inc.). In addition, only uncoated monoliths were used, which differs in terms of channels shape and void fraction when compared to monoliths with a washcoat of catalyst.

The cell configuration and monolith properties are described by a number of geometric and hydraulic parameters (Roy *et al.*, 2004). Figure 2.1 shows a typical

monolith with square channels.

Monoliths are named according to the number of channels per unit cross sectional area, the 'cell density'. For historic reasons this is still presented in channels per square inch (cpsi) - values from 50 to 1200 cpsi are generally available. The wall thickness, t_w, ranges between 0.06 and 0.5 mm. The void fraction, ϵ_v, usually expressed as the open frontal area fraction (OFA), is determined by the cell density and wall thickness, which are independent of each other. The geometric properties characterizing the monolith are cell density, and the OFA, $\epsilon_v = (1 + t_w/d_c)^{-2}$ (figure 2.1). The properties of monoliths used in the present study are presented in table 2.1.

Table 2.1: *Properties of square channel corderiete monoliths.*

Cell density (cpsi)	Channel size, d_c (mm)	Wall thickness, t_w (mm)	OFA, ϵ_v (%)
600	0.930	0.1092	80.0
400	1.090	0.1778	74.0
200	1.490	0.3048	68.9
100	2.110	0.4318	68.9
50	2.983	0.6096	68.9

2.2.2   Pressure drop

Monolith pressure drop is an important design parameter - in optimization the objective is often to find the lowest pressure drop for the maximum surface area (Heck *et al.*, 2001). A number of factors contribute to the overall pressure drop, although not all previous publications address all of these contributions. The main contribution is due to developing laminar flow inside the channels, with additional losses occurring at the inlet and outlet to the monolith.

Votruba *et al.* (1974) measured pressure drop for a range of L/d_c (see figure 2.1) ratios (3.75–37.6) and Reynolds numbers (100–2000). The data was correlated with a function proposed by Mühle (1972) for sieve trays:

$$\Delta p^* = 1.75 \cdot (1 - \epsilon_v) + \frac{64}{Re_c} \frac{d_c}{L} \tag{2.1}$$

The channel Reynolds number, Re_c, is defined in terms of the mean channel velocity, u_c, and the hydraulic channel diameter, d_c as

$$Re_c = \frac{\rho u_c d_c}{\mu} \tag{2.2}$$

The non-dimensional pressure drop, Δp^*, is defined as the pressure drop across the monolith normalized with the dynamic pressure:

$$\Delta p^* = \frac{2\Delta p}{\rho u_c^2} \tag{2.3}$$

In general the frictional pressure drop in pipes and ducts is correlated with a friction factor, f, defined as:

$$f = \frac{2\Delta p}{\rho u_c^2}\frac{d_c}{L} = \Delta p^* \frac{d_c}{L} \tag{2.4}$$

Hawthorn (1974) proposed to use the laminar flow friction factor with a correction for developing flow. No other losses were considered. They performed curve-fitting of the data of Kays & London (1964) and arrived at the following equation for the friction factor in round and hexagonal monolith channels:

$$f \cdot Re_c = f_{lam} \cdot Re_c \left(1 + 0.0445 Re_c \frac{d_c}{L}\right)^{0.5} \tag{2.5}$$

Here $(f_{lam} \cdot Re_c)$ is product of the laminar flow friction factor and the channel Reynolds number – for circular ducts this is equal to 64.

The term in brackets on the right hand side in equation 2.5 accounts for the contribution of the developing flow in the channel entrance. This correlation has been used extensively in subsequent studies of monolith flows, e.g., Wendland & Matthes (1986), Lai *et al.* (1992) and Edvinsson-Albers *et al.* (1998).

Later Benjamin *et al.* (1996) replaced equation 2.5 with the interpolation formula of Shah (1978) for developing flow in circular and non-circular ducts.

$$f \cdot Re_c = \left[\frac{13.76}{\sqrt{L^*}} + \frac{f_{lam} \cdot Re_c + \frac{K_\infty}{L^*} - \frac{13.76}{\sqrt{L^*}}}{1 + \frac{c}{(L^*)^2}}\right] \tag{2.6}$$

with L^* the dimensionless channel length defined as

$$L^* = \frac{L}{d_c Re_c} \tag{2.7}$$

Shah (1978) presented values of the constants $(f_{lam} \cdot Re_c)$, K_∞ and c for a variety of duct shapes. The values for three common shapes are presented in table 2.2 - see White (1988) for a longer list.

Closer inspection shows that equation 2.5 and equation 2.6 are based on the same data and are quite similar. The friction factor, with the correction for developing flow, can be written more generally as:

$$f \cdot Re_c = (f_{lam} \cdot Re_c) \left(1 + \frac{a}{L^*}\right)^{0.5} \tag{2.8}$$

Table 2.2: *Constants used in the laminar pressure drop equations*

channel shape	$f_{lam} \cdot Re_c$	Equation 2.6		Equation 2.8
		K_∞	c	a
round	64.0	1.25	0.000212	0.046
square	56.92	1.43	0.00029	0.058
triangular	53.32	1.69	0.00053	0.066

The first term on the right ($f_{lam} \cdot Re_c$) is the developed laminar friction factor, and a is a constant related to the developing flow correction. The difference with Hawthorn (1974), equation 2.5, is that a is a variable and not set as a constant $a = 0.0445$. Koltsakis & Stamatelos (2000) used a value of $a = 0.06$ for square cells, although citing Hawthorn (1974) as reference. Using equation 2.6, which is said to be accurate to within 2% for all data, the coefficients for the curve-fit (equation 2.8) were recalculated. The results show that a is a function of the cell shape with $a = 0.0445$ close to the value for circular channels. The recalculated curve-fit results are included in table 2.2.

A limited number of experimental studies on flow through monoliths are available in open literature. Most of the work focused on the overall pressure drop over a canned converter, that is a monolith including the inlet diffuser and exit contraction (see figure 1.1).

Wendland *et al.* (1991) investigated sources of pressure drop in monolith catalytic converters. In the analytic model for the monolith pressure drop they add an inlet and exit pressure loss (also called the contraction and expansion losses) to the developing laminar flow, using equations proposed by Benedict *et al.* (1966). The inlet or contraction loss is

$$\Delta p_{in}^* = (1 - \epsilon_v)^2. \tag{2.9}$$

This term represents the pressure drop due to the abrupt change in velocity as the fluid enters the monolith channels with smaller flow area. The exit loss, or expansion loss is

$$\Delta p_{out}^* = \frac{1}{(\lambda\varphi)^2} - \frac{2}{\varphi} + 1 \tag{2.10}$$

with the constant $\lambda = 0.975$ and φ a function of the monolith porosity, ϵ_v, given by:

$$\varphi = 0.6137 + 0.1332\epsilon_v - 0.2609\epsilon_v^2 + 0.51145\epsilon_v^3. \tag{2.11}$$

Unfortunately the experiments were performed for a converter assembly and the pressure drop results were presented for the total system (including the inlet diffuser and exit contraction) in such a way that the accuracy of the monolith pressure drop predictions can not be evaluated. The authors state that the contraction and expansion losses in the monolith amount to 5% of the total losses for normal (automotive) applications.
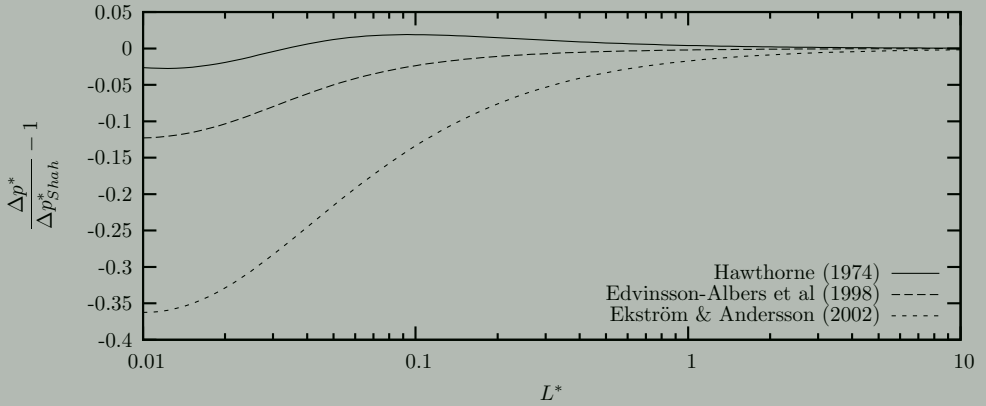
Figure 2.2: *Comparison dimensionless pressure drop from different authors to equation 2.6 of Shah (1978).*

Benjamin *et al.* (1996) performed experiments to characterize the pressure drop in washcoated and uncoated monoliths. The monoliths were installed behind a Börger contraction (Börger, 1973) which provided a flat velocity profile to the upstream face of the monolith. Equation 2.6 was used to correlate the experiments with good accuracy - no additional losses were considered.

In subsequent work (Benjamin *et al.*, 2001, 2003) an additional entrance loss due to oblique flow onto the face of the monolith was proposed. Quoting an earlier study of Haimad (1997), the proposed additional pressure drop was given as

$$\Delta p_e^* = \left(\frac{v_r}{u_c}\right)^2 \tag{2.12}$$

Here v_r is the velocity vector parallel to the monolith face. This additional pressure loss was motivated by poor comparison between measured and simulated velocity profiles at the exit of the monolith - leading to a poor prediction of the uniformity index (see equation 2.16).

An extensive experimental study of monolith pressure drop was presented by Ekström & Andersson (2002). Measurements were performed with uncoated and washcoated monoliths ranging from 350 cpsi to 600 cpsi. The pressure drop is said to consist of the contribution due to developed laminar flow friction, the developing inlet flow, as well as the inlet and outlet losses:

$$\Delta p^* = (A)\, L^* + B \tag{2.13}$$

In this equation the constant A was set equal to the developed laminar friction constant, that is $A = (f_{lam} \cdot Re_c)$ from table 2.2. A value of $B = 0.41$ was obtained from a regression analysis of the experimental data for uncoated square-channels.

From the above description it is clear that a number of pressure drop correlations have been used for monoliths, with the differences being the number of contributing sources taken into account. Figure 2.2 compares different pressure drop correlations with that of Shah (1978), i.e., equation 2.6. For $L^* \geq 10$ the difference between predictions is negligible. At smaller values of L^* (i.e., higher Re_c or smaller L/d_c) some differences appear. The generic Hawthorn equation (2.8) closely follows the Shah equation (2.6), with differences $< 3\%$ for the relevant range of L^* (see table 2.3). The maximum difference between the equation used by Edvinsson-Albers *et al.* (1998) and that of Hawthorne is 12% - this difference is due to a different constant, a used in equation 2.8. The curve-fit result presented by Ekström & Andersson (2002) does not compare well for $L^* \leq 1.0$. This is mainly due to the non-linear scaling of the developing flow for small L^* values. In some applications L^* may be sufficiently large and the additional loss due to the developing inlet profile can be neglected.

In order to investigate the need to include all of the contributions, an order of magnitude study of the pressure drop can be made. The first and most important assumption is that the monolith is operated in the laminar flow regime, $Re_c < 2000$. The aspect ratio of the channel L/d_c is a defining parameter – in this work it ranges from ~ 3 for 10mm long 50cpsi monolith to ~ 50 for a 55mm long 400cpsi monolith. In table 2.3 the increase in pressure drop due to the inlet profile development is expressed as a percentage of the laminar flow pressure drop:

$$E = \frac{\Delta p^*}{\Delta p^*_{lam}} - 1 = \left(1 + \frac{a}{L^*}\right)^{0.5} - 1. \tag{2.14}$$

An estimate of the contribution of the inlet (equation 2.9) and outlet (equation 2.10) loss to the total is presented as a percentage of the total friction pressure drop:

$$E_{add} = \frac{\Delta p^*_{in} + \Delta p^*_{out}}{\Delta p^*}. \tag{2.15}$$

The values in the table were calculated for a 400cpsi monolith with $\epsilon_v = 0.74$. With eqs. 2.9–2.11 this leads to $\Delta p^*_{in} = 0.068$ and $\Delta p^*_{out} = 0.169$. The correction by Benjamin *et al.* (2001) for oblique flow at the front of the monolith, equation 2.12 was not considered - see sections 2.2.3 and 2.4.4 for more information. The table illustrates the non-linear scaling of E for $L^* < 1$.

This summary shows that the developing flow can add significantly to the total pressure drop over a monolith channel. The application of the monolith on a stirrer will result in a range of possible velocities through the channels, but unlike automotive applications the flow rate is unknown and an estimate of the contribution of developing flow cannot be made in advance. In the present work the monolith pressure drop is modeled with equation 2.8 with the constants $(f_{lam} \cdot Re_c)$ and a taken from table 2.2. The effects of the inlet and exit as presented by Wendland *et al.* (1991) were initially neglected. However, the application of the monolith outside a conventional converter enclosure introduces differences that require closer

Table 2.3: *The effect of inlet profile development and inlet and outlet losses on the pressure drop over a monolith with square channels.*

	$L/d_c = 3$			$L/d_c = 10$			$L/d_c = 50$		
Re_c	L^*	E	E_{add}	L^*	E	E_{add}	L^*	E	E_{add}
1	3	0.96 %	0.41%	10	0.29%	0.42%	50	0.06%	0.42%
10	0.3	9.24 %	0.38%	1	2.86%	0.40%	5	0.58%	0.41%
100	0.03	71.3 %	0.24%	0.1	25.7%	0.33%	0.5	5.6%	0.39%
1000	0.003	351 %	0.09%	0.01	161%	0.16%	0.05	47%	0.28%

attention. The implementation of the monolith pressure drop correlation for the present CFD work is described in more detail in section 2.4.4.

2.2.3   Flow uniformity

In automotive applications the geometry of the converter package leads to a non-uniform velocity distribution through the monolith. This in turn can have a strong influence on the performance and lifetime of the catalytic converter (Kim *et al.*, 1995). The non-uniformity of the flow can be characterized in a number of ways. Following Wendland & Matthes (1986), a maldistribution index can be defined as the relative difference between the maximum velocity u_{max} and the average velocity u_c::

$$M_v = \frac{u_{max} - u_c}{u_c}. \tag{2.16}$$

Benjamin *et al.* (1996) presented a simpler definition for maldistribution based on the ratio of the peak to the mean velocity in the monolith:

$$M_u = \frac{u_{max}}{u_c} = M_v + 1. \tag{2.17}$$

Both these definitions only account for the difference between the maximum and the mean velocity. The 'most widely used' correlation uses the volume-weighted velocity instead (Badami *et al.*, 2003). In this case the uniformity index can be defined as

$$M_\phi = 1 - \frac{1}{2\phi} \sum_{i=1}^{n} ||u_i| - u_c| \, A_i. \tag{2.18}$$

Here, the flow rate $\phi = u_c A_c$ equals the product of the mean channel velocity and the channel flow area. In cases in which large density differences (often due to temperature gradients) exist, the uniformity index can also be defined on a mass-weighted basis.

A number of CFD studies on the flow uniformity have been performed. The level of agreement between measured and predicted results varies. One reason

may be due to differences in the experiments, more specifically, the position where the velocity profile through the monolith is measured. Lai *et al.* (1992) measured the profile $1mm$ upstream of the monolith face using Laser Doppler anemometry (LDA) Benjamin *et al.* (1996) and Holmgren (1998) measured profiles $30mm$ downstream from the monolith back face with a hot wire anemometer. Badami *et al.* (2003) also used a hot wire, but measure at $10mm$ behind the monolith, claiming that this is "according to common experimental practice".

Benjamin *et al.* (1996) obtained poor comparison between predicted and measured velocity profiles, especially in the center of the monolith. As a result their measured uniformity index M_u (equation 2.17) is poorly predicted. As remedy they propose to include an additional pressure drop contribution due to oblique flow on the face of the monolith (equation 2.12). However, results from other authors show, in my opinion, better agreement without this additional loss. The data presented by Holmgren (1998) show very good agreement between calculated and CFD results for a study very similar to that of Benjamin *et al.* (1996). The authors mention that to achieve good comparison, extra care was required in modeling the exact diffuser geometry used in the experiments. Lai *et al.* (1992) presented very good agreement between experiments and CFD on profiles measured just upstream of the monolith - in their case the turbulence modeling was deemed important to achieve good agreement. Holmgren (1998) used the developed laminar flow friction factor (without correcting for developing flow) for the monolith resistance, while Lai *et al.* (1992) included such correction by using equation 2.8. In sections 2.4.4 and 2.5.1 an alternative explanation is proposed for the discrepancy in the data observed by Benjamin *et al.* (1996).

2.3   Experiments

In the present work an experimental study was performed to investigate the flow through and around a monolith. A detailed description can be found in Deelder (2001). Three objectives were set: (i) monolith pressure drop measurement, (ii) monolith flow rate measurement, and (iii) obtaining experimental flow field data to compare with the CFD simulations. Water was used as the working fluid. The pressure drop measurements were performed with differential pressure sensors. The flow field was measured using laser Doppler anemometry (LDA). LDA is a non-intrusive, point measurement method capable of measuring with high temporal resolution (see appendix A for an introduction to LDA).

2.3.1   Experimental setup

A measurement section consisting of a $1m$ long, $0.15m \times 0.15m$ square duct, was constructed from clear Perspex. Monoliths could be installed in two different configurations inside the duct (figure 2.3): (i) Sealed duct: A vertical plate is installed, sealing the measurement section. The monolith is then installed in a hole through
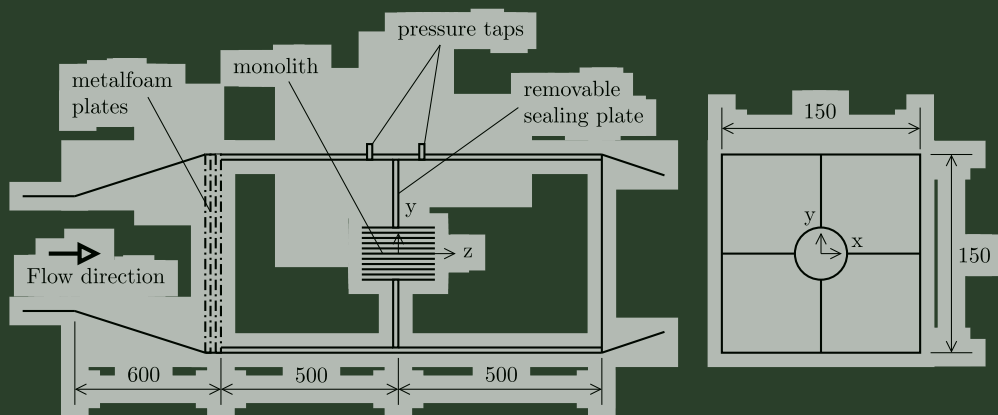
Figure 2.3: *Schematic drawing of the measurement section with a monolith installed. Fluid flows from left to right through the setup. The location of the up- and downstream pressure taps are shown as well.* Left: *Side view of section showing the porous metalfoam plates at the inlet and the removable sealing plate inside the square channel.* Right: *Monolith location in a cross-section of the square duct. All dimensions in mm.*

the plate. In this configuration all fluid in the measurement section must pass through the monolith. (ii) Open duct: The monolith is fixed inside the measurement section using four symmetric supports without the vertical plate. Fluid in the measurement section can now flow through and around the monolith (similar to the situation in the MSR). All monoliths were of circular cross-section and machined to have the same diameter, $d_m = 0.042m$, and length, $L_m = 0.05m$.

The measurement section was installed in a flow loop capable of delivering water flow rates up to $0.02\,m^3/s$. This corresponds to a mean velocity of $u_{ms} = 0.9\,m/s$ in the measurement section. The flow lines of the loop were $0.1\,m$ diameter PVC pipes. The transition from the circular pipes to the square measurement section were done with $0.6\,m$ long tapered sections. At the inlet to the measurement section a set of three $12\,mm$ thick metalfoam plates were installed to act as flow straightener - resulting in a uniform velocity profile at the start of the measurement section.

LDA measurements were performed using a 2-component probe in the backscatter mode. The probe had a $250\,mm$ focal length. An IFA750 (TSI Incorporated) signal analyzer was used to process the real-time measurement data. The layout of the LDA equipment is shown in figure 2.4. A detailed description of the components can be found in Kritzinger *et al.* (2001) or Groen (2004). Seeding was done with hollow glass beads with a mean diameter range of 8-12 μm and a density of $\rho_p = 1100kg/m^3$.
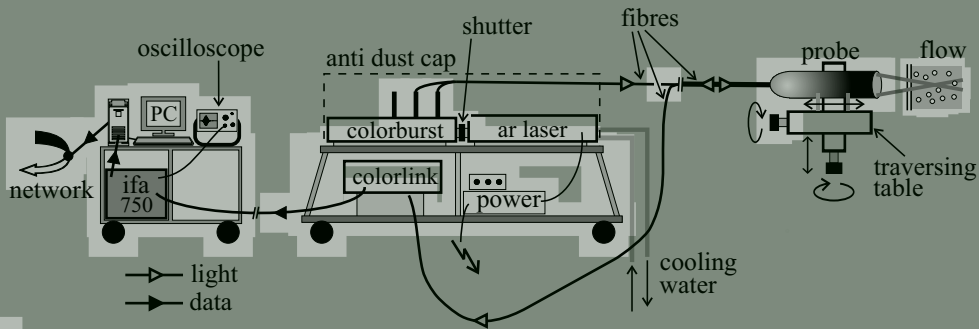
Figure 2.4: *Schematic layout of the LDA equipment used to measure the velocity field. Reproduced with kind permission from Groen (2004).*

2.3.2 Experimental procedure

Sealed duct

The sealed measurement section was used to evaluate the monolith characteristics and the surrounding flow field with a known flow rate through the channels; 100 and 400cpsi monoliths were used with flow rates from 5 to 65 litres per minute, l/min. This corresponds to $500 < Re_{ms} < 7000$ for the measurement section and $90 < Re_c < 2000$ for the monolith mean flow.

The pressure drop over the monoliths was determined by measuring the pressure differential over the sealing plate, as shown in figure 2.3. The flow field around the monolith was determined by measuring profiles of the axial velocity at selected up- and downstream locations in the measurement section.

A key question of this work is to determine the amount of fluid flowing through the monolith. The small size of the monolith channels makes it difficult to place a sensor inside a channel. The intrusive nature of such a sensor might also disturb the flow, resulting in unreliable data. Another option is to try and measure the flow entering or leaving the monolith. Performing such measurements with LDA is not simple for two reasons: (i) the finite size of the measuring volume and (ii) the angle between the two laser beams required to create the measurement volume. To measure the monolith flow rate the liquid velocity is measured as close as possible to the front face of the monolith. This requires the use of an angled probe to remove the 'shadow' formed by the laser beams in a normal (perpendicular) setup. Figure 2.5 illustrates the 'shadow' and how it is resolved by using an angled LDA probe. The probe was set at an angle of 9.5°, resulting (after deflection at the outer air-perspex interface of the measurement section) in an angle inside the measurement section of 7.1°. This was sufficient to position the measurement volume on the surface of the monolith. The tilted probe has negative effects. Due to different refraction at the air-Perspex and Perspex-water interfaces, the measurements volumes of the dual probe no longer overlap and the measurements are not taken at the same location.
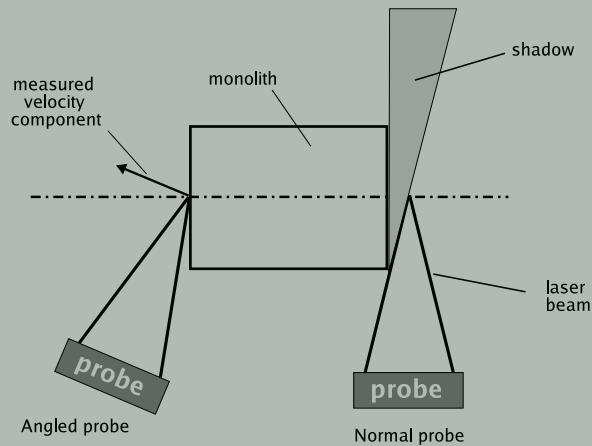
Figure 2.5: *The normal LDA setup results in a 'shadow' close to the monolith where no measurements can be made. Setting the LDA probe at a small angle removes the 'shadow' and allows measurements up to the solid surface of the monolith.*

This is not critical as only one component, the axial velocity, is important and the translation of the LDA probe is calculated according to the movement of the corresponding measurement volume. Secondly, the refraction causes a small shift in the location of the beam waists. As a result the measurement volume is no longer located exactly at the intersection of the two beam waists and this can lead to reduced data rates and even biased velocity measurements (Zhang & Eisele, 1998).

The application of the angled probe was evaluated by measuring the flow on the upstream surface of a 400cpsi with a set flow rate in the sealed duct. The measured values were integrated and the resulting mass flow compared to the set value. Differences were negligible. Measurements with the angled probe on the downstream face were abandoned due to the presence of multiple small jets at the exit of the monolith.

Open duct

In the open measurement section the fraction of liquid passing through the monolith channels is not known. This fraction was measured using an angled LDA probe. The 50, 100, 200 and 400cpsi monoliths were tested with flow rates from 250-1200 *l/min* ($28000 < Re_{ms} < 130000$). In addition, the axial velocities for a 400cpsi monolith were measured 20mm downstream from the monolith downstream surface.

2.4 Numerical study

The flow through the measurement section and the monolith (see section 2.3.1) were investigated using computational fluid dynamics (CFD). This study was motivated by the need to validate the CFD method, in particular the modeling of the monolith, for later use when investigating the MSR. The commercial CFD code Fluent[1] was used for all calculations.

2.4.1 Governing equations

The Reynolds-averaged Navier-Stokes (RANS) equations govern the transport of the averaged flow quantities, with the whole range of the scales of turbulence being modeled. Details of the derivation can be found in standard texts e.g., White (1991) or Ferziger & Perić (2002).

For incompressible flow the continuity equation is

$$\frac{\partial u_i}{\partial x_i} = 0. \tag{2.19}$$

The corresponding momentum equation can be written as

$$\rho \frac{\partial u_i}{\partial t} + \rho \frac{\partial}{\partial x_j} \left(u_i u_j \right) = -\frac{\partial p}{\partial x_i} + \frac{\partial}{\partial x_j} \left[\mu \left(\frac{\partial u_i}{\partial x_j} + \frac{\partial u_j}{\partial x_i} \right) \right] + \frac{\partial}{\partial x_j} \left(-\rho \overline{u_i' u_j'} \right) + s_i. \tag{2.20}$$

The variables now represent the ensemble-averaged values. The additional unknown terms $\overline{u_i' u_j'}$, called the Reynolds stresses, represent the effect of turbulence and must be modeled to obtain closure. Appendix D provides a reference to the transport equations and model constants as applied in this thesis. The turbulence model for this chapter is discussed in section 2.4.4. Furthermore, p is the static pressure and s_i body forces (including model-dependent source terms). The interaction of the monolith with the flow is modeled through the s_i term - see section 2.4.4.

2.4.2 Geometry and meshing

The simulations of the monolith in the square test section were performed with a quarter model (making use of the vertical and horizontal symmetry) of the complete square measurement section (see figure 2.3). Figure 2.6 shows a close-up of the CFD geometry and the surface mesh at the monolith location. The mesh consisted of 850000 hexahedral and tetrahedral cells.

The average mesh spacing in the region of the monolith was $1mm$. For simulations with the sealed measurement section the flow rate and mesh density resulted in a near wall mesh with $y_{max}^+ < 10$. For the open measurement section (with higher flow rates) the near wall mesh was such that $25 < y^+ < 120$.

---

[1] Versions used for this thesis: 6.1.22, 6.2.16, 6.3.26 and 12.1.2.
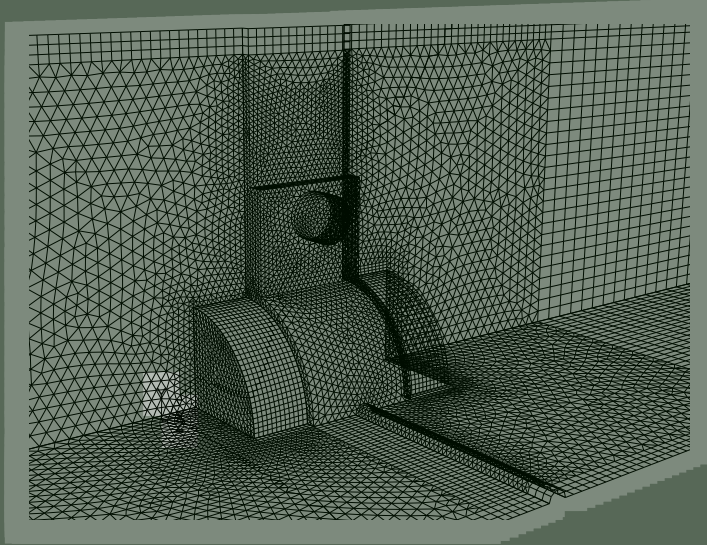
Figure 2.6: *Surface mesh around the monolith that was used in the quarter model of the monolith in a square duct.*

2.4.3   Boundary conditions

At the inlet to the flow domain, corresponding to the start of the square measurement section, a uniform velocity boundary condition was applied according to the flow rate of each case. Turbulence properties for the inlet were set to 5% turbulence intensity with a length scale of 3*mm*. The small size of the length scale was based on the pore size of the metal foam used to equalize the inlet flow in the experiments. An outflow boundary was used at the exit of the simulation domain. Standard symmetry conditions were applied on the horizontal and vertical symmetry planes. All walls were modeled as smooth, no-slip walls.

2.4.4   Physics and modeling

Turbulence model

The shear-stress transport k-ω (SST-KW) model of Menter (1994) was used for the simulations of the monolith in a duct (seec section D.8 for model information). This was motivated mainly by the fact that the k-ω models are less sensitive to the value of the wall normal distance. In the flow setup the large variation in velocity makes it difficult to build a high quality near wall mesh - i.e., a mesh with consistently acceptable near wall spacing in all areas for all flow rates. The latter is required for k-ϵ models. The transport equations for k and ω, as well as the model constants,

are presented in section D.8.

Monolith modeling

Simulations which include the flow in individual channels of the monolith are not feasible because the required computational grid would be very large and result in very long computations. Therefore, the presence of the monolith is included in the simulations with a momentum sink (through s_i in equation 2.20) that models the pressure drop behavior of the monolith. The momentum sink requires anisotropic loss coefficients to correctly account for the presence of the walls of the monolith channels.

The treatment of porous regions varies depending on the CFD code used. Earlier versions of Fluent (6.1.22, 6.2.26) did not have an option to model the relative velocity inside a porous region, i.e., account for a higher velocity as result of the obstruction to the flow in the porous cavities. For this reason (and the requirement of a rotating monolith for the monolith stirrer studies) the model for the monolith was developed as a momentum source and not through the porous media settings available in the graphical user interface (GUI).

The developing channel flow theory presented in section 2.2.2 excludes the contraction loss associated with the flow accelerating into the monolith channels. In 'canned' converter configurations, this energy is recovered to a certain extent at the exit of the monolith - the irreversible losses are small (see values for E_{add} in table 2.3). Where this flow exits the monolith into an unconfined or semi-confined volume (as in this study), this energy is dissipated downstream from the monolith. As a result, the contraction loss is included in the monolith loss term when modeling the monolith as a porous region.

This highlights a fundamental problem in modeling the monolith as a porous body. The assumption dictates that the flow at the exit face of the monolith will have a lower momentum in the porous model than in the actual monolith exit flow. To further illustrate, consider that the mass flow for both cases must be identical - for reaction calculations the mass flow through the monolith determines the reaction and conversion rates. However, the porous model exit flow area is larger than the actual flow area such that

$$\sum_{i=1}^{N} (A_c) = N \cdot A_c = \epsilon_v \cdot A_m \tag{2.21}$$

In this equation the summation is over N, the number of channels in the monolith, and the monolith cross sectional area is $A_m = \pi d_m^2$. Since the mass flows are equal, it follows that the equality

$$\rho(N \cdot A_c)u_c = \rho A_m u_m, \tag{2.22}$$

holds only if $u_c > u_m$. Momentum is the product of mass and velocity $u \cdot m$. Therefore the momentum of the flow leaving the monolith is less for the porous model than for the actual case.

The additional inlet flow pressure drop that must be added to the monolith source is derived from the difference in the kinetic energy of the flow outside the monolith, and the flow inside the monolith channel. This results in a dimensionless pressure drop

$$\Delta p_{ifl}^* = \left(1 - \epsilon_v^2\right) \tag{2.23}$$

The assumption is that this energy is not recovered at the exit of the monolith.

It is convenient to write the momentum source term as (ANSYS, 2009):

$$s_i = - \left(C_{ij} \mu u_j + \frac{1}{2} \rho D_{ij} |u| u_j \right) \tag{2.24}$$

In this form of the equation the velocity components, u_j, represent the superficial velocities in the porous zone and C_{ij} and D_{ij} are the viscous and inertial loss coefficient tensors respectively. Due to the non-linear behavior of equation 2.8 for small values of L^*, the loss coefficients C_{ij} are not constants, but functions of the velocity in the monolith. With Fluent the solver variables can be accessed and adjusted during the computation through the use of user defined functions (UDFs). A UDF, written in C, was developed to calculate the loss coefficients during the simulation using equation 2.8. The loss coefficient D_{ij} is used to include the inlet loss from equation 2.23 - this is a constant for a given monolith.

The loss coefficient tensors, C_{ij} and D_{ij}, are symmetric and each forms a diagonal matrix when the coordinate axes are parallel with the principal axes (Johnson, 1998). The effect of the monolith channel walls on the fluid must be included numerically as part of the momentum source (equation 2.24). The infinite flow resistance in the direction normal to the monolith channels (due to the non-permeable channel walls) cannot be modeled numerically. Instead, the loss coefficients in the normal direction is set to be three orders of magnitude higher than for the channel direction (ANSYS (2009)). If the x-axis is aligned with the monolith channel, the resulting components of the loss coefficient tensors are:

$$
\begin{aligned}
C_{xx} &= \frac{(f \cdot Re_c)}{2 \cdot \epsilon_v \cdot d_c^2} \\
D_{xx} &= \frac{\left(1 - \epsilon_v^2\right)}{L_c \cdot \epsilon_v^2} \\
C_{yy} &= C_{zz} = 1000 \cdot C_{xx} \\
D_{yy} &= D_{zz} = 1000 \cdot D_{xx} \\
C_{ij} &= D_{ij} = 0, \ i \neq j.
\end{aligned}
\tag{2.25}
$$

Details of the development and testing of the UDF, including extension to the rotating case for the MSR (Chapter 5), are presented in appendix F.
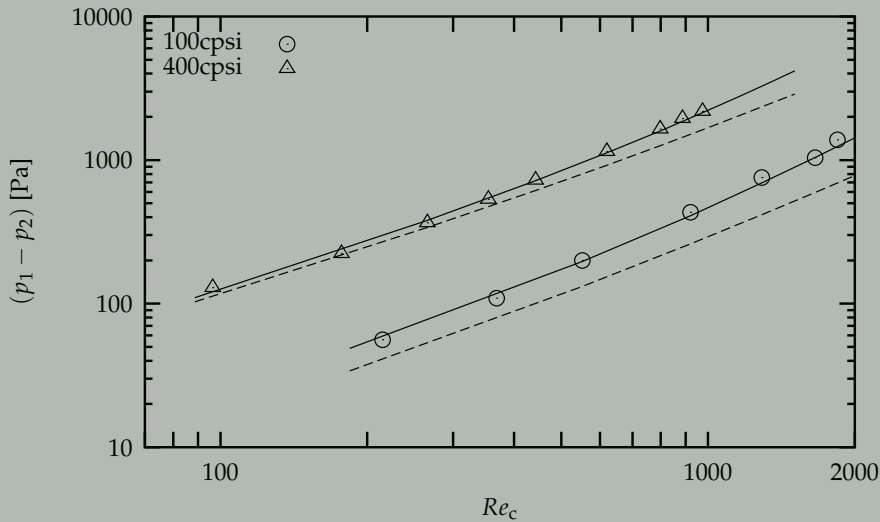
Figure 2.7: *Comparison of the experimental (symbols) and CFD (solid lines) results of the pressure difference over the monolith in a sealed duct. The comparison is based on the pressure drop measured over the pressure tappings. The dashed lines show the CFD pressure drop over the monolith channels.*

2.4.5 Solver settings

Second-order upwind spatial discretization was used for the momentum equation. The SIMPLE method was used for pressure-velocity coupling.

In addition to the normal residual monitoring, several probes were used to judge convergence of parameters of interest (e.g., pressure drop). Simulations were considered to be converged when the values were changing by less than 0.1% during further iterations.

2.5 Results and discussion

This section presents the results of the experimental and computational study of flow through and around a monolith in a square duct.

2.5.1 Flow through the monolith only

The first results are for the sealed measurement section - all fluid pass through the monolith with a known flow rate.
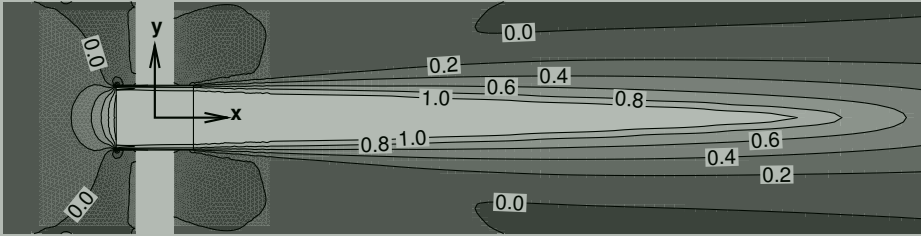
Figure 2.8: *Contours of u_x/u_m inside the measurement section for a 400 cpsi monolith in a sealed duct with a flow rate of 50 l/min. Flow is from left to right and the white area around the monolith represents the removable blocking plate that was not included in the model.*

Pressure drop

Experimental and CFD results for the pressure differential over the sealing plate are presented in figure 2.7. The CFD data were taken from the same location as the pressure tappings in the actual experiment (fig 2.3). The pressure difference between the front and rear of the monolith, obtained from CFD, is drawn with dashed lines - these values differ from the measured data due to a pressure gradient between the monolith and the wall of the measurement section where the pressure tappings were located. The agreement between simulation and experiment is very good for the range of flow rates considered. This shows that the pressure drop model, as implemented in the UDF, properly accounts for both the flow rate and the geometrical parameters (i.e., monolith void fraction and channel diameter).

Flow field - axial velocities

The general features of the flow for the sealed duct is shown in figure 2.8 with normalized axial velocity contours, obtained with CFD, on a vertical plane through the middle of the duct. The axial velocities for the sealed monolith are normalized by the monolith superficial velocity

$$u_m = \frac{\phi}{A_m} = \epsilon_v \cdot u_c. \qquad (2.26)$$

On the upstream side the flow is accelerated for the passage through the monolith. This acceleration results in a large positive velocity gradient in front of the monolith face. The exit flow from the monolith appears as a jet going down the axis of the measurement section.

Figure 2.9 shows axial velocity profiles, normalized with the mean axial velocity in the duct, u_{ms}, upstream of the monolith as a function of the non-dimensional radius, r^*. The non-dimensional radius, r^*, is defined as $2y/d_m$ for vertical and $2z/d_m$ for horizontal lines. The 400cpsi monolith data were measured on a vertical line 18mm upstream of the monolith and the 100 cpsi data at 20mm upstream. The
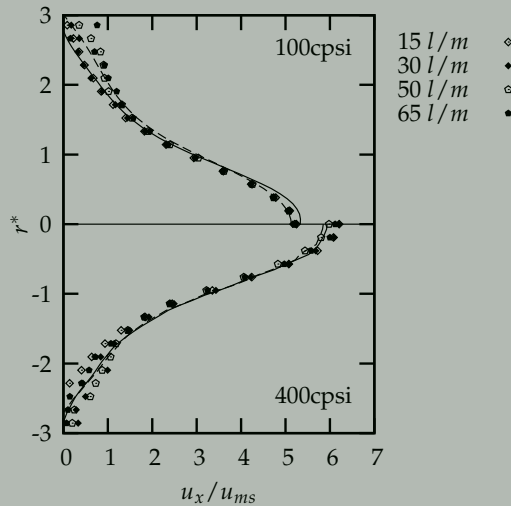
Figure 2.9: *Profiles of u_x/u_m on a vertical line upstream from the monolith. Experiments (symbols): 15, 30, 50 and 65 l/min. CFD results: 5 l/min (dashed line) and 65 l/min (solid line).*

profiles for each monolith are similar for all experimental data (symbols) and the lowest (5l/min) and highest (65l/min) flow rates simulated (lines). CFD results at other flow rates are similar as well.

Figure 2.10 compares LDA and CFD profiles of the axial velocity, normalized with the monolith mean velocity u_m, on a vertical line at 40mm (left) and 80mm (right) behind the monolith for the same flow rates as in figure 2.9. The experimental velocities are consistently higher than the CFD values in the 'jet' ($-1 < r^* < 1$). The most important factor affecting the axial flow behind the monolith is the lack of resolved monolith channels in the CFD. Therefore the maximum axial velocity in the physical monolith is always higher than the superficial value that is used by the CFD model. This is to be expected based on the discussion around equations 2.21 and 2.22 in section 2.4.4.

The discrepancy between the CFD and experimental exit profiles was investigated further by looking at the profiles closer to the monolith. Figure 2.11 shows the development of the normalized axial profile at 4 positions downstream from the monolith. At the monolith exit (4 mm) the experiments and CFD differ significantly. The experimental data show a high velocity around the outer radius of the monolith. This, together with the higher (than CFD) mean axial velocity further downstream in the jet, show a strong entrainment which is absent in the CFD data. Additional simulations with different turbulence models (realizable k-ϵ, Reynolds stress model) and increased grid density produced similar CFD results. This is ascribed to the fact that, at the monolith exit, the actual flow consists of a large number of square laminar jets. The momentum of the jets is higher than that of the mean monolith velocity used in the CFD as discussed in section 2.4.4.
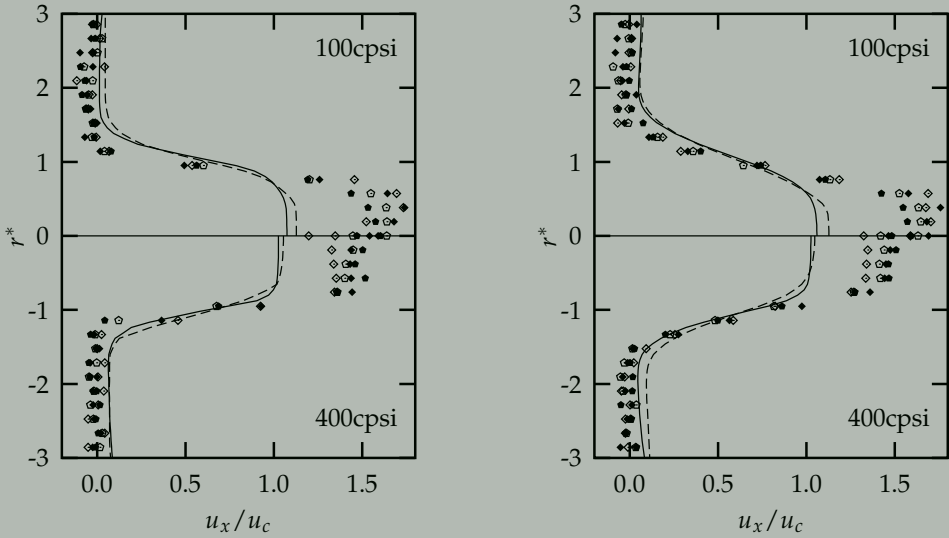
Figure 2.10: *LDA and CFD profiles of the axial velocity normalized with the monolith channel velocity, u_x/u_c, on a vertical line 40mm (left), and 80mm (right) downstream from a 100cpsi and a 400cpsi monolith. Symbols for the various flow rates are the same as in figure 2.9.*
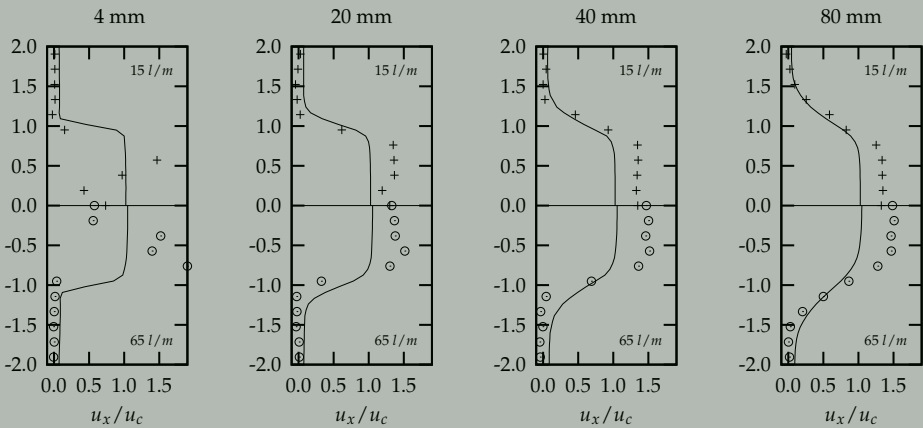
Figure 2.11: *Normalized axial velocity profiles on four positions downstream from a 400cpsi monolith. The top half of the graph displays data for a flow rate of 15l/min and the bottom for a flow rate of 65l/min.*
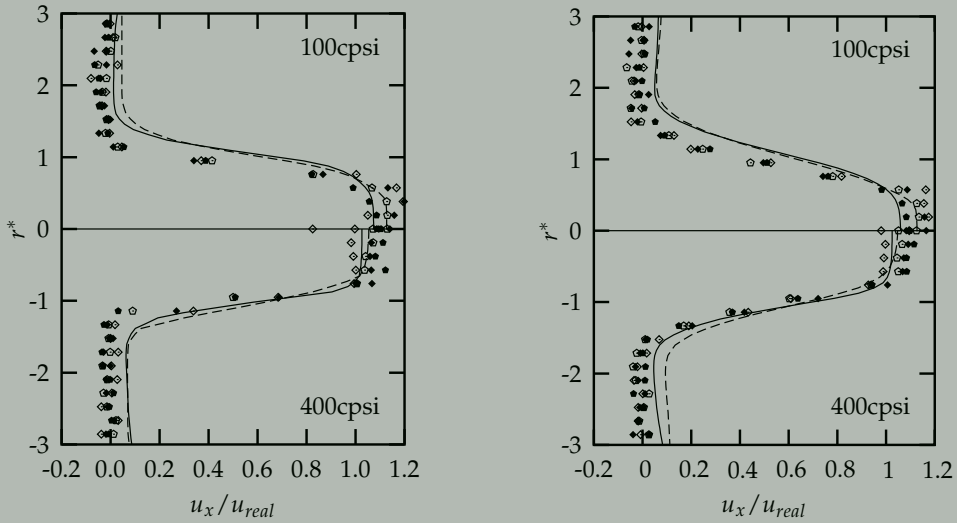
Figure 2.12: *LDA and CFD profiles of the axial velocity normalized by the physical (real) velocity on a vertical line 40mm (left), and 80mm (right) downstream from a 100cpsi and a 400cpsi monolith. The experiments are normalized with the mean channel velocity, u_c, and the CFD data by the mean superficial velocity u_m.*

Instead of normalizing both data sets with the monolith axial velocity, u_m, each data set is normalized with the physical velocity. Therefore CFD is normalized by u_m and the experiments by u_c. Figure 2.12 show the result of normalizing the axial velocity profiles with the physical velocity for each case - analogous to scaling with the 'jet' momentum. The data now show similar profiles for the CFD and experiments.

This hypothesis is further confirmed by simulations of a resolved 50cpsi monolith with the individual channels in the geometry. The resolved simulations, accounting for the higher velocities in the individual jets, show good agreement with experimental velocities. Results of these simulations are shown in appendix B.

Monolith flow rate - sealed duct

Axial velocities were measured on the upstream face of a 400cpsi monolith using the angled LDA probe (figure 2.5). Figure 2.13 compares profiles of the normalized axial velocity, u_x/u_m, on a vertical and horizontal line on the upstream face of a 400 cpsi monolith for a flow rate of 50 l/min. Due to the finite size of the LDA measurement volume the actual measurements were obtained on a plane slightly in front of the monolith surface - the offset is estimated to be $0.2 - 0.7mm$. Therefore the CFD data was extracted from a plane $0.5mm$ upstream from the monolith surface. The agreement between measurement and simulation is good.
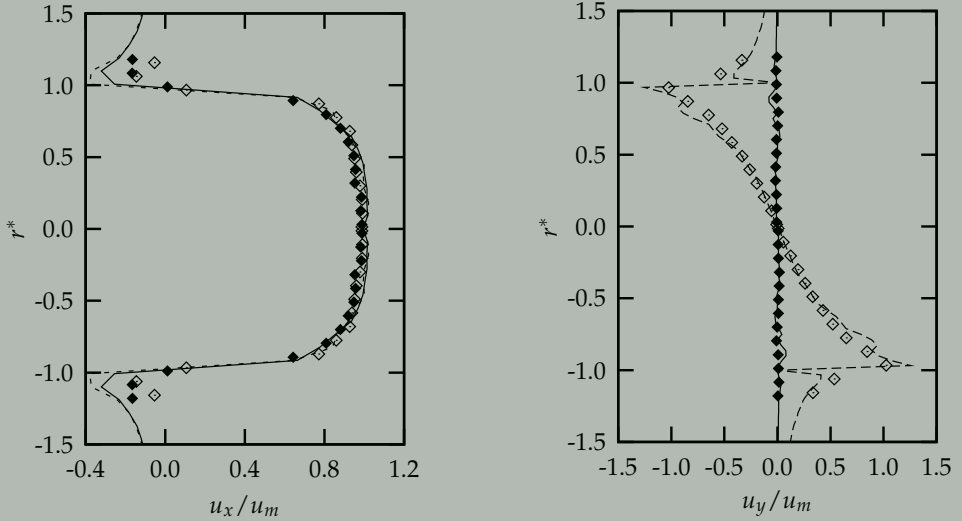
Figure 2.13: *Profiles of axial velocity (left) and the vertical velocity (right), normalized with the monolith superficial velocity u_m, on the surface of a 400cpsi monolith in a sealed measurement section with a flow rate of 50 l/min. Data were obtained from a horizontal line (EXP - solid symbols; CFD - solid line) and a vertical line (EXP - hollow symbols; CFD - dashed line) on the upstream surface of the monolith.*
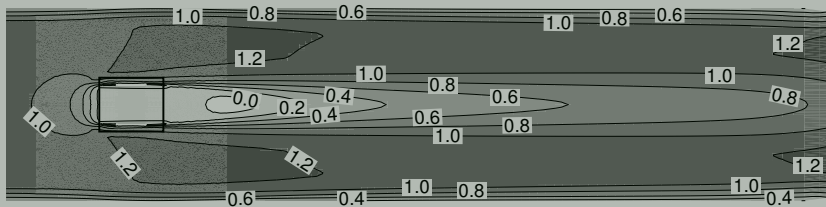
Figure 2.14: *Contours of the normalized axial velocity, u_x/u_{ms}, on a vertical plane through the open flow section with a 400cpsi monolith and a flow rate of 65 l/min.*
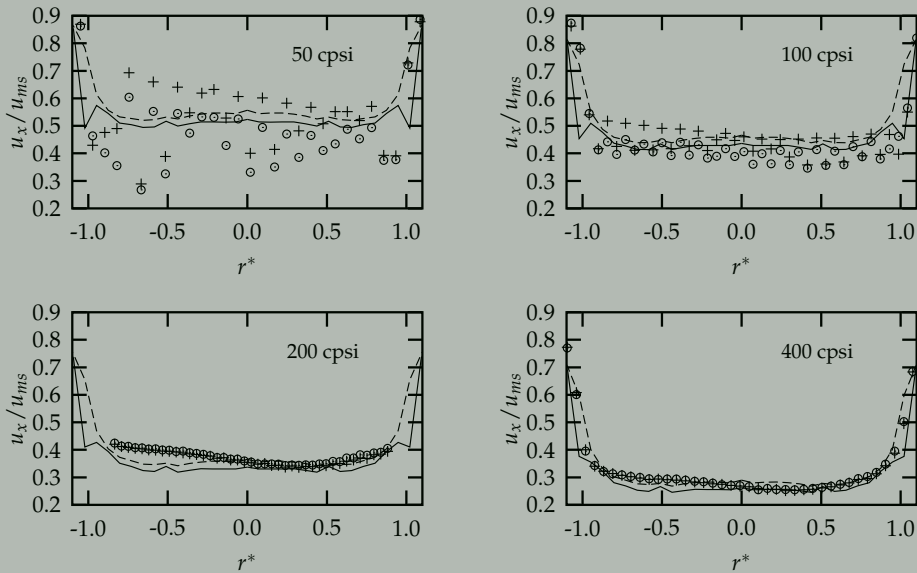
Figure 2.15: *Normalized axial velocity profiles for 4 different monoliths with a flow rate of 1000 l/min. Measurements were performed on 2 adjacent vertical lines (symbols) on the upstream surface of the monolith. CFD data were extracted from a vertical line on the upstream surface of the monolith (solid curve) and at 1mm upstream from the face (dashed curve).*

2.5.2 Flow through and around the monolith

Flow field - axial velocities

In the case of an open measurement section, the flow can pass either through the monolith or flow around it. Figure 2.14 shows axial velocity contours, now normalized with the mean velocity in the measurement section, u_{ms}, on a vertical plane through the flow domain.

In this case the monolith acts as a bluff body, decelerating the core of the flow as it approaches the upstream face of the monolith. This again leads to a large velocity gradient (now negative) in front of the monolith. The 'wake' of the monolith extends downstream and gradually mixes into the bulk flow again.

Monolith flow rate - open duct

Figure 2.15 shows examples of the LDA data used to determine the monolith flow rate. For each case the axial velocity was measured with an angled LDA probe on 2 vertical lines on the upstream face of the monolith. The selected cases, with a flow of 1000 l/min are representative of the full data set (4 monoliths and 5 flow rates - see section 2.3.2). CFD results are shown for 2 profiles - one extracted at the monolith face, and one located 1mm upstream of the monolith face. The difference
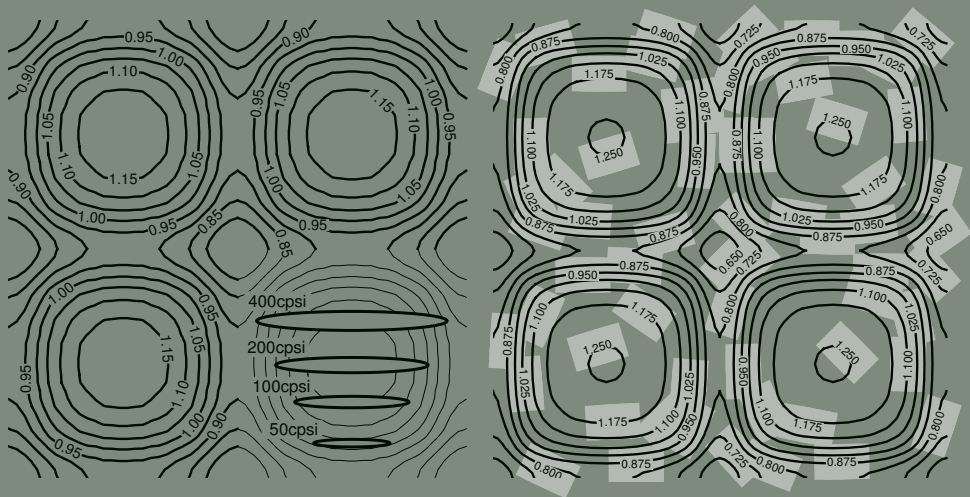
Figure 2.16: *Contours of the normalized axial velocity, u_x/u_m on a plane 0.5mm upstream from a monolith with square channels of diameter d_c. Left: Contours for a 400cpsi monolith with $d_c = 1.09mm$. Right: Contours for a 50cpsi monolith with $d_c = 2.98mm$. The insert shows the relative size of the LDA measurement volume for different monoliths.*

between the two CFD profiles is small compared to the scatter in the experimental data, except for the 400cpsi monolith. The experimental data agree reasonably with simulation results, but show significant scatter for the 50 and 100 cpsi monoliths. Two factors affect the scatter in the LDA data: (i) the size of the LDA measurement volume relative to the monolith channel size, and (ii) the effect of the monolith channels on the flow profile upstream of the inlet to the monolith.

Figure 2.16 shows simulated normalized axial velocity contours, u_x/u_m, on a plane, parallel to the monolith face, at 0.5mm upstream from the monolith. The size of the LDA measurement volume is shown overlayed to scale to show the relative size of the monolith channels for the different monoliths used in this study. The contours show that the flow field no longer has a uniform velocity, but that the effect of the channels and walls is present at this upstream position - normalized velocities differ up to $\approx 25\%$ from the mean. The size of the LDA measurement volume relative to a 400cpsi monolith is such that the probe samples over a large part of the flow field, acting like a spatial filter, and resulting in a 'mean' velocity measurement with small scatter in the data. In contrast, the probe volume is small relative to a 50cpsi monolith, providing a more detailed measurement which resolves the axial velocity field - this results in a larger scatter as observed in the measured data.

Figure 2.17 shows the mean axial velocity, normalized with mean velocity in the measurement section, as a function of the flow rate (expressed as the duct mean velocity) for all the experiments. The data show good agreement between the experiments and CFD for all but the lowest velocities. The monolith flow rate shows
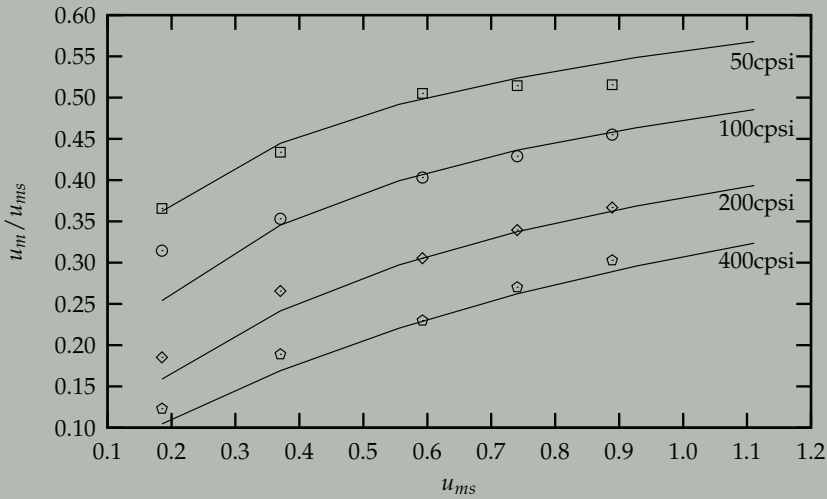
Figure 2.17: *The monolith flow rate, taken as the mean axial velocity on a profile measured upstream of the monolith face, as a fraction of the mean free stream velocity in the open measurement section for a range of flow rates and different monoliths.*

a non-linear dependence on the free stream velocity. A significant amount of liquid passes through the monolith.

2.6 Conclusions

The pressure drop through the monolith is important when modeling the flow through and around an open monolith. The present results show that the pressure drop characteristics of the monolith can be modeled accurately if the contribution of the developing flow in the inlet of the channels is taken into account - the correlation of Hawthorn (1974) provides such a pressure drop model. In addition, the assumption of modeling the monolith as a large number of parallel flow passages was shown to be acceptable. We show that attempts to linearize the pressure drop equation to a quadratic function of velocity, will work only if $L^* > 10.0$. For smaller L^* the non-linear behavior of the developing flow cannot be correlated in this manner.

The implementation of the pressure drop model in a UDF was successful. The agreement between the CFD and experimental pressure drop results, as well as flow velocity results upstream from the monolith, were confirmed for a range of flow rates and different monolith geometries. Comparison of the flow field downstream from the monolith showed that the UDF is unable to replace the actual monolith if an exact prediction of the flow field in the vicinity of the monolith is required. It was shown that downstream velocities can be predicted accurately

when performing a simulation which fully resolves the individual monolith channels. This, however, is not feasible for a full MSR simulation. The pressure drop prediction and the qualitative prediction of the flow field are satisfactory for the purposes required from the present modeling effort.

The monolith flow rate in the open measurement section was modeled with good accuracy. The results show that LDA with an angled probe can give a reliable estimate of the monolith flow rate, if the physical aspects such as the finite probe volume relative to the monolith channel size are taken into consideration.

Chapter 3

An engineering model for monolith channel flow

3.1 Introduction

Since the rate of mass transfer between the bulk fluid and the monolith channel walls is a function of the fluid velocity, the mass flow of fluid passing through the monolith in a monolith stirred reactor (MSR) is an important parameter for reactor design. This parameter is unknown as the fluid can flow either through the monolith or pass around it. One of the main aims of this study is to characterize the channel velocity.

Although CFD simulations can be used to calculate the flow distribution, it is not feasible to repeat simulations for every possible combination of parameters. Therefore, in this chapter an engineering model is proposed that allows calculation of the flow split from the parameters which define the configuration. As a first attempt, the model is used to calculate the flow split for the monolith in channel flow (Chapter 2).

The first section describes the model development. This is followed by a section on the drag of an axial cylinder, an important parameter for the model, for which no applicable literature was available. In the last part the model is used to calculate the flow split for a number of configurations. Results are compared to experimental data from the previous chapter.

3.2 Development of the model

Referring to figure 2.3 with the sealing plate removed, the fluid passing the monolith will either flow through the monolith channels or go around the monolith. In
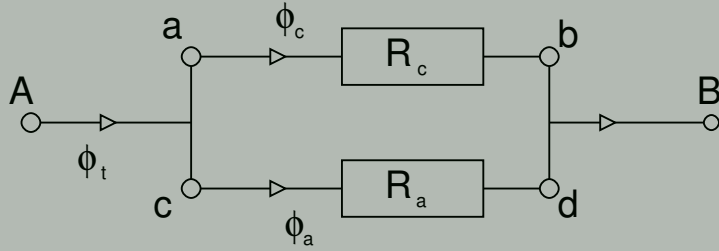
Figure 3.1: *Schematic drawing of the parallel flow paths: The total volume flow ϕ_t splits into a portion going through the monolith channels, ϕ_c, and the rest flows around the monolith, ϕ_a.*

our model the assumption is that these two options can be approximated by two flows in parallel with different losses (resistance), but similar pressure drop (potential). Figure 3.1 shows a schematic of the system where the flow around is denoted by subscript a and the flow through the monolith channels by subscript c.

The resistance to the flow is characterized by the flow losses associated with each path. In the corresponding analysis of electrical circuits, Ohm's law states that the resistance is proportional to the ratio of the electrical potential to the current.

$$R = \frac{V}{I}. \tag{3.1}$$

In the fluid analogy the resistance is proportional to the ratio of the pressure drop to the volume flow of fluid.

$$R = \frac{\Delta p}{\phi} \tag{3.2}$$

This allows for a consistent comparison of energy consideration as well. In electric circuit analyses the power dissipated in a resistor is equal to the product of the potential and the current. Using equation 3.2 the power dissipated in a 'flow resistor' can be calculated from the product of the pressure drop over, and the volume flow in that component - this implicitly assumes that the inlet and outlet velocity for the component are equal (constant area duct).

The volume flow rate for each component (path) can be written as a function of the total volume flow rate and the ratio of the flow resistances as follows:

$$\phi_c = \frac{\phi_t R_a}{R_c + R_a} \tag{3.3}$$

$$\phi_a = \frac{\phi_t R_c}{R_c + R_a} \tag{3.4}$$

There are two complications when using this approach: (i) In a MSR the flow around the monolith is not confined to a pipe and it is not obvious what resistance will be representative for that flow, and (ii) the flow resistance is a function of the unknown flow rate (velocity) and therefore requires iterative solutions.

3.2.1 Resistances

The relationship between pressure drop and flow rate for the monolith channel flow, R_c, was investigated in chapter 2. The loss coefficients presented in equation 2.25, resulted in good correlation with experiments and is used to determine the resistance to flow over the monolith.

The pressure drop for flow around the monolith is not known. For general bluff body flows, this pressure drop is correlated by means of a drag coefficient, C_d, such that:

$$\Delta p = \frac{1}{2}\rho u_a^2 C_d \tag{3.5}$$

Here u_a is the velocity of the flow around the object, which in an infinite domain, is equal to the velocity, u_∞, far upstream from the object.

To close the model, the drag coefficient of the monolith is required. Since the model actually superimposes two flow paths, the drag coefficient of an impermeable monolith (i.e., a solid cylinder) should be used. Literature data on this parameter are scarce and where available, they do not include wall effects (blockage) due to the finite dimensions of the surrounding channel. Therefore a set of numerical experiments was performed to try and characterize the drag coefficient for an axial cylinder in a confined duct (similar to the experiments of chapter 2). This is addressed in the following paragraph.

A second closure problem relates to the choice of the volume flow rate chosen for use in equations 3.3 and 3.4. In the limit, as the resistance to flow through the monolith tends to zero, i.e., $R_c \to 0$, the total flow should pass through the monolith and no pressure drop is recorded for flow around. As the channel resistance becomes large, i.e., $R_c \to \infty$, the flow through the monolith is blocked, $\phi_c \to 0$, and everything flows around. Then the equation should recover the pressure drop calculated from equation 3.5. If the affected region of the flow is assumed to be determined by the presence or absence of the monolith, the total volume flow rate calculation can be based on the area of the monolith normal to the flow.

$$\phi_t = u_\infty A_m \tag{3.6}$$

Here u_∞ is the free-stream velocity approaching the monolith and A_m is the monolith cross-sectional area.

3.2.2 Model implementation

The model parameters that define the system can be collected in three groups:

Fluid properties: density ρ, and viscosity μ, of the working fluid.

External flow: duct diameter D, monolith diameter d_m and length L_m, and drag coefficient C_d.

Internal flow: monolith channel diameter d_c and length L_m, monolith open frontal area fraction ϵ_v, and pressure drop correlation for channels $f \cdot Re_c$.

A small `perl` program was constructed to solve the flow split using an interval halving method. The logic of the program is given in table 3.1.

Table 3.1: *Program logic to calculate the monolith flow split.*

Set parameters for case
Guess $u_c^* = u_\infty/10$
Calculate channel resistance, $R_c(u_c^*)$
Calculate $\phi_a = \phi_\infty - \phi_c^*$
Calculate resistance around, $R_a(\phi_a)$
Determine u_c from equation 3.3
Set $u_c^* = u_c^* + (u_c - u_c^*)/2$
Repeat until $(u_c - u_c^*) \leq 10^{-7} \cdot u_c$

3.3   Drag coefficient of a confined axial cylinder

3.3.1   Background

The value of the drag coefficient is required for the monolith channel model. The drag force is most often reported in terms of the non-dimensional drag coefficient, C_d, defined as

$$C_d = \frac{F}{0.5\rho u^2 A_c} \tag{3.7}$$

Here F is the total drag force (sum of pressure and viscous contributions). Both in experiments and in CFD simulations, the drag force on a bluff obstacle is influenced by the surrounding walls of the confining channel. This is caused by a change in the pressure distribution on the surface of the obstacle due to the higher velocity in the gap between the obstacle and the wall. As shown by Di Felice *et al.* (1995), one of the first attempts at a correction for the effect of walls, was done by Newton (1687) who performed experiments on the terminal settling velocities of spheres. The terminal settling velocity of a sphere u_{st} in an unconfined fluid is related to the settling velocity in the confined case u_s by a factor k_N, such that $u_s = k_N \cdot u_{st}$. The correction factor given by (Newton, 1687) is

$$k_N = (1 - B)(1 - B/2)^{0.5} \tag{3.8}$$

Here B, the blockage ratio, is defined as the frontal area of the sphere divided by the flow cross-sectional area of the duct (the blockage ratio is sometimes defined as (d/D) for 2D cases). At the terminal settling velocity, the drag is balanced by the
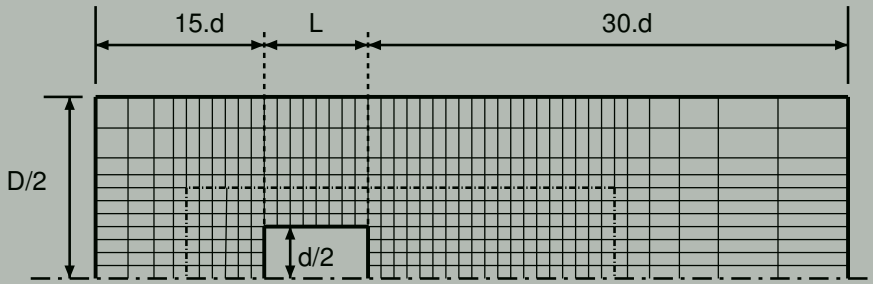
Figure 3.2: *Schematic drawing of a cylinder in axial flow, showing the extent of the computational domain. The inner region with uniform mesh extends from 1d upstream to 4d downstream of the cylinder and has a radius of 1d. The coarsest mesh is shown for clarity.*

gravitational force – therefore we can rewrite u in terms of C_d. The relation between the confined drag C_d and the unconfined value, C_{d0}, then becomes

$$\frac{C_d}{C_{d0}} = \frac{1}{k_N^2} = \frac{1}{(1-B)^2 \, (1-B/2)} \tag{3.9}$$

This effect has been investigated extensively with regards to wind-tunnel aero-dynamics, e.g., for cylinders and wings in cross-flow (West & Apelt, 1982). For a cylinder in cross-flow it was found that wall effects can be neglected for blockage ratios less than 6% (West & Apelt, 1982).

One source for axial cylinder drag coefficients is that of Hoerner (1965), who presented drag data from Eiffel (1907). Other data from Japan (Oda & Hoshino, 1974; Muto & Ueno, 1976) were available. White (1988) lists a few values without giving the origin of the data. More recently the work of Higuchi *et al.* (2008) added more data for this configuration. However, these sources do not contain information on the 'blockage effect'.

In this work we will study the effect of blockage on the drag coefficient for an axial cylinder through CFD simulations of the turbulent flow. The accurate simulation of turbulent flow over a bluff body is challenging. Turbulence models suffer for a number of reasons: strongly retarded stagnation, flow separation, streamline curvature, laminar to turbulent transitions, recirculation, vortex shedding and inherent 3-dimensionality of the flow (Sohankar *et al.*, 2000). Some relief can be had as the current geometry is axisymmetric. For the intended use of C_d in an engineering model we require less accuracy (than that obtainable from more complex modeling with e.g., Large-eddy simulation (LES) or direct numerical simulation (DNS)) and we will therefore investigate the problem in a steady, 2D axisymmetric system, using standard turbulence models available in a commercial solver (Fluent).

The rest of the section is organized as follows: First, the influence of a number of simulation parameters (grid, turbulence model, boundary conditions) were investigated for the case of an axisymmetric cylinder with zero aspect ratio, $AR =$

$L/d = 0$, i.e., a disc perpendicular to the flow. Next, the drag for a range of aspect ratios, $0 \leq AR \leq 4$, was calculated and compared to data from literature. Finally, the influence of blockage, B, on C_d was calculated for $0.0025 \leq B \leq 0.25$ and a fixed aspect ration $AR = 1$.

3.3.2   Simulations

General aspects

Simulations were performed on an axisymmetric section of diameter $D = d/\sqrt{B}$ and length $45d$ (figure 3.2). A cylinder of diameter of d and length L is positioned on the pipe axis with the leading face at $15d$ from the inlet.

The working fluid was water, considered as incompressible and with constant properties: $\rho = 1000kg/m^3$, $\mu = 10^{-3}kg/(m.s)$. At the inlet a mean velocity, u, was set with a 1% turbulence intensity and the turbulent length scale estimated at $0.07 \cdot D$. The obstacle (cylinder) walls were set as no-slip boundaries. The outer wall of the pipe was set as a slip wall. An outflow (convective) boundary was used at the domain exit. Reynolds numbers can be defined using either the mean pipe velocity, u, or the mean gap velocity $u_b = u/(1 - B)$. Therefore

$$Re = \frac{ud}{\nu} \quad \text{and} \quad Re_b = \frac{u_b d}{\nu} \tag{3.10}$$

A commercial finite-volume solver (Fluent) was used to solve the steady-state flow equations (2.19 and 2.20) and relevant turbulence equations (see below and appendixD). Convective terms were discretized using a 2nd order upwind-differencing scheme. Pressure interpolation was done with PRESTO! and the pressure-velocity coupling with the standard SIMPLE algorithm (ANSYS, 2009).

Influence of the grid

The basic grid consisted of an inner and outer region with different mesh densi-ties. The inner region was meshed with a uniform grid of spacing $\triangle x$ ($0.1d$, $0.05d$ or $0.02d$). The upstream boundary of this inner mesh region was at $1d$ from the leading face of the cylinder, its trailing boundary was at $4d$ from the downstream face, and its radial boundary was at a radius of $1d$. The outer region consisted of a mesh stretching uniformly away from the inner mesh region with a geometric rate ($\triangle x_{(i+1)}/\triangle x_i$) of 1.08.

Variations on the basic grid included: (i) a set of three grids with grid spac-ings of $\triangle x = 0.1d$, $0.05d$ or $0.02d$ respectively in the inner region, but for which the boundary layer (first cell distance) was fixed at a distance of $0.0125d$, (ii) three uniform grids with $\triangle x = 0.1d$, $0.05d$, or $0.02d$, and (iii) all grids from (i) with the boundary layer refined to give a dimensionless wall distance $0.75 < y^+ < 1.5$. As a test case, the drag coefficient of a circular disc (or axial cylinder with $AR = 0$), was computed. In general, the drag is a function of the Re number – but in the range $Re > 50000$ the value for a disc is constant at $C_d = 1.17$ (Hoerner, 1965).

Turbulence modeling

Turbulence modeling is an important issue in these calculations. As summarized by Durbin (1996), two-equation models in general, and the standard k-ϵ model (SKE) in particular, predict a too large growth of turbulent kinetic energy in stagnation point flows. The SKE model is therefore not suited to the current configuration, however, it is included for completeness and to illustrate the error made when using it to calculate C_d.

An alternative is to use the realizable k-ϵ model (RKE) (Shih *et al.*, 1995). Briefly, this model includes a variable C_μ in the definition of the eddy viscosity and a different model equation for the dissipation (ϵ) based on a dynamic equation of the mean-square vorticity fluctuations.

The RNG k-ϵ model (RNG-KE) was derived using a mathematical technique called renormalization group theory. The aim was to enhance the standard model to be more accurate and reliable for a wider class of turbulent flows.

Two variations of the standard (SKW and SKW2), as well as the shear-stress transport (SST) k-ω model were also evaluated. The SKW model uses a strain-based relation for turbulence production, while the SKW2 model uses a vorticity based production equation.

The Reynolds stress model (RSM) is a more comprehensive model which solves additional transport equations for each of the individual Reynolds stresses $\overline{u_i' u_j'}$. However, closure of the equations still requires that some properties be modeled. The model applied here makes use of a linear pressure-strain relationship.

The one-equation Spalart-Allmaras model (S-A) is included for comparison.

These turbulence models can be applied either with standard wall-functions (Launder & Spalding, 1974) or without. In the latter case the near wall region is resolved with a higher mesh density.

The turbulence model equations and applicable constants for each model are included in appendix D for reference. Appendix D also presents the detail of the near wall treatment for turbulent flows. The information was taken from the Fluent manual (ANSYS, 2009).

3.3.3   Results and discussion

Influence of meshing and turbulence models

Several combinations of grids and turbulence models were evaluated for the case of an axisymmetric disc. The results of C_d and the length of the recirculation zone behind the obstacle, L_r/d, are presented in table 3.2 for a selected number of cases. Results obtained with wall-functions are shown in the columns 2–5. The mesh for columns 2–5 was based on the smallest grid size, i.e., 0.02d, in the inner region and stretching in the outer region. The results with integration to the wall are presented in columns 6–9. The mesh for these simulations were based on the wall function meshes (columns 2—5), but with the near wall region mesh refined repeatedly until

Table 3.2: *CFD results for a disc, computed with standard wall functions (columns 2-5) and without wall functions (columns 6-9), compared to experimental values of C_d (Muto & Ueno, 1976) and L_r/d (Carmody, 1964). Abbreviations are: exp. = experiment; S-A = Spalart-Allmaras; SKE = Standard k-ϵ; RNG-KE = RNG k-ϵ; RKE = realizable k-ϵ; SKW = Standard k-ω; SKW2 = Standard k-ω with voricity based production; SST-KW = Shear-stress transport k-ω; RSM = Reynolds stress model. Averaged y^+ values on the front, $\langle y^+ \rangle_f$, and the back face of the disk, $\langle y^+ \rangle_b$, are included.*

model	$\langle y^+ \rangle_f$	$\langle y^+ \rangle_b$	C_d	L_r/d	$\langle y^+ \rangle_f$	$\langle y^+ \rangle_b$	C_d	L_r/d
exp.	-	-	1.17	2.6	-	-	1.17	2.6
S-A	64	54	1.39	1.80	0.71	0.58	1.37	1.78
SKE	118	99	1.65	1.61	0.67	0.62	1.59	1.68
RNG-KE	96	67	1.28	2.35	0.71	0.45	1.26	2.37
RKE	93	53	1.17	3.00	0.70	0.42	1.15	2.89
SKW	93	53	3.60	1.16	0.70	0.42	3.50	1.23
SKW2	18	16	1.26	2.68	0.54	0.44	1.24	3.31
SST-KW	93	53	1.19	2.56	0.70	0.42	1.18	2.48
RSM	79	30	1.18	3.03	0.75	0.22	1.12	3.38

the viscous sublayer was resolved. The non-dimensional wall-coordinate, y^+, was averaged on the front, $\langle y^+ \rangle_f$, and rear surfaces, $\langle y^+ \rangle_b$, of the disc to check that the values were appropriate for the respective wall treatments.

Based on all the simulations, a few remarks can be made:

1. Results from the standard k-ω (SKW) model are incorrect, regardless of the near-wall mesh or mesh refinement level. When activating the option of using vorticity based production (in the solver Fluent), the model (SKW2 in table 3.2) gives results in much better agreement with the experiments. It is not clear from the theory manual what the differences are and it was not investigated in more detail here - more information is available from a summary of different k-ω models that are maintained on-line by the NASA Langley Research Centre (Rumsey, 2009).

2. Results from the standard k-ϵ (SKE) model are incorrect, regardless of the near-wall mesh or mesh refinement level. The problem is probably related to the inability of the model to handle anisotropy in the stagnation point on the upstream side of the disc (see Durbin (1996) for a more comprehensive discussion).

3. Results for the the realizable k-ϵ (RKE) and the shear-stress transport k-ω (SST-KW) are similar to the full Reynolds-stress (RSM) model on the finest grid used (and compare well on most others), although RKE gives a somewhat better prediction of the recirculation zone.

4. Comparison of grids where the location of the 1st node was the same as the grid spacing in the inner region, with grids where this distance was fixed
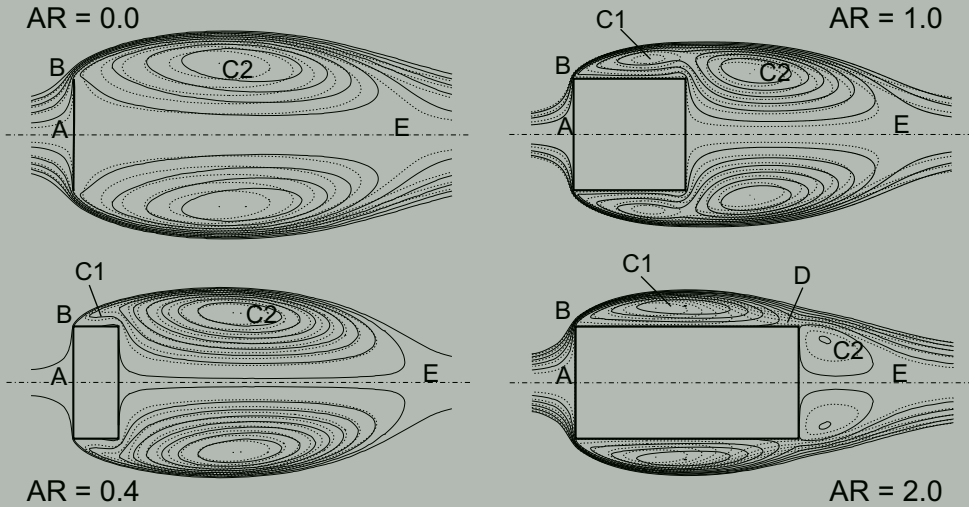
Figure 3.3: *Main features of the flow field characterized with 10 stream function contours in the range 0–1 kg/s, with 0.1kg/s increments. The four figures are for: $AR = 0.0$, $AR = 0.4$, $AR = 1.0$ and $AR = 2.0$. The dashed contours are RKE and the solid contours are RSM results.*

(0.0125d), show that the result is insensitive to the boundary layer height. The result is determined by the mesh resolution away from the disc (on the fine grid spacing, 0.02d, similar C_d values were obtained although the y^+ on the disc surface varied by one order of magnitude in some cases).

5. Comparison of results from grids with a uniform mesh (inner and outer regions) with results where the outer region has a coarser mesh, show negligible difference - this local grid refinement saves CPU time (uniform mesh 736k cells, stretched mesh 33k).

6. The base drag (drag from rear of disc) dominates the C_d.

7. Recirculation lengths are sensitive to a number of parameters and Huang *et al.* (1994) indicate contradictions in existing experimental data. However, values of L_r/d compare well with the data from Calvert (1967), which were measured at similar conditions.

Flow field characteristics

Figure 3.3 shows the streamlines for the flow around axial cylinders with aspect ratios $AR = 0, 0.4, 1.0$ and 2.0 as computed with the RKE and RSM turbulence models. This shows the behavior of the flow in the vicinity of the cylinder. A number of areas can be identified as marked in the figure. At the front of the cylinder there is a stagnation point (A). For $AR > 0$ the flow detaches (separation) at the leading

corner (B) and forms one recirculation zone (C1). For $AR > 2$ the flow re-attaches to the outer surface of the cylinder (D). Behind the cylinder a 2nd recirculation bubble forms (C2), which ends at the location where the axial velocity is zero on the axis (E). The data shown compare the results for RKE (dashed contours) and RSM (solid contours).

Since first reporting on these results (Kritzinger *et al.*, 2004), the drag and flow field around axial cylinders of varying aspect ratio have been measured experimentally by Higuchi *et al.* (2008). PIV results of the time-averaged flow field around an $AR = 1.31$ and an $AR = 1.68$ cylinder are shown in figure 3.4 for comaparison.

Results for different AR

The C_d was calculated for a range $0 \leq AR \leq 4$ using four different turbulence models, SKE, RKE, SKW and RSM. Simulations were performed with the finest inner mesh ($\triangle x = 0.02d$) and using standard wall-functions. The results are presented in figure 3.5 with data from a number of literature sources - Eiffel (1907); Oda & Hoshino (1974); Muto & Ueno (1976); White (1988); Higuchi *et al.* (2008).

As shown in figure 3.5, the RKE, SST-KW and RSM models give results in fair agreement with the available experiments. The values obtained with the SKE are too high and for increasing AR values also show a different trend than the other data. In the region $0 \leq AR \leq 2$ there are some differences between various experimental values (up to 15% at $AR = 0.5, 0.7$). For $0 \leq AR \leq 2$ the RSM C_d values are consistently higher than the RKE data (again up to 15% at $AR = 1.25$). Inspection of the results shows a difference in the size and shape of the re-attachment bubble which forms on the top leading edge of the cylinder. For short cylinders this area interacts with the recirculation bubble located behind the cylinder and therefore could be the source of the differences. The exact reason why the re-attachment bubble shapes are different is most probably related to the differences in the turbulence model physics. This was not investigated in more depth. The results of Higuchi *et al.* (2008) show that the recirculation zone C1 (figure 3.3) re-attached to the cylinder wall at some aspect ratio in the range $1.3 \leq AR \leq 1.6$. This range corresponds to a rapid change in the value of C_d with AR.

No experimental data could be found to compare the variation of the recirculation length with AR. In figure 3.6 the numerical results for four different turbulence models are presented. The recirculation length decreases with increasing AR for $AR < 2$, after which it starts to increase slowly with AR.

The SKE model predicts a short L_r/d for $AR < 2$, after which the values are similar to the RKE, SST-KW and RSM model predictions, but with a smaller rate of increase for $AR > 2$.

Recirculation lengths calculated with RKE and RSM are similar at $AR = 0$, but differ slightly at higher AR. The SST-KW value at $AR = 0$ is lower and closest to the experiments. At $AR = 1.75$ the slope of the RKE and SST-KW data changes, while for the RSM model this occurs only at $AR = 2$. The maximum difference ($\sim$25%) between values of L_r/d for the RSM model compared to RKE and SST-KW, occurs
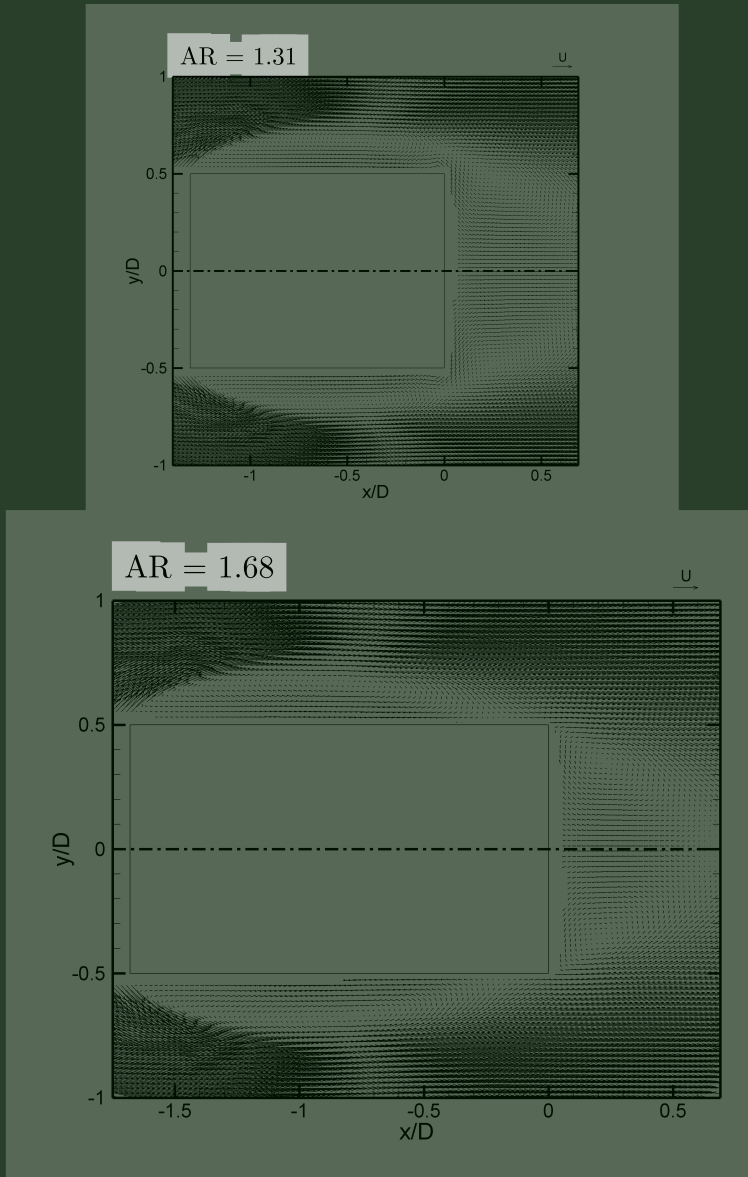
Figure 3.4: *Time-averaged vectors of the flow field around axial cylinders as obtained from PIV experiments. Results are from Figure 13 in Higuchi* et al. *(2008), reproduced here with kind permission from Prof. H. Higuchi.*
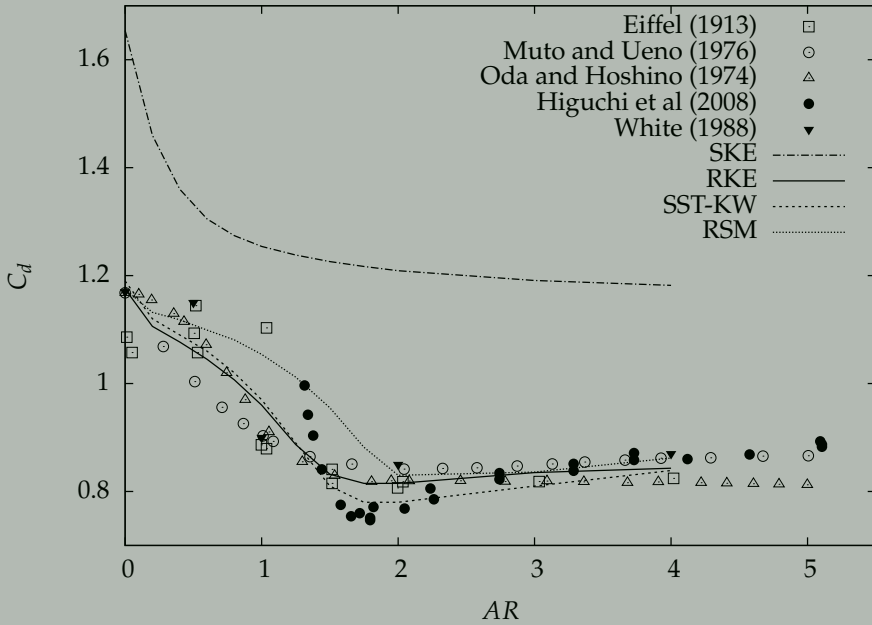
Figure 3.5: *Simulated drag coefficients plotted with experimental data from a number of sources. Lines represent CFD results for standard k-ε (SKE), realizable k-ε (RKE), Shear-stress transport k-ω (SST-KW) and a Reynolds stress transport model (RSM) obtained with standard wall functions.*
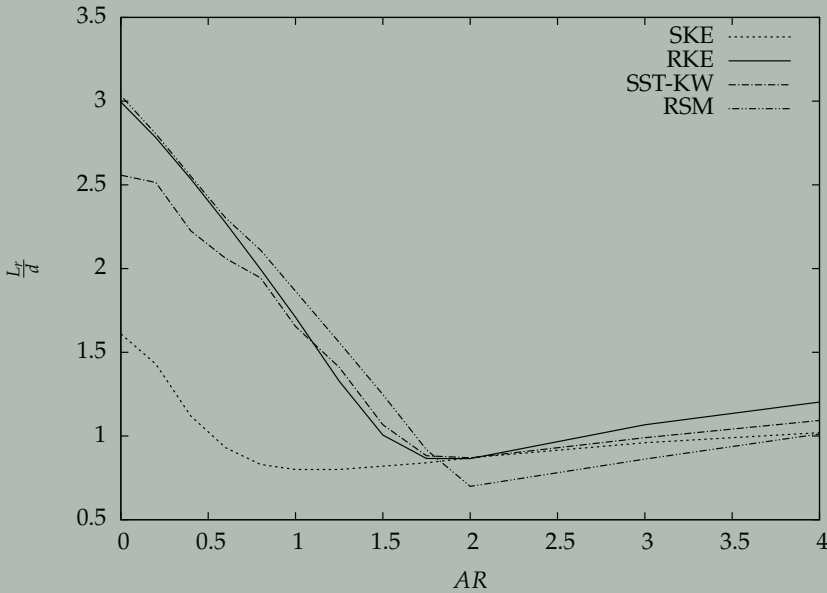
Figure 3.6: *Variation of the recirculation length with AR for standard k-ε(SKE), realizable k-ε(RKE) and Reynolds stress transport (RSM) turbulence models. All results were obtained with standard wall functions.*

at $AR = 2$. The rate of change in recirculation length (slope) for $AR > 2$ is similar for RKE and RSM, although the values are different. The SST-KW r ecirculation length values moves from the RKE values at $AR = 1.75$ ot be closer to the RSM values at $AR = 4$.

Blockage effects for an axial cylinder with $AR = 1$

The effect of blockage on the drag of an axial cylinder was investigated in the range $0 \leq B \leq 0.25$. A single AR (= 1) was selected as this corresponds to values of interest in the MSR research. Drag coefficients are presented in figure 3.7 for 2 sets of simulations with different velocities: *Lines - $Re = 50.10^3$* (with varying Re_b), and *symbols - $Re_b = 50.10^3$* (with varying Re). The drag coefficient can be calculated using either the free-stream velocity, u_∞, or the mean gap velocity, u_b, as the characteristic velocity in equation 3.7.

With increasing blockage, the velocity in the gap between the obstacle and the wall increases and the drag force on the cylinder increases. At $B = 0.25$, the drag force has almost doubled. This trend is independent of Re in the range investigated.

When the mean gap velocity u_b is used as characteristic velocity scale in equation 3.7, the resulting drag coefficient is written as $C_{d,b}$. Figure 3.7 shows that this provides a very good scaling of the drag coefficient ($C_{d,b} \sim$ constant) with B. How-
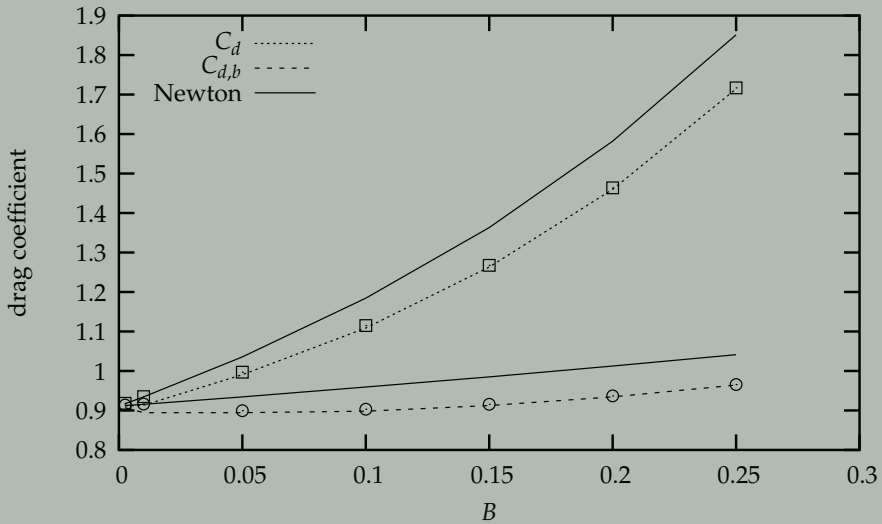
Figure 3.7: *Simulated drag coefficients for a confined axial cylinder with $AR = 1.0$: C_d based on the free-stream velocity u and $C_{d,b}$ based on the mean gap velocity u_b. The solid line is Newton's correction as given in equation 3.9.*

ever, it should be kept in mind that although this scaling leads to an almost constant $C_{d,b}$ value, the force on the object is not constant.

The scaling rule of Newton (equation 3.9) is drawn as solid lines in figure 3.7. Although not a perfect match, it corresponds well with the numerical data. At higher B, the discrepancy is larger, but still acceptable for general engineering calculations (at $B = 0.25$ the error is 6%).

Reynolds number effects

The value of the drag coefficient is only a constant value for sufficiently high values of Re. However, the behavior of the flow for lower Re is complicated by turbulence transition in the boundary layer and therefore not simple to characterize. In the case of a disc ($AR = 0$) data from White (1988) are reproduced in figure 3.8 which shows that the drag coefficient increases as Re becomes smaller. CFD data for $Re = 6250, 12500, 25000$ and 50000 are shown as well.

Turbulence intensity effects

The turbulence intensity at the inlet to the computational domain has a significant effect on the calculated value of the drag coefficient for k-ϵ type models. The effect is less pronounced for the SST-KW and the RSM model. Table 3.3 shows the value of C_d calculated for these turbulence models with different values of the turbulence intensity.
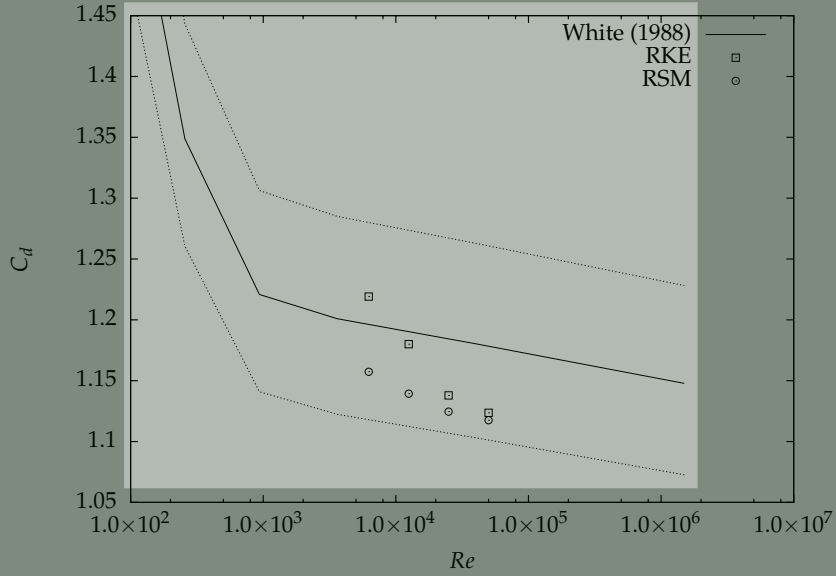
Figure 3.8: *Variation of the drag coefficient, C_d, as a function of Re for a disc. Data for the line from White (1988) with $\pm7\%$ error band due to interpolation from original log scale plot. Symbols from simulations in present study.*

Table 3.3: *Effect of inlet turbulence intensity on the calculated drag coefficient.*

turb. intensity	C_d, RKE	C_d, SST-KW	C_d, RSM
1 %	1.15	1.18	1.11
5 %	1.29	1.19	1.15
10 %	1.53	1.27	1.20

3.3.4   Summary

In this section the drag on an axial cylinder was investigated for a range of conditions. The information is required as input to the engineering model for the monolith flow rate. The influence of aspect ratio, AR, and blockage, B, was characterized. It was shown that the Re and inlet turbulence intensity can also affect the value of C_d. For simulations, the choice of the turbulence model has a big influence on the results. The standard k-ϵ model should be avoided. The realizable k-ϵ model gives more realistic results, but results are sensitive to the level of free-stream turbulence intensity. Results from the shear-stress transport k-ω model are in good agreement with available experimental data and show a reduced sensitivity to the free-stream turbulence intensity at the inlet to the domain.

3.4   Results in channel flow

The drag coefficient for the flow over an axial cylinder from the previous section can now be included in the channel flow model to predict the flow split for a variety of conditions. The flow split is a function of a number of physical parameters as listed in section 3.2.2. Results in this section were obtained with a computer program as described in table 3.1. An indication of the influence of the various input parameters can be gained from writing the equations for the flow resistances, R_c and R_a, in terms of the governing parameters. After some manipulation, it follows that:

$$R_a = \frac{\Delta p_a}{\phi_a} = \frac{\rho}{2} \frac{(u_\infty - u_c \cdot \epsilon_v)}{(1 - B)^2} \cdot C_d, \tag{3.11}$$

and

$$R_c = \frac{\Delta p_c}{\phi_c} = \frac{2\,\mu\,L_c}{\pi\,(\epsilon_v\,d_m\,d_c)^2} \cdot (f \cdot Re_c) + \frac{2\,\rho\,u_c\,(1 - \epsilon_v^2)}{\pi\,d_m^2\,\epsilon_v^3} \tag{3.12}$$

where

$$(f \cdot Re_c) = (f_{lam} \cdot Re_c)\sqrt{\left(1 + \frac{a}{L^*}\right)} \tag{3.13}$$

and

$$L^* = \frac{L_c}{d_c\,Re_c}. \tag{3.14}$$

The constants are $(f_{lam} \cdot Re_c) = 56.92$ and $a = 0.058$ for square channels (see table 2.2). For the model, the sum of the flows around and through the monolith must equal the approach flow, This gives a relation for the velocities in the model:

$$u_a = u_\infty - u_c \cdot \epsilon_v \tag{3.15}$$

Substition of R_a and R_c with equation 3.15 into equation 3.3, yields, after simplification:

$$\frac{u_c}{u_\infty} = \left[\epsilon_v\left(1 + \frac{R_c}{R_a}\right)\right]^{-1}. \tag{3.16}$$
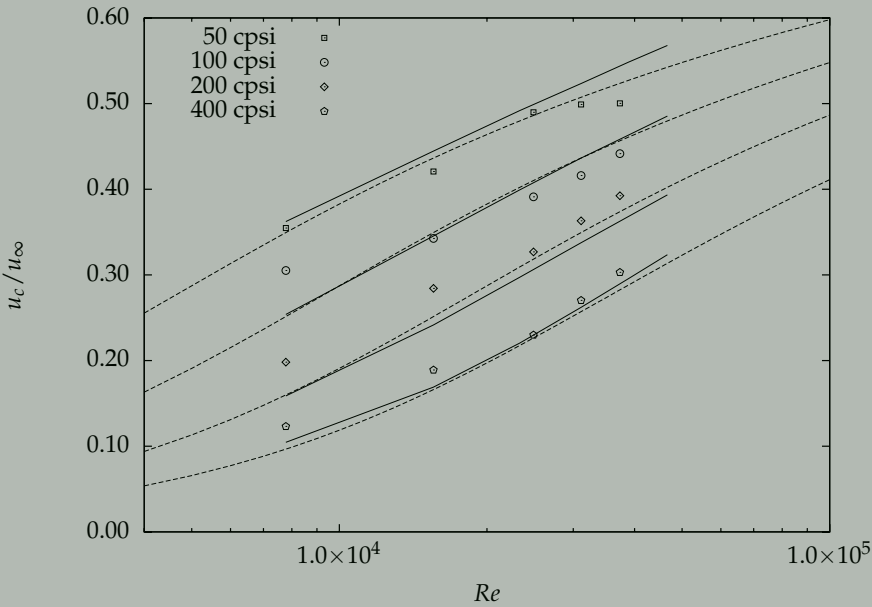
Figure 3.9: *The mean channel velocity through the monolith as a fraction of the free-stream velocity. Comparison of the engineering model prediction (dashed line), experiments (symbols) and CFD (solid lines) for four different monoliths.*

This is an implicit equation for the flow split because R_a and R_c are functions of u_c and u_∞. However, it exhibits the required quality that as $R_c \to \infty$, $u_c \to 0$, and when $R_c \to 0$, $u_c \to u_\infty$.

In the first part of this section the model predictions are compared to the actual values as measured experimentally (Chapter 2). This is followed by various results showing the influence of the different parameters. The results section concludes with a review of the sensitivity of the model to various input parameters.

3.4.1 Comparison with loop experiment

The model is derived for an ideal situation where the monolith is contained in a much larger pipe such that $B \to 0$. In section 2.3 the geometry of the experiment was presented, in which the blockage and aspect ratios were: $B = 0.135$, $AR = 1.09$. The value of the blockage includes the blockage due to the monolith fastening mechanism.

As shown in figure 3.7, the value of the drag coefficient is a constant if the actual gap velocity, u_b, is used. This will be the default for the remainder of the chapter and all references to C_d implies its use as $C_{d,b}$. With these values of B and AR and referring to figures 3.5 and 3.7, a value of $C_d = 0.9$ was chosen for the drag coefficient in the engineering model of the experiment.
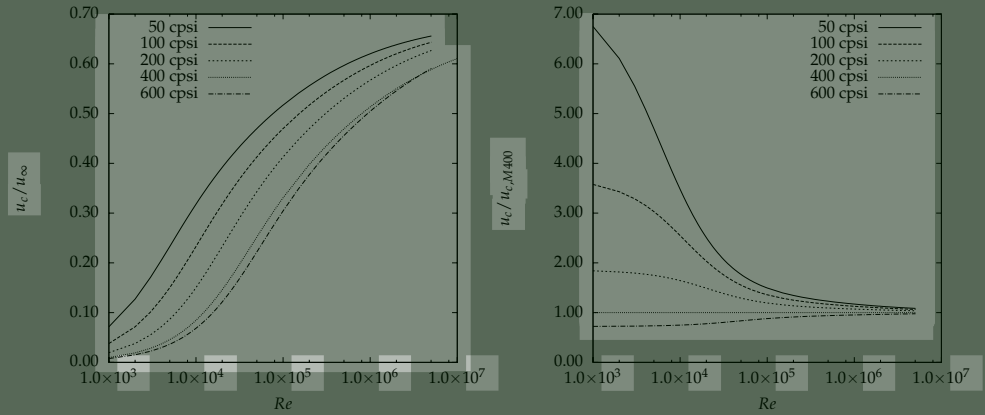
Figure 3.10: *Left: The mean channel velocity through the monolith as a function of Re for different monoliths with $AR = 1$ and $B = 0.0025$ Right: The mean channel velocity, now given relative to the value for a 400 cpsi, $u_{c,M400}$, for different values of Re. The Re number is based on the monolith diameter and free-stream velocity, i.e., $(\rho u_\infty d_m / \mu)$.*

Different monoliths were evaluated over a range of mass flow rates. Results for the flow ratio u_c / U_∞ with $C_d = 0.9$ are presented in figure 3.9. The plot is zoomed in to show the range of *Re* where the experiments were conducted.

The results compare very well with the experiments for all monoliths. This indicates that the model captures the important physics of the configuration. The intention of the channel velocity model is to reduce or remove the need for parameters that require fitting to experimental data. This would allow the model to be applied more widely than the present experimental data set. The next sections expand on the effects of the various parameters on the flow ratio.

3.4.2   Influence of geometry

Different monoliths

Table 2.1 lists the properties of the cordierite-based monoliths used in this study. A monolith diameter of $0.042m$ was selected as it is one of the standard manufactured sizes. The monolith length was selected as $L = 0.042m$ to set $AR = 1$. The blockage was set to $B = 0.0025$. The monolith channel diameter d_c ranges from 0.9mm–3mm, and the open frontal area fraction, ϵ_v, varies from 69%-80%. The results, presented in figure 3.10, highlight the effect of different values of channel resistance, R_c, on the flow ratio.

The velocity ratio, u_c / u_∞, varies widely over the range of *Re* from less than 10% to an asymptotic value around 65% at high *Re*. For $Re < 1.0 \times 10^5$ the difference in channel velocity between different monoliths is large (up to a factor of 7). However, above this value the channel velocities tend to convergence.

Figure 3.11: *Left: The mean channel velocity through the monolith, scaled with the free-stream velocity, u_∞, as a function of Re number for different blockage ratios with $AR = 1$ and a 400cpsi monolith. Right: The mean channel velocity through the monolith, now given relative to the value for a blockage of $B = 0.0025$, $u_{c,B0.25\%}$, for different values of Re. The Re number is based on the monolith diameter and free-stream velocity, i.e., $(\rho u_\infty d_m / \mu)$.*

Blockage effect

A variation in the blockage, B, affects the drag force on the monolith (and therefore R_a) without affecting the monolith channel length (important for R_c). A 400 cpsi monolith was used and the blockage varied as $0.0025 < B < 0.2$. The results are presented in figure 3.11. A larger blockage results in a higher relative channel velocity. On the left graph of figure 3.11 the data for $B = 0.25\%$ and $B \approx 0$ collapse on a single curve. This shows that low blockage has little or no effect on the experiment. The higher blockage causes a significant increase in the flow through the monolith.

Effects of changing AR

For this calculation the length of a 400 cpsi monolith was varied such that $0.25 < AR < 2$. The change in aspect ratio affects both R_a and R_c. The results for different aspect ratios in figure 3.12 show similar trends to figure 3.10 for different monoliths. This is due to a wide variation in the channel resistance, R_c, while the value of C_d, and therefore R_a is almost constant.

3.4.3   Sensitivity

The model sensitivity to the various parameters was evaluated by adjusting R_a and R_c by $\pm 10\%$ for a 400cpsi monolith with $AR = 1$ and $B = 0.0025$. Figure 3.13 shows the results. The effect of these variations are of the same order and affects the value
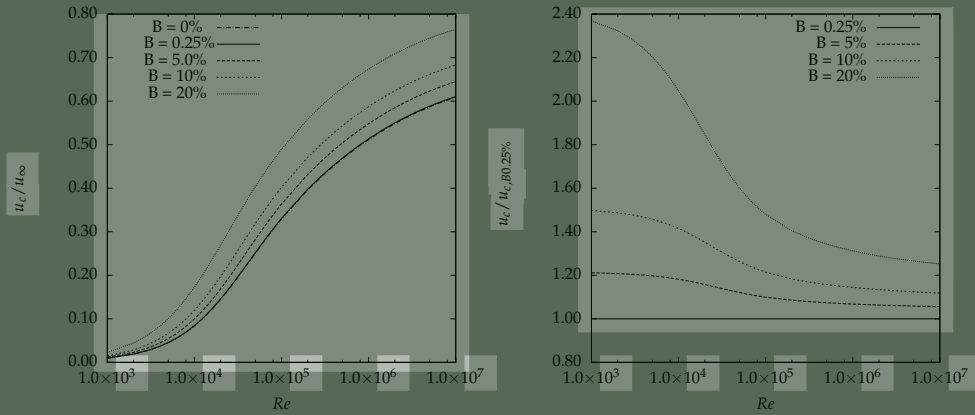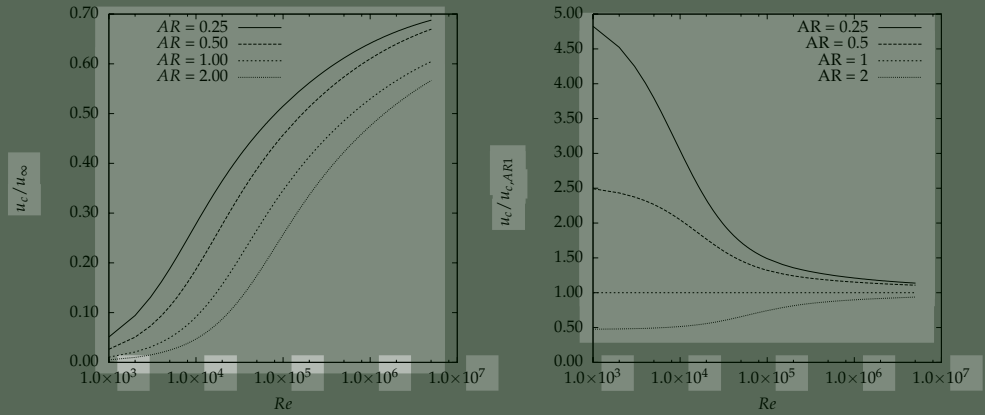
Figure 3.12: *Left: The mean channel velocity through the monolith, scaled with the free-stream velocity, u_∞, as a function of Re number for different values of AR with $B = 0.0025$ and a 400cpsi monolith. Right: The mean channel velocity, now given relative to the value for $AR = 1.0$, $u_{c,AR1}$, for different values of Re. The Re number is based on the monolith diameter and free-stream velocity, i.e., $(\rho u_\infty d_m / \mu)$.*

of the channel velocity in a linear manner - effectively forming a $\pm 10\%$ uncertainty band. A number of other factors can influence the results, e.g., uncertainty in C_d, B, d_c, L_m or thermophysical properties. It is probable that the uncertainty in the value for C_d for the range $0 \leq AR \leq 2.0$ (figure 3.5), will be the most significant of these factors. This is still considered acceptable because the main aim of the model is to provide a tool for rapid comparison of the effect of different configurations on the monolith channel velocities.

3.5   Conclusions

An engineering model for the rapid calculation of the monolith channel velocity has been developed. The results show that the model can accurately predict the behavior of different monolith configurations in a confined duct without the need for fitting of correlations. It is however limited to a configuration where the monolith is located in a duct. Application to the MSR configuration will be investigated in chapter 5.

The drag coefficient of an axial cylinder configuration was also investigated. This information is required for the monolith channel velocity model. Results from the CFD study of the drag coefficient showed a strong influence of turbulence modeling on results. The RKE model was found to perform reasonably well for the present work (bluff, external flow), but showed sensitivity to the settings for inlet turbulence intensity level. The RSM model provided answers in good agreement with literature.
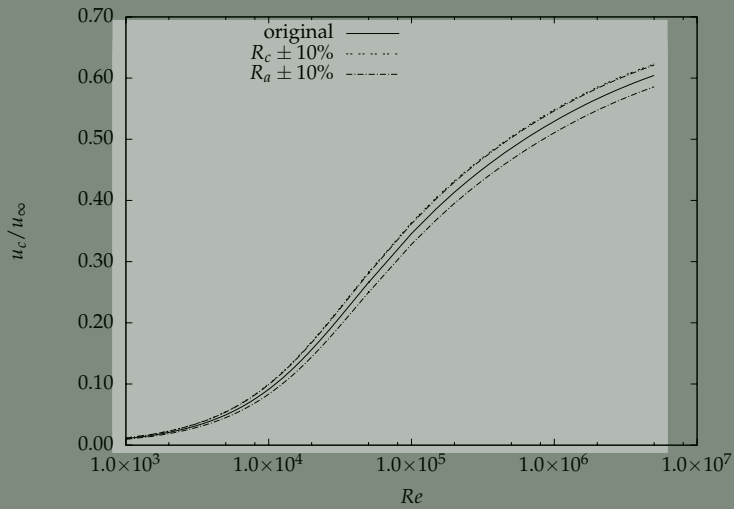
Figure 3.13: *The effect of variation in R_c and R_a for a 400 cpsi monolith with $AR = 1$ and $B = 0.0025$ on the normalized mean channel velocity.*

Chapter 4

Experiments on flow and mixing in an MSR

4.1 Introduction

Previous work on the MSR concept by Edvinsson-Albers *et al.* (1998) and Hoek (2004) have focused on investigating the catalytic application of the reactor. However, the need remains to develop a modeling strategy for the accurate simulation of the MSR to study flow patterns, liquid circulation, power draw and the amount of fluid flowing through the monolith channels.

This chapter describes the experimental investigation of the operating characteristics of a single-phase prototype monolithic stirrer reactor (MSR) with a vertical shaft. The MSR experiments were performed to provide a data set for CFD validation. Results include power numbers, mixing times and a detailed description of the 3-dimensional, time-varying flow field inside the prototype reactor for different operating conditions. The mass flow rate through the monolith channels was measured as well. The investigation was performed for a range of stirrer speeds and with five different blade configurations on the stirrer.

Apart from four different sets of monoliths, a set of two solid cylinders was also used as blades on the stirrer. This was done to generate a data set which could be used for the CFD without the added complication of a monolith model (c.f. chapter 5).

After a brief literature review of the relevant experimental techniques, the rest of this chapter describes the experimental setup and methodology for the measurements to determine the MSR flow field, the monolith channel velocities, the power draw and the mixing. Results are presented for all experiments and the chapter closes with a summary and conclusions.

57

4.2   Literature review

The importance of mechanical agitation in industrial mixing has resulted in a vast body of research. In this brief overview, the focus is on experimental methods deemed relevant for the present investigation. At the outset, the aim of the experiments is to establish the operating characteristics of the MSR by measuring (i) flow field features, (ii) monolith channel velocities, (iii) power draw, and (iv) the bulk mixing behavior.

4.2.1   Velocity and channel velocity measurements

In recent decades, velocity measurement methods, like pitot tubes, hot-wire and hot-film anemometer probes, have made way for non-intrusive optical methods like laser Doppler anemometry (LDA), particle image velocimetry (PIV) and particle tracking velocimetry (PTV).

Early work on the flow in stirred tanks (Van't Riet & Smith, 1973; Nienow & Wisdom, 1974) used photographic techniques to show the existence of trailing vortex pairs generated by Rushton turbines in the wake of each blade in a stirred tank. Initial work on global and averaged flow fields was extended with phase resolved velocity measurements (Stoots & Calabrese, 1995; Yianneskis *et al.*, 1987). Derksen *et al.* (1999), using LDA, measured resolved, 3-dimensional velocities and were able to calculate detailed turbulent stress components. Recent works have further extended the focus on the detailed turbulent flow properties with PIV (e.g., Michelet *et al.* (1997); Hill *et al.* (2000); Escudié & Liné (2003)).

None of the optical methods can measure the flow rate inside the monolith channel, unless special efforts are made to make the monolith optically accessible. This has been done before for automotive applications, however for the present application this is not feasible due to the large number of monoliths tested and the challenges posed by refractive index matching (Dorsman, 2001) inside the experiment.

Although micro sensors have been developed of sufficiently small size (e.g., Baviere & Ayela (2004) developed a sensor for use in a 7.5 μm channel), the recording and transmitting electronics would still require installation inside or on the monolith. It was not feasible to instrument a large number of monoliths for testing in this manner, although it could still be an option for future work.

A technique that would be able to measure monolith channel velocities is called "Computer automated radioactive particle tracking" (CARPT) (Larachi *et al.*, 1997). This method enables reconstruction of the track of a radioactive tracer particle inside the stirred tank and could therefore also be used to measure the velocity of fluid passing through the monolith. At present the particle size and density required for the tracking particle is too intrusive to be applied for the monolith channels.

In this work we adopted LDA for the measurements of the velocities. This utilizes existing experimental equipment and has been proven to be effective in mea-

suring stirred tank flows. The high temporal resolution is sufficient to measure the relative velocities around the the monolith face, similar to Chapter 2, even though the monolith is non-stationary.

4.2.2 Stirred tank power consumption measurements

Power consumption during mixing is an important operating characteristic and has been investigated extensively. Chapple *et al.* (2002) and Ascanio *et al.* (2004) reviewed the various measurement methods available for stirred tanks. These include: measuring the power consumption of the electric motor, measuring the torque on the stirrer and motor assembly, measuring the torque on the stirred tank, and measuring the torque on the stirrer shaft. The first two methods both require compensation for additional losses, i.e., electrical efficiency of the motor, and losses in the bearings and drive train. The latter two methods can measure the power input to the liquid directly, but the mounted stirred tank can introduce additional bearing friction which would require compensation. As a result the last method of measuring the torque directly on the shaft of the stirrer, is most commonly used. The method relies on using a strain gauge to detect the deformation of the shaft under an applied torque.

Kraume & Zehner (2001) reported on a comparative experimental study conducted at a number of sites in Germany. Each site was requested to manufacture (from drawings) and measure the characteristics of the same Rushton stirrer. Power number measurements varied by up to 10% amongst results from the 6 participants. In addition they found that all torque meters (based on strain gauge measurement) exhibited unreliable response for torque values less than 10% of the rated nominal value.

4.2.3 Mixing studies

An extensive review of mixing measurements has been presented by Nere *et al.* (2003). The most common methods involve measuring the response of a scalar (pH, conductivity or temperature) to a step change in the input. Kramers *et al.* (1958) used conductivity probes to measure the variation in conductivity between two points in the stirred tank after an injection of saline solution. The system is considered mixed when the difference has decreased to within a certain margin, α%, of the final value - typical values for the margin are 1, 5 or 10%. The resulting mixing times are then reported as obtained with the $(100 - \alpha)$% criterion.
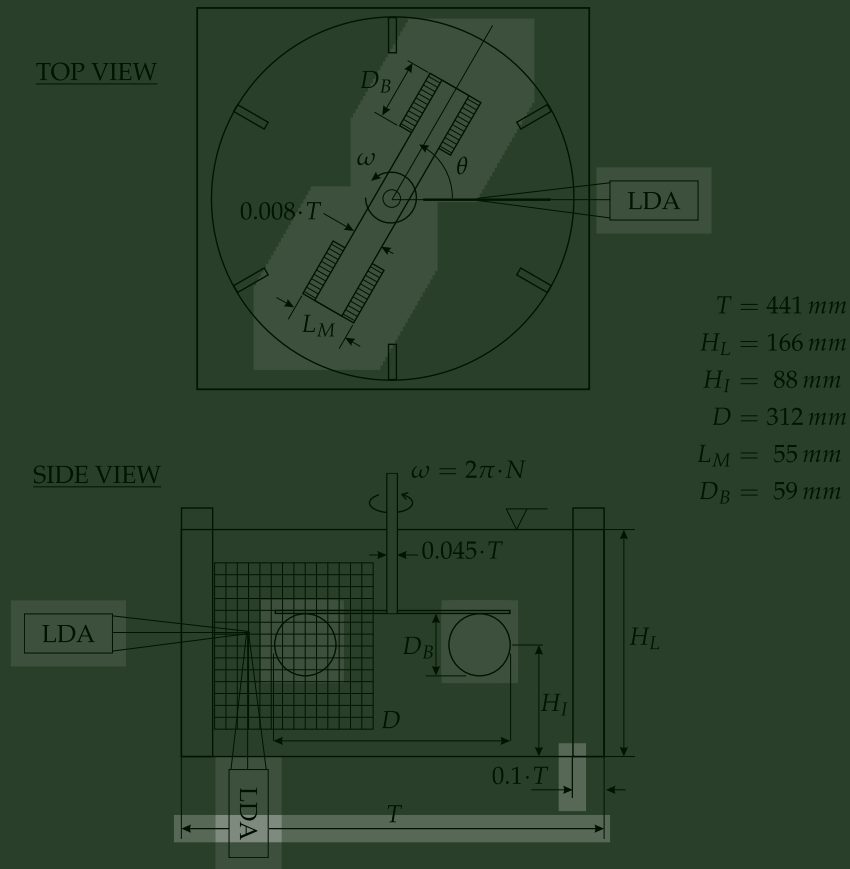
Figure 4.1: *Geometry and dimensions for the MSR with the layout of the LDA measurement grid.*

4.3 Experimental set-up and data analysis

4.3.1 Geometry of the MSR prototype

The basic geometry of the prototype reactor follows the design investigated by Edvinsson-Albers *et al.* (1998). Using the preliminary investigation as starting point, a prototype monolithic stirrer reactor (MSR) was constructed. The diameter of the new vessel was 10% larger than that used by Edvinsson-Albers *et al.* (1998) – all geometric features were scaled accordingly.

A cylindrical tank, shown in figure 4.1, with diameter T = 441 *mm*, was built from clear Plexiglas. The tank had a flat bottom also made from Plexiglas to maximize optical accessibility. To minimize the refraction of the laser beams over the outer cylindrical surface of the vessel, it was placed inside another Plexiglas vessel with square sides, which was also filled with water during measurements. The

water height in the tank was kept at H_L = 166 mm. Six equi-spaced, 44.1 mm wide vertical baffles were used to prevent solid body rotation of the liquid.

The monolith stirrer was installed with a bottom clearance of H_I = 88 mm. All relevant dimensions are given in figure 4.1 The stirrer Reynolds number, Re, can be defined as

$$Re = \frac{ND^2}{\nu}. \tag{4.1}$$

Impeller speeds ranged from N=0.25 to 2.0 rev/s. This amounted to Reynolds number range from $Re = 2.4 \times 10^4$ to 1.9×10^5 (using water at 20°C). The range of stirrer speeds was limited by the entrainment of air at the top surface at stirrer speeds above 2.0 rev/s.

The stirrer was constructed to hold two (uncoated) monolith blocks with diameter D_M = 55 mm and channel length L_M = 55 mm. The total blade diameter (with the monolith attachment rings) amounted to D_B = 59 mm. Solid cylinders with the same dimensions as the monolith blocks were used to compare the results with an impermeable stirrer (referred to as the solid stirrer case). The center to center distance between the stirrers on either side of the shaft is 253 mm; resulting in a stirrer diameter D = 312 mm. The maximum eccentricity of the stirrer shaft was measured as 0.1 mm (i.e., 0.03% of the stirrer diameter). The instantaneous stirrer angle, θ, was measured with a phase encoder mounted on the stirrer shaft (Derksen *et al.*, 1999).

4.3.2 Flow field measurements

The characteristics of the flow in the bulk of the reactor volume (i.e., surrounding the monolith) were measured with LDA. The LDA system described in chapter 2 was used for the measurements. Figure 4.1 shows the layout for the LDA measurements. From the horizontal probe position, tangential and axial velocity components were measured. Vertical measurements through the floor of the vessel provided independent data on tangential and radial components. A measurement grid of 15 × 15 points (grid spacing $\Delta r = \Delta z = 10$ mm) was defined in a vertical plane located midway between two baffles. Figure 4.1 also shows the phase angle, θ, as the stirrer position relative to the measuring plane. The position $\theta = 0°$ was defined as the midpoint of the stirrer blade coinciding with the measuring plane. The tangential direction was divided into 45 angular bins of 4° (at the inner bound 4.5 mm and at the outer bound 14.3 mm between consecutive angle slices). The phase resolution of the 16 bit clock resulted in a resolution of 0.072° for the angle measurements (0.26 mm at the outer bound of the grid) at the highest stirrer speed. The clock output was added to each measured data point through the LDA system - thereby recording the stirrer position for each measured velocity record.

The probe was mounted on a 2-axis positioning table that enabled accurate positioning of the measurement volume inside the vessel. The set screws allowed positioning in the axial and radial direction with 0.1 mm increments. Per grid point

(at each r, z and θ) a minimum of 1000 data points were collected for each of the three velocity components.

The flow was seeded with neutrally buoyant hollow glass spheres (10 μm average diameter).

The bulk flow measurements were performed on the full LDA grid for the solid and 400 cpsi monolith stirrer and a speed of $N = 1.0 rev/s$. Additional measurements were performed on the 3 horizontal grid lines though the middle of the stirrer for 50, 100 and 200 cpsi monoliths on the stirrer at $N = 1.0 rev/s$. The 400 cpsi stirrer was used to further measure data for stirrer speeds of N=0.25 and N=2.0 rev/s.

The IFA750 flow analyzer (TSI Incorporated) produced a binary data file for each measurement with a number of LDA variables and the time measured by the phase-encoder clock. A custom HP-UX Fortran program was used to process the raw data. The output for each measurement contained the phase resolved, time-averaged velocity-component (u_z, u_r or u_θ), the velocity fluctuation (u'_z, u'_r or u'_θ), and the number of data points. Data were sorted in 45 angular bins (using the $180°$ symmetry of the stirrer and $4°$ slots). An additional program was used to collect the data from the 225 (15x15 grid) discrete results files and combine them into a single file for post-processing (see Deelder (2001) for detail).

The axial, radial and tangential (u_z, u_r and u_θ) mean velocities in the tank are scaled by the stirrer tip speed ($u_s = \pi ND$). The turbulent kinetic energy can be defined as

$$k = \frac{1}{2} \left(u'^2_z + u'^2_r + u'^2_\theta \right). \tag{4.2}$$

In this work k is scaled with u_s^2. For presenting data around the stirrer it is convenient to define the velocity vector in the stirrer reference frame as

$$\overline{v} = \overline{u} - 2\pi rN \cdot \overline{e}_\theta. \tag{4.3}$$

In this chapter all tangential velocities reported in the stirrer reference frame will use v_θ. Since the axial, v_z, and radial v_r components are not affected by equation 4.3, u_z and u_r will be used for all reporting of axial and radial velocity components.

Following Benedict & Gould (1996), the 95% confidence interval of the average velocity and the rms value were determined from

$$\overline{u} \pm 1.96 \sqrt{\frac{\overline{u'^2}}{N}}, \tag{4.4}$$

$$u' \pm 1.96 \sqrt{\frac{\overline{u'^2}}{2N}}. \tag{4.5}$$

Based on these equations the 95% confidence interval for the data was calculated as $0.008u_s$ for the mean and $0.005u_s$ for the rms values of the velocities. No velocity bias correction was performed on the present data. The difference between

maximum and minimum velocities is much reduced by averaging in angular bins Stoots & Calabrese (1995), and it is not expected that velocity bias will affect the conclusions drawn from the work.

4.3.3   Monolith channel velocity measurements

The use of an angled LDA probe to measure the fluid velocities up to the face of the monolith was presented in section 2.3.2 and shown in figure 2.5. The same method was employed for the MSR with all measurements performed through the bottom of the vessel.

Due to the movement of the stirrer relative to the measuring plane, the determination of the velocities on the monolith face are complicated by: (i) effect of stirrer movement on the measured velocity, and (ii) determination of the monolith face position relative to the position of the LDA measurement volume. For (i) above, the monolith face velocity at each radial position (calculated from the stirrer speed) can be subtracted from the measured velocity to obtain the velocity relative to the monolith (c.f. equation 4.3). Additional work is then required to estimate the instance when the monolith face passes through the LDA probe volume - we need to measure the velocity just upstream from the monolith, similar to the work in chapter 2. The selection of the reported velocity is discussed in more detail with the results in section 4.5.

The measured velocity in the stirrer reference frame, v_θ, represents the velocity of the fluid entering the monolith channels. In order to obtain the channel velocity, v_c, this value must be adjusted by the monolith open frontal area, ϵ_v, such that

$$v_c = \frac{v_\theta}{\epsilon_v}. \tag{4.6}$$

The stirrer speed, $u_s(r) = 2\pi r \cdot N$, at each radial measurement position is used to scale the resulting channel velocity profiles.

4.3.4   Power consumption measurements

The electrical power required by a stirred tank is an important component of the running cost. In stirred tanks, the dimensionless power number is often used to compare the performance of typical mixers. The power number is defined as:

$$N_P = \frac{P}{\rho N^3 D_s^5}. \tag{4.7}$$

In equation 4.7 the shaft power, P, is obtained from the product of torque and angular velocity, N is the stirrer speed and D_s is the stirrer diameter. In appendix C a brief discussion on the use of the power number is presented, including comments on alternative formulations presented by Houterman (1997).

For different configurations and speeds, torque measurements were performed on the prototype MSR with a strain gauge type transducer. The output from the torque transducer, a voltage signal in the range -10 to 10V, was captured online with a standard PC and analogue-to-digital (AD) converter card. The torque transducer rotor calibration value was used to convert the output signal to a corresponding torque. A measurement using a standard Rushton stirrer was used to validate the measurement method.

Impeller speeds for the torque measurements ranged from 0.33 to 2.5 rev/s. All available monoliths were tested on the stirrer, i.e., solid, 50, 100, 200 and 400 cpsi.

4.3.5   Mixing time measurements

The mixing or blending times for different stirrers are important in stirred tank applications. In the MSR, bulk mixing will ensure a supply of new reactants to the catalyst coated surfaces inside the monolith. Mixing times were determined by measuring the change in bulk concentration after an addition of saline solution on the surface of the liquid (Kramers *et al.*, 1958). The concentration of the bulk saline solution was measured with a conductivity probe. Using the 95% criterion, the mixing times for solid, 50 cpsi, 100 cpsi, 200 cpsi, and 400 cpsi stirrer configurations were measured at speeds in the range N = 0.5 - 2.5 rev/s.

The conductivity probe output signal for each measurement was recorded with a data logger. The experiment was repeated 5 times for each data point. The five measurements for each configuration were averaged to produce a single response curve per data point. Each curve was then normalized with the final voltage (i.e., concentration) value (taken as the last value in the time series, V_∞). Figure 4.2 shows the resulting normalized response curves for 5 data points (obtained for a 50cpsi stirrer operated at 5 different stirrer speeds).

Lines drawn at 0.95 and 1.05 indicate the bounds used to evaluate the mixing time according to the 95% criterion. A `perl` program was used to process each response curve to determine the time after which the signal remained inside the $\pm5\%$ band (drawn in solid lines).

4.4   Results for the bulk flow

The flow in the tank determines the mixing and availability of fresh reactants to the monolith (catalyst). The prototype MSR featured a shallow water depth and some surface oscillation were observed. The extent of this movement is briefly discussed before continuing with the measured bulk flow field. The first results aim to describe the general features of the three-dimensional flow field generated in the bulk of the tank - a solid and a 400 cpsi monolith are compared. Subsequent results shows the influence of the monolith characteristics (channel size, d_c, length, L_M, open frontal area fraction, ϵ_v) and the stirrer speed respectively.
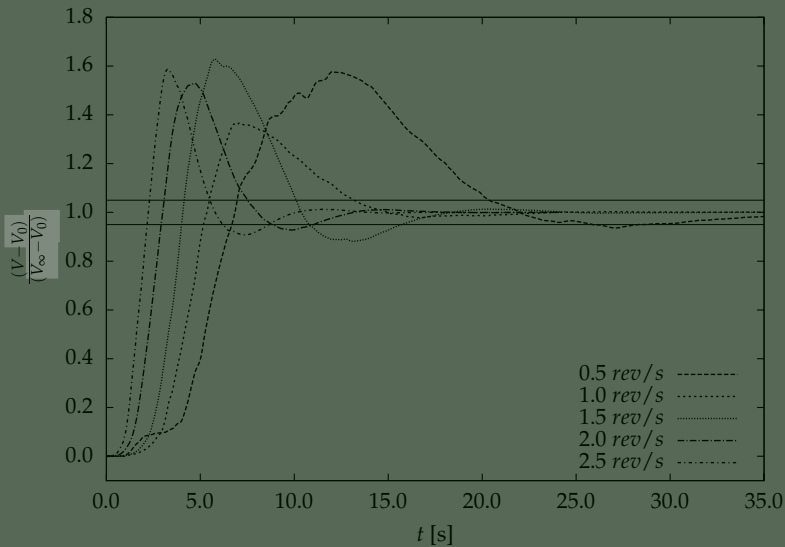
Figure 4.2: *Examples of the averaged, normalized voltage output from the conductivity probe for a 50cpsi monolith for 5 different stirrer speeds. Five individual measurements are averaged for each response curve and then normalized with the final asymptotic value, V_∞. The $\pm5\%$ band is indicated with solid lines at 0.95 and 1.05.*
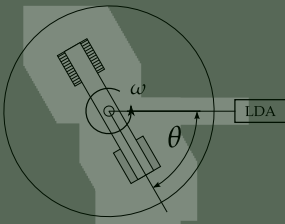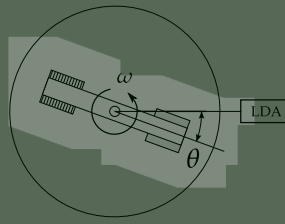
$\theta = -3\pi/9$ $\theta = -\pi/9$ $\theta = 0$
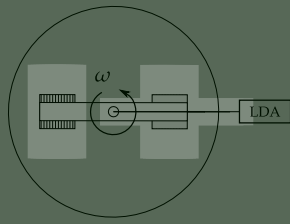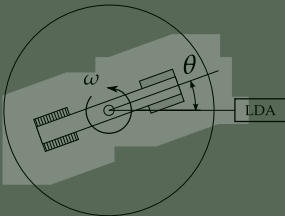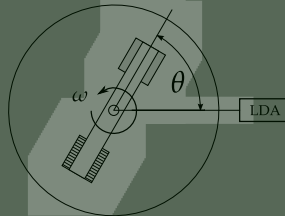
$\theta = \pi/9$ $\theta = 3\pi/9$ $\theta = 5\pi/9$
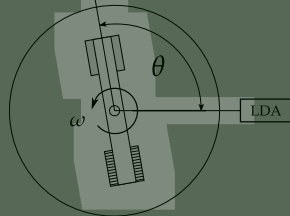
Figure 4.3: *Graphical description of the stirrer angle, θ, used for reporting velocities around the stirrer. Negative angles reflect measurements upstream from the stirrer (the shaded blade is used as reference). The zero position is defined as the middle of the blade coinciding with the LDA measuring plane. Positive angles denote measurements in the wake of the blade.*

The phase-resolved velocities are reported in terms of the angle between the stirrer and the LDA measuring plane. Figure 4.3 gives a graphical view of the stirrer angle, θ, used to present the results. Negative values of θ indicate measurements done on the upstream side of the reference blade (shaded in the figures). The zero position is defined as the angle where the blade is located on the measuring plane. Positive values of θ indicate measurements taken in the wake of the reference blade.

4.4.1   Free-surface movement

A regrettable omission in the present study was the absence of a lid at the upper surface of the stirred tank. The main motivation was to repeat the previous experiments of Houterman (1997) as closely as possible. However, this resulted in an experimental data set where the presence of the surface movement must be kept in mind for all comparisons with simulations.

In the original thesis Houterman (1997) reported results only for stirrer speeds up to 0.92 rev/s (55rpm) - stating that surface instability at higher speeds made testing impossible. The monoliths in that study were attached to the shaft by means of non-rigid wiring, which would have become unstable with increased surface instability (resulting in increasingly uneven torque on the monolith blades). In the present investigation the monoliths were attached rigidly to the shaft with monolith holders. As a result, stirrer speeds were not limited by the stirrer stability during free-surface oscillation. An increased surface instability was observed in the range 0.92 - 0.98 rev/s for the present work. Speeds from 1.0 rev/s and higher were observed to produce a flattened surface with reduced oscillation.

In the companion study by Hoek (2004), the stirrer speeds were deliberately increased to the point where gas was entrained from the free-surface into the bulk of the fluid. This was done to enable mass transfer studies to be conducted without the use of a gas sparger. Based on power number measurements, the entrainment occurred at stirrer speeds above 4.2 rev/s (250rpm).

Free-surface movement in stirrer stirred tanks are usually evaluated with a Froude number defined as

$$Fr = \frac{N^2 D}{g}. \tag{4.8}$$

Here g is the gravitational acceleration. The Froude number relates centrifugal force due to liquid rotation to the gravitational force and is generally used to predict formation of a standing vortex around the shaft of a stirred tank. Using the parameters of the experiment with equation 4.8 results in Fr numbers ranging from 0.001 to 0.1. Vortex formation is therefore not expected.

The shallow water depth and low stirrer speeds result in a different phenomenon in the present experiment. An alternative formulation for Froude number, typically used in shallow channel flows, compares the characteristic flow velocity with the wave speed as

$$Fr_c = \frac{u_s}{\sqrt{gH_L}}. \tag{4.9}$$

(a) t_0

(b) $t_0 + 0.12s$

(c) $t_0 + 0.24s$

(d) $t_0 + 0.36s$

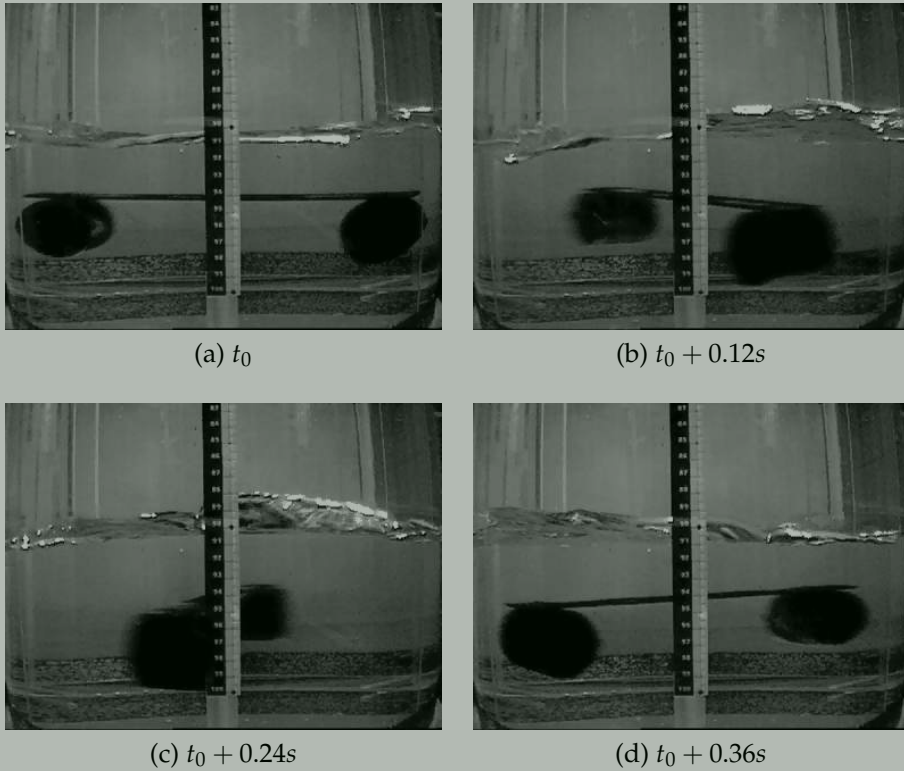**Figure 4.4:** *Snapshots of the MSR operating with a solid stirrer at N = 1.0 rev/s. The capture frame rate of 25 Hz resulted in an image spacing of 0.04s - the sequence shows every third picture which corresponds to a 0.24π radians ($43.2°$) rotation between each frame.*

In this equation H_L is the liquid depth, and u_s a characteristic velocity, here taken as the stirrer tip speed. For values of $Fr_c \approx 1$, the flow is critical and the stirrer tip equals the wave speed. For the prototype MSR and selected stirrer speeds, the value of Fr_c ranges from 0.2 to 2.0. The critical stirrer speed ($Fr_c = 1$) occurs at $N = 0.75 rev/s$.

During the experiments the maximum surface oscillations were observed at a stirrer speed of $N \approx 0.9 \ rev/s$. This agrees fairly well with the critical value for Fr_c.

Figure 4.4 shows a sequence of images from the experiment that illustrates the surface movement for a solid stirrer at $N = 1.0 \ rev/s$. The camera was aligned with the stationary liquid surface level before starting the stirrer. The images show that the passage of the blade creates an upward displacement of the liquid surface (image c). Less clear on this sequence is a corresponding downward displacement in the immediate wake of the blade (image b) that was also observed in the experiments.

4.4.2   Comparison of solid and 400 cpsi stirrers

This paragraph discusses the features of the bulk flow in the MSR. It further compares differences between results with the solid stirrer and one with a 400 cpsi monolith stirrer.

Figure 4.5 shows vectors of the axial and radial velocity components on the LDA measurement grid for four consecutive angles: $-\pi/9$, $\pi/9$, $3\pi/9$, and $5\pi/9$. The outline of the stirrer blade is drawn in each figure as a guide, but is not actually present in the measurement plane for any of the angles shown.

Each blade generates a radial jet, flowing outwards to the tank wall at an angle below the horizontal. This generates a pair of trailing vortices following each blade (similar to observed in Rushton turbines) that contribute to the mixing of the bulk fluid in the tank.

At $\pi/9$, just behind the trailing face of the blade, the difference between the solid and monolith stirrer results is most obvious. For the solid stirrer the vectors show strong recirculation in the wake of the blade (c.f. figure 3.3). In contrast, the monolith stirrer results show almost no axial and radial components in the area immediately behind the blade. This is the area where the laminar jets exit the monolith and the flow is expected to be still aligned with the monolith channels.

There is a difference in the angle and strength of the jet between the two sets of results. The vectors for the 400 cpsi stirrer start almost horizontally whereas for the solid stirrer the jet is angled towards the floor of the tank. The strength of the jet is also less for the monolith stirrer - this can be attributed to a smaller amount of liquid forced out of the way of the porous blade due to the flow through the monolith channels.

The results can be further analyzed by studying the velocity and turbulent kinetic energy (TKE) profiles at different locations and stirrer angles. Figures 4.6 and 4.8 show profiles on a horizontal line of the measurement grid at mid stirrer height
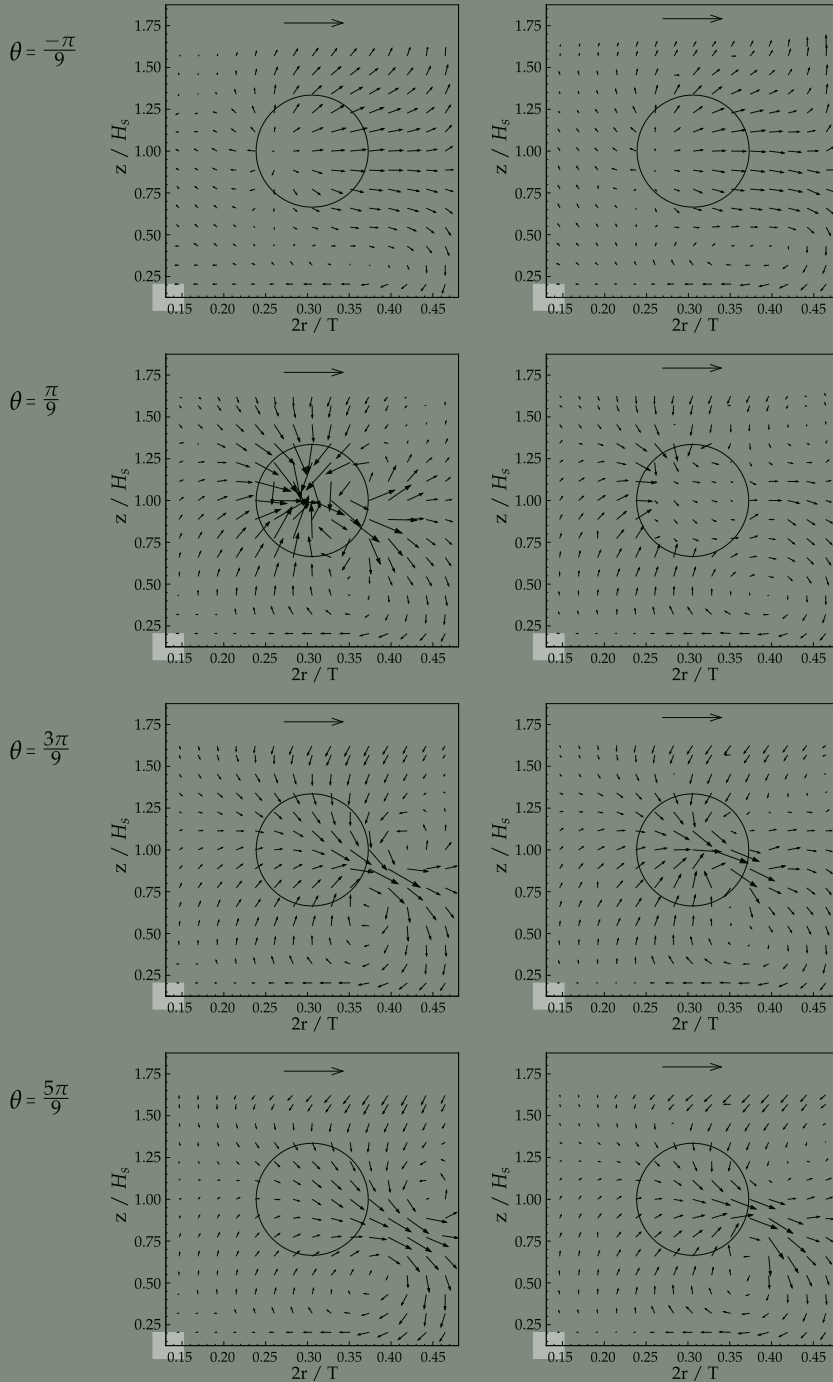
Figure 4.5: *Velocity vectors (constructed from axial and radial components) shown on the LDA measurement grid for four stirrer angles $-\pi/9$ (top), $\pi/9$, $3\pi/9$, and $5\pi/9$ (bottom row). The left hand column shows results for the solid stirrer and the right hand for the 400 cpsi stirrer. The stirrer speed was $N = 1\,rev/s$. The reference vector in each image is equal to the tip speed, u_s.*
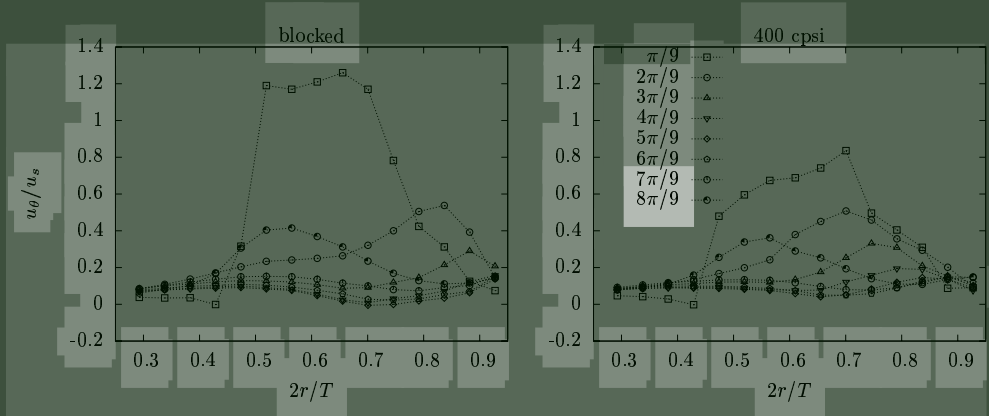
Figure 4.6: *Profiles of tangential velocity for a solid and 400 cpsi stirrer for $N = 1\,rev/s$ at mid stirrer height, $z/H_s = 1$. Left - solid and Right - 400 cpsi monolith. Velocities scaled with stirrer tip speed u_s.*

($z/H_s = 1$). Profiles of tangential velocity and TKE on a vertical grid line at a radius of $2R/T = 0.79$ are presented in figures 4.7 and 4.9.

Figure 4.6 shows the tangential velocity (scaled with stirrer tip speed u_s) on a horizontal grid line through the middle of the stirrer. Data are shown for angles in $\pi/9$ ($20°$) increments from $\pi/9$ behind the blade up to $8\pi/9$ (or $\pi/9$ ahead of the next blade). Figure 4.8 shows the corresponding profiles of TKE (scaled with u_s^2 at the same location.

In figure 4.6 data at $\pi/9$ for the solid stirrer show the strong recirculation observed in the vector plot as a velocity higher than the stirrer tip speed. This is consistent with the recirculating flow flowing towards the trailing face of the blade, which is itself moving at the stirrer speed. Values for the 400 cpsi stirrer are significantly lower. The profiles for $2\pi/9$, $3\pi/9$, and $4\pi/9$ show the evolution of the radial jet as it moves outward (figure 4.6)and downward (figure 4.7) in the wake of the blade.

The TKE (figure 4.8) profiles show larger differences between the solid and monolith stirrer results. Both results show the passage of the radial jet, but the solid stirrer generates higher TKE than the 400 cpsi stirrer. This is due in part to the flow through the monolith which reduces the effect of the volumetric blade on the surrounding flow by displacing a smaller volume of fluid during its passage - as a result the velocities in the bulk flow are lower. In addition, the flow passing through the monolith channels will re-laminarize inside the small channels and on exit from the monolith, would have a much lower TKE than the recirculating flow of the solid stirrer. This difference propagates into the bulk of the fluid with the radial jet and would result in weaker bulk mixing for the porous stirrers. Peaks in the TKE at $2R/T = 0.5$ and $2R/T = 0.7$ are located where the monolith holder walls passes through the measurement plane.
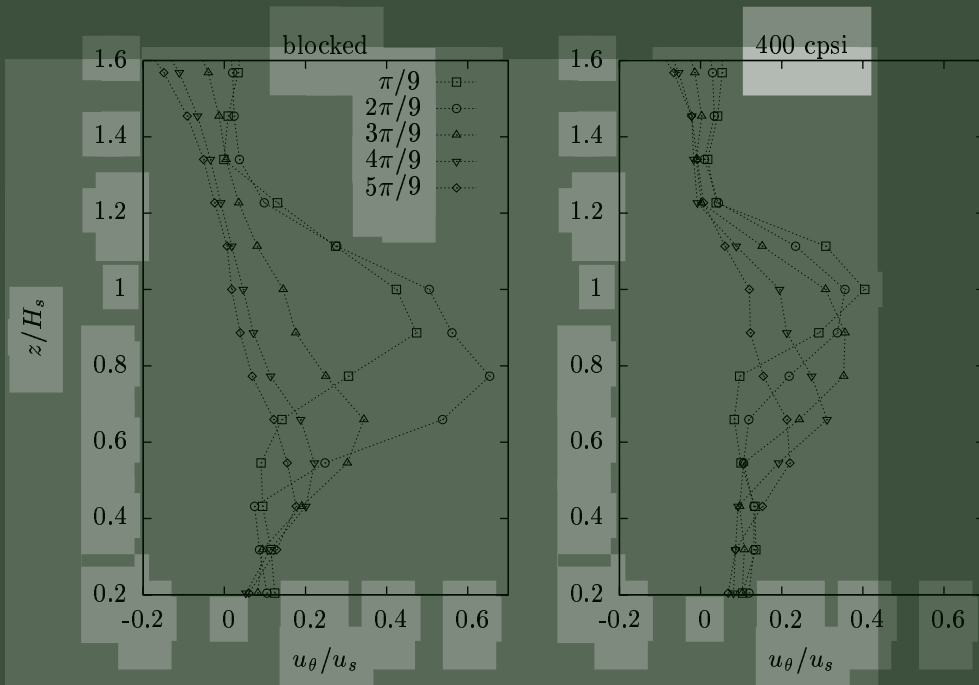
Figure 4.7: *Profiles of tangential velocity for a solid and 400 cpsi stirrer for $N = 1\ rev/s$ at a radius of 174.5 mm (vertical line at $2R/T = 0.79$).Left - solid and Right - 400 cpsi monolith. Velocities scaled with stirrer tip speed u_s.*
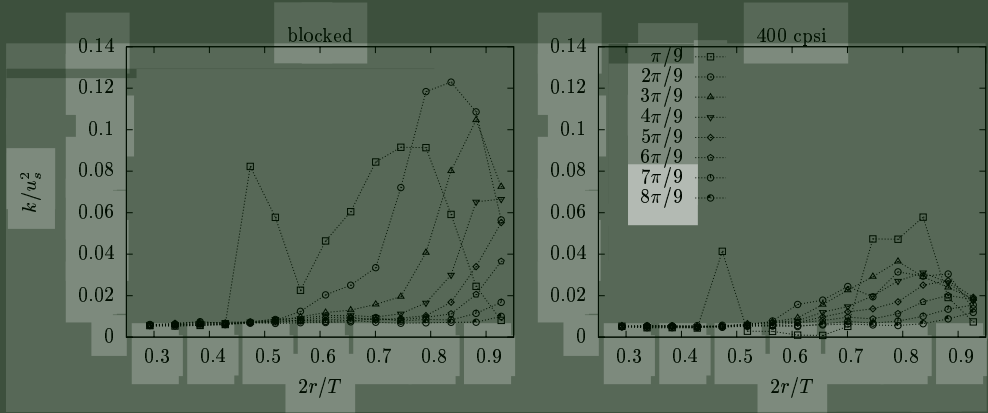
Figure 4.8: *Profiles of turbulent kinetic energy scaled with u_s^2 on a horizontal line at mid stirrer height, $z/H_s = 1$. Data for a solid (left) and a 400 cpsi (right) stirrer rotating at $N = 1\,rev/s$.*

At $4\pi/9$ the tangential velocity is down to the level in the bulk of the tank. This is important for cases where the stirrer will be fitted with four blades (to increase catalyst content in the reactor). The channel velocities inside the monolith are generated by the pressure difference across the monolith, which depends in turn on the relative difference in tangential velocities between the blade and the bulk fluid. This suggests that for a stirrer with four blades in the same horizontal plane, the blades would not be significantly affected by the wakes of preceding blades.

The same data (angle resolved tangential velocities and TKE) are presented on a vertical grid line at $2R/T = 0.79$ in figures 4.7 and 4.9. This position is located 20 mm beyond the tip of the stirrer. It also shows the existence and passage of the radial jet behind the blade. The difference in the initial direction of the jet is visible in figure 4.7 with the monolith stirrer profiles showing a maximum value at the mid stirrer height $z/H_s = 1$, whereas the solid stirrer peak is lower in the tank. The maximum velocity is also lower for the monolith stirrers. The difference in the jet direction can also be due to the effect of the flow leaving the monolith aligned to the channel direction - this flow will not have a vertical velocity in the immediate wake of the blade.

Figure 4.9 again shows the difference in the levels of TKE generated by the solid and monolith stirrers. The solid stirrer shows TKE up to 3 times higher than the monolith stirrer in the wake of the blade. However both jets dissipate in the bulk flow and the maximum level of TKE at $5\pi/9$ behind the blade is equal for the solid and monolith stirrers - the solid peak is located slightly lower in the tank. TKE results from figures 4.8 and 4.9 show that the bulk of the tank has similar levels of TKE for the solid and monolith stirrers. The area immediately around the blades show the largest differences with the solid stirrer generating higher TKE. This should result in better mixing for the solid stirrer cases.
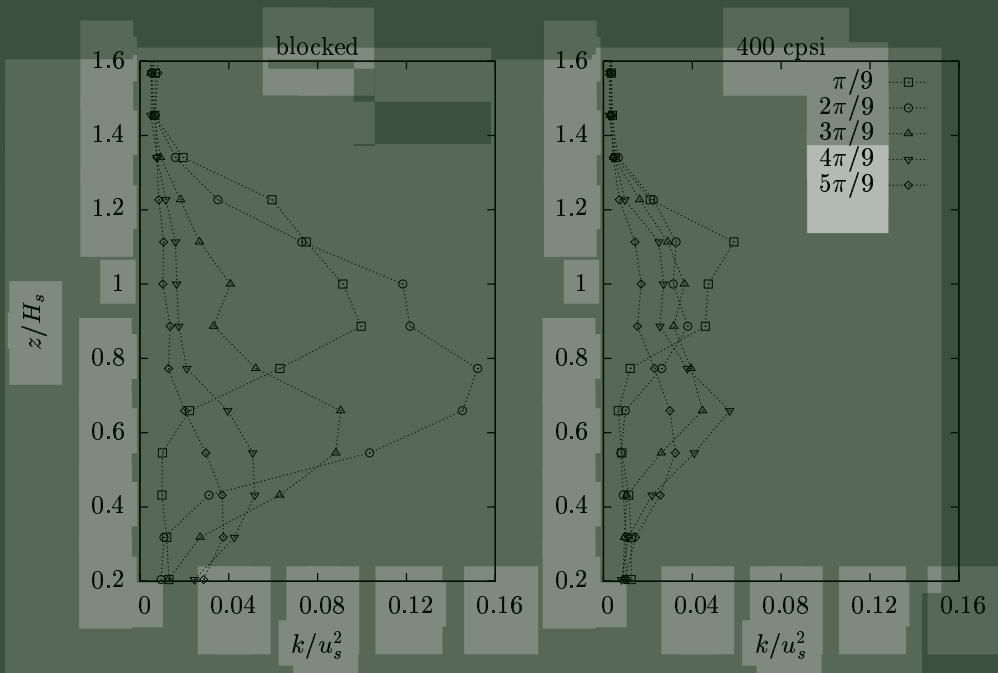
Figure 4.9: *Profiles of turbulent kinetic energy scaled with u_s^2 on a vertical line at radius, $2R/T = 0.79$. Data for a solid (left) and a 400 cpsi (right) stirrer rotating at $N = 1\,rev/s$.*
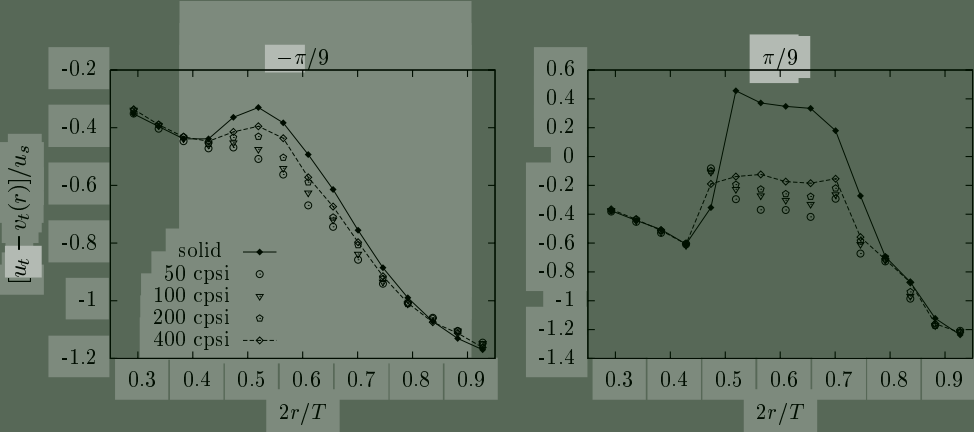
Figure 4.10: *Profiles of relative tangential velocity, v_θ, for a 50, 100, 200, 400 cpsi and a solid stirrer at a stirrer speed of $N = 1\,rev/s$. Left - $\pi/9$ before monolith and Right - $\pi/9$ after the monolith. All velocities scaled with stirrer tip speed u_s.*

4.4.3   Influence of monolith type

The effect of monolith type was investigated by measuring data for solid and 50, 100, 200, and 400 cpsi stirrers operating at a speed of $N = 1\,rev/s$. Profiles of the relative tangential velocity v_θ (c.f. equation 4.3) and the scaled TKE around the stirrer are presented in figures 4.10 and 4.11. The profiles are presented on a horizontal grid line for stirrer angles just upstream ($-\pi/9$) and downstream ($\pi/9$) from the blade. Upstream from the blade the solid stirrer generates the highest value of v_θ (figure 4.10). The value for the 400 cpsi stirrer is lower, followed by the results of the other monoliths in order of channel size. The 50 cpsi values are the lowest - this is consistent with the expectation that the 50 cpsi monolith will have the highest channel velocity.

The downstream profiles (figure 4.10, right) clearly show the recirculation behind the solid stirrer. In the wake of the blade the solid stirrer shows a positive relative velocity - meaning that the fluid is flowing in the same direction as the stirrer, i.e., towards the blade. Data for the monolith stirrers are consistent with flow passing through the monolith and flowing away from the monolith face. The results are again arranged according to the channel size for the monoliths with the 50 cpsi monolith showing the largest negative velocity behind the blade.

The turbulence levels upstream from the monolith (figure 4.11, left) are negligible compared to values in the wake (figure 4.11, right). In addition, the bulk levels from the various types of stirrers are very similar. Behind the blade the monolith holder causes peaks in the TKE at the same locations as noted previously. All monolith stirrers show a low TKE value in the area behind the blade compared to the solid stirrer cases.
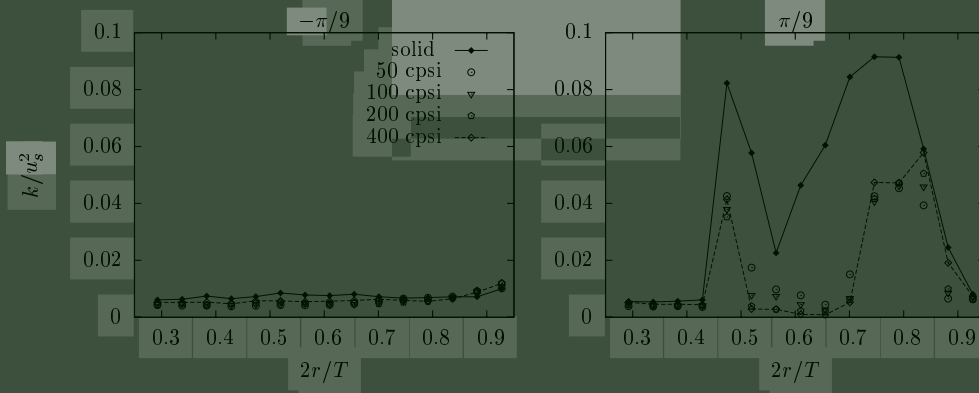
Figure 4.11: *Profiles of turbulent kinetic energy scaled with u_s^2 for a 50, 100, 200, 400 cpsi and a solid stirrer at a stirrer speed of $N = 1\,rev/s$. Left - $\pi/9$ before monolith and Right - $\pi/9$ after the monolith.*

4.4.4 Influence of stirrer speed

The influence of stirrer speed on the flow around the monolith was investigated with a 400cpsi monolith at three stirrer speeds 0.25, 1, and 2 rev/s. Profiles of the relative tangential velocities and TKE around the monolith are shown in figures 4.12 and 4.13 with data from a solid stirrer at $N = 1\,rev/s$ added for reference. The profiles are presented on a horizontal grid line for stirrer angles just upstream ($-\pi/9$) and downstream ($\pi/9$) from the blade.

Upstream from the stirrer, all scaled velocities are similar. Downstream from the stirrer the 1.0 and 2.0 rev/s cases are similar and consistent with expectations in that higher stirrer speeds produce proportionally higher relative velocities in the wake of the blade. These results are similar to those observed for the various monoliths as discussed in the previous paragraph.

The notable exception is data for a speed of $N = 0.25\,rev/s$. The profiles downstream from the blade are similar to the solid stirrer values. This seems to indicate the the stirrer speed is too low to force the liquid through the monolith channels and the blade acts as a solid blade. The profiles of TKE shown in figure 4.13 again show the low speed case to behave like the solid stirrer.

4.5 Results of channel velocity measurements

4.5.1 Selection of reported channel velocity

The monolith channel velocities were measured with the skewed LDA probe setup (c.f. section 2.3.2 and figure 2.5). In this case the rotating stirrer passes through the measurement plane, and it is not possible to adjust the LDA measurement volume to a known offset from the monolith face as in the case for a stationary mono-
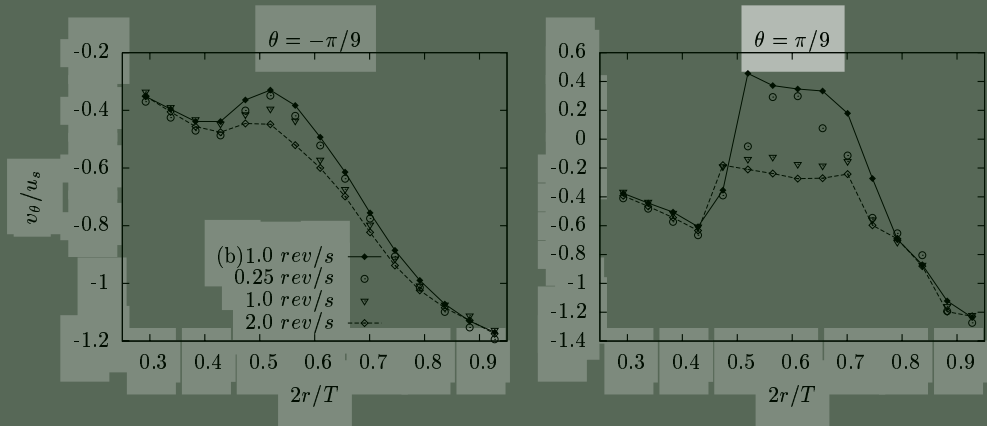
Figure 4.12: *Profiles of relative tangential velocity for a 400 cpsi stirrer running at 0.25, 1.0 and 2.0 rev/s. Left - π/9 before monolith and Right - π/9 after the monolith. All velocities scaled with stirrer tip speed u_s. The (b) refers to the solid blade stirrer.*
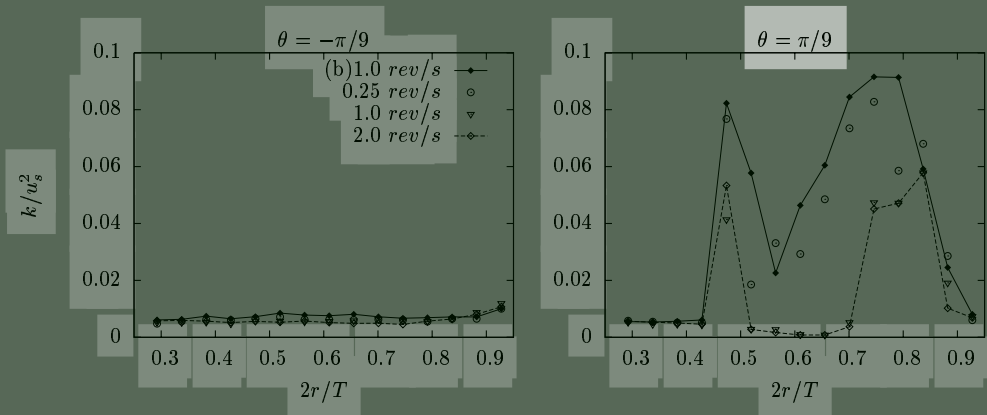
Figure 4.13: *Profiles of turbulent kinetic energy scaled with u_s^2 for a 400 cpsi stirrer running at 0.25, 1.0 and 2.0 rev/s. Left - π/9 before monolith and Right - π/9 after the monolith. The (b) refers to the solid blade stirrer.*

lith. The data extraction procedure is discussed in detail in Deelder (2001), here we present the essentials of the process.

The skewed LDA probe data were processed into $0.25°$ angular bins (as opposed to the standard $4.0°$ bins used for other data in this chapter). This was done to improve the measurement resolution in the region of the monolith face (e.g., at $N = 1\,rev/s$ one bin corresponds to a $0.68\,mm$ translation of the outer edge of the stirrer). At this resolution the differences in data from the two blades on the stirrer were such that each blade was treated individually.

The open squares series in figure 4.14 illustrates the measurement data in the vicinity of the stirrer face. As the monolith passes through the measuring plane, the probe detects both fluid and solid velocities. Data in each bin were sorted by mean measured velocity and then tested to determine if the velocity distribution contained a single or a double peak. Bins with a double peak were separated into two and the average velocity and number of data for each peak reported - this is used to distinguish between the fluid and solid velocity measurements.

The result of this procedure is shown in figure 4.14. Open symbols are measured data and the boxes represented the number of data points in each bin. Bins with a double peak distribution are split into two with the shaded box used to indicate the number of points for the high velocity (solid) value. Bins with too few data points were not used (e.g., data at $-15°$ and $-16.5°$ with only two data points). The point selected for reporting the channel velocity was the fluid velocity from the 'last' bin where the number of fluid data points were still higher than the number of solid velocities detected. This point is indicated with a solid symbol in figure 4.14. The solid velocity was similarly chosen from the 'first' bin with no fluid velocities.

The measured solid velocities were compared to the speed of the stirrer, calculated from the measurement location (radius) and stirrer speed setting for the case. The agreement was excellent in all cases and served as further validation for the use of the skewed LDA probe in the present investigation.

4.5.2 Influence of monolith type

The monolith channel size influences the flow resistance through the channel diameter d_c and aspect ratio L_M/d_c. Figure 4.15 shows the measured channel velocities, v_c (see equation 4.6), on a horizontal line across the mid-plane of the monolith face. The symbols are the original data for blade 1 and blade 2 on the stirrer and the drawn lines represent the averaged values. The results follow the expectation in that the largest channel sizes show the highest monolith velocities. The second figure (bottom) presents the same data, but now scaled with the local stirrer speed at each radius. The result is a flatter curve. Data towards the outer edge of the monolith show unanticipated lower velocities. A possible explanation may be that the flow around the monolith may be affecting the pressure distribution at the front and back face of the monolith. This issue will be revisited when discussing results from the CFD simulations (chapter 5).
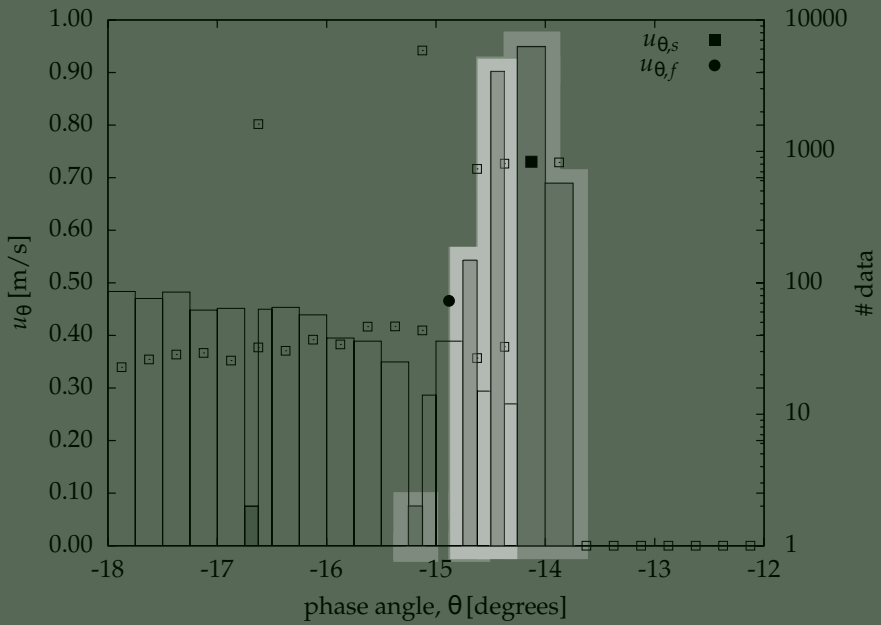
Figure 4.14: *Illustration of data extraction for channel velocity measurements. The measured tangential velocities, including the data points measured per bin, are shown. Results of the extracted data points are shown with larger solid symbols. See text for description.*
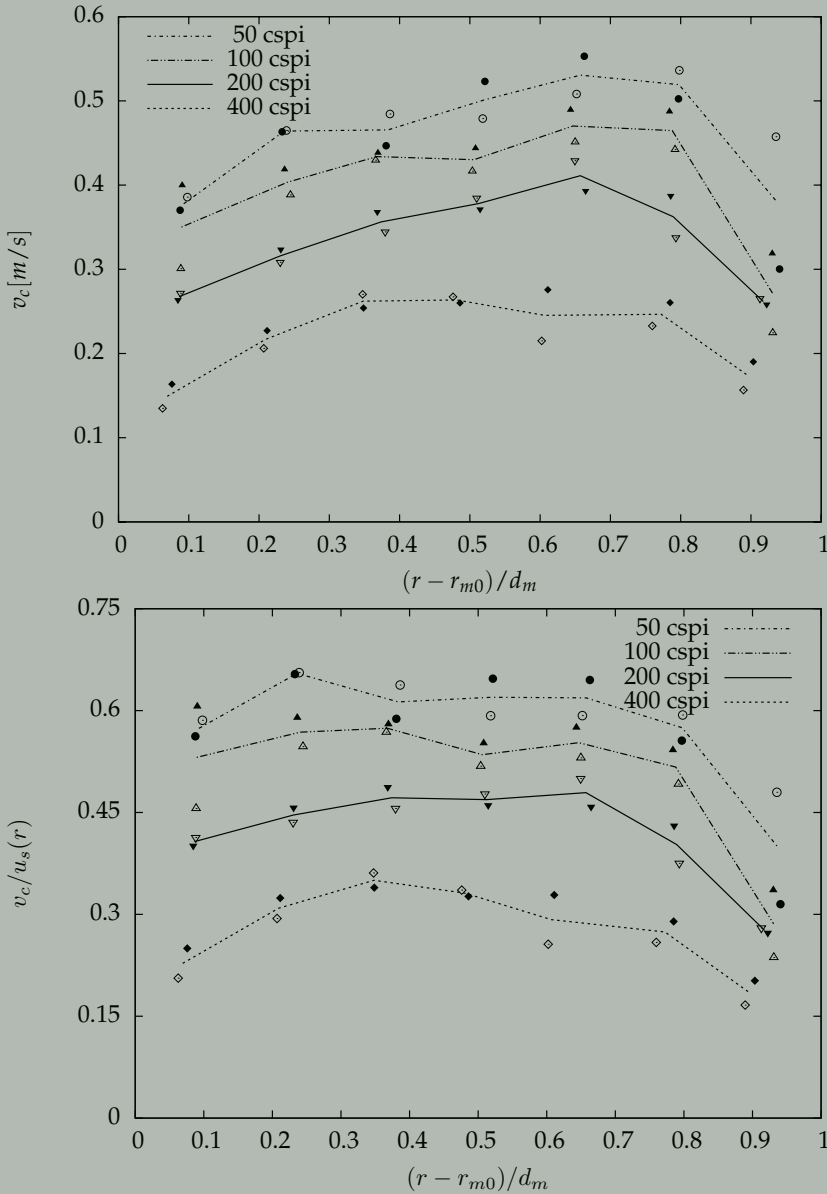
Figure 4.15: *Results of the channel velocities for four different monoliths operating at $N = 1\,rev/s$. Top: Measured channel velocity, v_c. Bottom: Channel velocity normalized with the local stirrer velocity, $u_s(r)$. Individual monolith measurements are depicted by open and closed symbols respectively - drawn lines represent the averaged values.*

Table 4.1: *Geometry of different MSR cases for which power measurements were made*

Source	T	H_L	D	D_b	B
present	0.441	0.167	0.312	0.059	0.074
Edvinsson-Albers *et al.* (1998)	0.400	0.160	0.280	0.050	0.061
Edvinsson-Albers *et al.* (1998)	0.400	0.160	0.280	0.080	0.157
Hoek (2004)	0.160	0.083	0.120	0.043	0.219

4.5.3 Influence of stirrer speed

Figure 4.16 shows the measured channel velocity data now as a function of the stirrer speed. All results are for a stirrer with 400 cpsi monoliths. The measured velocities are consistent with expectations in that the highest stirrer speed results in the highest channel velocities. Again the velocities towards the outer edge of the monolith are lower. Data for the lowest speed (0.25rev/s) show a negative value which would suggest reverse flow through the monolith. In the second figure (bottom), the scaled data shows that the negative velocity is only measured at the innermost radius, however the data from the 2 blades are consistent.

4.6 Results of stirrer power measurements

In the present study the power draw by a solid stirrer was measured for a range of stirrer speeds (0.25 – 2.5 rev/s). The results of two other studies were available for comparison: Houterman (1997) (also reported in Edvinsson-Albers *et al.* (1998)) and Hoek (2004). Table 4.1 summarizes the main geometric properties of the different cases. As explained in section 4.3.1, the present study is a scaled version of the experiment of Houterman (1997).

The stirrer speeds for the present study repeated that of Houterman (1997) and extended the data set with higher stirrer speeds as well. The experiments by Hoek (2004) were performed at higher stirrer speeds (N = 1.0 to 5.0 rev/s) and resulted in significant gas entrainment from the liquid surface for speeds above N = 4.2 rev/s. Figure 4.17 shows the power number data for the solid stirrer from the three different experiments in terms of stirrer Re number. The results show that power number comparisons can only be made for geometrically similar cases. The present study and the data from Houterman (1997) with a 5cm diameter monolith compare very well. The mean value of the present study was found to be $N_P = 0.75$. Houterman (1997) tested with both cold (293K) and warm (323K) water - the temperature effects appear to be small. Geometric effects are dominant, as can be seen when comparing the Houterman (1997) data for different blade diameters (D_B = 5cm or 8cm).

The data from Hoek (2004) show the effects of changing the fluid properties. The data consist of two sets of two measurements each. Two data sets were measured in water, and two were measured in a 56%wt aqueous glycerol mixture. The power
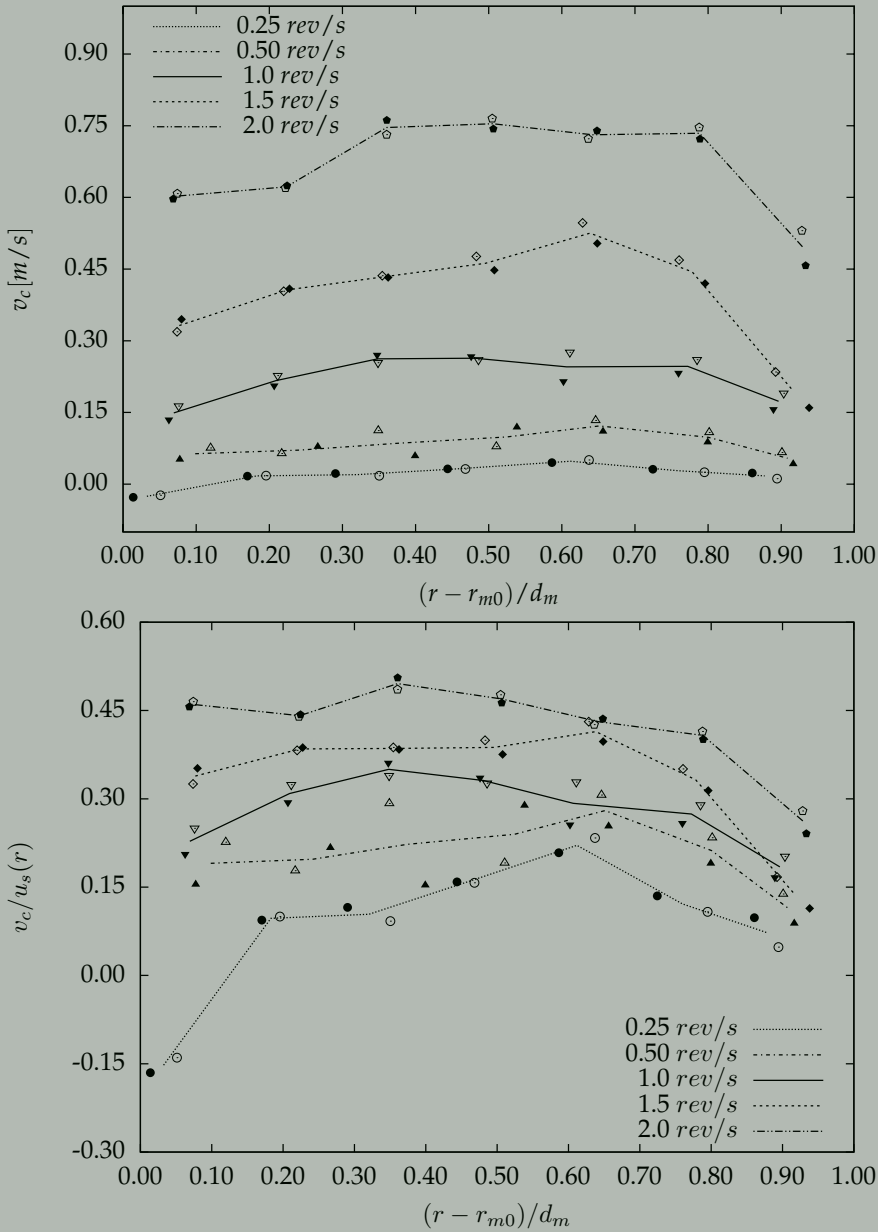
Figure 4.16: *Results of the channel velocities for different stirrer speeds with a 400 cpsi monolith. Top: Measured channel velocity, v_c. Bottom: Channel velocity normalized with the local stirrer velocity, $u_s(r)$. Individual monolith measurements are depicted by open and closed symbols respectively - drawn lines represent the averaged values.*
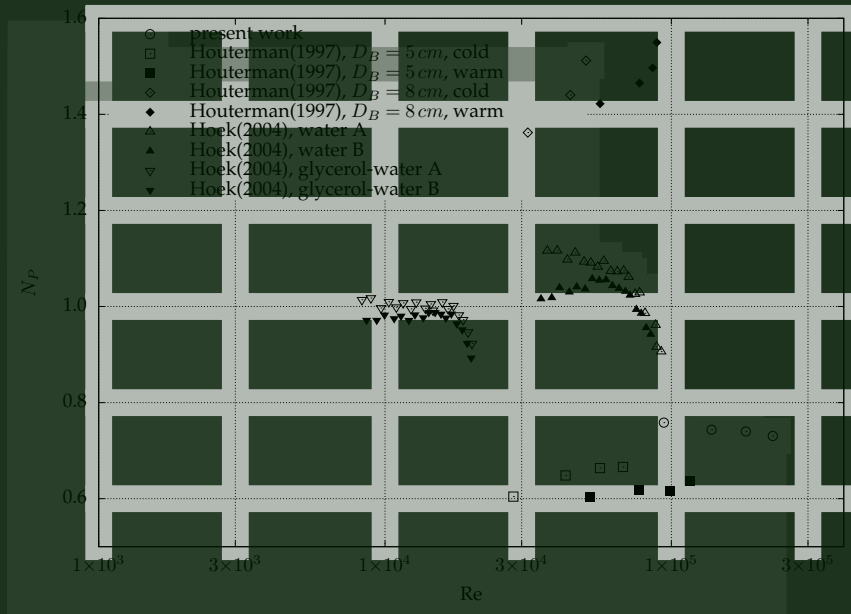
Figure 4.17: *Power number data as a function of Reynolds number for different experiments as summarized in table 4.1.*

numbers are similar (same geometry), but the point at which the gas entrainment causes a sharp drop in the power number, occurs at different Reynolds numbers.

The power number results for the MSR measured with different monoliths are shown in figure 4.18. The results show that the monolith stirrers have a smaller N_P. In the measured range N_P remains constant for the solid stirrer, but exhibits a negative slope for the monolith stirrer data. Different channel sizes (resulting in different channel flow resistances) result in a small spread of the values of N_P. In general the lowest N_P is measured for the 50cpsi monolith (largest channels) and the highest for the 400cpsi (smallest channels). Results from Hoek (2004) (not shown here) exhibit similar trends.

4.7   Mixing time results

Results of the mixing time experiment are presented in figure 4.19 in terms of the dimensionless mixing time, $N \cdot t_m$. The values for all monoliths are at the lowest for a speed of $N = 1\,rev/s$ ($Re = 1 \times 10^5$). As mentioned in section 4.4.1, this corresponded to the point at which the free-surface instability was most pronounced for a solid stirrer. Above this speed, the dimensionless mixing time increases with speed. The 50cpsi monolith data show a maximum at $N = 2\,rev/s$ ($Re = 2 \times 10^5$). In contrast to the above, the dimensionless mixing time in standard
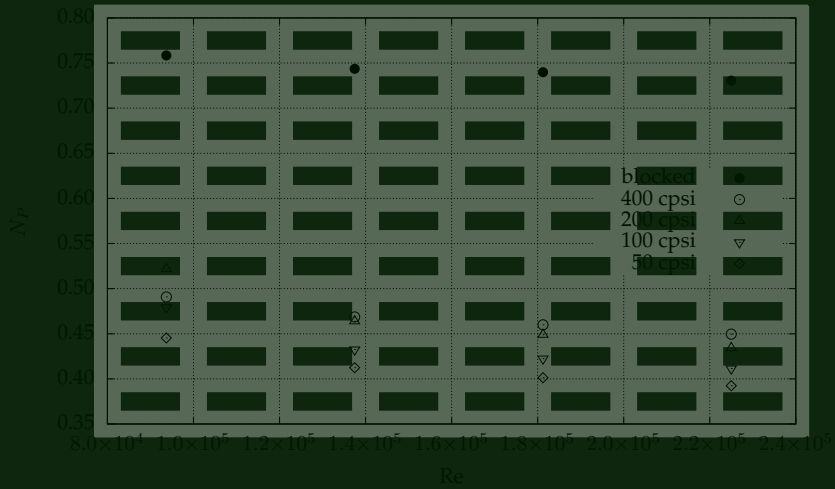
Figure 4.18: *Power number data as a function of Reynolds number for the prototype MSR and a number of different monoliths.*
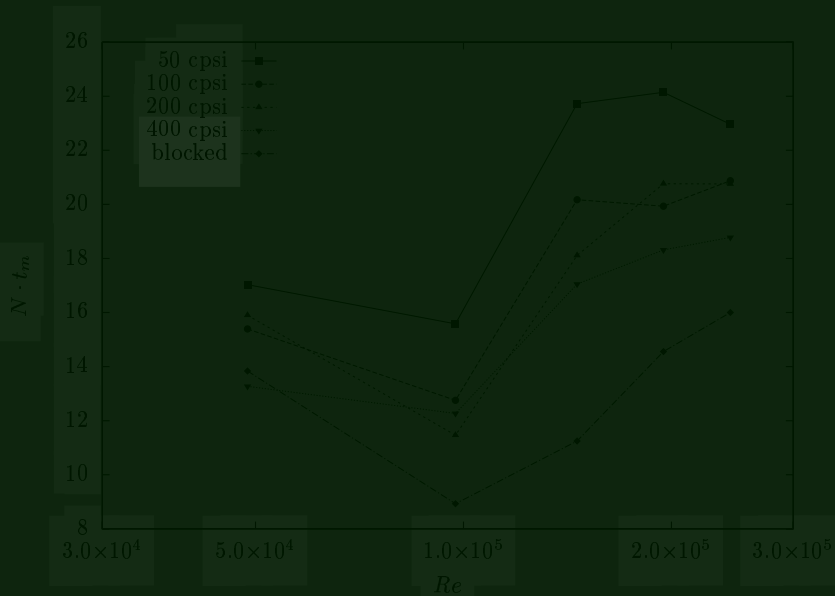
Figure 4.19: *Dimensionless mixing time, $N \cdot t_m$, vs Reynolds number for all monoliths and a solid stirrer. The stirrer speeds tested were 0.5, 1.0, 1.5, 2.0, and 2.5 rev/s). Lines added to guide the eye.*

configurations and over the range of Re numbers used in industry is typically constant e.g., $30 \leq N \cdot t_m \leq 40$ for a standard Rushton turbine and $40 \leq N \cdot t_m \leq 50$ for a pitched blade turbine (Kraume & Zehner, 2001).

Although these mixing data do not include comprehensive mass transfer testing, it shows that the bulky monolith stirrer can be used to mix the bulk flow in the reactor. The dimensionless mixing times for the monolith stirrer are lower than that found for standard stirrers. This difference may be due to the difference in the volumetric power density P/V (measured in W/m^3 for mixing studies) between the MSR and conventional stirrer configurations.

4.8   Summary and conclusions

This chapter described a detailed experimental program to characterize the hydrodynamics inside a prototype MSR. The bulk flow, channel velocities, power draw and mixing characteristics were determined for a range of stirrer speeds and different stirrer configurations.

The monolith stirrers generate a radial jet with a pair of trailing vortices in the bulk flow, similar to classic disc turbine stirrers. Velocity profiles could be qualitatively compared when scaled with the stirrer tip speed. The strength of the radial jet is affected by the amount of flow through the monolith blade. The strongest jet is present for the solid stirrer - this also results in the highest power draw and fastest mixing.

The rotating monoliths generate flow through the channels. The mean channel velocity ranged from 15 to 60% of the stirrer speed. The magnitude of the channel velocity is a coupled function of the stirrer speed (driving force) and channel characteristics (loss coefficient) as shown earlier in section 3.2. The channels at the outer edge of the monolith show a reduced velocity. For the lowest stirrer speed (0.25 rev/s) reversed flow was observed at the innermost measurement point on the monolith face.

Power number results were shown to be highly dependent on the geometry. The present data will therefore only apply to geometrically similar configurations. There is a strong correlation between the power input and mixing times for stirred tanks. This would mean that the present mixing results should also not be used for cases with different geometric configurations.

The aim of this chapter was to present the experimental work performed for the prototype MSR. A more detailed discussion of the MSR operation is deferred to the end of chapter 5, where the information from the numerical work can be included.

Chapter 5

Simulation of an MSR

5.1 Introduction

This chapter describes work done to simulate the operation of a prototype monolithic stirrer reactor (MSR). The numerical (CFD) investigation of the single-phase hydrodynamics of the prototype reactor, described in the previous chapter, is discussed. The aim is to develop a modeling strategy for the simulation of the MSR to study flow patterns, liquid circulation, power draw and the amount of fluid flowing through the monolith channels.

Stirred tanks have been investigated experimentally and numerically for a number of decades. The chapter starts with a review of previous work that is of interest to the current effort. This is followed by a description of the CFD performed.

A solid block stirrer is used to test the numerical modeling without the need for the porous simplification that is required to model the monoliths (c.f. section 2.4.4). The evaluation includes (i) different strategies to model the stirrer movement, (ii) turbulence modeling, (iii) the effect of having a free liquid surface on top of the reactor, and (iv) and the influence of mesh and geometry.

Subsequently we model a monolithic stirrer. The global flow field in the reactor is elucidated. We evaluate the power draw of the stirrer. The amount of flow through the monolith is calculated and compared to experiments and models. The chapter concludes with a review of the work and a summary of the findings.

5.2 Literature on CFD for stirred tank hydrodynamics

A review by Sommerfeld & Decker (2004) discussed the "State of the Art and Future Trends..." with regards to the use of numerical simulation for stirred tank hydrodynamics. It is clear that there is a considerable body of knowledge available on the

topic, and equally clear that a number of issues remain to be addressed in future work.

According to Bakker (1992) and Brucato *et al.* (1998) the first reported stirrer CFD study was done by Harvey & Greaves (1982*a*,*b*). The 2-dimensional, axi-symmetric domain was solved with a few hundreds of control volumes. Later Middleton *et al.* (1986) reported the first 3-dimensional CFD results with approximately 7000 cells. Recent papers report results from DNS (Ertem-Müller (2003); 16 million cells) and LES (Hartmann *et al.* (2006); 13.8 million cells) simulations with significantly larger cell counts. These detailed simulations are the combined product of decades of research and the continuous improvements in the availability of computational power.

Simulation of single phase stirred tank hydrodynamics involves a number of challenges, e.g., transient flow field with a moving stirrer or agitator, turbulence, and free-surface effects. The standard research configurations for a stirred tank include the Rushton (radial flow) or pitch-blade (axial flow) turbine in a baffled tank. Although the prototype MSR differs significantly in geometry and function, much of the available stirred tank literature applies. With the current lack of knowledge (apart from the experimental work in the previous chapter) on the hydrodynamics of the MSR, it made sense to focus on the flow patterns and power draw in the present work. This implies that the finer level of detail available from LES and DNS is not required at present - a convenient choice to reduce mesh size and computational requirement. Instead, the standard RANS or U-RANS (unsteady Reynolds averaged Navier Stokes, also called T-RANS, for Transient RANS) approach to modeling can be adopted. A secondary motivation for choosing the simpler RANS approach stems from the fact that the proposed CFD of the monolith stirrer will always have an inherent simplification, i.e., the modeling of the monolith as a porous zone (or momentum sink). As shown in chapter 2, the use of a porous zone introduces an (apparently) unavoidable change to the nature of the flow exiting the monolith - as a result even a direct simulation of the bulk flow (assuming the monolith is not resolved) is expected to differ from the experimental values.

Stirred tanks (solved with a RANS or U-RANS method) have traditionally employed standard k-ϵ models for the turbulence. Wall-functions are used to model the boundary layer. The present study also evaluated different turbulence models.

The moving stirrer can be modeled in a number of ways – a comprehensive review is presented by Brucato *et al.* (1998). One option is to use experimental data to set velocity and turbulence boundary conditions on a bounding surface surrounding the stirrer. Some of the first work (Harvey & Greaves, 1982*a*) used this approach, but it has also been used for LES simulations by Yoon *et al.* (2003). This approach limits calculations to situations where experimental data exist.

The preferred approach is to model the stirrer as part of the simulation of the stirred tank. This can be achieved by using multiple reference frames or explicit stirrer movement.

Luo *et al.* (1994) developed the multiple reference frames (MRF) method. The

mesh surrounding the stirrer is modeled in a rotating reference frame - i.e., the appropriate Coriolis and centrifugal forces are added to the fluid momentum equations. The domain around the stirrer region is modeled in the normal static reference frame - hence the name. At the interface between the two domains, the velocities between the rotating and stationary frames are coupled. The main advantage of the method is that it is static (a snapshot) and therefore does not require transient (long) simulation. The disadvantage is that stirrer-baffle interaction is smeared through azimuthal averaging which occurs at the interface between the two frames of reference. In addition, the result tend to be snapshot of the flow for the particular stirrer angle relative to the tank - a complete flow field result requires that a number of stirrer angles be evaluated.

The most realistic modeling of the stirrer is achieved by using explicit mesh movement. This approach is inherently transient and requires longer run times. However, it can model the stirrer movement accurately and can also be used to evaluate startup conditions in detail. Explicit stirrer movement can be included with:

Sliding mesh method (SMM) The mesh is partitioned into a moving and stationary part. The interface between the two regions is termed a sliding interface and is used to couple the two regions together.

Deforming mesh method with dynamic re-meshing The movement of the stirrer surfaces are prescribed and the mesh is continuously adapted in the bulk flow region around the new stirrer position.

Overset (chimera) moving mesh The movement of the stirrer is prescribed in a separate mesh that moves and interacts with the stationary mesh in the tank interior.

In most stirrer simulations the stirrer movement is confined to a well-defined cylindrical region where the sliding mesh method provides a good solution. The widespread use of the sliding mesh methods are due in part to them having been available in most commercial CFD solvers, including Fluent, Star-CD and CFX (CFDS-FLOW3D) from around 1995.

5.3   CFD simulation approach for the MSR

The goal of this section is to develop a CFD methodology for accurate simulation of a stirred tank with a bulky stirrer. With the solid stirrer the influence of the geometry, mesh resolution, turbulence model and free-surface movement are investigated.

5.3.1   Geometry

A model geometry of the experimental facility (c.f. figure 4.1) was created in the pre-processor Gambit. The model includes the tank, baffles and stirrer. The height of the model was set to the height of the liquid fill level, H_L. For investigation of the free-surface effects, the geometry was extended in the vertical direction with an additional $H_L/2$. Making use of the symmetry in the geometry, a $180°$ model of the vessel could be used. The faces on the vertical symmetry plane were modeled as rotationally periodic boundaries. Each geometry contained an inner (rotating) section encompassing the stirrer, and an outer (stationary) section with the baffles and tank walls. The selection of the tank symmetry plane can be made in two ways, figure 5.1 shows the two options graphically as B1 and B2.

The stirrer geometry included two changes to the prototype geometry to simplify meshing. In the first instance the area where the monoliths attached to the horizontal bar was modified. Material was added to remove the infinitely small angle formed where the circular holder touches the horizontal bar - see A in figure 5.2.

During manufacturing the leading edge of the monolith holder was machined with a 2mm deep, $45°$ chamfer (see figure 5.2, right). This chamfer was excluded from the initial models in an attempt to reduce the mesh requirements. Later, inclusion of the chamfer established that it significantly influences the stirrer power number due to its effect on the drag of the monolith blade. Simulations with the chamfer in later geometries resulted in much improved agreement between measured and modeled power numbers.

5.3.2   Meshing

The models were meshed using hybrid meshes containing hexahedral, pyramid, tetrahedral and polyhedral cells. Evaluation of mesh effects were performed on a range of mesh densities as summarized in table 5.1. Images of the meshes have been included in appendix E for reference.

5.3.3   Physics and models

The flow in the MSR was modeled using RANS equations as implemented in the commercial CFD solver Fluent (c.f. section 2.4.1). A number of standard two-equation turbulence models were evaluated and compared: these included the standard, realizable and RNG k-ϵ models, as well as the standard and the SST-kω model. A Reynolds stress model (RSM) was included for comparison. The model equations and model constant for the various models are included in appendix D. In the bulk of the cases the simulations were performed with standard wall functions as implemented in Fluent.

The fluid was modeled as incompressible. Water (and air for the free-surface cases) was used with the material properties set to the values for a pressure of one
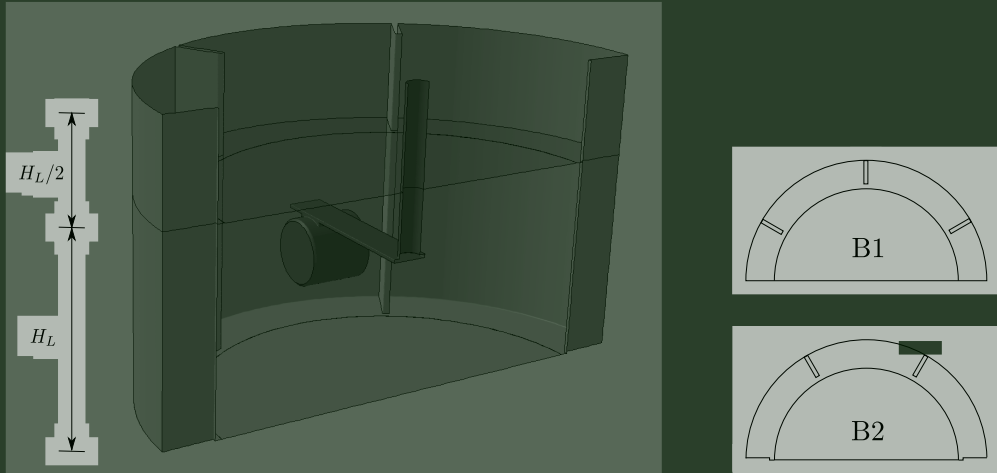
Figure 5.1: *Images of the geometries created for the CFD of the MSR. The image on the left shows the extent of the domain for the case with and without the inclusion of a free surface. Due to the symmetry, only half of the vessel was included in the model - on the right the two options for the tank baffle symmetry are displayed.*
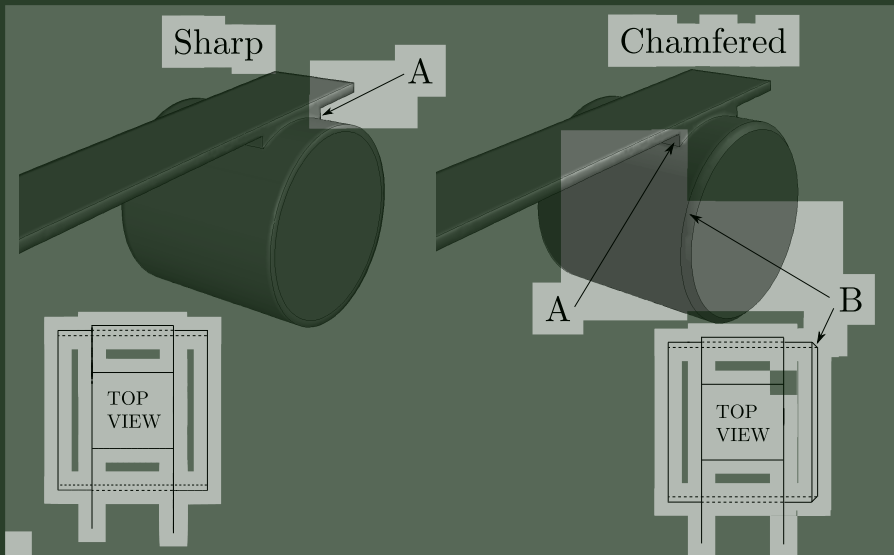
Figure 5.2: *Impeller geometry modifications included additional material added to the stirrer at location A. The stirrer holder on the left has a sharp leading edge, and the right hand figure shows the holder with a chamfered leading edge at B. In addition, the inside of the monolith could be modeled for the monolith stirrer cases, or omitted for the solid blade cases.*

Table 5.1: *Summary of different combinations for geometry and meshes generated for the MSR simulations - images of the various meshes are included in appendix E.*

Index	Surface	Impeller	Holder	Baffle type	Cell types	Cellcount
M1	lid	solid	sharp	B2	tet/hex	613K
M2	lid	solid	sharp	B2	poly/hex	307K
M3	lid	solid	sharp	B1	poly/hex	3 246K
M4	vof	solid	sharp	B1	tet/hex	8 835K
M5	lid	solid	chamfer	B2	tet/hex	547K
M6	lid	solid	chamfer	B2	poly/hex	292K
M7	lid	monolith	chamfer	B2	poly/hex	320K
M8	vof	solid	chamfer	B2	poly/hex	383K
M9	lid	solid	chamfer	B1	poly/hex	2 926K
M10	lid	monolith	chamfer	B1	poly/hex	3 147K

atmosphere (101325 Pa) and a temperature of 20°C.

Free-surface modeling was included in the simulations with a multiphase volume of fluid (VOF) method. The geometric reconstruction method was used for interface capturing, while away from the interface Fluent employs standard discretization schemes for the VOF equation. The geometric reconstruction method in Fluent is based on work by Youngs (1982), generalized for use with unstructured meshes (ANSYS, 2009) and is required for maintaining a sharp interface between phases. The latter point is important as simulations with the sliding mesh method require thousands of time-steps to reach stationary states. Schemes that do not employ explicit interface capturing, tend to smear the interface and produce unphysical results when simulating a large number (>5) of stirrer revolutions.

5.3.4   Boundary conditions

Wall boundaries are used on the vessel floor, walls and on the baffles (no wall roughness was modeled). In the inner rotating section the stirrer wall was set as stationary relative to the surrounding (rotating) mesh. The tank floor was set to be stationary in the absolute reference frame. The top surface is modeled as a symmetry plane (free slip boundary) in both the rotating and stationary part of the domain for all model configurations: MRF without a free surface, SMM without a free surface and SMM with a free surface (VOF).

The MRF and SMM methods (section 5.2) were applied to model the stirrer movement. Due to the large diameter of the monolith stirrer, the conditions for application of the MRF are not all satisfied. In particular, large periodic velocity fluctuations in the region of the inner-outer interface are expected due to the passage of the bulky blades. The effect of this was evaluated as part of the study. However the MRF approach still provides a faster start-up for rotating problems than that of the SMM (Campolo *et al.*, 2003).

5.3.5 Simulation process

The simulations were performed using second-order discretization of spatial variables. Second-order time-stepping was used except for the free surface cases – this was done because the VOF with geometric reconstruction could not be solved with second-order temporal discretization. The PRESTO! scheme was used for the pressure interpolation.

Simulations were started with the MRF method that were then used as initial condition to the further time-dependent SMM calculations. Iterations were terminated if normalized residuals were reduced by 3 orders of magnitude and monitor values of shaft torque were constant. In the transient simulations the shaft torque was used as a monitoring value to check that a "pseudo steady-state" had been reached in the vessel. For the monolith stirrers the monolith flow rate was also monitored. Several stirrer revolutions ($\approx$ 10) were required to reach the stationary state.

5.3.6 Anisotropic porosity model for rotating mesh

The motivation for using a model for the monolith was explained in section 2.4.4. The model makes use of a momentum sink to account for the presence of the monolith in the flow field. Although the CFD code allows porous modeling for such cases, the following unique features of the rotating monolith requires a customized approach:

- As the monolith rotates on the shaft in the MSR, the monolith channel orientation changes with each time step - this requires constant updates to the direction of the anisotropy in the source term.

- The momentum source is a function of the relative fluid velocity inside the monolith and requires recalculation at each time step.

Section 2.4.4 includes details on the source term calculation. The implementation and testing in a user-defined function (UDF) is described in more detail in appendix F.

5.3.7 Sensitivities

A number of parameters influence the results produced by CFD. When using a well-verified code, the bulk of these errors relate to choices with regards to inputs to the simulation and the model selection. The following items were considered:

Free-surface effects In the prototype reactor the liquid surface was free to move, and as shown in figure 4.4 the movement was not negligible. Resolving the interface requires a more costly simulation and the effect of fixing the interface location was evaluated by comparing results with a moving interface to that of a fixed (horizontal) surface.

Impeller movement The stirrer movement can be modeled using MRF or SMM. In case of using the MRF method, three stirrer positions (relative to the baffles) were modeled. For the prototype MSR the baffles are 60° apart and the three stirrer locations were selected to be 20° apart. In terms of the stirrer angle as defined in chapter 4, the MRF stirrer was located at $-20°$ ($-\pi/9$ radians), 0° (0 radians) and 20° ($\pi/9$ radians).

Turbulence A number of different turbulence models were applied. These included the standard, realizable and RNG k-ϵ models, the standard and SST-kω models and a Reynolds-stress model (RSM). The aim was to evaluate the effectiveness of the models typically included in commercial CFD codes.

Geometry The geometry of the prototype reactor was used to create the numerical model. As mentioned, two different tank configurations were created to allow modeling with and without a free surface. In addition, two stirrer models were used: one with a sharp edged monolith holder, and a subsequent model with a 45° chamfer on the leading edge of the monolith holder (see figure 5.2).

Meshing The mesh constitutes the most important single input parameter to a numerical simulation. During the course of this project a large number of different meshes were generated. In this work we report on a selection of the more recent attempts (cf. section 5.3.2).

A detailed description of the sensitivity study and the findings are presented in appendix G. The most significant parameter in terms of the power number was found to be the leading edge of the monolith holder. The chamfered (as in experiment) geometry produced the best comparison with experimental values. The fine mesh cases, modeled with the sliding mesh method (SMM) and including the free-surface movement provided the best agreement with experimental data. However, the results also show that the standard mesh, with MRF stirrer model (with three stirrer angles) and a fixed top surface, can be used to model the MSR with a fair degree of accuracy. This approach provides for fast simulation turnarounds and has been used for most of the simulations in the rest of this chapter.

5.4   Application of the engineering model

Section 3.2 introduced an engineering model to calculate monolith flow rates. This model can be applied to the MSR as well. The model inputs require characterization of the internal (channel flow) resistance - this is simply the monolith geometry. The external resistance depends on a drag coefficient and some representative bypass velocity (u_∞ in table 3.1). In chapter 3 the drag coefficient was determined through simulation and it was established that the blockage effect could be captured accurately by using the representative velocity in the affected area.

In this section we calculate the required drag coefficient from the solid blade torque measurement data. In stirred tanks, power draw (torque) is expressed in

Table 5.2: *Modified drag coefficients applied in the engineering model for the MSR.*

Case	Monolith	Drag coefficient, C_d
M050	50cpsi	1.10
M100	100cpsi	1.00
M200	200cpsi	0.90
M400	400cpsi	0.83

terms of a dimensionless power number. In Rushton turbine and axial flow stirred tanks Rushton *et al.* (1950) showed that the power draw by the stirrer can be described by a dimensionless power number, N_P, defined as

$$N_P = \frac{P}{\rho N^3 D^5}. \tag{5.1}$$

As shown in appendix C, the power number and drag coefficient on the monolith blade is proportional. This can be equated in the following way: The power consumed in the tank is the product of the moment (torque) and angular velocity. The torque is due to the drag force on each blade. In a reactor with two blades, this can be written as:

$$P = T \cdot \omega = F_d \cdot D \cdot \omega \tag{5.2}$$

The drag force F_d is a function of relative speed between the blade and surrounding fluid, the blade area and the drag coefficient. Using the tip velocity (with blockage) and the blade frontal area, the drag force is:

$$F_d = \frac{1}{2}\rho \left(\frac{\pi N D}{1 - B} \right)^2 \left(\frac{\pi D_b^2}{4} \right) C_d \tag{5.3}$$

Replace F_d in equation 5.2 and simplify to find:

$$C_d = \frac{4}{\pi^4} \cdot \left(\frac{D}{D_b} \right)^2 \cdot (1 - B)^2 \cdot N_P \tag{5.4}$$

For the prototype MSR with a constant $N_P = 0.75$ for the solid blade stirrer, this would result in a drag coefficient of $C_d = 0.74$. Although results with this single setting are similar to the experimental and CFD data, better agreement can be obtained by adjusting the value of C_d for each monolith data set. Motivations for this adjustment is deferred to the discussion of the results. The data reported in this study were obtained by setting C_d for the engineering model according to table 5.2. All other parameter in the model were set to the dimensions and characteristics of the experiments.

The power draw can be calculated from the product of pressure drop and volume flow in a system - this formed the basis of the engineering model development. Therefore the engineering model can also be used for the prediction of the power draw in monolith blades.

5.5   Results of the MSR simulations

The simulation results are presented in this section and compared with experimental data and predictions of the engineering model (EM). The velocity distribution in the tank is shown first. This is followed by the power number data. The mass flow predictions are presented last. All CFD simulation results with the case number and the full model detail for each case are included in the MSR simulation register in appendix H.

5.5.1   Flow distribution in the MSR

The characteristics of the bulk flow in the MSR have been described in section 4.4. Figure 5.3 presents results of the flow field obtained from CFD. The liquid surface is shown together with the trailing vortices in the bulk of the tank.
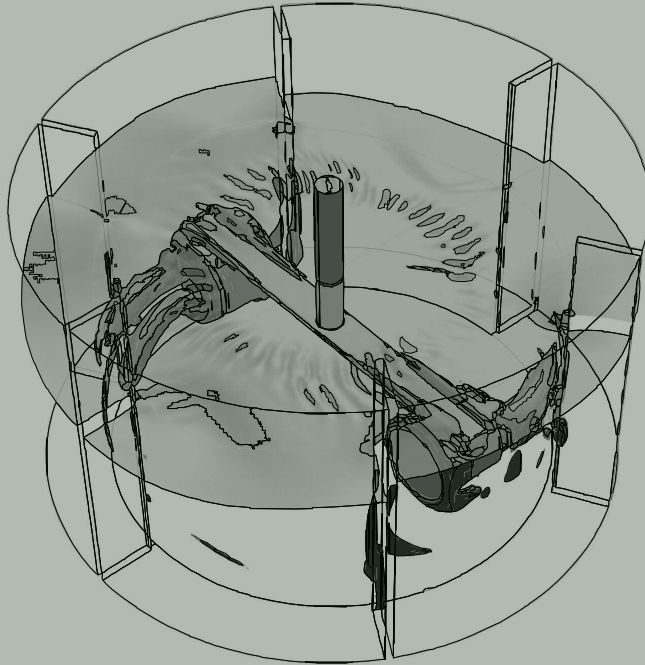
Figure 5.3: *CFD simulation of the flow field inside the MSR. The liquid surface can be seen to oscillate with the movement of the stirrer blades. A pair of trailing vortices is generated behind each blade. The vortex structure is visualized using an iso-surface of the Q-criterion (Hunt et al., 1988) at Q = 165 for a simulation with a solid stirrer rotating at N = 1rev/s.*

In this section the experimental and simulation data are compared by looking at

profiles of the normalized tangential velocity, u_θ/u_s, and the normalized turbulent kinetic energy, k/u_s^2. Profiles are compared at three stirrer locations: $\theta = -\pi/9$, $\pi/9, 4\pi/9$ (see figure 4.3 for the definition of stirrer angle, θ). Comparison of solid stirrer profiles have been included in the sensitivity study (appendix G) and are not repeated. The influence of monolith geometry and stirrer speed are presented and discussed next.

Influence of monolith geometry on velocity profiles

The monolith type affects the flow fields as a result of the flow resistance of the individual monolith channels. The resistance is a function of the channel diameter (cell density) and the monolith open frontal area, ϵ_v. In these data the 400cpsi monolith has the most, and the 50cpsi monolith the least resistance. Reported values are for a stirrer speed of $N = 1\,rev/s$.

Figure 5.4 shows measured and simulated profiles of u_θ/u_s at three angles. Agreement between the experiments and CFD is good in the immediate vicinity of the stirrer blade i.e., for $0.4 \leq 2r/T \leq 0.8$ and for $\theta = -\pi/9$ and $\pi/9$. In the region $2r/T \geq 0.8$ the agreement is less good - this is to be expected due to the use of the MRF model for stirrer movement in combination with the large stirrer diameter (see section G.2.2). This region is at the interface between the rotating and stationary mesh regions. In the wake of the monolith ($\theta = 4\pi/9$) the peak velocities are captured well, but the shape of the experimental and CFD profiles are different. At $2r/T = 0.6$ the experiments show lower velocities than CFD. This could be due to the difference in the modeled and actual momentum of the flow leaving the monolith (see section 2.4.4). Apart from that, the far field profiles collapse to similar curves when scaled with the stirrer tip speed, u_s.

A comparison of the turbulent kinetic energy profiles, k/u_s^2, is shown in figure 5.5. Experimental and CFD data collapse to similar curves when scaled with the square of the stirrer tip speed, u_s^2, but in general, scaled turbulence levels are higher for smaller (400cpsi) channels. Differences between the CFD and experiments are more noticeable than for the velocity results. In general, CFD profiles show a larger spread between the minimum and maximum values between the 50cpsi and 400cpsi monoliths. In the wake the peak values for the experiments are higher than the CFD. The shape of the wake is also different with the experimental peak values shifted to larger radii than the CFD.

The area behind the monolith shows suppressed values of TKE due to the laminar jets exiting the monolith channels. At $2r/T = 0.44$ and 0.7 the monolith holder passes through the measurement plane. This results in high peak values which might be as a result of the solid velocity being detected at this angle.

The trends for the CFD and experiments are similar in that the highest values of TKE are measured for the 400cpsi monolith, and the lowest values for 50cpsi. Because the 50cpsi monolith presents a lower flow resistance, the velocity differential between the jets and the surrounding fluid is smaller, which would account for reduced values of k/u_s^2.

Figure 5.4: *Comparison of measured and simulated profiles of the tangential velocity, scaled with stirrer tip speed, u_s. Data are shown for four different monoliths with N=1.0 rev/s at three different stirrer angles.*

Figure 5.5: *Comparison of measured and simulated profiles of the turbulent kinetic energy, scaled with the square of the stirrer tip speed. Data are shown for four different monoliths with N=1.0 rev/s at three different stirrer angles. CFD data were obtained with the MRF method and no free-surface modeling.*

Influence of stirrer speed on velocity profiles

The influence of stirrer speed on the flow field is depicted with profiles of tangential velocity scaled with the stirrer tip speed, u_θ/u_s, and scaled turbulent kinetic energy, k/u_s^2, for a 400cpsi monolith. Figure 5.6 shows profiles for three stirrer speeds $N = 0.25$, 1.0 and 2.0rev/s at the same stirrer angles as previously. The best comparison between experiments and CFD is once again in the immediate vicinity of the stirrer blade. In the wake ($\theta = 4\pi/9$) where the velocities are low, the agreement is poor. The influence of the MRF interface at $2r/T = 0.75$ is noticeable.

CFD results for $N = 0.25rev/s$ show a slight difference in the profile shape compared to the higher stirrer speeds. This is most apparent at $\theta = 4\pi/9$, but also visible at other angles. As the stirrer speed slows, the centrifugal force and resulting radial flow behind the stirrer will be reduced, which in turn will reduce the braking of the tangential flow by the baffles. As a result, the low stirrer speed might start to introduce a rotation in the bulk flow, lowering the relative speed between the blade and the fluid and thereby reducing the amount of liquid flowing through the monolith.

Profiles for k/u_s^2 for different stirrer speeds are presented in figure 5.7. Again, scaling with u_s^2 results in similar profiles, but scaled turbulence intensities are higher for lower stirrer speeds. Agreement is reasonable around the blade, but the wake is not well represented by the CFD. The peak values upstream from the monolith are over-predicted, while the values in the wake are under-predicted. The spike in the experimental data at $2r/T = 0.44$ is again due to the monolith holder passing through this location.

The scaled turbulence is higher for high cell densities and low stirrer speeds. In both cases the monolith becomes less permeable, and therefore behaves more like a solid stirrer. This leads to increased turbulence of the flow over the stirrer, and reduces the amount of laminar flow at the exit from the monolith.

The CFD model results, obtained with standard meshes, no free-surface, an MRF model for the stirrer, and using a two-equation turbulence model (realizable k-ϵ), do a credible job of capturing the flow features in the MSR.

5.5.2   Simulated power numbers for the MSR

As discussed in section 5.3.7, the values of the power number, N_P, obtained from CFD simulations, are sensitive to the model parameters. The most significant was found to be the chamfer on the leading edge of the monolith holder. Mesh density, turbulence models and the stirrer movement model had no significant effect. Simulations that include a free liquid surface have approximately 3.5% lower values of N_P. Here we look at the effect of stirrer speed and monolith geometry on the stirrer power. The stirrer power number comparisons include experimental, CFD and engineering model data.
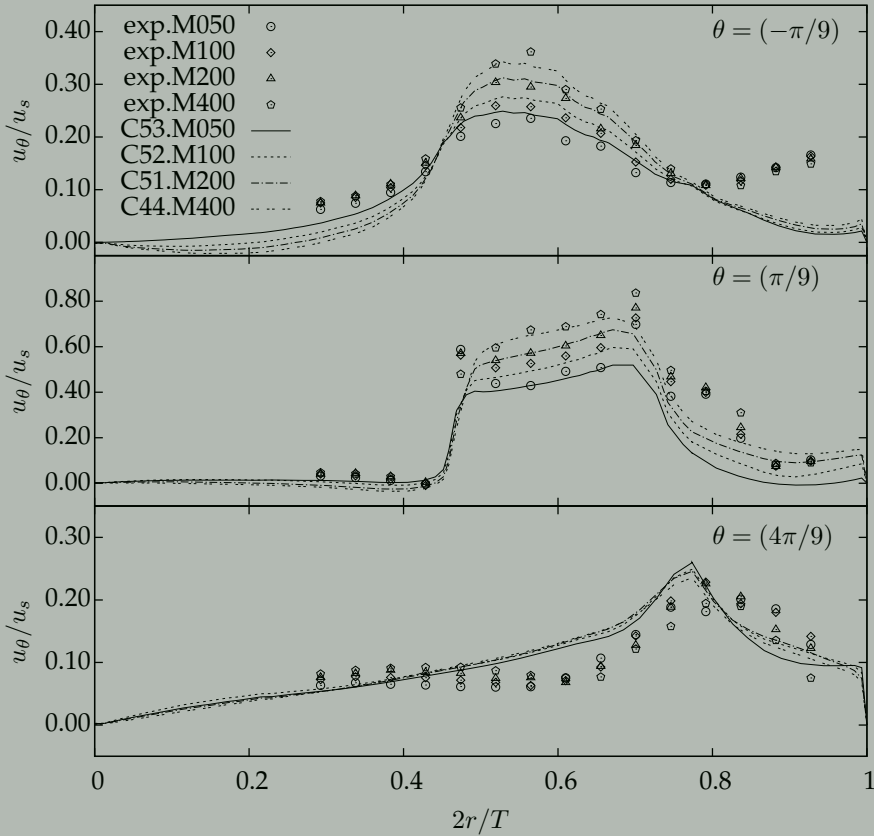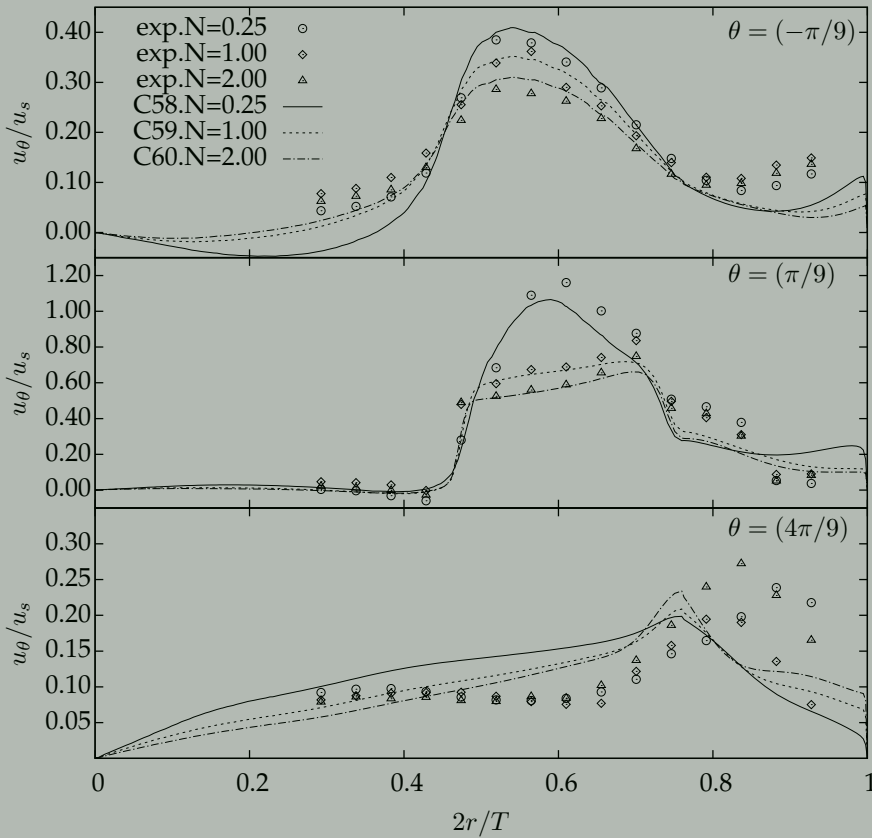
Figure 5.6: *Comparison of measured and simulated profiles of the tangential velocity, scaled with stirrer tip speed, u_s. Data are shown for three stirrer speeds at three different stirrer angles. CFD data were obtained with the MRF method and no free-surface modeling.*
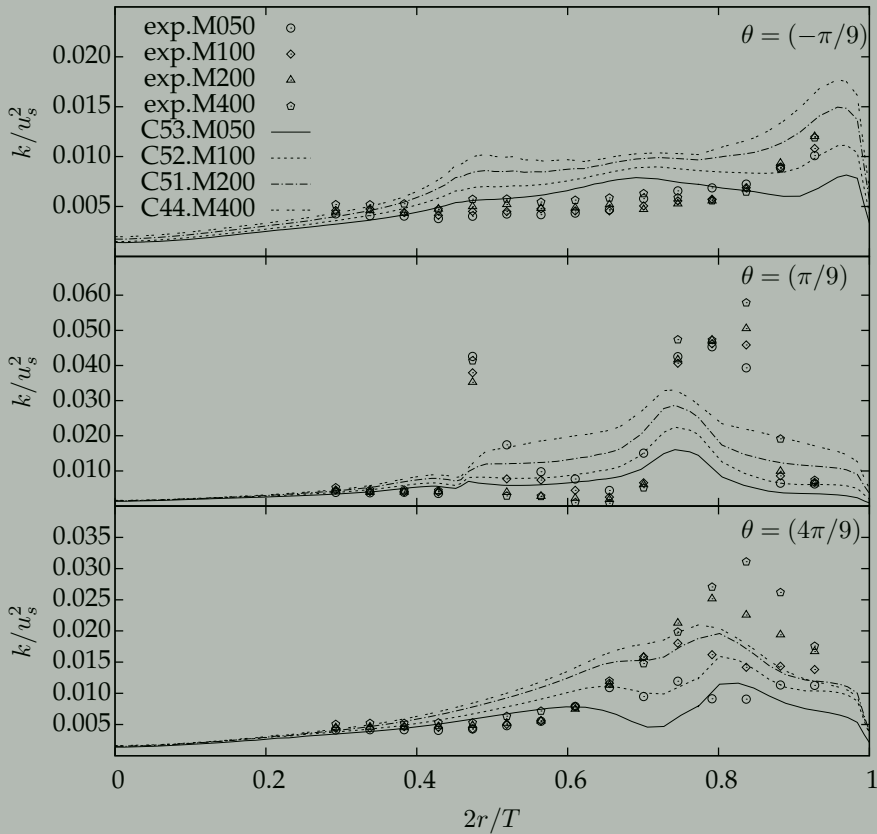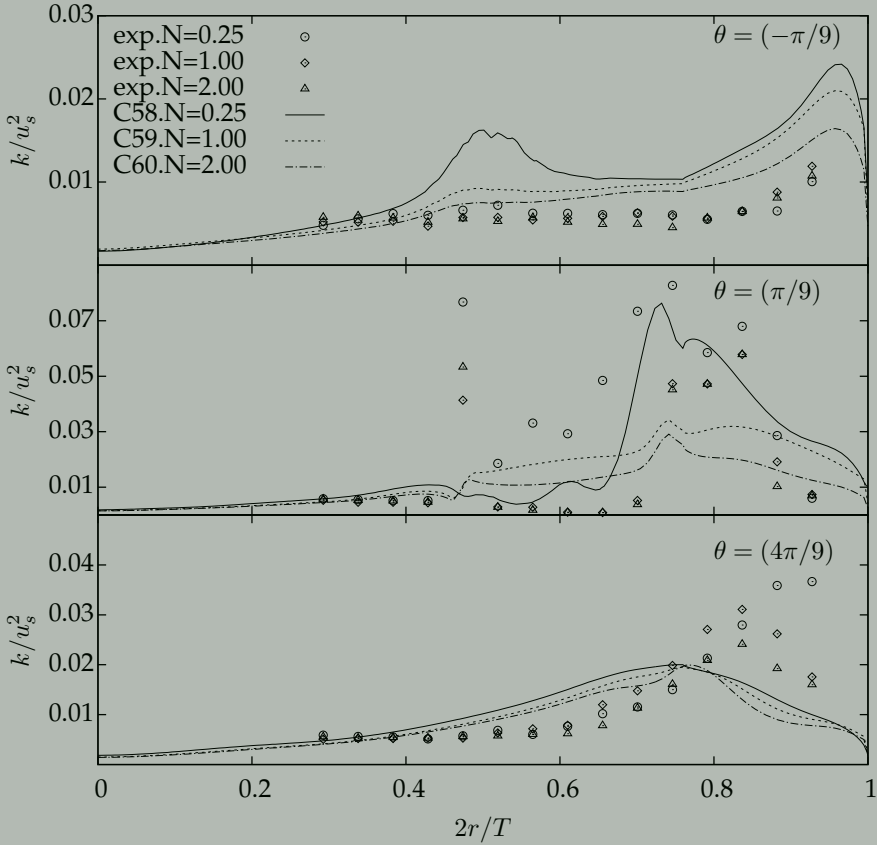
Figure 5.7: *Comparison of measured and simulated profiles of the turbulent kinetic energy, scaled with the square of the stirrer tip speed. Data are shown for three stirrer speeds at three different stirrer angles. CFD data were obtained with the MRF method and no free-surface modeling.*
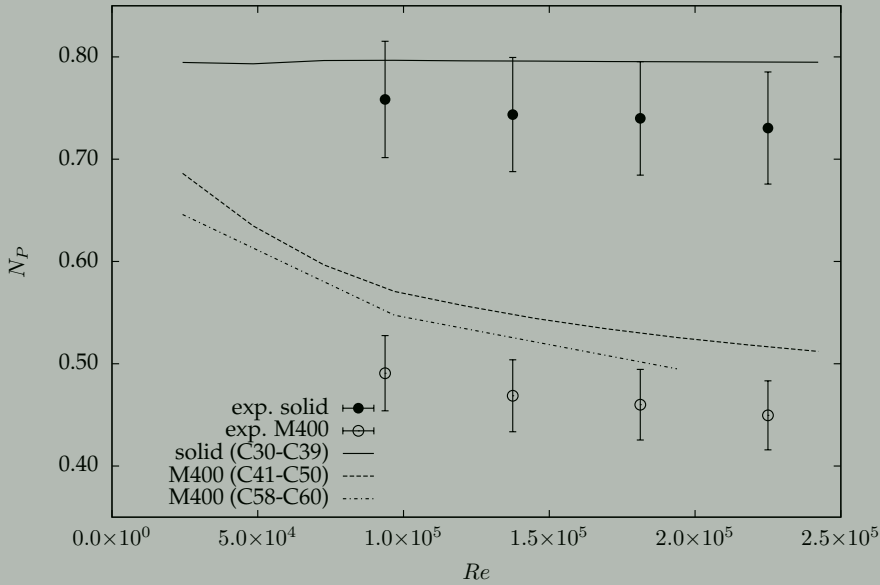
Figure 5.8: *Comparison of measured and calculated values of N_P for a range of stirrer speeds. Simulation data are shown for a solid stirrer and an M400 stirrer. The monolith data are shown for two different mesh densities. The measurement uncertainty $\Delta N_P / N_P$ was calculated to be $\pm 7\%$ of N_P.*

Influence of stirrer speed on N_P

Figure 5.8 shows N_P as a function of stirrer Re (stirrer speed). Experimental data are displayed with a measurement uncertainty that was estimated to be 7% of N_P. CFD data were obtained from MRF simulations, with a fixed liquid surface.

The solid stirrer CFD results are consistently 5-7% higher than experiments. As indicated by the sensitivity study (appendix G), inclusion of a free liquid surface should result in a 3-4% reduction in the CFD values of N_P - leading to a good agreement with the experimental data. The CFD N_P is constant for the range of Re, while the experimental data show a decreasing trend for higher Re. It is possible that the decrease in N_P with increase in Re could also be recovered with full VOF simulations, however it was not explored further in the present work.

The monolith results for a 400cpsi monolith are obtained with both the standard $307K$ cells mesh (C41-C50) and the fine $3147K$ mesh (C58-C60). The fine mesh results are lower (7%) than the standard mesh, but still higher than the 400cpsi experimental data. Adding VOF to the modeling should decrease N_P further, but not as close to the experimental data as for the solid stirrer case. In figure 5.9 the engineering model predictions of N_P are shown with the experimental data for different monoliths and stirrer speeds. The fine mesh CFD data for a 400cpsi stirrer (C58-C60) are included. The engineering model data were obtained after adjusting the individual values of C_d for each monolith according to table 5.2.
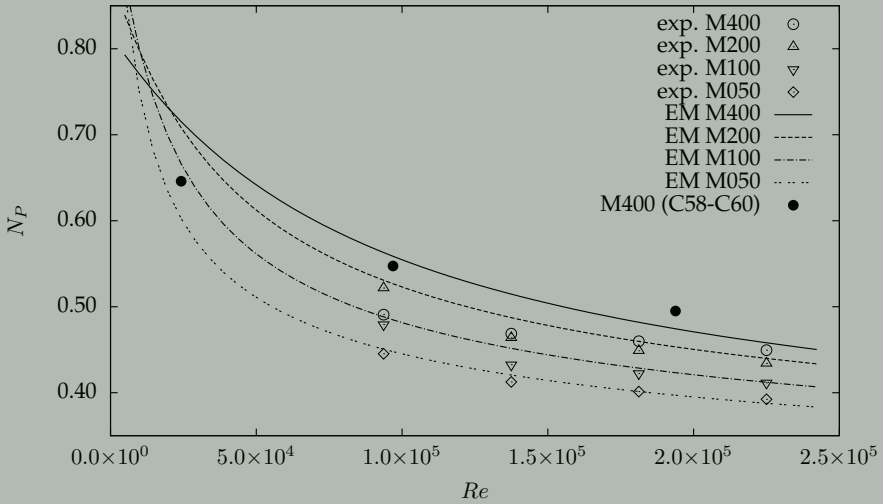
Figure 5.9: *Comparison of experimental data and engineering model (EM) predictions for N_P for various monoliths and stirrer speeds (expressed as Re). Data from the fine mesh CFD set (C58-C60) are included as well.*

One noticeable difference is that the experimental curves are somewhat "flatter" over the range of the data. Although higher, the CFD data set shows a similar trend. This exposes the imposed simplicity of the engineering model and indicates that additional work might be required for a more realistic model. Further discussion on the possible enhancements is presented at the end of the chapter.

Influence of monolith geometry on N_P

Figure 5.10 compares N_P as a function of monolith channel diameter, d_c, for a stirrer speed of N = 1rev/s. CFD data from the standard- (C44,C51-C53) and fine mesh (C59, only 400cpsi) are compared to the engineering model and experiments. The experimental value of N_P for the 400cpsi ($d_c \approx 1mm$) monolith is $\approx$ 10% lower than expected if compared to the trend and other data. It might be an indication of a measurement or data-processing error for the 400cpsi monolith data as the same trend, i.e., lower than expected value of N_P, is present in figure 5.9 as well. The other data points show good agreement between the various methods - it should however be noted that this is to be expected for the engineering model as it was the objective of adjusting the value of C_d. For the rest the trend is as expected with the smallest d_c (highest flow resistance) yielding the highest power numbers.
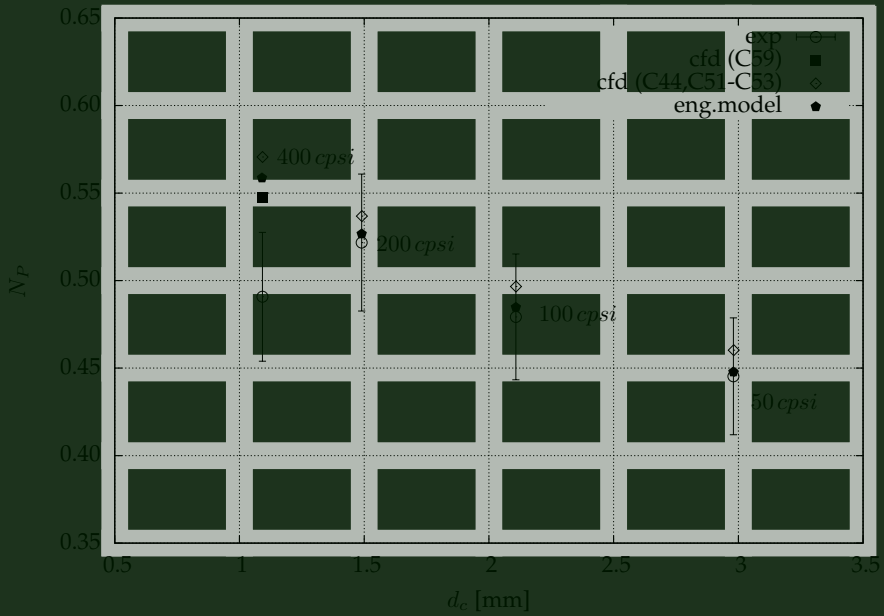
Figure 5.10: *Comparison of experimental, simulated and predicted values of N_P for different monoliths operating at a speed of $1\,rev/s$. The measurement uncertainty $\Delta N_P/N_P$ was calculated to be $\pm 7\%$ of N_P.*

5.5.3   Monolith flow rates

The prediction of the monolith flow rates is critical for MSR operation as a catalytic reactor. The channel flow rate will dictate the mass transfer rates inside the monolith. In this section the flow rates are presented as channel velocities, scaled with the stirrer tip velocity, i.e., v_c/u_s.

Influence of monolith geometry on monolith flow rate

Measured and simulated profiles of v_c/u_s are presented in figure 5.11. Data for the monolith face are presented relative to the inner edge of the monolith, in terms of a normalized monolith diameter. The radial location of the inner edge of the monolith is denoted as $(r - r_{m0})$. Both the experiments, measured upstream from the monolith channels, and the CFD values that do not model channels explicitly, have been scaled to the physical velocity by dividing with the open frontal area fraction, ϵ_v. The profiles for v_c/u_s agree well. LDA results on the inside of the monolith $((r - r_{m0})/d_m < 0.3)$ are lower than CFD values. The CFD data for the 100cpsi and 50 cpsi are over-predicted, with the worst comparison evident for the 50cpsi case.

One of the possible issues with the monolith model implemented in the CFD is the assumption that the monolith face area consists of perfect square monolith channels. In reality, all channels on the perimeter are affected by the circular shape of the monolith - the effects include reduced channel flow area and different channel shapes. In the 50cpsi and 100cpsi cases this affects a non-trivial percentage of the total flow area. Adjusting the model to account for the increased flow resistance on the monolith perimeter should improve the CFD monolith flow predictions for the large channels.

Figure 5.12 shows the variation of the mean $\bar{v}_c/u_s$ (i.e., averaged over all channels) as a function of d_c for the different monoliths and a stirrer speed of N=1.0 rev/s. The engineering model results are included as well. CFD and experiments compare well for small channel sizes, but the comparison deteriorates as the channel size gets larger - this is in line with observations made in the previous section. The engineering model does a fair job of predicting the monolith flow rates. The mesh density for the CFD cases leads to a negligible difference in flow rate prediction, despite the distinct difference observed for the N_P prediction.

Influence of stirrer speed on monolith flow rate

The influence of stirrer speed on mass flow through a 400cpsi monolith is presented in figure 5.13 for three stirrer speeds. CFD and experiments compare well for the maximum values. Agreement towards the edges of the monoith is less good. For N=0.25 rev/s the measured and simulated profiles differ the most. The negative velocities observed experimentally for N=0.25 rev/s are not present in the CFD data.
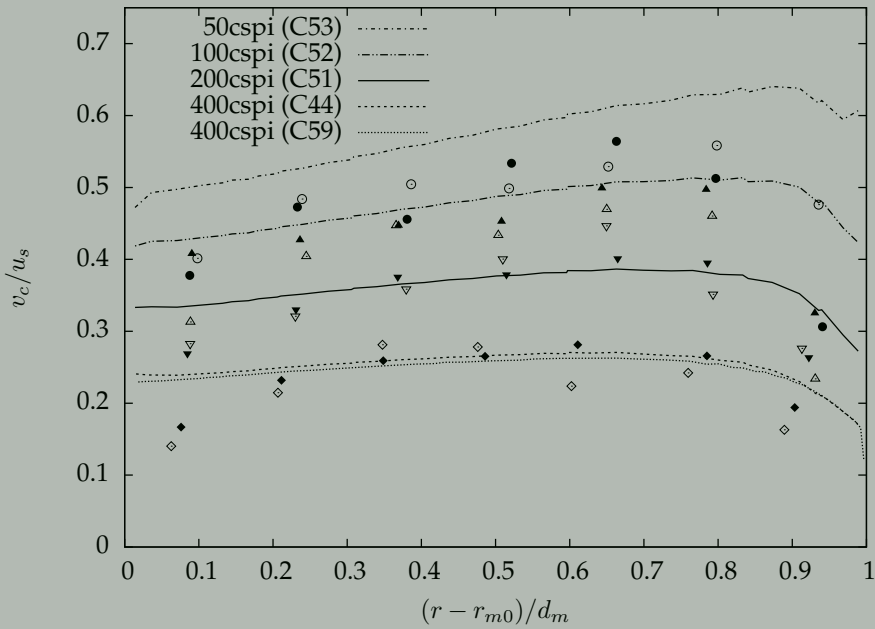
Figure 5.11: *Comparison of experimental (symbols) and simulation data for channel velocity profiles in the monolith, scaled with the stirrer tip velocity u_s, for different monolith channel densities. All data are for a stirrer speed of N=1.0 rev/s. The open and closed symbols represent individual monolith measurements for each case and give an indication of the scatter in the data.*
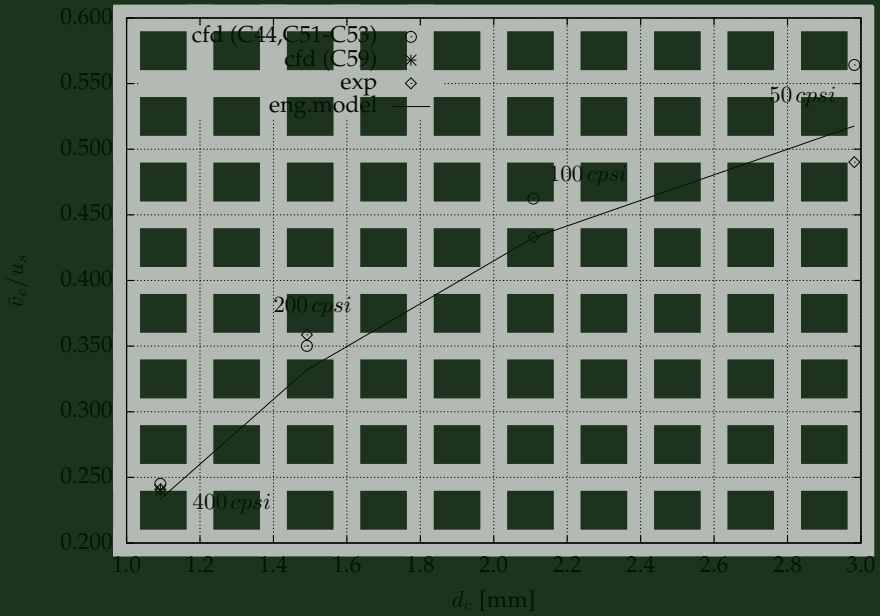
Figure 5.12: *Comparison of experimental, simulation and engineering model data for monolith mass flow (expressed as averaged, scaled channel velocities, $\bar{v}_c/u_s$) for various monoliths with N=1.0 rev/s.*
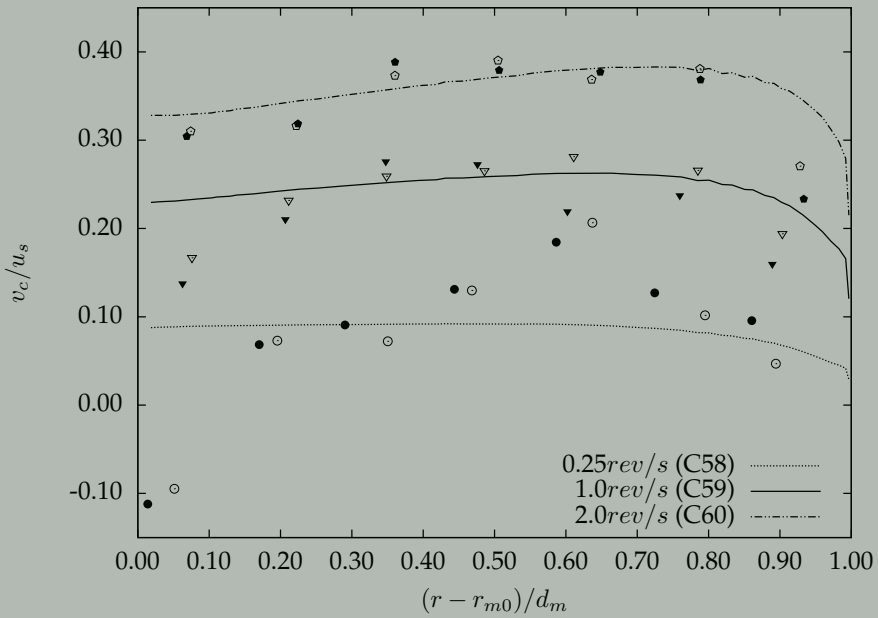
Figure 5.13: *Comparison of experimental (symbols) and simulation data for channel velocity profiles in a 400cpsi monolith for different stirrer speeds. The open and closed symbols represent individual monolith measurements for each case and give an indication of the scatter in the data.*
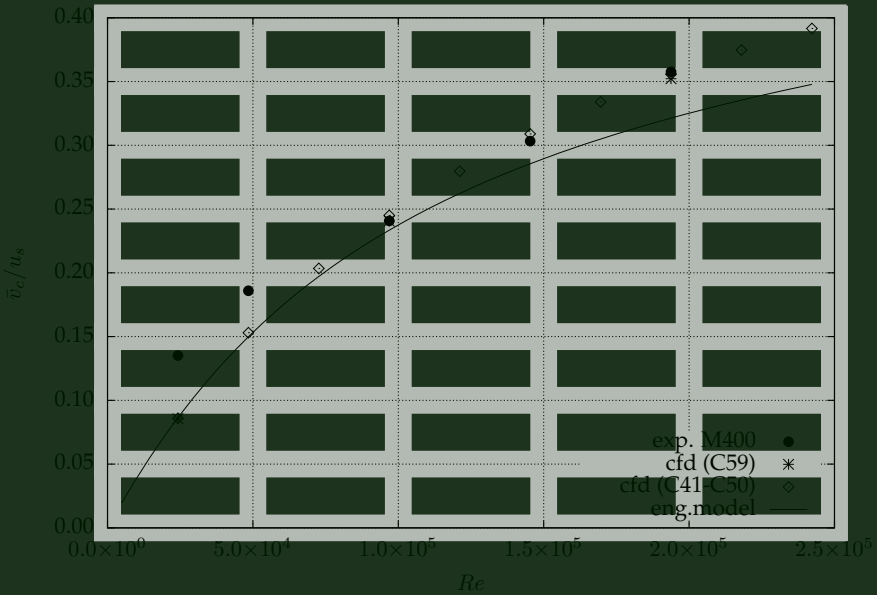
Figure 5.14: *Comparison of experimental, simulation and engineering model data for monolith mass flow (expressed as averaged, scaled channel velocities, $\bar{v}_c/u_s$) for a 400cpsi monolith at a range of stirrer speeds (expressed as Re).*

The average values, $\bar{v}_c/u_s$, for a range of stirrer speeds are compared in figure 5.14. The CFD and experiments compare very well, except at low stirrer speeds where the CFD under predicts the experimental data. The engineering model shows reasonable agreement with the other data, but tends to under predict the values for higher stirrer speeds. At higher stirrer speeds the assumption that the pressure (base) drag dominated may become weaker, as other phenomena such as free-surface motion, air-entrainement and higher centrifugal force may start to become more important. This would affect the drag coefficient that is currently assumed to be a constant in the engineering model.

5.6   Conclusions

This chapter presented the work performed to simulate the MSR with CFD. It presented a methodology that does not require large computational resources, but still allows for reasonable results of the flow field and power draw in the MSR. It also includes predictions from the engineering model developed in chapter 3.

As part of this chapter a sensitivity study was performed to investigate the influence of various modeling options on the results of the CFD simulations. Various two-equation turbulence models were evaluated with standard wall-functions.

As observed in chapter 3, the results for the bluff body are not so sensitive to the wall resolution - probably because form drag is much more important than the viscous drag. Fine mesh results did improve the prediction of power numbers, but the monolith mass flow proved to be relatively insensitive to the mesh density. Likewise, including the free liquid surface affected the prediction of N_P, but did not have a significant effect of monolith flow rate. The conclusion of the sensitivity study showed that good results could be obtained with a simple modeling approach: steady-state simulations with an MRF stirrer model, no free liquid surface, reasonable mesh density and standard turbulence models.

In particular, for the MSR, the MRF approach performed very well where the individual snapshots (stirrer angle positions) were compared with corresponding sliding mesh simulations. This proved to be a significant saving in computational requirements: a standard MRF simulation required $\sim$5000 iterations for a converged solution, for three stirrer angles this results in 15000 iterations to obtain a dataset e.g., C44 in the simulation register. The corresponding sliding mesh model would required 10 stirrer revolutions, each revolutions takes 720 time steps and each time step requires $\sim$10 iterations to converge - amounting to 72000 iterations. A model including the free surface would require a smaller time-step to keep the interface tracking Courant number in a realistic range - typically doubling the computing requirement.

The monolith modeling approach also proved to be effective in reducing the mesh requirements. All monolith results in this chapter were obtained by employing the user-defined function for simulation of the rotating anisotropic source term. During the simulation with sliding meshes it was found that round-off errors in sine and cosine terms of the transformation matrix, q_{ij} would result in unrealistic flow profiles in the monolith when the sources perpendicular to the channel direction were set $1000\times$ the values along the channel (see equation 2.25). The SMM cases were therefore performed with a factor of $10\times$ to force the anisotropy in the flow - this still resulted in flow aligned with the monolith channel direction.

Predictions from the engineering model proved to be relatively robust and compared well with experimental and CFD data. The model was deliberately kept very simple, but the predicting capability might be improved by considering additional effects. In particular, the effect of the circular perimeter on the number of actual square channels could be incorporated in the calculation of the resistance for flow through the monolith. The channels affected by the perimeter will reduce the flow area and increase the resistance, in proportion to the percentage of the area affected. Another improvement might be to consider the variation in C_d for different flow rates around the monolith - as more fluid passes through the monolith, the flow around is reduced. It is known that the value of C_d increases as Re decreases - this physical effect might be incorporated into the engineering model to enable more realistic results. And finally, the model presumes that the fluid around the monolith is stationary in the absolute frame. In cases where it is known that the bulk fluid has a rotating velocity component, the predictions would be improved by taking this into account.

In a design environment, it would be feasible to use a small number of CFD simulations to calibrate the engineering model. Thereafter, most of the design evaluations could be performed by using the engineering model to determine the operating envelope of the proposed MSR.

Chapter 6

Conclusions

6.1   Review of work

The aim of this thesis was to investigate the hydrodynamics of a monolithic stirrer reactor (MSR) in order to develop correlations for use in engineering calculations. In the course of developing these correlations, a number of related issues were investigated with experiments and simulations.

In the first part of the thesis the flow through and around a monolith in a duct was investigated in detail. The work included both experimental and simulation work. Several literature correlations were evaluated for flow through monoliths. The work of Shah (1978) and the correlation of Hawthorn (1974) gave accurate results when compared to experiments. The results of the detailed investigation were a better understanding of the physics of the flow through the monolith and a monolith model that could be used in CFD simulations. The advantage of using the monolith model is that it reduces the mesh requirements for MSR modeling because the individual monolith channels do not need to be resolved in the simulation. As shown, the application of the monolith model introduces an error in the momentum of the fluid leaving the monolith. The actual monolith jets leave with a higher velocity than in the porous medium CFD model - this affects the liquid entrainment and the flow profiles in the region immediately behind the monolith.

The duct flow case was used to develop a model for predicting the amount of flow passing through the monolith. This is an important design parameter in the application of the MSR in industry since all calculations hinge on the rate of the mass transfer inside the channels. In support of the model, the drag on an axial cylinder was investigated - in particular to establish the influence of the cylinder aspect ratio and the blockage ratio. During this investigation it was found that the historic correlation of Newton (1687) yielded fairly accurate results for the effect of blockage on the drag.

The need for an experimental data set to validate the CFD work was identified early in the project. The bulk of the LDA measurements were performed by MSc student Bas Deelder. As part of the work, the use of the skewed laser probe made it possible to measure the flow in very close proximity to the monolith face.

In chapters 2 and 5 the application of CFD for the MSR investigation was developed and compared to the experiments. A number of parameters were evaluated to gauge the sensitivity of CFD results on the inputs. The monolith model from chapter 3 was expanded to enable operation with rotating mesh simulations.

The engineering model developed in chapter 3 was applied to the MSR. Good agreement could be obtained by adjusting the input value of C_d for each monolith case. Once the C_d value was determined, the model proved to be able to predict both the mean monolith mass flow and the monolith power draw with good accuracy.

In general, this work confirmed that the MSR concept could be of practical use in the process industry. The flow velocities obtained through the monolith were shown to be 20–65% of the stirrer tip velocity. The relationship between impeller speed, monolith geometry and stirrer geometry has been investigated with the engineering model, experiments and CFD. It was shown that the channel velocities are strongly correlated to the stirrer speeds - lower stirrer speeds and smaller channels tend to reduce the channel velocity. However, the model shows that the effect is due to two different mechanisms. Slower stirrer speeds reduce the drag, and hence the pressure differential over the monolith. Smaller channels in the monolith tend to increase the resistance to flow along the channels - thereby reducing the monolith velocities. However, the two mechanisms are coupled, as slower velocities would reduce the flow resistance thought the monolith (and result in higher flows), while smaller channels with an increased channel flow resistance, increases the drag of the monolith (which tend to increase the velocities).

The dimensionless power number was found to range from 0.4 to 0.65. Smaller channel sizes resulted in higher power numbers - as the channels become smaller, the monolith becomes less porous to the flow due to the increased channel flow resistance. One can expect that the power number would approach the values for a solid stirrer blade as the channels becomes smaller and smaller.

The dimensionless mixing times were determined experimentally and found to range from $10 < N \cdot t_m < 24$. Standard stirrers in industry show higher values (30–50). This confirms that the bulky impeller configuration can act as a stirrer for the bulk liquid in the tank. Mixing times are correlated to power input - the present work found a similar trend in that the fastest mixing (solid stirrer) required the highest power input, conversely, the slowest mixing occurred for the 50cpsi stirrer which also has the lowest power number.

The coupled nature of the interactions dictate that the design of an MSR for production purposes, would require optimization to select the best option for each particular application. In order to achieve this objective, the mass transport inside the monolith will have to be included, with the findings of the hydrodynamic study, to set up the optimization problem.

6.2   Recommendations for further study

The most obvious continuation of this project would be to include accurate modeling of catalytic reactions in the calculation. It would allow a more rigorous investigation of the interaction between the in-channel and extra-channel hydrodynamics of the reactor. As an alternative, the engineering model could be used to provide input to models of the bulk chemistry for fast turnaround times and scoping studies.

Direct simulation of the entrance region of the monolith channel would establish the characteristics of the hydrodynamic flow development, as well as the impact on the development of the mass transfer. There has been evidence suggesting that the turbulence characteristics upstream from the monolith play a role here (Ekström & Andersson, 2002). In addition, the angle of attack of the flow on the face of the monolith could influence the efficiency. In this work it has been assumed that the flow approaches the monolith faces in a perpendicular direction. This was justified by the large diameter of the stirrer compared to the monolith blades. However, for a smaller stirrer to monolith diameter, the flow will approach the monolith face and channel entrances at an oblique angle. This could reduce the effectiveness of the monolith to force flow through the channels.

The presence of a gas bubble inside the monolith channel dramatically increases the mass transfer rates (Kreutzer, 2003). Hoek (2004) observed bubbles in experiments. A vertical shaft stirrer is not optimal for gas-liquid operation. An alternative is to mount the monoliths on a horizontal shaft. In a half-filled reactor, the monolith will pass alternately through the liquid and gaseous phase. Such a reactor, requiring a low rotation speed to maintain the interface, might prove more energy efficient.

Appendix A

Basics of Laser Doppler Anemometry

A.1   Overview

Laser Doppler Anemometry (LDA) is an experimental method that enables non-intrusive measurement of fluid velocities (with the condition that the seed particles should have a negligible effect on the bulk flow). It is an indirect method because the flow velocity is determined by measuring the Doppler shift of light scattered by small particles moving with the flow – care is required to ensure that the particle velocities match the flow velocity with the desired degree of accuracy. The technique was introduced by Yeh & Cummins (1964) and since then it has been applied widely in research and industrial applications. Apart from being non-intrusive (requiring no probe in the flow), other advantages include (Tummers, 1999): a single velocity component is measured as determined by the optical arrangement; the relation between Doppler frequency and velocity is linear and requires a single calibration factor; the method is directionally sensitive, that is it can measure flow reversal; and good spatial and high temporal resolution is possible.

Despite these positive effects there are a number of issues associated with the use of LDA: the method relies on optical access for the laser light, it cannot be used in opaque fluids, or in situations where the light path is interrupted; the random sampling of particles passing through the measuring volume depends on the flow velocity – the phenomena is known as velocity bias (McLaughlin & Tiederman, 1973) and may lead to erroneous flow statistics; as mentioned, the method measures the velocities of small particles in the flow – the fluid velocity can only be determined if the relationship between the particle velocity and the fluid velocity is known. In addition, it is a complex method which requires expensive hardware

and an experienced operator.

In the next section the basics of LDA are reviewed. For comprehensive information the reader is referred to textbooks devoted to the topic of LDA (Drain, 1980; Durst *et al.*, 1981; Albrecht *et al.*, 2003).

A.2   Operating principle

When a particle passes through the intersection volume formed by the two coherent laser beams, the scattered light, received by a detector, has components from both beams. The Doppler frequency can be determined with an 'optical mixing' or 'heterodyne' technique on the detector. When two light waves with slightly different frequencies, f_1 and f_2, are mixed on the surface of a square-law detector (typically a photo-multiplier tube), the output signal oscillates with the difference of the frequencies $f_1 - f_2$. A signal processor is used to extract the Doppler frequency from the photomultiplier output.

Fringe model The fringe model (Rudd, 1969) is often used to visualize aspects of the dual-beam configuration for LDA. When discussing LDA with reference to the fringe model, it should be kept in mind that the model ignores the fact that heterodyning occurs on the photomultiplier and not on the particle. Apart from this, it gives a straightforward interpretation of the proportionality between the velocity and the Doppler frequency. In the intersection volume of two coherent laser beams an interference pattern will form. The two waves will amplify when they are in phase, and will extinguish when in anti-phase. The resulting pattern is given by a set of parallel light and dark bands, called fringes, as seen in figure A.1.
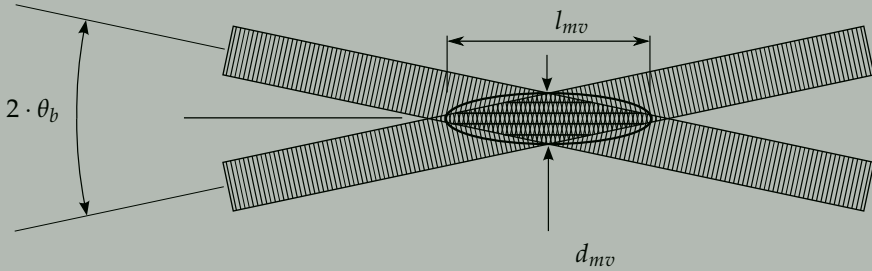
Figure A.1: *The geometry of two laser beams crossing to create a measuring volume. The interference pattern can be seen as a series of fringes. In 3-dimensional space the measurement volume is ellipsoidal with length l_{mv} and diameter d_{mv}.*

The distance between fringes, d_f, is called the fringe spacing and is a function of the wavelength, λ, and the half-angle of intersection, θ_b, between the laser beams:

$$d_f = \frac{\lambda}{2sin\theta_b}. \tag{A.1}$$

The half-angle of intersection can be determined from the focal length of the sending lens, F, and the distance between the 2 parallel beams when reaching the lens (the beam spacing), s_b:

$$tan(\theta_b) = \frac{s_b}{2F} \tag{A.2}$$
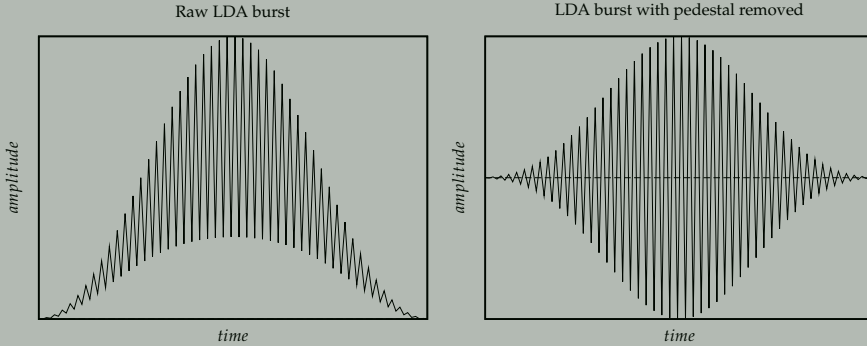
Figure A.2: *Example of the signal from the photomultiplier tube when a particle passes through the LDA measuring volume.* Left: *Raw signal including a non-oscillating component due to reflected light as the particle pass through the light.* Right: *An LDA 'burst' with only the oscillating part of the signal from which the particle velocity can be determined.*

Particles crossing the interference pattern will alternatively be illuminated by alternating light and a dark bands. The light scattered from these particles is measured with a photomultiplier tube and converted into an electrical signal. The raw signal from the photomultiplier includes a non-oscillating component (the pedestal) due to reflection from the particle as it passes through the measuring volume (figure A.2, left). This low frequency component is subtracted, leaving only the oscillating signal, commonly called the LDA 'burst' (figure A.2, right).

This oscillating pattern is recorded and processed to obtain the Doppler frequency. The measured frequency corresponds to the particle velocity component, u_x, that lies in the plane of the laser beams and is perpendicular to the bisector of the beams. The Doppler frequency is related to the velocity component and the fringe spacing as:

$$f_D = \frac{u_x}{d_f} \tag{A.3}$$

This equation lacks directional information since the Doppler frequency will always be a positive value, irrespective of the direction in which the particle crosses the measuring volume. In practice this problem is addressed by adding a preshift frequency, f_s, to one of the 2 beams. In terms of the fringe model this causes the fringes to move with a velocity $u_f = f_s d_f$ in the measurement volume. As a result zero velocities can also be detected. The Doppler frequency measured at the detector now becomes:

$$f_{Ds} = f_D + f_s. \tag{A.4}$$

The required velocity component u_x can now be calculated as:

$$u_x = (f_{DS} - f_S)\, d_f. \tag{A.5}$$

For unambiguous results $f_{Ds} - f_s > 0$ – a practical guide is to choose the preshift frequency twice the expected maximum measured Doppler frequency, i.e. $f_s > 2 \cdot u_{x,max} \cdot d_f$. With this setup zero velocities can be detected.

Measuring volume
The intersecting volume of two laser beams forms an ellipsoidal volume as shown in figure A.1. The relationship beween the length and the diameter of the measuring volume is given by

$$l_{mv} = \frac{d_{mv}}{sin\theta_{LDA}}. \tag{A.6}$$

A.3   Error sources in LDA

Several factors influence the quality of the data obtained from LDA. These factors can be attributed to the experimental setup, the LDA hardware or to the sampling process of LDA. Extensive investigations on these errors have been presented by (Edwards, 1987; Absil, 1995; Van Maanen, 1999; Tummers, 1999) and can be found in LDA textbooks.

The experimental setup is important with regards to accurate positioning of the measurement volume. Uncertainty in positioning and probe orientation may be much more important than other errors. In the present study all probe traversing was achieved by using a fixed translation table with 3-axis movement. The setup was able to position the LDA-probe with micrometer precision – thereby minimizing errors related to the positioning.

LDA hardware is a collective term for the equipment used to detect and process the reflected light from the measurement volume. The effect of hardware on the data has been termed validation bias by De Graaff (1999) and extends the previous concept of filter bias to include other hardware effects. In practice a number of parameters control the hardware operation: filter settings, laser power, photo multiplier tube voltage and threshold value. A detailed discussion on these settings for the hardware used in this work have been presented by Deelder (2001) and Groen (2004). By careful selection of the operating parameters, most hardware related errors are minimized and can be disregarded – the exception is multiple validation. Also termed multiple validation bias, it occurs when a single LDA burst is interpreted as more than one velocity realization by the hardware. This is often due to low signal-to-noise ratio or due to irregularly shaped bursts. Although the LDA system includes a switch to detect only one measurement per burst, some multiple validation occurred. It can be detected on a histogram of the time between data (time between consecutive velocity measurements as detected by the system). A

peak will be present in the histogram around the smallest values of the time between data. This can be corrected to some extent by discarding samples where the time between data is zero or very small (smaller than the transit time associated with that particle crossing the measurement volume).

A number of bias effects are associated with the random sampling of particles in LDA and the finite size of the measurement volume: angular (fringe, directional) bias, velocity gradient bias and velocity bias. Each will be discussed briefly.

Angular bias Also known as fringe or directional bias, this bias stems from the fact that several fringe crossings are needed in order to validate a measurement, so a particle passing through the measurement volume at a large angle may not be registered. This can be reduced by applying a Bragg shift to one of the beams (equation A.5). By setting the shift frequency higher than twice the value for free-stream velocity the fringe bias becomes insignificant (Edwards, 1987).

Velocity gradient bias When a strong velocity gradient is present within the flow, gradient bias can occur. This error arises due to the small but finite size of the measurement volume, which may spread across the velocity gradient in the flow. If the gradient is linear in the measuring volume there is no effect on the mean velocity. However, the measured velocity variance is higher due to the variation in the mean velocity. A method to correct this bias was presented by Durst *et al.* (1995) – in the present study velocity gradient bias was negligible.

Velocity bias McLaughlin & Tiederman (1973) were the first to observe a correlation between the instantaneous data rate and the instantaneous velocity in a uniformly seeded flow. Such a dependence is confirmed by the fact that velocities with a large magnitude are more frequently sampled than velocities with a small magnitude. The arithmetical average of sampled velocities is higher than the velocity average based on equidistant time intervals. This shift of the mean velocity toward the high value is known as the velocity bias (also called particle bias). Meyers (1991) presents a concise review of the effect of McLaughlin & Tiederman (1973) on subsequent LDA work: velocity bias became one of the most active research areas. The focus on velocity bias overshadowed the importance of other biasing factors mentioned above. The publication of Meyers (1991) serves as an example – entitled *Biasing Errors and Corrections* it only dealt with velocity bias.

Theoretical prediction (McLaughlin & Tiederman, 1973) estimates the bias to be a function of the turbulence intensity, Tu,

$$\frac{\bar{u}_b}{\bar{u}} = 1 + Tu^2. \tag{A.7}$$

Here $\bar{u}_b$ is the biased mean velocity and $\bar{u}$ the true mean velocity. The turbulence intensity is defined as $\sigma/\bar{u}$, the standard deviation normalized by the mean velocity. Zhang (2002) shows this estimate to be valid for $Tu < 30\%$.

Velocity bias became a controversial issue as different methods were developed for detection and correction of the phenomenon. Tummers (1999) gives a good review and includes detailed investigations into various factors influencing the velocity bias. Following Tummers (1999), corrections methods for velocity bias can be either through sampling methods, or with weighing factors. If LDA samples are acquired with a fixed time between data, the correlation between velocity and the data rate no longer exists and velocity bias has no effect on arithmetical averaging. However this requires high data rates that is not always possible. The second correction method is weighting factors that compensate for the velocity bias during processing of the velocity samples. The weighting factors can be based on the inverse velocity, the particle transit time through the measurement volume or the inter arrival time (time between successive samples). Correction methods provide the best results if all three velocity components in the flow are measured simultaneously (coincidence mode) and the data rate is high. The guideline on data rate is:

$$\nu_{LDA} \cdot \lambda_t > 10, \tag{A.8}$$

where ν_{LDA} is the mean data rate, and λ_t is the Taylor time scale. All three velocity components are measured by operating the LDA acquisition system in the *coincidence* mode – this means that the data is only accepted if a burst is detected simultaneously (or within a small prescribed time window) on all three channels. Forcing coincidence mode results in a lower data rate. In this study coincidence measurements were not performed to maximize the data rate during acquisition. During post-processing the data could be resampled with in-house LDA software (Harteveld, 2005) to obtain coincident data. The coincidence data were used to evaluate the influence of velocity bias by correcting the data with an inverse velocity weighing method, $2D^+$ of Nakayama (1985).

Appendix B

Resolved 50cpsi monolith simulations

B.1   Background

In section 2.5.1 the comparison between experimental and CFD profiles of the flow downstream from the monolith showed consistent differences with the experimental data showing higher velocities. Simulations that include individual monolith channels were performed to investigate the details of the flow behind the monolith. Only the case of a 50cpsi monolith was considered as smaller channel diameters (for higher monolith cell densities) would require a larger mesh to resolve the individual channels with sufficient resolution.

B.2   Geometry and mesh

The geometry for the sealed monolith in a square duct was used (see figure 2.6) with the porous monolith replaced with a 50cpsi monolith. A fine mesh was generated to resolve the channel flow, as well the flow in exit region of the monolith where each individual channel is expected to produce a jet. Figure B.1 show the geometry outline with the mesh density in selected locations. Only one quarter of the duct was modelled, however both the inlet and exit of the monolith were included in the simulation. The simulations were performed on a mesh with 8.533 million cells.
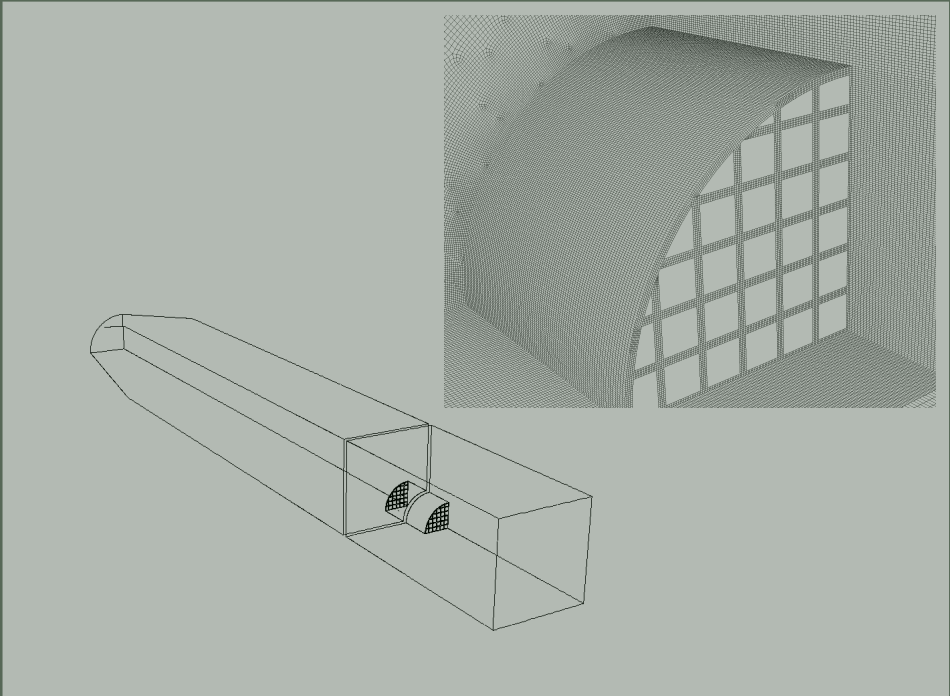
Figure B.1: *Images of the geometry and mesh generated for the resolved simulations of the 50cpsi monolith.*

B.3   Model setup

The simulations were performed with water as working fluid, similar to the work in chapter 2. In reality the flow physics presents the challenge of turbulent flow entering relatively small diameter channels where it is expected to re-laminarize. Upon exiting the monolith, it should once again become unstable and turbulent. Such simulations are possible with direct calculations, but would require a full domain (without symmetry planes that would affect the turbulent structures) and a transient calculation. Such simulations would require significant computational resources and were not attempted for this study. Instead, a number of steady state simulations, using turbulence models, was performed to investigate the flow behind the monolith.

The flowrates were selected to be the same as for the experimental study, i.e. 15, 30, 50 and 65 l/min. Results were obtained with the realizable k-ϵ turbulence model using enhanced wall functions (i.e., where the mesh is sufficiently fine the code integrates to the wall, and otherwise wall functions are applied for the boundary layers).

B.4   Results

The flow field upstream from the monolith is similar to that obtained with a porous monolith as presented in chapter 2. The velocity profiles in the wake of the monolith were found to be different from the earlier simulations where the monolith was modeled as a porous medium. The results from chapter 2 are repeated here with the resolved simulation data included. Figure B.2 shows the normalized velocity profiles at three locations downstream from the monolith for two different flow rates: the top half of each graph shows 15l/min and the bottom half 65l/min. The resolved data (for a 50cpsi monolith) is added as the dashed lines; the experimental (symbols) and porous CFD results (solid lines) were obtained for a 400cpsi monolith (compare to figure 2.11). The resolved CFD results show very good agreement with the experiments in terms of the peak values of normalized velocities.

Figure 2.10 in chapter 2 also showed the obvious difference between the experimental data and the CFD results obtained with the porous monolith. Figure B.3 presents the same data, but with the CFD data from the resolved monolith simulations included.

The velocity profiles for the resolved CFD simulations are in good agreement with the experimental data. A comparison of the original porous medium results with the resolved channel CFD clearly shows the difference in the downstream results. This confirms that the fluid momentum at the exit of the monolith can not be captured with a porous model approach, but would require a resolved simulation if this is of importance.
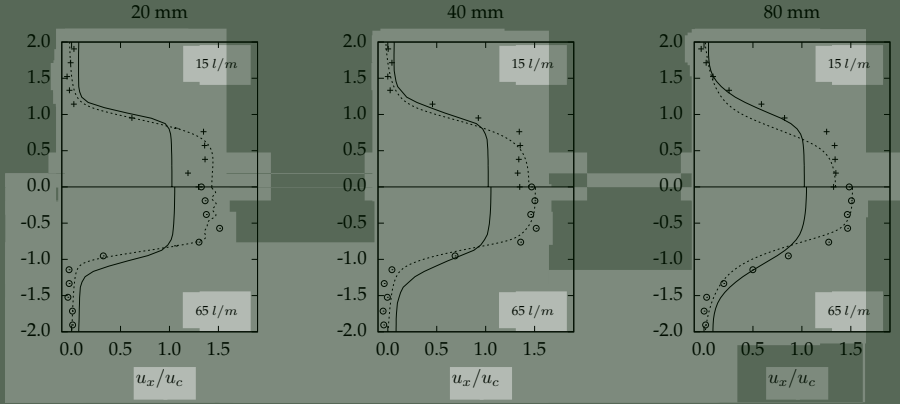
Figure B.2: *Normalized axial velocity profiles on three positions downstream from the monolith in a sealed duct. The top half of each graph shows a flow rate of 15l/min and the bottom half a flow rate of 65l/min. Symbols are experimental data, solid lines are the CFD from chapter 2 and dashed lines the results from the 50cpsi resolved monolith case.*
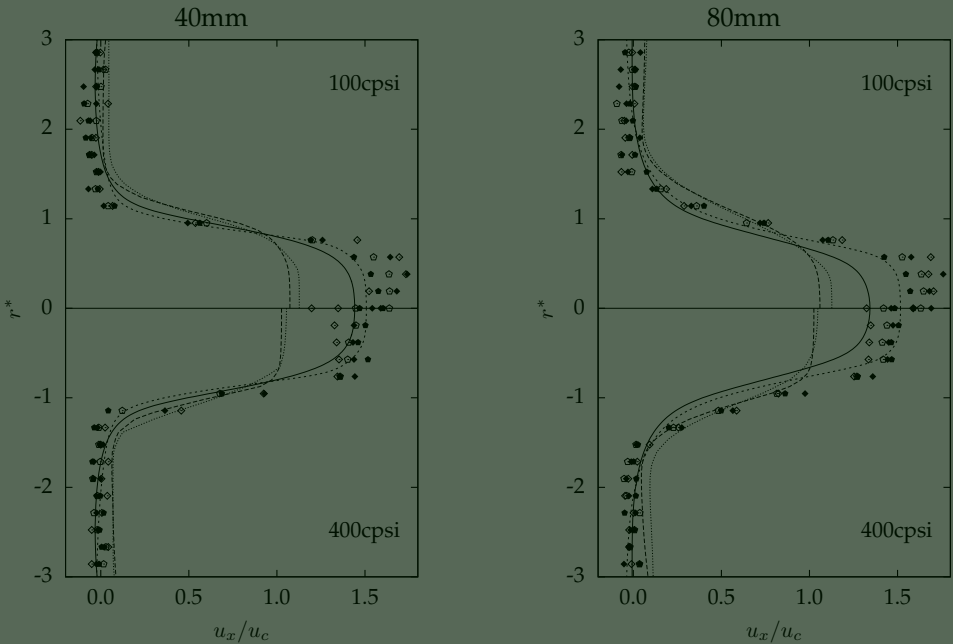
Figure B.3: *LDA (symbols) and CFD profiles (lines – – – –, ...) of the axial velocity normalized with the monolith channel velocity, u_x/u_c, on a vertical line 40mm (left), and 80mm (right) downstream from a 100cpsi and a 400cpsi monolith. Symbols for the various flow rates are the same as in figure 2.9. Two new lines are added for the 15l/min (——) and 65l/min (- - - -) results obtained with the 50cpsi resolved simulations.*

Appendix C

MSR power numbers

C.1 Overview

The generic definition for the power number as applied in mixing studies have been derived originally for disc type stirrers. This appendix evaluates alternatives.

C.2 MSR power number

In Rushton turbine and axial flow stirred tanks Rushton *et al.* (1950) showed that the power draw by the stirrer can be described by a dimensionless power number, N_P, defined as

$$N_P = \frac{P}{\rho N^3 D^5}.$$ (C.1)

For a stirrer Reynolds number, *Re*, defined as

$$Re = \frac{\rho N D^2}{\mu},$$ (C.2)

the value of N_P is approximately constant for $Re > 10^4$.

In the case of the monolith stirrer, a dimensional analysis indicates that both the stirrer diameter and the blade diameter may be important. Following similar reasoning as for the development of the engineering model (c.f. section 3.2), the power draw was assumed to be mainly due to drag on the monolith. The drag force on a monolith was calculated as:

$$F_d = \frac{1}{2} \rho U_b^2 A_b C_d$$ (C.3)

Here U_b is some velocity related to the stirrer tip speed, with blockage included, A_b is the blade frontal area and C_d is some drag coefficient. As shown, (section 3.3) the drag coefficient is influenced by the 'confinement' or blockage of an object. Since there are substantial differences between the various MSR geometries considered in this work, this effect should be included in the N_P calculation. The stirrer tip speed U should be adjusted by a blockage factor defined as:

$$B = \frac{A_b}{A} = \frac{\pi \cdot D_b^2/4}{T/2 \cdot H_L}. \tag{C.4}$$

The relation between the velocity U and the confined velocity U_B is

$$\frac{U}{U_B} = (1 - B). \tag{C.5}$$

The expected power consumption of the stirrer is related to the torque on the shaft, $P = M_m \cdot \omega$, and the torque is due to the drag force on the monolith, $M_m = F_d \cdot \frac{D}{2}$. Combining this with equation C.3, and omitting constants results in:

$$P \propto \frac{\rho N^3 D^3 D_b^2}{(1 - B)^2}. \tag{C.6}$$

Finally, when following this reasoning, the definition of Re should also be adapted as well. Therefore an alternative Reynolds number and power number for MSR's can be written as:

$$N_{P,MSR} = \frac{P (1 - B)^2}{\rho N^3 D^3 D_b^2} \text{ and} \tag{C.7}$$

$$Re_{MSR} = \frac{\rho N D D_b}{\mu (1 - B)}. \tag{C.8}$$

A similar argument was proposed by Houterman (1997) in the original study, but it did not account for blockage and it did not have a different Reynolds number definition.

C.3 Application of the modified power number

The experimental data from various sources were presented in figure 4.18. Table C.1 compares the data for the constant power number values as read from the graph.

Although the data from the $5cm$ diameter blade of Edvinsson-Albers *et al.* (1998) and the present experiments agree, the other values are not that close. It is clear that the modified power number is no more successful at correlating the data than the traditional method. A possible explanation can be found by including the drag force in the derivation of the power number. Using the stirrer tip velocity for U

Table C.1: *Comparison of standard and modified stirrer power numbers*

Source	B	L_m/D_b	N_P	$N_{P,MSR}$
present	0.074	0.93	0.75	18.0
present (sharp edge)	0.074	0.93	0.85	20.4
Edvinsson-Albers *et al.* (1998)	0.061	1.00	0.65	18.0
Edvinsson-Albers *et al.* (1998)	0.157	1.60	1.5	13.0
Hoek (2004)	0.219	1.83	0.074	4.75

in equation C.5, it follows that the traditional power number is proportional to the drag coefficient:

$$C_d \propto N_P \left(1 - B\right)^2 \left(\frac{D}{D_b}\right)^2. \tag{C.9}$$

In other words, the modified power number is similar to a drag coefficient for the monolith blade. This explains the failure of the power number approach to characterize the different experiments - each geometry will have a different drag coefficient and therefore a different power number. Small differences like the sharp and chamfered leading edge on the blade of the current MSR result in significant differences in predicted power numbers. This discussion could be extended to take into account the angle of attack of the blade, and the resulting influence on the drag coefficient, but the conclusion would be similar, i.e. power numbers cannot be used to compare monolith stirrer reactors with different geometrical layouts. The one advantage of this is that for a specific geometry a limited amount of experiments (or simulations) would be required to determine the appropriate drag coefficient, and hence the power number.

D

Turbulence models in Fluent

D.1 Background

This section is intended as a reference for the implementation of turbulence models in Fluent. The equations and constants for the models used in this study and included here, were taken directly from the Fluent manual (ANSYS, 2009). Information regarding buoyancy, compressibility and heat and mass transfer are not included here as it was not used in simulations. Refer to the manual for more detailed descriptions of the models.

The need for turbulence modeling arises from the process of ensemble averaging of the exact Navier-Stokes equations. The resulting Reynolds-averaged Navier-Stokes (RANS) equations (equation 2.20) contain the Reynolds stresses, $-\rho \overline{u_i' u_j'}$, which need to be modeled. The SA model, the k-ϵ family of models, and the k-ω family of models employ the Boussinesq approach to couple the Reynolds stresses to the mean velocity gradients. Boussinesq (1887) proposed that Reynolds stresses might be proportional to mean rates of deformation through a turbulent (eddy) viscosity, μ_t, analogous to molecular viscosity:

$$-\rho \overline{u_i' u_j'} = \mu_t \left(\frac{\partial u_i}{\partial x_j} + \frac{\partial u_j}{\partial x_i} \right) - \frac{2}{3} \rho k \delta_{ij} \tag{D.1}$$

The assumption of a scalar turbulent (eddy) viscosity, μ_t, implies isotropic turbulence. For the Reynolds stress model (RSM) the individual Reynolds stresses are included and the Boussinesq approach is not required.

The next sections present transport equations and model constants for the individual turbulence equations. The final section presents the near-wall modeling approach for the models used in this study.

D.2   The Spalart-Allmaras model (SA)

The Spalart-Allmaras (SA) model is a semi-empirical model based on a model transport equation for the turbulent kinematic viscosity. It was applied in the study of drag on an axial cylinder (section 3.3.2). As opposed to the k-ϵ family and k-ω family, which add two tranport equations for turbulent quantities, the SA model solves for only one transported variable, $\widetilde{\nu}$, which is identical to the turbulent kinematic viscosity except in the near-wall (viscosity-affected) region. The transport equation for $\widetilde{\nu}$ is

$$\rho \frac{\partial}{\partial t}(\widetilde{\nu}) + \rho \frac{\partial}{\partial x_i}(\widetilde{\nu} u_i) = G_\nu + \frac{\rho}{\sigma_{\widetilde{\nu}}} \left[\frac{\partial}{\partial x_j} \left\{ (\nu + \widetilde{\nu}) \frac{\partial \widetilde{\nu}}{\partial x_j} \right\} + C_{b2}\rho \left(\frac{\partial \widetilde{\nu}}{\partial x_j} \right)^2 \right] - Y_\nu \quad \text{(D.2)}$$

where G_ν is the production of turbulent viscosity, and Y_ν is the destruction of turbulent viscosity that occurs in the near-wall region due to wall blocking and viscous damping. $\sigma_{\widetilde{\nu}}$ and C_{b2} are constants and ν is the molecular kinematic viscosity. Since the turbulence kinetic energy, k, is not calculated in the SA model, the last term in equation D.1 is ignored when estimating the Reynolds stresses.

The turbulent viscosity, μ_t, is computed from

$$\mu_t = \rho \widetilde{\nu} f_{v1} \quad \text{(D.3)}$$

where the viscous damping function, f_{v1}, is given by

$$f_{v1} = \frac{\chi^3}{\chi^3 + C_{v1}^3} \text{ with } \chi \equiv \frac{\widetilde{\nu}}{\nu}. \quad \text{(D.4)}$$

The production term, G_ν, is modeled as

$$G_\nu = C_{b1}\rho \widetilde{S}\widetilde{\nu} \quad \text{(D.5)}$$

where

$$\widetilde{S} \equiv S_{SA} + \frac{\widetilde{\nu}}{\kappa^2 d^2} f_{v2} \quad \text{(D.6)}$$

and

$$f_{v2} = 1 - \frac{\chi}{1 + \chi f_{v1}}. \quad \text{(D.7)}$$

C_{v1}, C_{b1} and κ are constants, d is the distance from the wall, and S_{SA} is a scalar measure of the deformation tensor. In this work a modified version of the model (Dacles-Mariani *et al.*, 1995) has been used that combines the measures of both vorticity and the strain tensors in the definition of S_{SA}:

$$S_{SA} \equiv \Omega + C_{\text{prod}} \min(0, S - \Omega) \quad \text{(D.8)}$$

where $C_{\text{prod}} = 2.0$. Ω and S are moduli of the mean rate-of-rotation and mean rate-of-strain tensors respectively. The definitions are as follows:

$$\Omega \equiv \sqrt{2\Omega_{ij}\Omega_{ij}} \tag{D.9}$$

$$S \equiv \sqrt{2S_{ij}S_{ij}} \tag{D.10}$$

$$\Omega_{ij} = \frac{1}{2}\left(\frac{\partial u_i}{\partial x_j} - \frac{\partial u_j}{\partial x_i}\right) \tag{D.11}$$

$$S_{ij} = \frac{1}{2}\left(\frac{\partial u_j}{\partial x_i} + \frac{\partial u_i}{\partial x_j}\right). \tag{D.12}$$

The destruction term is modeled as

$$Y_\nu = C_{w1}\rho f_w \left(\frac{\widetilde{\nu}}{d}\right)^2 \tag{D.13}$$

where

$$f_w = g\left[\frac{1 + C_{w3}^6}{g^6 + C_{w3}^6}\right]^{1/6} \tag{D.14}$$

and

$$g = r + C_{w2}\left(r^6 - r\right) \text{ where } r \equiv \frac{\widetilde{\nu}}{\widetilde{S}\kappa^2 d^2}. \tag{D.15}$$

The model constants C_{b1}, C_{b2}, $\sigma_{\widetilde{\nu}}$, C_{v1}, C_{w1}, C_{w2}, C_{w3}, and κ (the Von Kàrmàn constant) have the following default values:

$$C_{b1} = 0.1355, \; C_{b2} = 0.622, \; \sigma_{\widetilde{\nu}} = \frac{2}{3}, \; C_{v1} = 7.1$$

$$C_{w1} = \frac{C_{b1}}{\kappa^2} + \frac{(1 + C_{b2})}{\sigma_{\widetilde{\nu}}}, \; C_{w2} = 0.3, \; C_{w3} = 2.0, \; \kappa = 0.4187.$$

At walls, the modified turbulent kinematic viscosity, $\widetilde{\nu}$, is set to zero. When the mesh is fine enough to resolve the viscosity-dominated sublayer, the wall shear stress is obtained from the laminar stress-strain relationship:

$$\frac{u}{u_\tau} = \frac{\rho u_\tau y}{\mu}. \tag{D.16}$$

If the mesh is too coarse to resolve the viscous sublayer, then it is assumed that the centroid of the wall-adjacent cell falls within the logarithmic region of the boundary layer, and the law-of-the-wall is employed:

$$\frac{u}{u_\tau} = \frac{1}{\kappa}\ln E\left(\frac{\rho u_\tau y}{\mu}\right) \tag{D.17}$$

where u is the velocity parallel to the wall, u_τ is the friction velocity ($\sqrt{\tau_w/\rho}$), y is the distance from the wall, and $E = 9.793$.

D.3   The Standard k-ϵ model

Models in the k-ϵ family are semi-empirical models based on model transport equations for the turbulence kinetic energy (k) and its dissipation rate (ϵ). The standard k-ϵ (SKE) model is based on the work of Launder & Spalding (1974) and has been widely used in CFD. The merits and pitfalls of the model have been well established, e.g., see Durbin & Petterson Reiff (2001), Davidson (2004) and Versteeg & Malalasekera (2007), and are not discussed here.

The turbulence kinetic energy, k, and its rate of dissipation, ϵ, are obtained from the following transport equations:

$$\rho \frac{\partial k}{\partial t} + \rho \frac{\partial}{\partial x_i}(ku_i) = \frac{\partial}{\partial x_j}\left[\Gamma_k \frac{\partial k}{\partial x_j}\right] + G_k - \rho\epsilon \tag{D.18}$$

and

$$\rho \frac{\partial \epsilon}{\partial t} + \rho \frac{\partial}{\partial x_i}(\epsilon u_i) = \frac{\partial}{\partial x_j}\left[\Gamma_\epsilon \frac{\partial \epsilon}{\partial x_j}\right] + C_{1\epsilon} \frac{\epsilon}{k} G_k - C_{2\epsilon}\rho \frac{\epsilon^2}{k} \tag{D.19}$$

In these equations, Γ_k and Γ_ϵ represents the model specific treatment of the effective diffusivity of k and ϵ respectively, G_k represents the generation of turbulence kinetic energy due to the mean velocity gradients, $C_{1\epsilon}$, $C_{2\epsilon}$, and $C_{3\epsilon}$ are constants.

The term G_k, representing the production of turbulence kinetic energy, is modeled identically for the SKE, RNG k-ϵ, and the Realizable k-ϵ models. To evaluate G_k in a manner consistent with the Boussinesq hypothesis,

$$G_k = \mu_t S^2 \tag{D.20}$$

where S is the modulus of the mean rate-of-strain tensor (equation D.10). When using the high-Reynolds number k-ϵ versions, μ_{eff} ($= \mu + \mu_t$) is used instead of μ_t in equation D.20.

The turbulent (eddy) viscosity μ_t, is computed by combining k and ϵ as follows:

$$\mu_t = \rho C_\mu \frac{k^2}{\epsilon} \tag{D.21}$$

where C_μ is a constant.

For the SKE model, the effective diffusivity of k is modeled as

$$\Gamma_k = \left(\mu + \frac{\mu_t}{\sigma_k}\right). \tag{D.22}$$

The effective diffusivity of ϵ is modeled as

$$\Gamma_\epsilon = \left(\mu + \frac{\mu_t}{\sigma_\epsilon}\right). \tag{D.23}$$

σ_k and σ_ϵ are the turbulent Prandtl numbers for k and ϵ, respectively.

The model constants $C_{1\epsilon}$, $C_{2\epsilon}$, C_μ, σ_k, and σ_ϵ for the SKE model have the following default values:

$$C_{1\epsilon} = 1.44, \ C_{2\epsilon} = 1.92, \ C_\mu = 0.09, \ \sigma_k = 1.0, \text{ and } \ \sigma_\epsilon = 1.3.$$

D.4   The RNG k-ϵ model (RNG-KE)

The RNG-KE Model was derived using a rigorous statistical technique (called renormalization group theory) and the version in Fluent is based in the work of Orszag *et al.* (1993). It is similar in form to the SKE model, but includes the following refinements:

- The RNG-KE model has an additional term in its ϵ equation that improves the accuracy for rapidly strained flows.

- The effect of swirl on turbulence is included in the RNG-KE model, enhancing accuracy for swirling flows.

- The RNG theory provides an analytical formula for turbulent Prandtl numbers, in contrast to the SKE model that uses user-specified, constant values.

- The RNG theory provides an analytically-derived differential formula for effective viscosity that accounts for low-Reynolds-number effects - the effectiveness depends on an appropriate treatment of the near-wall region.

The transport equations for the RNG-KE model are identical to that of the SKE model, but with certain terms and constants treated differently. For the RNG-KE model, the Γ_k term is defined as

$$\Gamma_k = (\alpha_k \mu_{\text{eff}}) \tag{D.24}$$

and the Γ_ϵ term is defined as

$$\Gamma_\epsilon = (\alpha_\epsilon \mu_{\text{eff}}) \tag{D.25}$$

α_k and α_ϵ are the inverse effective Prandtl numbers.

The remaining differences are discussed below for the k equation (D.18) and then the ϵ equation (D.19).

The scale elimination procedure in RNG theory results in a differential equation for turbulent viscosity:

$$d\left(\frac{\rho^2 k}{\sqrt{\epsilon \mu}} \right) = 1.72 \frac{\hat{v}}{\sqrt{\hat{v}^3 - 1 + C_v}} d\hat{v} \tag{D.26}$$

where $\hat{v} = \mu_{\text{eff}}/\mu$ and $C_v \approx 100$. Equation D.26 is integrated to obtain an accurate description of how the effective turbulent transport varies with the effective Reynolds number (or eddy scale), allowing the model to better handle low-Reynolds-number and near-wall flows.

In the high-Reynolds-number limit, equation D.26 gives

$$\mu_t = \rho C_\mu \frac{k^2}{\epsilon}$$

(D.27)

with $C_\mu = 0.0845$, derived using RNG theory.

In this work we did not use the default, μ_{eff}, which is computed using the high-Reynolds-number form, but instead selected the use of the differential relation given in equation D.26.

The Fluent RNG-KE model includes a model to account for the effects of swirl or rotation by modifying the turbulent viscosity. The functional form of the modification is given as:

$$\mu_t = \mu_{t0} \; f\left(\alpha_s, \Omega, \frac{k}{\epsilon}\right)$$

(D.28)

where μ_{t0} is the value of turbulent viscosity calculated without the swirl modification using either equation D.26 or equation D.27. Ω is a characteristic swirl number evaluated within Fluent, and α_s is a swirl constant that assumes different values depending on whether the flow is swirl-dominated or only mildly swirling. For mildly swirling flows (the default), $\alpha_s = 0.07$. For strongly swirling flows, however, a higher value of can be used. Detailed information on the modification does not appear in the manual. This option was included by default for all the models reported in this work.

The inverse effective Prandtl numbers, α_k and α_ϵ, are computed using the following formula derived analytically by the RNG theory:

$$\left|\frac{\alpha - 1.3929}{\alpha_0 - 1.3929}\right|^{0.6321} \left|\frac{\alpha + 2.3929}{\alpha_0 + 2.3929}\right|^{0.3679} = \frac{\mu_{\text{mol}}}{\mu_{\text{eff}}}$$

(D.29)

where $\alpha_0 = 1.0$. In the high-Reynolds-number limit $\mu_{\text{mol}}/\mu_{\text{eff}} \ll 1$, $\alpha_k = \alpha_\epsilon \approx 1.393$.

The main difference between the RNG-KE and SKE models lies in an additional term in the ϵ equation. To maintain similar functional forms of the transport equations, this term can be included as a non-constant term, $C_{2\epsilon}^*$, which replaces the constant $C_{2\epsilon}$ in equation D.19. The modified term, $C_{2\epsilon}^*$, is defined as

$$C_{2\epsilon}^* \equiv C_{2\epsilon} + \frac{C_\mu \eta^3 (1 - \eta/\eta_0)}{1 + \beta \eta^3}$$

(D.30)

where $\eta \equiv Sk/\epsilon$, $\eta_0 = 4.38$, and $\beta = 0.012$.

The model constants $C_{1\epsilon}$ and $C_{2\epsilon}$ in equation D.30 have values derived analytically by the RNG theory. These values, used by default in Fluent, are

$$C_{1\epsilon} = 1.42, \text{ and } C_{2\epsilon} = 1.68.$$

D.5   The Realizable k-ϵ model (RKE)

The realizable k-ϵ (RKE) model proposed by Shih *et al.* (1995) differs from the SKE model in two ways:

- A new eddy-viscosity formula involving a variable C_μ originally proposed by Reynolds.

- A new model equation for dissipation, ϵ, based on the dynamic equation of the mean-square vorticity fluctuation.

The RKE model transport equation for k is identical to that of the SKE model, but with model specific term Γ_k is defined as

$$\Gamma_k = \left(\mu + \frac{\mu_t}{\sigma_k} \right) \tag{D.31}$$

However, the treatment of the turbulent viscosity is different as discussed below.

The ϵ transport equation for the RKE model differs substantially from the SKE and RNG-KE model versions:

$$\rho \frac{\partial \epsilon}{\partial t} + \rho \frac{\partial}{\partial x_j}(\epsilon u_j) = \frac{\partial}{\partial x_j}\left[\left(\mu + \frac{\mu_t}{\sigma_\epsilon} \right) \frac{\partial \epsilon}{\partial x_j} \right] + \rho C_1 S \epsilon - \rho C_2 \frac{\epsilon^2}{k + \sqrt{\nu \epsilon}} \tag{D.32}$$

where

$$C_1 = \max\left[0.43, \frac{\eta}{\eta + 5} \right], \quad \eta = S \frac{k}{\epsilon}, \quad S = \sqrt{2 S_{ij} S_{ij}}, \tag{D.33}$$

and C_2 is a constant.

The production term in the ϵ equation (the second term on the right-hand side of equation D.32) does not involve the production of k; i.e., it does not contain the same G_k term as the other k-ϵ models. The destruction term (the term containing the constant C_2 on the right-hand side of equation D.32) does not have any singularity; i.e., its denominator never vanishes, even if k becomes zero. This feature is contrasted with traditional k-ϵ models, which have a singularity due to k in the denominator (in equation D.19 the destruction term is the one with the constant $C_{2\epsilon}$).

The turbulent (eddy) viscosity is computed from

$$\mu_t = \rho C_\mu \frac{k^2}{\epsilon} \tag{D.34}$$

However, for the RKE model C_μ is no longer constant. It is computed from

$$C_\mu = \frac{1}{A_0 + A_s \frac{kU^*}{\epsilon}} \tag{D.35}$$

where

$$U^* \equiv \sqrt{S_{ij}S_{ij} + \widetilde{\Omega}_{ij}\widetilde{\Omega}_{ij}} \tag{D.36}$$

and

$$\widetilde{\Omega}_{ij} = \Omega_{ij} - 2\epsilon_{ijk}\omega_k \tag{D.37}$$

$$\Omega_{ij} = \overline{\Omega}_{ij} - \epsilon_{ijk}\omega_k. \tag{D.38}$$

$\overline{\Omega}_{ij}$ is the mean rate-of-rotation tensor viewed in a rotating reference frame with angular velocity ω_k. The model constant $A_0 = 4.04$ and A_s is given by

$$A_s = \sqrt{6}\cos(\phi) \tag{D.39}$$

with

$$\phi = \frac{1}{3}\cos^{-1}\left[\frac{\sqrt{6}\,S_{ij}S_{jk}S_{ki}}{\left(\sqrt{S_{ij}S_{ij}}\right)^3}\right]. \tag{D.40}$$

In Fluent the term $-2\epsilon_{ijk}\omega_k$ is, by default, not included in the calculation of $\widetilde{\Omega}_{ij}$. This is an extra rotation term that is not compatible with cases involving sliding meshes or multiple reference frames, because it produces non-physical turbulent viscosities in situations when the computational domain contains both rotating and stationary fluid zones. The term can be activated in Fluent, but this was not attempted in the present study. As shown in appendix G, the results from the RKE model were broadly similar to other models for the stirred tank simulations, and the effect of this modification can therefore not be evaluated from the results of this study.

The model constants for the RKE model are:

$$C_{1\epsilon} = 1.44, \ C_2 = 1.9, \ \sigma_k = 1.0, \text{ and } \ \sigma_\epsilon = 1.2. \tag{D.41}$$

D.6   The Standard k-ω model (SKW)

The standard k-ω (SKW) model in Fluent is based on the version of the model as reported by Wilcox (1998). The model is an empirical model based on model transport equations for the turbulence kinetic energy, k, and the specific dissipation rate, ω, which can also be thought of as the ratio of ϵ to k. Here we will present the model as implemented in its high Reynolds form, which was used for the work in this thesis. The transport equations for k and ω can be written as follows:

$$\frac{\partial}{\partial t}(\rho k) + \frac{\partial}{\partial x_i}(\rho k u_i) = \frac{\partial}{\partial x_j}\left(\Gamma_k \frac{\partial k}{\partial x_j}\right) + G_k - Y_k \tag{D.42}$$

and

$$\frac{\partial}{\partial t}(\rho\omega) + \frac{\partial}{\partial x_i}(\rho\omega u_i) = \frac{\partial}{\partial x_j}\left(\Gamma_\omega \frac{\partial\omega}{\partial x_j}\right) + G_\omega - Y_\omega \qquad \text{(D.43)}$$

In these equations, G_k represents the generation of turbulence kinetic energy due to mean velocity gradients. G_ω represents the generation of ω. Γ_k and Γ_ω represent the effective diffusivity of k and ω, respectively. Y_k and Y_ω represent the dissipation of k and ω due to turbulence.

The effective diffusivities for the SKW model are:

$$\Gamma_k = \mu + \frac{\mu_t}{\sigma_k} \qquad \text{(D.44)}$$

$$\Gamma_\omega = \mu + \frac{\mu_t}{\sigma_\omega} \qquad \text{(D.45)}$$

where σ_k and σ_ω are the turbulent Prandtl numbers for k and ω, respectively. The turbulent viscosity, μ_t, is computed by combining k and ω as follows:

$$\mu_t = \alpha_\infty^* \frac{\rho k}{\omega} \qquad \text{(D.46)}$$

In the high-Reynolds-number form of the SKW model, α_∞^* is a constant.

The term G_k represents the production of turbulence kinetic energy. To evaluate G_k in a manner consistent with the Boussinesq hypothesis,

$$G_k = \mu_t S^2 \qquad \text{(D.47)}$$

where S is the modulus of the mean rate-of-strain tensor (equation D.10).

The production of ω is given by

$$G_\omega = \alpha_\infty \frac{\omega}{k} G_k \qquad \text{(D.48)}$$

where G_k is given by equation D.47. In the high-Reynolds-number form of the k-ω model, α_∞ is a constant.

The dissipation of k is given by

$$Y_k = \rho \beta_\infty^* f_{\beta^*} k \omega \qquad \text{(D.49)}$$

where

$$f_{\beta^*} = \begin{cases} 1 & \chi_k \le 0 \\ \frac{1+680\chi_k^2}{1+400\chi_k^2} & \chi_k > 0 \end{cases} \qquad \text{(D.50)}$$

with

$$\chi_k \equiv \frac{1}{\omega^3}\frac{\partial k}{\partial x_j}\frac{\partial\omega}{\partial x_j} \qquad \text{(D.51)}$$

and ζ^* and β_∞^* are constants and $Re_t = (\rho k)/(\mu\omega)$.

The dissipation of ω is given by

$$Y_\omega = \rho\, \beta_i\, f_\beta\, \omega^2 \tag{D.52}$$

where

$$f_\beta = \frac{1 + 70\chi_\omega}{1 + 80\chi_\omega} \tag{D.53}$$

$$\chi_\omega = \left| \frac{\Omega_{ij}\Omega_{jk}S_{ki}}{(\beta_\infty^*\omega)^3} \right| \tag{D.54}$$

$$\tag{D.55}$$

and β_i is a constant.

The model constants for the SKW model are:

$$\alpha_\infty^* = 1, \quad \alpha_\infty = 0.52, \quad \beta_\infty^* = 0.09, \quad \beta_i = 0.072$$

$$\zeta^* = 1.5, \quad \sigma_k = 2.0, \quad \sigma_\omega = 2.0$$

D.7 The Standard k-ω model and vorticity-based production (SKW2)

This model was applied for the axial cylinder drag calculations (section 3.3.2) after particularly poor results were obtained with SKW model. This model is identical to the SKW model, except that the turbulent kinetic energy production is based on vorticity instead of the mean rate-of-strain. Therefore equation D.47 now becomes

$$G_k = \mu_t\, \Omega^2 \tag{D.56}$$

where Ω is defined as in equation D.9. This option can only be activated in Fluent through the text user interface and does not appear in the Fluent manual. Information on the model was obtained from the Fluent support team, as well as the excellent repository maintained by Rumsey (2009).

D.8 The Shear-stress transport k-ω model (SST-KW)

The Shear-Stress Transport k-ω (SST-KW) model was developed by Menter (1994). The aim was to combine the accuracy of the SKW model in the near-wall region with the accuracy of the SKE model in the far field turbulent regions. The transport equations for the SST-KW model are:

$$\rho\frac{\partial k}{\partial t} + \rho\frac{\partial}{\partial x_i}(ku_i) = \frac{\partial}{\partial x_j}\left(\Gamma_k\frac{\partial k}{\partial x_j}\right) + \widetilde{G}_k - Y_k \tag{D.57}$$

and

$$\rho\frac{\partial\omega}{\partial t} + \rho\frac{\partial}{\partial x_i}(\omega u_i) = \frac{\partial}{\partial x_j}\left(\Gamma_\omega\frac{\partial\omega}{\partial x_j}\right) + G_\omega - Y_\omega + D_\omega. \tag{D.58}$$

In these equations, $\widetilde{G}_k$ represents the generation of turbulence kinetic energy due to mean velocity gradients, G_ω represents the generation of ω. Γ_k and Γ_ω represent the effective diffusivity of k and ω, respectively, which are calculated as described below. Y_k and Y_ω represent the dissipation of k and ω due to turbulence. D_ω represents the cross-diffusion term, calculated as described below.

The effective diffusivities for the SST-KW model are given by

$$\Gamma_k = \mu + \frac{\mu_t}{\sigma_k} \tag{D.59}$$

$$\Gamma_\omega = \mu + \frac{\mu_t}{\sigma_\omega} \tag{D.60}$$

where σ_k and σ_ω are the turbulent Prandtl numbers for k and ω, respectively. The turbulent viscosity, μ_t, is computed as follows:

$$\mu_t = \frac{\rho k}{\omega}\frac{1}{\max\left[\frac{1}{\alpha^*},\frac{SF_2}{a_1\omega}\right]} \tag{D.61}$$

where S is the strain rate magnitude (equation D.10) and

$$\sigma_k = \frac{1}{F_1/\sigma_{k,1} + (1-F_1)/\sigma_{k,2}} \tag{D.62}$$

$$\sigma_\omega = \frac{1}{F_1/\sigma_{\omega,1} + (1-F_1)/\sigma_{\omega,2}}. \tag{D.63}$$

α^* is defined as

$$\alpha^* = \alpha_\infty^*\left(\frac{0.024 + \mathrm{Re}_t/6.0}{1 + \mathrm{Re}_t/6.0}\right) \tag{D.64}$$

where

$$\mathrm{Re}_t = \frac{\rho k}{\mu\omega}. \tag{D.65}$$

The blending functions, F_1 and F_2, are given by

$$F_1 = \tanh\left(\Phi_1^4\right), \text{ where} \tag{D.66}$$

$$\Phi_1 = \min\left[\max\left(\frac{\sqrt{k}}{0.09\omega y}, \frac{500\mu}{\rho y^2\omega}\right), \frac{4\rho k}{\sigma_{\omega,2}D_\omega^+ y^2}\right], \text{ and}$$

$$D_\omega^+ = \max\left[2\rho\frac{1}{\sigma_{\omega,2}}\frac{1}{\omega}\frac{\partial k}{\partial x_j}\frac{\partial\omega}{\partial x_j}, 10^{-10}\right].$$

$$F_2 = \tanh\left(\Phi_2^2\right), \text{ where} \tag{D.67}$$

$$\Phi_2 = \max\left[2\frac{\sqrt{k}}{0.09\omega y}, \frac{500\mu}{\rho y^2 \omega}\right]$$

Here y is the distance to the next surface and D_ω^+ is the positive portion of the cross-diffusion term (equation D.77).

The term $\widetilde{G}_k$ represents the production of turbulence kinetic energy, and is defined as:

$$\widetilde{G}_k = \min(G_k, 10\rho\beta^* k\omega) \tag{D.68}$$

where G_k is defined in the same manner as in the SKW model (equation D.47).

G_ω represents the production of ω and is given by

$$G_\omega = \frac{\alpha}{\nu_t}\widetilde{G}_k. \tag{D.69}$$

Here α is given by

$$\alpha = \frac{\alpha_\infty}{\alpha^*}\left(\frac{\alpha_0 + \text{Re}_t/2.95}{1 + \text{Re}_t/2.95}\right), \tag{D.70}$$

and α_∞ is calculated from

$$\alpha_\infty = F_1\alpha_{\infty,1} + (1 - F_1)\alpha_{\infty,2} \tag{D.71}$$

with the blending function, $F1$, from equation D.66, and where

$$\alpha_{\infty,1} = \frac{\beta_{i,1}}{\beta_\infty^*} - \frac{\kappa^2}{\sigma_{w,1}\sqrt{\beta_\infty^*}} \tag{D.72}$$

$$\alpha_{\infty,2} = \frac{\beta_{i,2}}{\beta_\infty^*} - \frac{\kappa^2}{\sigma_{w,2}\sqrt{\beta_\infty^*}} \tag{D.73}$$

and κ is the Von Kármán constant.

The dissipation of turbulence kinetic energy, Y_k, is similar to the SKW model (equation D.49), but f_{β^*} is a constant equal to 1. Thus,

$$Y_k = \rho\beta^* k\omega. \tag{D.74}$$

The dissipation of ω, Y_ω, is defined in a similar manner as in the SKW model (equation D.52). The differences are that f_β is a constant equal to 1, and β_i is given in equation D.76. For the SST-KW model

$$Y_k = \rho\beta\omega^2 \tag{D.75}$$

For incompressible flow β_i is given by

$$\beta_i = F_1\beta_{i,1} + (1 - F_1)\beta_{i,2} \tag{D.76}$$

where F_1 is obtained from equation D.66 and $\beta_{i,1}$ and $\beta_{i,2}$ are constants.

To blend the SKW and the SKE models into the SST-KW model, the SKE model has been transformed into equations based on k and ω, which leads to the introduction of a cross-diffusion term (D_ω in equation D.58):

$$D_\omega = 2\left(1 - F_1\right)\rho\sigma_{\omega,2}\frac{1}{\omega}\frac{\partial k}{\partial x_j}\frac{\partial \omega}{\partial x_j} \tag{D.77}$$

The SST-KW model constants are:

$$\sigma_{k,1} = 1.176, \quad \sigma_{\omega,1} = 2.0, \quad \sigma_{k,2} = 1.0, \quad \sigma_{\omega,2} = 1.168$$

$$a_0 = \frac{1}{9}, \quad a_1 = 0.31, \quad \beta_{i,1} = 0.075 \quad \beta_{i,2} = 0.0828$$

Additional model constants (α_∞^*, α_∞, β_∞^*, and ζ^*) have the same values as for the SKW model.

The wall boundary conditions for the k equation in the k-ω models are treated in the same way as the k equation is treated when enhanced wall treatments are used with the k-ϵ models (refer to section D.10.2). This means that all boundary conditions for wall-function meshes will correspond to the wall function approach, while for the fine meshes, the appropriate low-Reynolds-number boundary conditions will be applied.

In Fluent the value of ω at the wall is specified as

$$\omega_w = \frac{\rho\left(u^*\right)^2}{\mu}\omega^+ \tag{D.78}$$

The asymptotic value of ω^+ in the laminar sublayer is given by

$$\omega^+ = \min\left(\omega_w^+, \frac{6}{\beta_i(y^+)^2}\right) \tag{D.79}$$

where

$$\omega_w^+ = \begin{cases} \left(\frac{50}{k_s^+}\right)^2 & k_s^+ < 25 \\[2ex] \frac{100}{k_s^+} & k_s^+ \geq 25 \end{cases} \tag{D.80}$$

where

$$k_s^+ = \max\left(1.0, \frac{\rho k_s u^*}{\mu}\right) \tag{D.81}$$

and k_s is the roughness height. In the logarithmic (or turbulent) region, the value of ω^+ is

$$\omega^+ = \frac{1}{\sqrt{\beta^*_\infty}} \frac{du^+_{\text{turb}}}{dy^+}$$

(D.82)

which leads to the value of ω in the wall cell as

$$\omega = \frac{u^*}{\sqrt{\beta^*_\infty} \kappa y}$$

(D.83)

In the case of a wall cell being placed in the buffer region, Fluent will blend ω^+ between the logarithmic and laminar sublayer values.

D.9 The Reynolds stress model (RSM)

The Reynolds stress model (RSM) (Launder *et al.*, 1975; Gibson & Launder, 1978; Launder, 1989*b*) is the most elaborate type of turbulence model that Fluent provides. It does not use the isotropic eddy-viscosity hypothesis, but rather the RSM closes the RANS equations by solving transport equations for the Reynolds stresses, together with an equation for the dissipation rate. Due to symmetry of the Reynolds stress tensor, this requires five additional transport equations in 2 dimensional flows and seven additional transport equations in 3 dimensions.

The fidelity of RSM predictions is still limited by the closure assumptions employed to model various terms in the exact transport equations for the Reynolds stresses. The modeling of the pressure-strain and dissipation-rate terms is particularly challenging, and often considered to be responsible for compromising the accuracy of RSM predictions.

The exact transport equations for the transport of the Reynolds stresses, $\rho \overline{u_i' u_j'}$, may be written as follows:

$$\underbrace{\frac{\partial}{\partial t}\left(\rho\,\overline{u_i' u_j'}\right)}_{\text{Local Time Derivative}} + \underbrace{\frac{\partial}{\partial x_k}\left(\rho u_k \overline{u_i' u_j'}\right)}_{C_{ij} \equiv \text{Convection}} = \underbrace{-\frac{\partial}{\partial x_k}\left[\rho\,\overline{u_i' u_j' u_k'} + \overline{p\left(\delta_{kj} u_i' + \delta_{ik} u_j'\right)}\right]}_{D_{T,ij} \equiv \text{Turbulent Diffusion}}$$

$$+ \underbrace{\frac{\partial}{\partial x_k}\left[\mu \frac{\partial}{\partial x_k}\left(\overline{u_i' u_j'}\right)\right]}_{D_{L,ij} \equiv \text{Molecular Diffusion}} \underbrace{- \rho\left(\overline{u_i' u_k'}\frac{\partial u_j}{\partial x_k} + \overline{u_j' u_k'}\frac{\partial u_i}{\partial x_k}\right)}_{P_{ij} \equiv \text{Stress Production}}$$

$$+ \underbrace{\overline{p\left(\frac{\partial u_i'}{\partial x_j} + \frac{\partial u_j'}{\partial x_i}\right)}}_{\phi_{ij} \equiv \text{Pressure Strain}} - \underbrace{2\mu\overline{\frac{\partial u_i'}{\partial x_k}\frac{\partial u_j'}{\partial x_k}}}_{\epsilon_{ij} \equiv \text{Dissipation}} - \underbrace{-2\rho\Omega_k\left(\overline{u_j' u_m'}\epsilon_{ikm} + \overline{u_i' u_m'}\epsilon_{jkm}\right)}_{F_{ij} \equiv \text{Production by System Rotation}}$$

$$\text{(D.84)}$$

The terms, C_{ij}, $D_{L,ij}$, P_{ij}, and F_{ij} do not require any modeling and $D_{T,ij}$, ϕ_{ij}, and ϵ_{ij} need to be modeled to close the equations. The following sections describe the modeling assumptions required to close the equations.

The turbulent diffusive transport, $D_{T,ij}$, can be modeled by the generalized gradient-diffusion model of Daly & Harlow (1970), but this can lead to numerical instabilities. Following Lien & Leschziner (1994), it has been simplified in Fluent to use a scalar turbulent diffusivity as follows:

$$D_{T,ij} = \frac{\partial}{\partial x_k}\left(\frac{\mu_t}{\sigma_k}\frac{\partial \overline{u_i' u_j'}}{\partial x_k}\right) \tag{D.85}$$

The turbulent viscosity, μ_t, is computed similarly to the k-ϵ models:

$$\mu_t = \rho C_\mu \frac{k^2}{\epsilon} \tag{D.86}$$

with $C_\mu = 0.09$. Lien & Leschziner (1994) derived a value of $\sigma_k = 0.82$. This value of σ_k is different from that in the SKE and RKE models, where $\sigma_k = 1.0$.

In this thesis the pressure-strain term is modeled with the default Fluent linear pressure strain model that is based on work from Gibson & Launder (1978); Fu *et al.* (1988); Launder (1989*a,b*). The pressure-strain term, ϕ_{ij}, is usually decomposed as:

$$\phi_{ij} = \phi_{ij,1} + \phi_{ij,2} + \phi_{ij,w} \tag{D.87}$$

where $\phi_{ij,1}$ is the slow pressure-strain term, also known as the return-to-isotropy term, $\phi_{ij,2}$ is called the rapid pressure-strain term, and $\phi_{ij,w}$ is the wall-reflection term.

The slow pressure-strain term, $\phi_{ij,1}$, is modeled as

$$\phi_{ij,1} \equiv -C_1 \rho \frac{\epsilon}{k}\left[\overline{u_i' u_j'} - \frac{2}{3}\delta_{ij}k\right] \tag{D.88}$$

with $C_1 = 1.8$.

The rapid pressure-strain term, $\phi_{ij,2}$, is modeled as

$$\phi_{ij,2} \equiv -C_2\left[(P_{ij} + F_{ij} + 5/6G_{ij} - C_{ij}) - \frac{2}{3}\delta_{ij}(P + 5/6G - C)\right] \tag{D.89}$$

where $C_2 = 0.60$, P_{ij}, F_{ij}, G_{ij}, and C_{ij} are as defined in equation D.84, $P = \frac{1}{2}P_{kk}$, $G = \frac{1}{2}G_{kk}$, and $C = \frac{1}{2}C_{kk}$.

The wall-reflection term, $\phi_{ij,w}$, is responsible for the redistribution of normal stresses near the wall. It tends to damp the normal stress perpendicular to the wall, while enhancing the stresses parallel to the wall. It is modeled as

$$\begin{aligned}\phi_{ij,w} \equiv{} & C_1' \frac{\epsilon}{k}\left(\overline{u_k' u_m'}n_k n_m \delta_{ij} - \frac{3}{2}\overline{u_i' u_k'}n_j n_k - \frac{3}{2}\overline{u_j' u_k'}n_i n_k\right)\frac{C_\ell k^{3/2}}{\epsilon d} \\ & + C_2'\left(\phi_{km,2}n_k n_m \delta_{ij} - \frac{3}{2}\phi_{ik,2}n_j n_k - \frac{3}{2}\phi_{jk,2}n_i n_k\right)\frac{C_\ell k^{3/2}}{\epsilon d}\end{aligned} \tag{D.90}$$

where $C_1' = 0.5$, $C_2' = 0.3$, n_k is the x_k component of the unit normal to the wall, d is the normal distance to the wall, and $C_\ell = C_\mu^{3/4}/\kappa$, where $C_\mu = 0.09$ and κ is the Von Kármán constant ($= 0.4187$). $\phi_{ij,w}$ is included by default in the Reynolds stress model.

When the RSM is applied to near-wall flows using the enhanced wall treatment described in section D.10.2, the pressure-strain model needs to be modified. The modification used in Fluent specifies the values of C_1, C_2, C_1', and C_2' as functions of the Reynolds stress invariants and the turbulent Reynolds number as proposed by Launder & Shima (1989):

$$C_1 = 1 + 2.58AA_2^{0.25}\left\{1 - \exp\left[-(0.0067\mathrm{Re}_t)^2\right]\right\} \tag{D.91}$$

$$C_2 = 0.75\sqrt{A} \tag{D.92}$$

$$C_1' = -\frac{2}{3}C_1 + 1.67 \tag{D.93}$$

$$C_2' = \max\left[\frac{\frac{2}{3}C_2 - \frac{1}{6}}{C_2}, 0\right] \tag{D.94}$$

with the turbulent Reynolds number defined as $\mathrm{Re}_t = (\rho k^2 / \mu\epsilon)$. The flatness pa-

rameter A and tensor invariants, A_2 and A_3, are defined as

$$A \equiv \left[1 - \frac{9}{8} (A_2 - A_3) \right] \tag{D.95}$$

$$A_2 \equiv a_{ik} a_{ki} \tag{D.96}$$

$$A_3 \equiv a_{ik} a_{kj} a_{ji} \tag{D.97}$$

a_{ij} is the Reynolds-stress anisotropy tensor, defined as

$$a_{ij} = - \left(\frac{-\rho \overline{u'_i u'_j} + \frac{2}{3} \rho k \delta_{ij}}{\rho k} \right) \tag{D.98}$$

The modifications detailed above are employed only when the enhanced wall treatment is selected.

In general, when the turbulence kinetic energy is needed for modeling a specific term, it is obtained by taking the trace of the Reynolds stress tensor:

$$k = \frac{1}{2} \overline{u'_i u'_i} \tag{D.99}$$

Fluent has an option to solve a transport equation for the turbulence kinetic energy in order to obtain boundary conditions for the Reynolds stresses. This option was evaluated as part of the sensitivity study for the MSR CFD, but was not found to be significant. In this case, the following model equation is used:

$$\rho \frac{\partial k}{\partial t} + \rho \frac{\partial}{\partial x_i} (k u_i) = \frac{\partial}{\partial x_j} \left[\left(\mu + \frac{\mu_t}{\sigma_k} \right) \frac{\partial k}{\partial x_j} \right] + \frac{1}{2} P_{ii} - \rho \epsilon \tag{D.100}$$

where $\sigma_k = 0.82$. It is essentially identical to the k transport equation used for the SKE model. Equation D.100 is solved globally throughout the flow domain, but the calculated values of k are used only for boundary conditions. In every other case, k is obtained from equation D.99.

The dissipation rate tensor, ϵ_{ij}, for incompressible flows is modeled as

$$\epsilon_{ij} = \frac{2}{3} \delta_{ij} \rho \epsilon \tag{D.101}$$

The compressibility modifications available in Fluent have been omitted. The scalar dissipation rate, ϵ, is computed with a model transport equation similar to that used in the SKE model:

$$\rho \frac{\partial \epsilon}{\partial t} + \rho \frac{\partial}{\partial x_i} (\epsilon u_i) = \frac{\partial}{\partial x_j} \left[\left(\mu + \frac{\mu_t}{\sigma_\epsilon} \right) \frac{\partial \epsilon}{\partial x_j} \right] C_{\epsilon 1} \frac{\epsilon}{2k} P_{ii} - C_{\epsilon 2} \frac{\rho \epsilon^2}{k} \tag{D.102}$$

where $\sigma_\epsilon = 1.0$, $C_{\epsilon 1} = 1.44$, and $C_{\epsilon 2} = 1.92$.

The RSM model in Fluent requires boundary conditions for individual Reynolds stresses, $\overline{u'_i u'_j}$, and for the turbulence dissipation rate, ϵ. These quantities can be input directly or derived from the turbulence intensity and characteristic length. The latter option was used in the present work. At walls, Fluent computes the near-wall values of the Reynolds stresses and ϵ from wall functions (sections D.10.1 and D.10.2). Fluent applies explicit wall boundary conditions for the Reynolds stresses by using the log-law and the assumption of equilibrium, disregarding convection and diffusion in the transport equations for the stresses (equation D.84). Using a local coordinate system, where τ is the tangential coordinate, η is the normal coordinate, and λ is the binormal coordinate, the Reynolds stresses at the wall-adjacent cells (assuming standard wall functions) are computed from

$$\frac{\overline{u'^2_\tau}}{k} = 1.098, \quad \frac{\overline{u'^2_\eta}}{k} = 0.247, \quad \frac{\overline{u'^2_\lambda}}{k} = 0.655, \quad -\frac{\overline{u'_\tau u'_\eta}}{k} = 0.255 \tag{D.103}$$

To obtain k, Fluent solves the transport equation of equation D.100. By default, the values of the Reynolds stresses near the wall are fixed using the values computed from equation D.103 and the transport equations in equation D.84 are solved only in the bulk flow region.

Alternatively, the Reynolds stresses can be explicitly specified in terms of wall-shear stress, instead of k:

$$\frac{\overline{u'^2_\tau}}{u^2_\tau} = 5.1, \quad \frac{\overline{u'^2_\eta}}{u^2_\tau} = 1.0, \quad \frac{\overline{u'^2_\lambda}}{u^2_\tau} = 2.3, \quad -\frac{\overline{u'_\tau u'_\eta}}{u^2_\tau} = 1.0 \tag{D.104}$$

where u_τ is the friction velocity defined by $u_\tau \equiv \sqrt{\tau_w/\rho}$, and τ_w is the wall-shear stress. When this option is chosen, the k transport equation is not solved. When using enhanced wall treatments as the near-wall treatment, Fluent applies zero flux wall boundary conditions to the Reynolds stress equations.

D.10 Near-wall treatment

In the near-wall region the solution variables have large gradients, and vigorous momentum and other scalar transports occur. Resolving these steep gradients requires a fine near-wall mesh resolution with a corresponding high computational cost. The k-ϵ, and the RSM models are primarily valid for turbulent core flows (i.e., the flow in the regions somewhat far from walls). Consideration therefore needs to be given as to how to make these models suitable for wall-bounded flows. The SA and k-ω models were designed to be applied throughout the boundary layer, provided that the near-wall mesh resolution is sufficient. This section was obtained from paragraph 4.12 of the Fluent Theory Manual, which contains more information, and is included here as a reference to the methods and models applied in this thesis. For further discussion on wall treatments, see Durbin & Petterson Reiff (2001).

In most industrial problems, the viscosity-affected inner region (viscous sub-layer and buffer layer) is not resolved. Instead, semi-empirical formulas called "wall functions" are used to bridge the viscosity-affected region between the wall and the fully-turbulent region. The use of wall functions removes the need to modify the turbulence models to account for the presence of the wall. It also significantly reduces the computational cost because a coarser near-wall mesh resolution can be used. See section D.10.1 below.

When the viscosity-affected region is resolved with a mesh all the way to the wall (including the viscous sublayer), modifications to the turbulence model equations are required. This will be termed the "near-wall modeling" approach, and is discussed below in section D.10.2.

D.10.1 Standard Wall Functions

The standard wall functions in Fluent are based on the work of Launder & Spalding (1974), and have been most widely used in industrial flows. They are provided as the default option in Fluent and was used for the bulk of the modeling reported in this thesis.

The law-of-the-wall for mean velocity yields

$$U^* = \frac{1}{\kappa} \ln(Ey^*) \tag{D.105}$$

where

$$U^* \equiv \frac{U_P C_\mu^{1/4} k_P^{1/2}}{\tau_w / \rho} \tag{D.106}$$

is the dimensionless velocity.

$$y^* \equiv \frac{\rho C_\mu^{1/4} k_P^{1/2} y_P}{\mu} \tag{D.107}$$

is the dimensionless distance from the wall, and

$$
\begin{aligned}
\kappa &= \text{Von Kármán constant } (= 0.4187) \\
E &= \text{empirical constant } (= 9.793) \\
U_P &= \text{mean velocity of the fluid at the near-wall node } P \\
k_P &= \text{turbulence kinetic energy at the near-wall node } P \\
y_P &= \text{distance from point } P \text{ to the wall} \\
\mu &= \text{dynamic viscosity of the fluid}
\end{aligned}
$$

The logarithmic law for mean velocity is known to be valid for $30 < y^* < 300$. In Fluent, the log-law is employed when $y^* > 11.225$. When the mesh is such

that $y^* < 11.225$ at the wall-adjacent cells, Fluent applies the laminar stress-strain relationship that can be written as

$$U^* = y^* \qquad \text{(D.108)}$$

In Fluent the laws-of-the-wall for mean velocity is based on the wall unit, y^*, rather than y^+ ($\equiv \rho u_\tau y / \mu$). These quantities are approximately equal in equilibrium turbulent boundary layers.

In the k-ϵ models and in the RSM (when the option to obtain wall boundary conditions from the k equation is enabled), the k equation is solved in the whole domain including the wall-adjacent cells. The boundary condition for k imposed at the wall is

$$\frac{\partial k}{\partial n} = 0 \qquad \text{(D.109)}$$

where n is the local coordinate normal to the wall.

The production of kinetic energy, G_k, and its dissipation rate, ϵ, at the wall-adjacent cells, which are the source terms in the k equation, are computed on the basis of the local equilibrium hypothesis. Under this assumption, the production of k and its dissipation rate are assumed to be equal in the wall-adjacent control volume.

Thus, the production of k is based on the logarithmic law and is computed from

$$G_k \approx \tau_w \frac{\partial U}{\partial y} = \tau_w \frac{\tau_w}{\kappa \rho k_P^{1/2} y_P} \qquad \text{(D.110)}$$

and ϵ is computed from

$$\epsilon_P = \frac{C_\mu^{3/4} k_P^{3/2}}{\kappa y_P} \qquad \text{(D.111)}$$

The ϵ equation is not solved at the wall-adjacent cells, but instead is computed using equation D.111. ω and Reynolds stress equations are solved as detailed in sections D.8 and D.9 respectively.

D.10.2 Enhanced Wall Treatment

Enhanced wall treatment is a near-wall modeling method that combines a two-layer model with so-called enhanced wall functions. The goal is to have a near-wall modeling approach that will possess the accuracy of the standard two-layer approach for fine near-wall meshes and that, at the same time, will not significantly reduce accuracy for wall-function meshes.

In Fluent's near-wall model, the viscosity-affected near-wall region is completely resolved all the way to the viscous sublayer. The two-layer approach is an integral part of the enhanced wall treatment and is used to specify both ϵ and the turbulent viscosity in the near-wall cells. In this approach, the whole domain is subdivided into a viscosity-affected region and a fully-turbulent region. The demarcation of

the two regions is determined by a wall-distance-based, turbulent Reynolds number, Re_y, defined as

$$Re_y \equiv \frac{\rho y \sqrt{k}}{\mu} \tag{D.112}$$

where y is the wall-normal distance calculated at the cell centers. In Fluent, y is interpreted as the distance to the nearest wall:

$$y \equiv \min_{\vec{r}_w \in \Gamma_w} \|\vec{r} - \vec{r}_w\| \tag{D.113}$$

where $\vec{r}$ is the position vector at the field point, and $\vec{r}_w$ is the position vector of the wall boundary. Γ_w is the union of all the wall boundaries involved. This interpretation allows y to be uniquely defined in flow domains of complex shape involving multiple walls. Furthermore, y defined in this way is independent of the mesh topology.

In the fully turbulent region ($Re_y > Re_y^*$; $Re_y^* = 200$), the k-ϵ models (sections D.3-D.5) or the RSM (section D.9) are employed.

In the viscosity-affected near-wall region ($Re_y < Re_y^*$), the one-equation model of Wolfstein (1969) is employed. In the one-equation model, the momentum equations and the k equation are retained as described in sections D.3-D.5 and D.9. However, the turbulent viscosity, μ_t, is computed from

$$\mu_{t,2\text{layer}} = \rho \, C_\mu \ell_\mu \sqrt{k} \tag{D.114}$$

where the length scale that appears in equation D.114 is computed from Chen & Patel (1988)

$$\ell_\mu = y C_\ell^* \left(1 - e^{-Re_y/A_\mu}\right). \tag{D.115}$$

The two-layer formulation for turbulent viscosity described above is used as a part of the enhanced wall treatment, in which the two-layer definition is smoothly blended with the high-Reynolds-number μ_t definition from the outer region, as proposed by Jongen (1999):

$$\mu_{t,\text{enh}} = \lambda_\epsilon \mu_t + (1 - \lambda_\epsilon)\mu_{t,2\text{layer}} \tag{D.116}$$

where μ_t is the high-Reynolds-number definition as described in previous sections for the k-ϵ models or the RSM. A blending function, λ_ϵ, is defined in such a way that it is equal to unity away from walls and is zero in the vicinity of the walls. The blending function has the following form:

$$\lambda_\epsilon = \frac{1}{2}\left[1 + \tanh\left(\frac{Re_y - Re_y^*}{A}\right)\right] \tag{D.117}$$

The constant A determines the width of the blending function. By defining a width such that the value of λ_ϵ will be within 1% of its far-field value given a

variation of ΔRe_y, the result is

$$A = \frac{|\Delta \text{Re}_y|}{arctanh(0.98)}. \tag{D.118}$$

Typically, ΔRe_y would be assigned a value that is between 5% and 20% of Re_y^*. The main purpose of the blending function λ_ϵ is to prevent solution convergence from being impeded when the value of μ_t obtained in the outer layer does not match with the value of μ_t returned by the Wolfstein model at the edge of the viscosity-affected region.

The ϵ field in the viscosity-affected region is computed from

$$\epsilon = \frac{k^{3/2}}{\ell_\epsilon} \tag{D.119}$$

The length scales that appear in equation D.119 are computed from Chen & Patel (1988):

$$\ell_\epsilon = y C_\ell^* \left(1 - e^{-\text{Re}_y/A_\epsilon}\right) \tag{D.120}$$

If the whole flow domain is inside the viscosity-affected region ($\text{Re}_y < 200$), ϵ is not obtained by solving the transport equation; it is instead obtained algebraically from equation D.119. Fluent uses a procedure for the blending of ϵ that is similar to the μ_t-blending in order to ensure a smooth transition between the algebraically-specified ϵ in the inner region and the ϵ obtained from solution of the transport equation in the outer region.

The constants in equations D.119 and D.120, are taken from Chen & Patel (1988) as:

$$C_\ell^* = \kappa C_\mu^{-3/4}, \quad A_\mu = 70, \quad A_\epsilon = 2C_\ell^* \tag{D.121}$$

To have a method that can extend its applicability throughout the near-wall region (i.e., viscous sublayer, buffer region, and fully-turbulent outer region) it is necessary to formulate the law-of-the wall as a single wall law for the entire wall region. Fluent offers the enhanced wall function which blends the linear (laminar) and logarithmic (turbulent) laws-of-the-wall using a function suggested by Kader (1981):

$$u^+ = e^\Gamma u_{\text{lam}}^+ + e^{\frac{1}{\Gamma}} u_{\text{turb}}^+ \tag{D.122}$$

where the blending function is given by:

$$\Gamma = -\frac{a(y^+)^4}{1 + by^+} \tag{D.123}$$

with $a = 0.01$ and $b = 5$. Similarly, the general equation for the derivative $\frac{du^+}{dy^+}$ is

$$\frac{du^+}{dy^+} = e^\Gamma \frac{du_{\text{lam}}^+}{dy^+} + e^{\frac{1}{\Gamma}} \frac{du_{\text{turb}}^+}{dy^+} \tag{D.124}$$

This approach allows the fully turbulent law to be easily modified and extended to take into account other effects such as pressure gradients or variable properties. This formula also guarantees the correct asymptotic behavior for large and small values of y^+ and reasonable representation of velocity profiles in the cases where y^+ falls inside the wall buffer region ($3 < y^+ < 10$).

The enhanced wall functions were developed by smoothly blending an enhanced turbulent wall law with the laminar wall law. The enhanced turbulent law-of-the-wall for compressible flow with heat transfer and pressure gradients has been derived by combining the approaches of White & Christoph (1971) and Huang *et al.* (1993):

$$\frac{du^+_{\text{turb}}}{dy^+} = \frac{1}{\kappa y^+} \left[S'(1 - \beta u^+ - \gamma (u^+)^2) \right]^{1/2} \tag{D.125}$$

where

$$S' = \begin{cases} 1 + \alpha y^+ & \text{for } y^+ < y_s^+ \\ 1 + \alpha y_s^+ & \text{for } y^+ \geq y_s^+ \end{cases} \tag{D.126}$$

and

$$\alpha \equiv \frac{\nu_w}{\tau_w u^*} \frac{dp}{dx} = \frac{\mu}{\rho^2 (u^*)^3} \frac{dp}{dx} \tag{D.127}$$

$$\beta \equiv \frac{\sigma_t q_w u^*}{c_p \tau_w T_w} = \frac{\sigma_t q_w}{\rho c_p u^* T_w} \tag{D.128}$$

$$\gamma \equiv \frac{\sigma_t (u^*)^2}{2 c_p T_w} \tag{D.129}$$

where y_s^+ is the location at which the log-law slope is fixed. By default, $y_s^+ = 60$. The coefficient α in equation D.125 represents the influences of pressure gradients while the coefficients β and γ represent the thermal effects. Equation D.125 is an ordinary differential equation and Fluent will provide an appropriate analytical solution. If α, β, and γ all equal 0, an analytical solution would lead to the classical turbulent logarithmic law-of-the-wall.

The laminar law-of-the-wall is determined from the following expression:

$$\frac{du^+_{\text{lam}}}{dy^+} = 1 + \alpha y^+ \tag{D.130}$$

In Fluent this expression only includes effects of pressure gradients through α, while the effects of variable properties due to heat transfer and compressibility on the laminar wall law are neglected. These effects are neglected because they are thought to be of minor importance when they occur close to the wall. Integration of equation D.130 results in

$$u^+_{\text{lam}} = y^+ \left(1 + \frac{\alpha}{2} y^+ \right). \tag{D.131}$$

The boundary conditions for the turbulence kinetic energy are similar to the ones used with the standard wall functions (equation D.109). However, the production of turbulence kinetic energy, G_k, is computed using velocity gradients that are consistent with the enhanced law-of-the-wall (equations D.122 and D.124), ensuring a formulation that is valid throughout the near-wall region.

Appendix **E**

Mesh images

E.1 Background

Geometries and the associated meshes listed in table 5.1 is presented in graphical form.
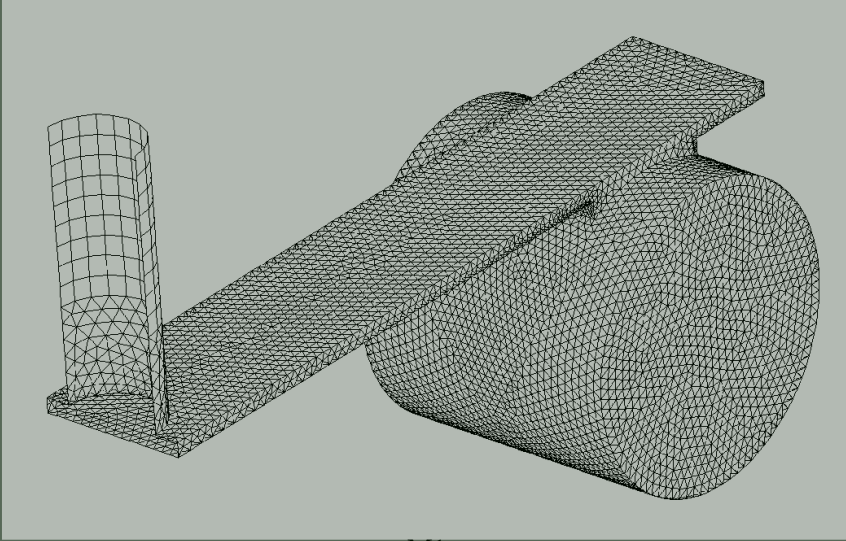
M1
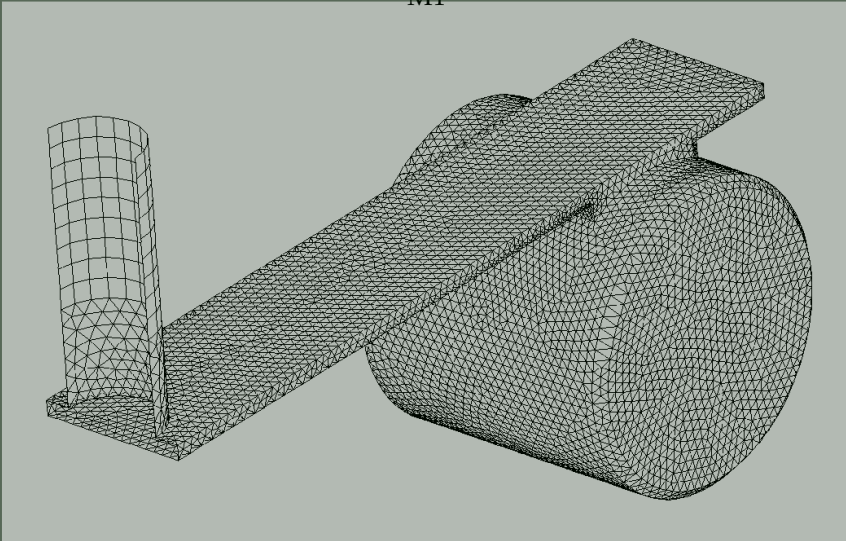
M5

Figure E.1: *Coarse, tetrahedral impeller meshes.*

M2

M6, M7, M8

Figure E.2: *Coarse, polyhedral impeller meshes.*

M3

M9, M10

Figure E.3: *Fine, polyhedral impeller meshes.*

Layout B2 with coarse mesh: M1, M2, M5-M8.

Layout B1 with fine mesh: M3, M4, M9 and M10.

Figure E.4: *Images of the tank mesh and geometry used in the present work.*

Appendix F

Monolith momentum source

F.1 Background

The rotation of the monolith with the stirrer requires additional work when modeling the monolith as a momentum sink in the flow. Equation 2.24, with the losses as shown in equation 2.25, are sufficient for a st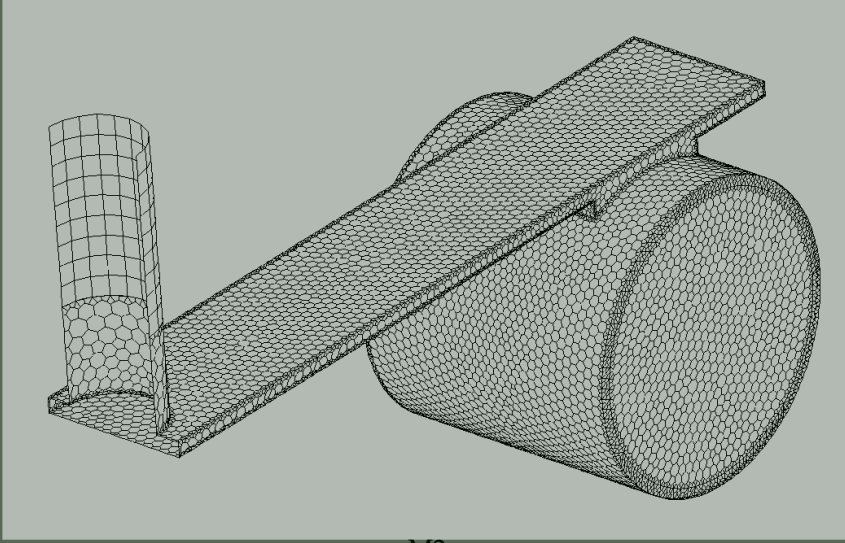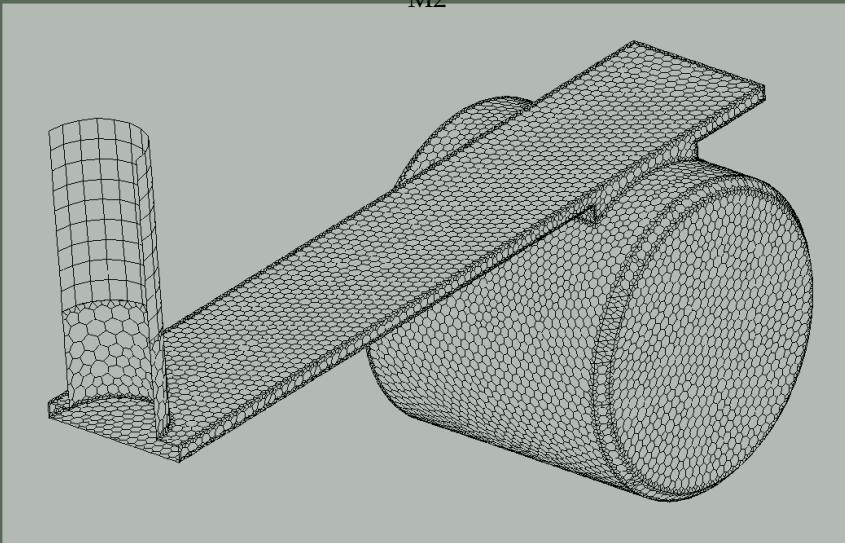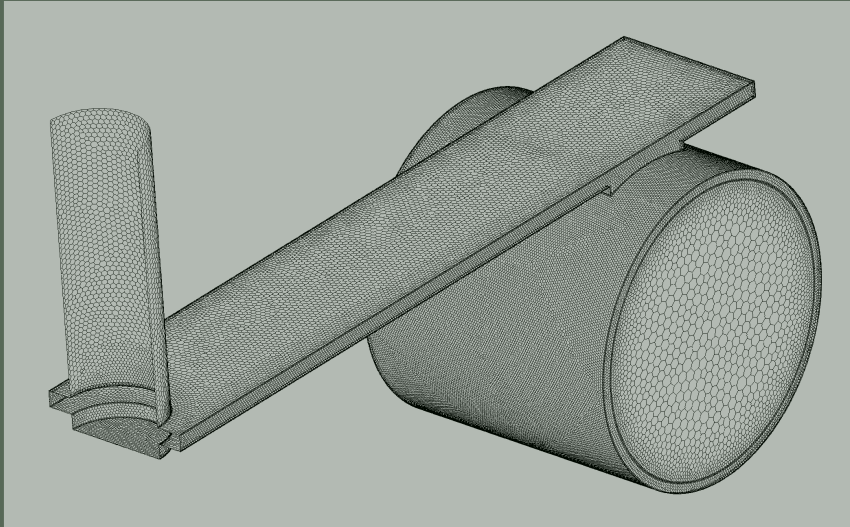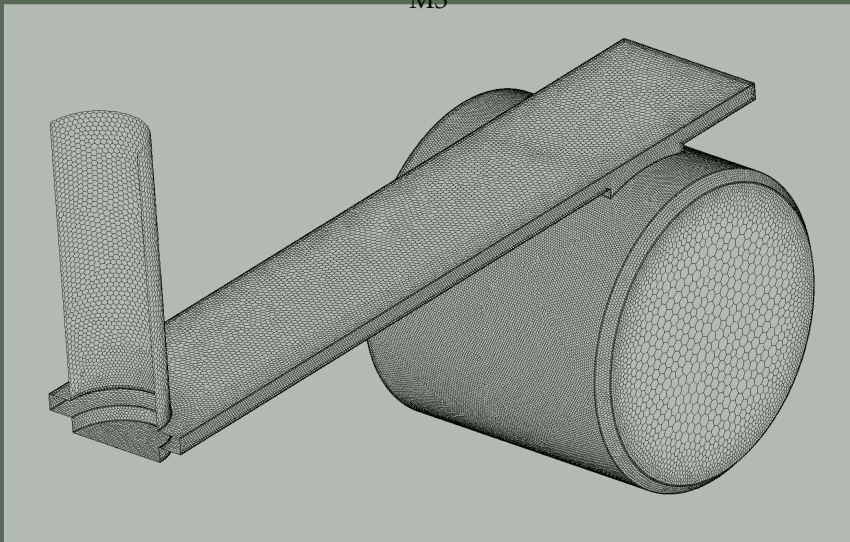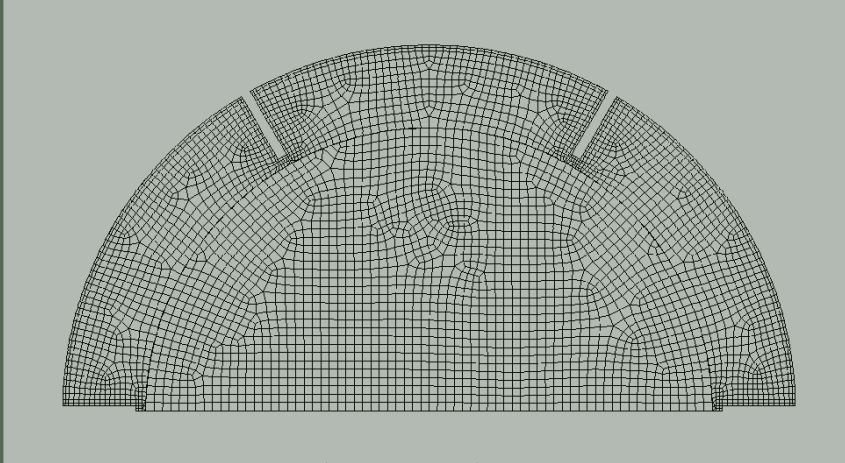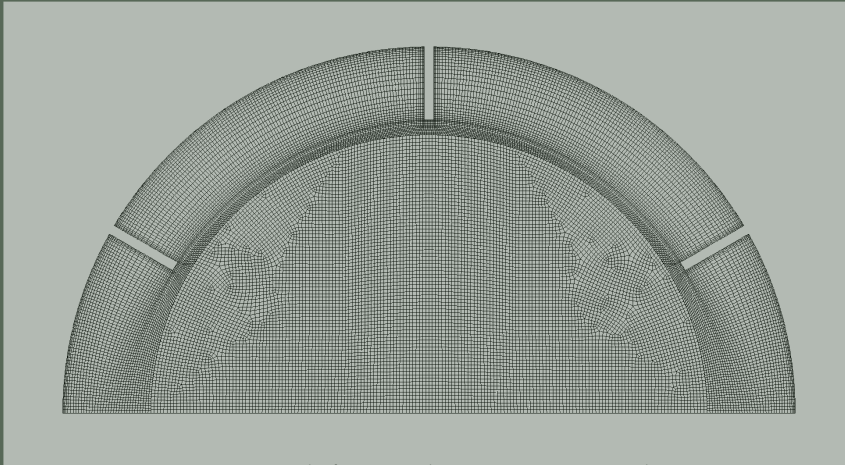ationary monolith. For the rotating case we consider a Cartesian reference frame F^* fixed to the monolith, with the x-axis parallel to the monolith channels and the z-axis the same as that of the solver (absolute) reference frame F. The difference between F and F^* is then characterized by a rotation, θ in the x-y plane.

Transformation of the momentum source, s_i^*, in the monolith reference frame to the solver frame, s_i^*, can be achieved with an appropriate transformation using the transformation matrix q_{ij}. Let e_i be the unit normal vector for F, and e_i^* by the unit normal for F^*. It follows that the transformation matrix qij to transform from frame F^* to frame F, is defined as

$$q_{ij} = e_i \cdot e_i^* = \begin{bmatrix} cos\,\theta & sin\,\theta & 0 \\ -sin\,\theta & cos\,\theta & 0 \\ 0 & 0 & 1 \end{bmatrix} \tag{F.1}$$

It can be shown that the momentum source in the solver frame can be obtained from equation 2.24 by simply transforming the loss coefficient tensors C_{ij}^* and D_{ij}^* from the monolith frame to the solver frame. The relative velocity magnitude remains the same in either frame. The relative velocity $\vec{v}_r$ is defined as the difference between the solver velocity $\vec{v}$ and the grid velocity $\vec{v}_g$ ($= \vec{\omega} \times \vec{r}$).

$$\vec{v}_r = \vec{v} - \vec{v}_g \tag{F.2}$$

The loss coefficients C_{ij}^* and D_{ij}^* are calculated with the relative velocity magnitude because the anisotropy forces flow in only one direction along the monolith

channels. The loss coefficients are transformed to the solver frame:

$$
\begin{aligned}
C_{il} &= q_{ij} C^*_{ik} q_{kl} \\
D_{il} &= q_{ij} D^*_{ik} q_{kl}
\end{aligned}
\tag{F.3}
$$

In this equation $q_{kl} = q_{ji}$, the transpose of the transformation matrix q_{ij}.

F.2   Implementation

The monolith source term was included in calculations with a UDF specifying an additional momentum source in each coordinate direction. This was done through the standard macro DEFINE_SOURCE (name,c,t,dS,eqn). The solver scheme used for the the segregated solver is shown in figure F.1 and show at what point the UDF will be activated.
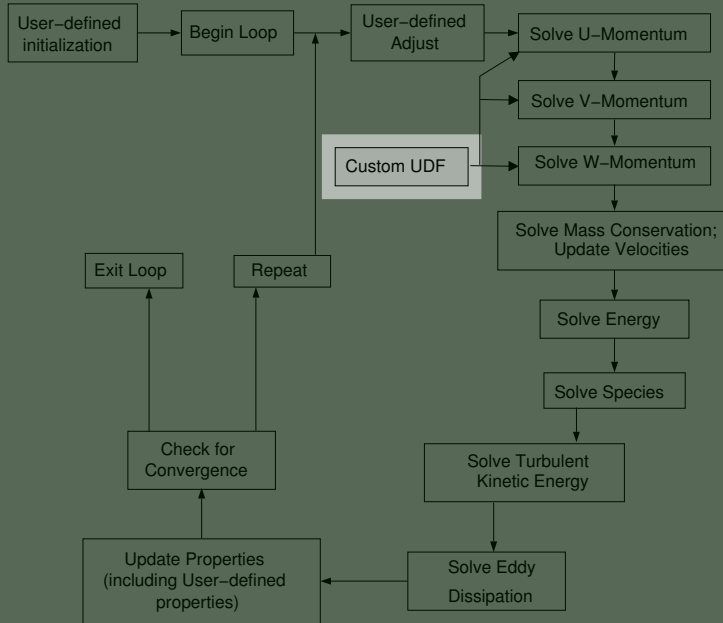
Figure F.1: *The Fluent segregated solver scheme, showing the progression of the numerical procedure.*

In each coordinate direction, the momentum equations loops over all cells in the solution domain. In the monolith domain thread (specified by t in the options list), the UDF is activated to calculate the additional source term for each cell (specified by c). The algorithm is shown schematically in figure F.2. It is written in such way that the transformation of the loss coefficients is calculated only once in each time step (and not for each cell in the monolith domain). During the coding, the

Fluent parameters RP_3D and ND_ND were used to allow 2-dimensional (x-y plane rotation) use of the source terms.
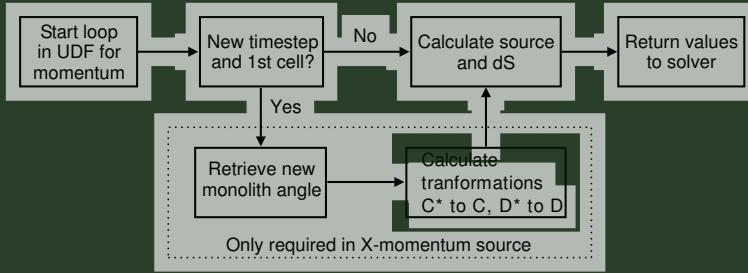
Figure F.2: *The monolith UDF algorithm.*

Additional coding was employed to include calculation of the loss coefficients based on the monolith and tank parameters. Finally, to improve the solution speed, the source terms were linearized for each coordinate direction (Patankar, 1980). After some algebra it follows that the linearized form of the viscous term in the x-direction is

$$\left[\frac{ds_{C_x}}{dv_x} \right] = -\mu C_{xx} \tag{F.4}$$

The linearized form of the inertial term in the x-direction is

$$\left[\frac{ds_{D_x}}{dv_x} \right] = -\frac{\rho D_{xx}}{2|\vec{v}_r|} \left[v_{r_x}^2 + |\vec{v}_r| \right] \tag{F.5}$$

The total linearized source is the sum of equations F.4 and F.5. Terms in the other directions have a similar form.

Appendix G

Sensitivity study on CFD for an MSR

G.1 Introduction

Modeling invariably allows for a multitude of options and different combinations which may yield similar, accurate results. This appendix outlines the efforts made to try and characterize the sensitivity of the CFD results to various modeling options. Each simulation requires a mesh, a number of model settings and boundary conditions to yield a solution. As far as possible, comparisons reported here are made between two cases in which only the parameter of interest is different. The bulk of the results are for a solid stirrer - the main motivation for this was that the inclusion of the monolith model adds additional complexity to the simulation that involves the choice of porous versus resolved monoliths and the associated treatment of the momentum deficit in the wake of the monolith (see discussions in section 2.4.4 and appendix B). The use of a solid stirrer allows the parameters mentioned in section 5.3.7 to be treated independently to investigate their individual contributions.

G.1.1 Comparison of results

The flow field in the reactor is compared by looking at radial profiles of the scaled tangential velocities, u_θ / u_s, and scaled turbulent kinetic energy, k/u_s^2, at different stirrer angles. The profiles are extracted on a horizontal line at $z = 0.088m$ ($H_L/2$) through the middle of the stirrer face.

The power consumption of mixing equipment, expressed as a dimensionless power number, is another important parameter in the design of mixing equipment.

For the numerical work it presents a single integral property for comparison between the various simulations and experimental results. As part of each simulation, the torque on the tank walls were compared to that measured on the stirrer and shaft. CFD results were only considered to be converged when the sum of the two was sufficiently close to zero (balance of forces).

Although not shown in chapter 4, the torque measurements were performed with the shaft encoder enabled, and are therefore available as angle resolved data. Figure G.1 shows N_P, measured on the stirrer and on the tank walls, as a function of stirrer angle for one complete stirrer revolution for an SMM simulation with a solid stirrer rotating at $N = 1\,rev/s$. The average value of the torque on the stirrer and on the tank walls are equal, but with opposite signs. This confirms that the simulation predicts a zero sum of moments, as would be expected for steady-state operation. The six baffles on the tank are reflected in the 60° periodicity of the results. The 0° position (and each multiple of 60°) corresponds to the stirrer located exactly between two baffles, i.e. at the LDA measurement plane. The maximum torque (on the stirrer) occurs just past this position ($\approx$15° later), and coincides with a local minimum in the tank wall torque.

The MRF simulations were performed with the stirrer located 20° before the LDA plane (midway between two baffles), at the LDA plane and at 20° after the LDA plane. This corresponds to the stirrer locations as reported in chapter 4 for $\theta = -\pi/9$, 0, and $\pi/9$. In reporting power numbers from MRF simulations the average value of the three simulations are used. This represents an equi-spaced sample with three data points in a periodic signal. Testing on the torque data from an SMM simulation showed that the three-point averaged value was within 3% of the mean, regardless of where the first point was selected.

Figure G.2 compares the measured stirrer power number to results from three simulations. Data from the simulation with a sharp leading edge on the monolith holder (C17) show higher values than the experiment. The data from the chamfered leading edge are shown with a lid (C40) and with a free surface (C55). The average values compare very well with the measured data, but the magnitude of the oscillations are smaller for the simulated data. The free-surface result shows larger oscillations than the model with a flat surface at the air-water interface. In addition, the experimental data show significant randomness over the range shown, whereas all the modeled data are much closer to being periodic. This is probably due to shaft eccentricity and other manufacturing imperfections in the experiment that were not included in the numerical models.

The next section discusses the results from the sensitivity studies. In the experiments the LDA data were averaged in 4° bins. This averaging is not possible with MRF data, but the effect can be evaluated with the SMM data set. As such it is discussed as part of the results on impeller movement in the following. Comparisons of the power number are made with the angle-averaged values in the rest of this appendix.

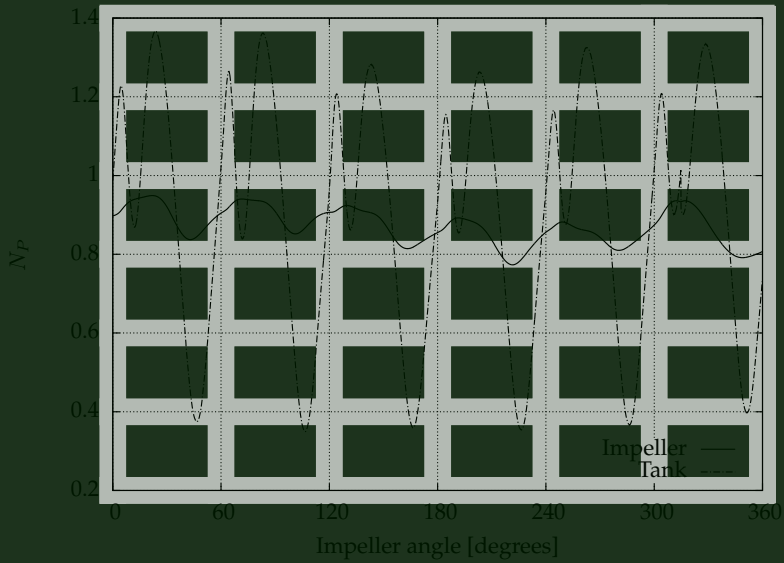**Figure G.1:** *N_P as a function of the stirrer position (angle) for one complete revolution. Values for the stirrer and tank wall are shown with the sign of the tank wall torque inverted.*
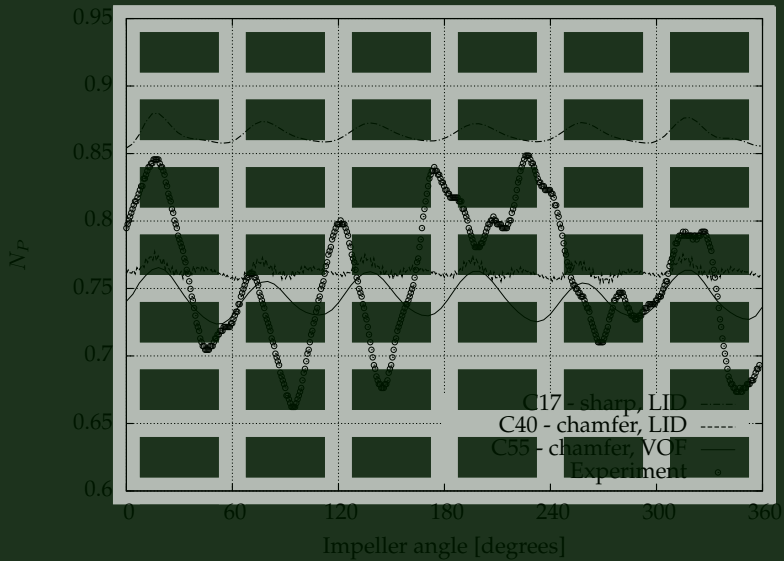

Figure G.2: *Comparison of measured and modeled values of N_P (stirrer) as a function of stirrer location (angle) for one complete stirrer revolution. The data are shown for a solid stirrer, operating at $N = 1\,rev/s$.*

Table G.1: *Influence of inclusion of the free-surface on the power number results for the MSR.*

Case	Mesh	MOV	EDGE	SURF.	TURB.	TANK	CELLS	N_P
C18	M3	SMM	sharp	LID	SST-KW	B1	$3246k$	0.91
C27	M4	SMM	sharp	VOF	SST-KW	B1	$8835k$	0.84
C40	M6	SMM	chamfer	LID	RKE	B2	$292k$	0.76
C55	M8	SMM	chamfer	VOF	RKE	B2	$383k$	0.73

G.2   Sensitivity parameters

In this section the influence of different parameters on the CFD results are evaluated. Results are selected, as much as possible, from cases such that only the parameter of interest is different.

G.2.1   Fluid surface movement

The top surface of the CFD simulation can be modeled as a fixed surface, or with a free liquid surface using the volume of fluid (VOF) approach. The VOF approach require transient, sliding mesh simulations and therefore represents the most expensive type of simulation (in terms of solution time). Table G.1 lists data from two comparisons sets where the difference in simulations are the free-surface at the top of the liquid. There is also a difference in mesh size because models with a fixed surface (LID) does not require the additional volume of air above the surface. The mesh in the bulk of the tank, i.e., below the level of the surface were kept the same.

The results show that the VOF simulations predict a lower value for the stirrer power number (7% for sharp, and 4% for chamfered stirrer). This is consistent with the expectation that the passage of the blade would cause the liquid surface to rise - as a result the flow area around the monolith is increased. The fluid velocity is reduced due to the larger flow area and this results in a lower drag force on the blade.

The flow profiles in the tank are compared for C18 vs. C27 (figure G.3) and C40 vs. C55 (figure G.4). The first data pair C18:C27 were obtained from a fine mesh with the SST-KW turbulence model. The C40:C55 data were obtained from a standard mesh with the RKE turbulence model.

The fine mesh results do not show a significant variation between LID and VOF for both u_θ/u_s and k/u_s^2 profiles. The standard mesh show larger variations in k/u_s^2 and it does not capture the wake profile as well as the fine mesh result.
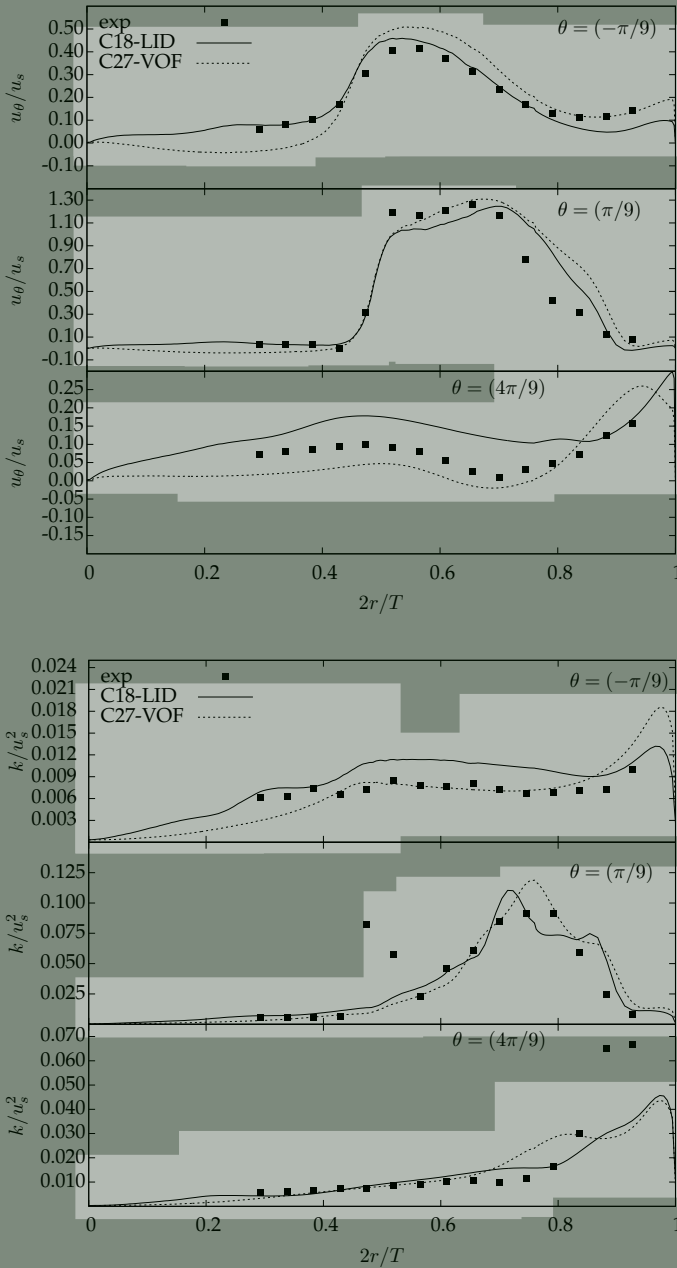
Figure G.3: *Effect of liquid surface modeling on tangential velocity profiles (top) and turbulent kinetic energy profiles (bottom).*
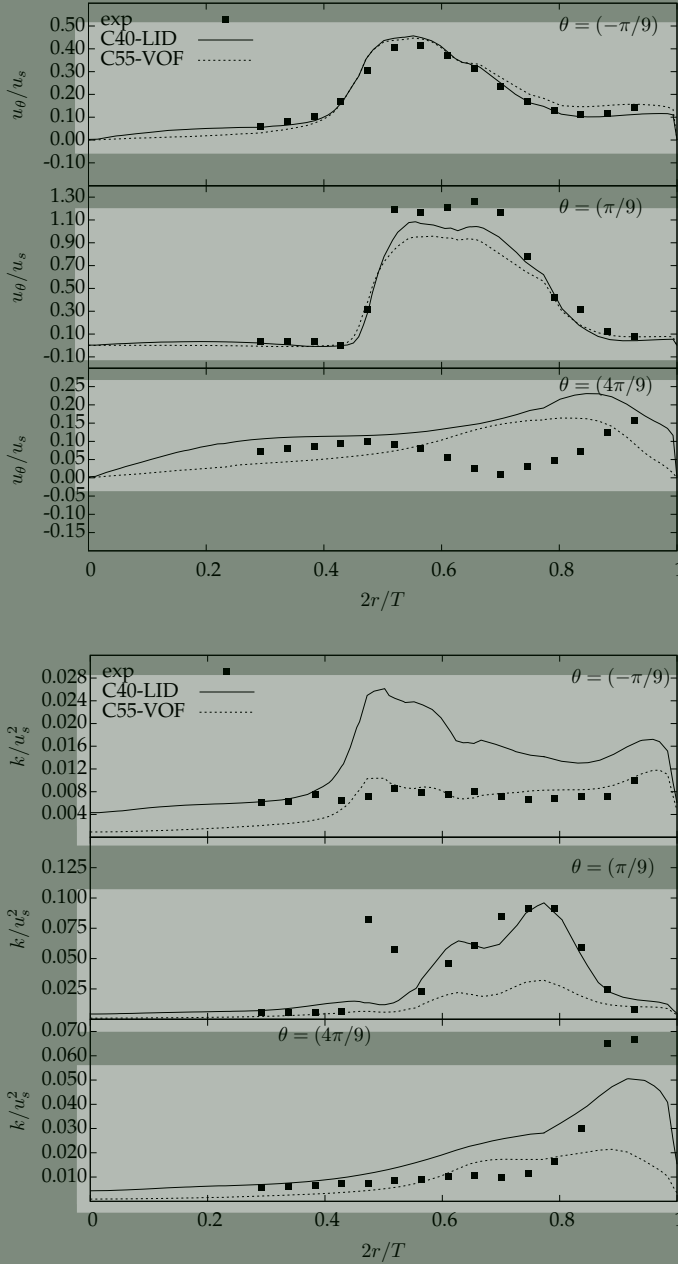
Figure G.4: *Effect of liquid surface modeling on tangential velocity profiles (top) and turbulent kinetic energy profiles (bottom).*

Table G.2: *Influence of stirrer movement model on the power number results for the MSR.*

Case	Mesh	MOV	EDGE	SURF.	TURB.	TANK	CELLS	N_P
C05	M2	MRF	sharp	LID	RKE	B2	307k	0.89
C17	M2	SMM	sharp	LID	RKE	B2	307k	0.86
C22	M3	MRF	sharp	LID	SST-KW	B1	3246k	0.88
C18	M3	SMM	sharp	LID	SST-KW	B1	3246k	0.91
C33	M6	MRF	chamfer	LID	RKE	B2	292k	0.76
C40	M6	SMM	chamfer	LID	RKE	B2	292k	0.76

G.2.2 Stirrer movement

The selection of the stirrer movement model has a significant impact on the computational requirement - the MRF cases require three steady-state results, whereas the SMM models require long transient simulations. A standard MRF simulation typically requires ∼5000 iterations for a converged solution; for three stirrer angles this results in 15000 iterations to obtain a dataset, e.g., C33 in the simulation register (appendix H). The corresponding sliding mesh model requires a transient simulation of ∼10 stirrer revolutions, each revolution consists of 720 time steps and each time step requires ∼10 iterations to converge - this amounts to 72000 iterations per dataset, e.g., C17 in the simulation register. A model including the free surface would require a smaller time-step to keep the interface tracking Courant number in a realistic range - typically doubling the computing requirement.

Results obtained with the MRF and SMM methods give similar values for N_P, on condition that the MRF results are averaged at a number of stirrer positions relative to the baffles. In this work three locations were used, spaced $\pi/9$ (20°) apart at $\theta = -\pi/9$, 0 and $pi/9$, to cover the $\pi/3$ (60°) periodicity of the six baffles.

Table G.2 show comparisons for 3 pairs of CFD data. There are no significant or consistent difference between the MRF and SMM result for N_P.

The flow profiles are compared in figures G.5, G.6 and G.7. Results are similar in the area surrounding the monolith. However, the mesh interface between the rotating and stationary mesh zones is clearly visible in the profiles at $2r/T$=0.78. The SMM profiles have a similar shape to the experiments, whereas the MRF results exhibit a sharp change in gradient at the interface - especially for profiles in the wake ($\theta = \pi/9$) where the absolute values of variables are small.

Since the power numbers and the flow around the monolith are similar, the stirrer movement model is not expected to have a significant influence on the prediction of the monolith flow rates.

Figure G.5: *Effect of stirrer movement model on tangential velocity profiles (top) and turbulent kinetic energy profiles (bottom).*
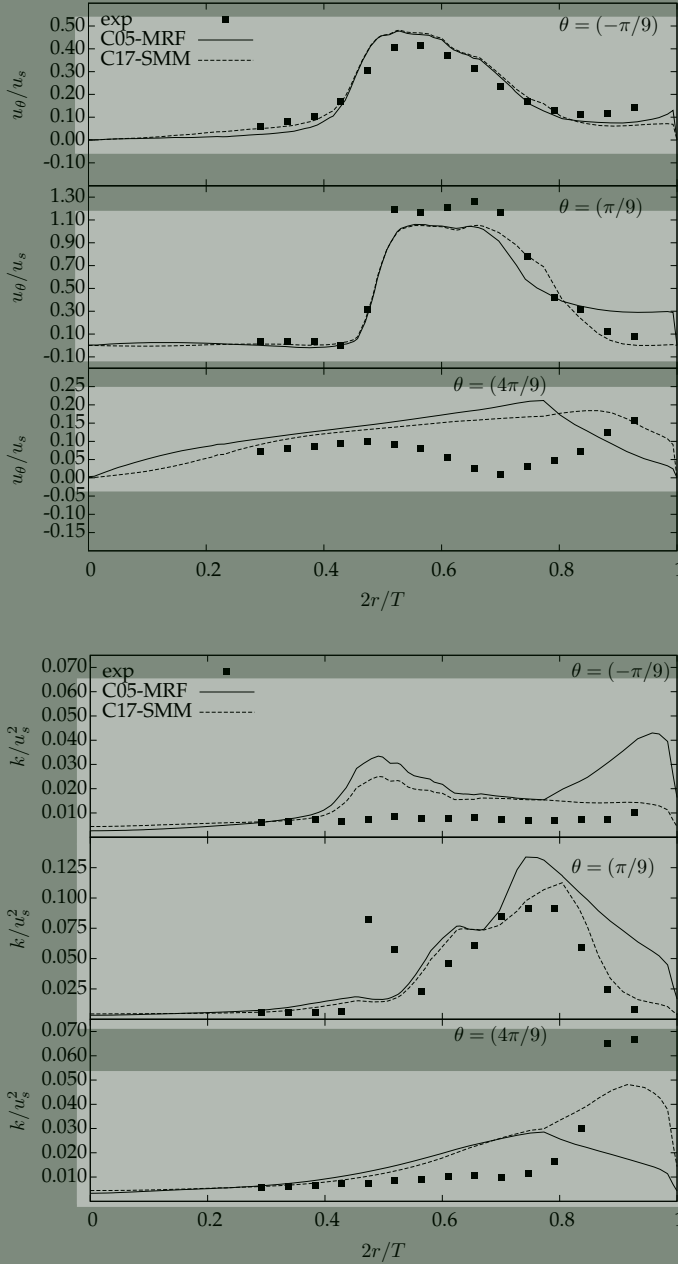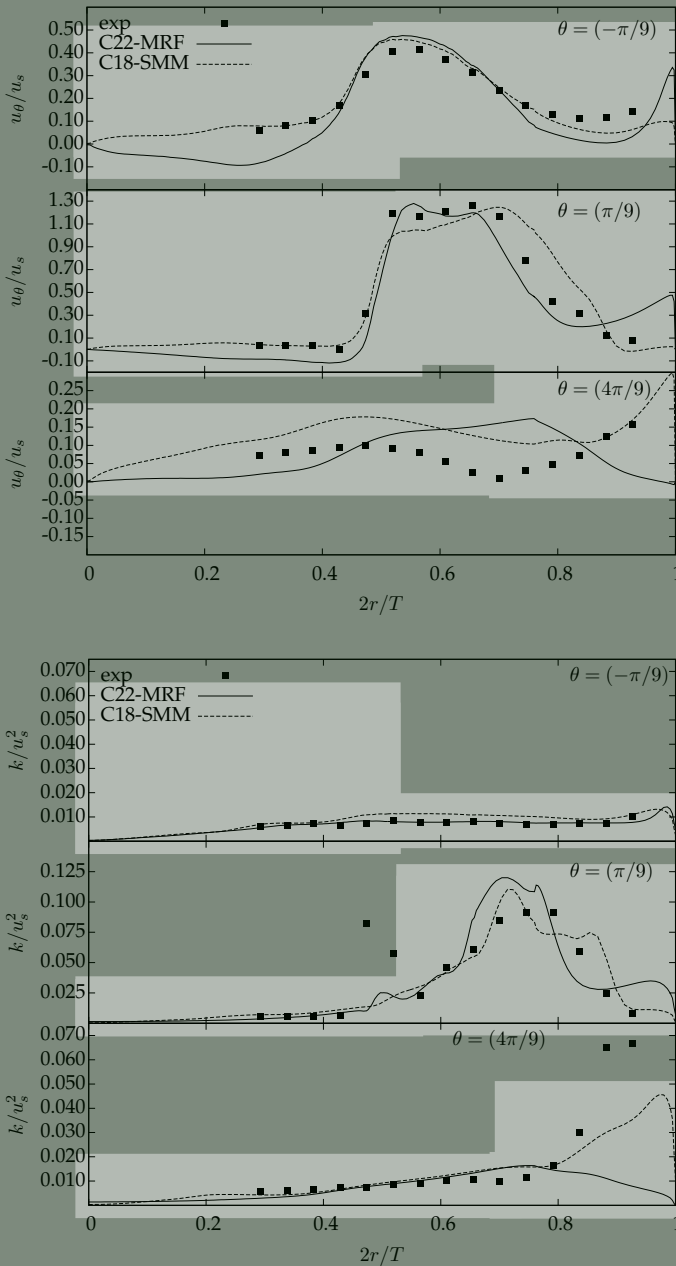
Figure G.6: *Effect of stirrer movement model on tangential velocity profiles (top) and turbulent kinetic energy profiles (bottom).*
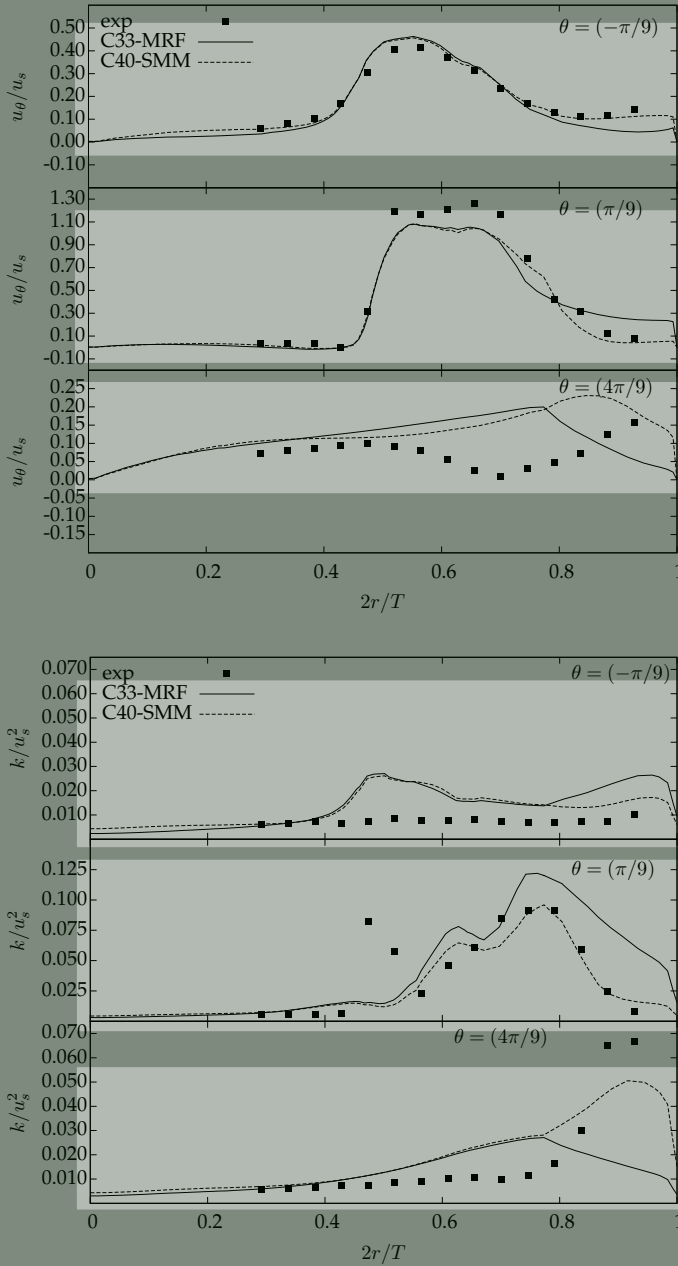
Figure G.7: *Effect of stirrer movement model on tangential velocity profiles (top) and turbulent kinetic energy profiles (bottom).*

Table G.3: *Influence of turbulence modeling on N_P.*

Case	Mesh	MOV	EDGE	SURF.	TURB.	TANK	CELLS	N_P
C05	M2	MRF	sharp	LID	RKE	B2	307k	0.89
C06	M2	MRF	sharp	LID	SKE	B2	307k	0.94
C07	M2	MRF	sharp	LID	SKW	B2	307k	0.87
C08	M2	MRF	sharp	LID	SST-KW	B2	307k	0.84
C09	M2	MRF	sharp	LID	RNG-KE	B2	307k	0.82
C10	M2	MRF	sharp	LID	RSM	B2	307k	0.92

G.2.3 Turbulence modeling

A selection of power number results is shown in table G.3 for an MRF model of the stirrer with a sharp leading edge, solid blades and rotating at $N = 1\,rev/s$. The top surface is fixed - no free-surface affects were considered. The bulk of the results are in the range $0.8 < N_P < 1.0$.

Differences between the turbulence results for different turbulence models are not significant - data are within 7% of the mean value for all cases. The RKE is closest (1%) and the RNG-KE data (-6.7%) the furthest from the mean.

Figure G.8 show profiles of the scaled tangential velocity, u_θ/u_s, and scaled turbulent kinetic energy, k/u_s^2, for the different turbulence models at three stirrer angles. The results for the different models are similar and compare well with the experimental data around the monolith. In the wake of the monolith ($\theta = 4pi/9$) the issue with the mesh interface between the rotating and stationary mesh regions, as observed in section G.2.2, is evident again.

Figure G.8: *Influence of turbulence modeling on tangential velocity profiles (top) and turbulent kinetic energy profiles (bottom).*

Table G.4: *Influence of mesh density on the power number results for the MSR.*

Case	Mesh	MOV	EDGE	SURF.	TURB.	TANK	CELLS	N_P
C01	M1	MRF	sharp	LID	RKE	B2	613k	0.87
C05	M2	MRF	sharp	LID	RKE	B2	307k	0.89
C23	M3	MRF	sharp	LID	RKE	B1	3246k	0.89
C08	M2	MRF	sharp	LID	SST-KW	B2	307k	0.84
C22	M3	MRF	sharp	LID	SST-KW	B1	3246k	0.88

G.2.4   Mesh density

A systematic mesh refinement study was not performed for this work, instead re-ported results were in general obtained from two meshes which differ in cell count by an order of magnitude. TableG.4 shows that values of N_P are not sensitive to the cell count for the present simulations. This is similar to the drag results from chapter 3 which showed that the bluff body drag was not sensitive to the near-wall mesh resolution. From this it can be concluded that the low cell count (coarse mesh) would be sufficient to obtain fairly accurate N_P values for the MSR - the stirrer leading edge and free-surface models are more important.

The flow profiles are compared in figures G.9 and G.10. Results are similar for different mesh densities. The profiles of k/u_s^2 at $\theta = 4\pi/9$ show some variation but this may rather be due to the non-stationary nature of the flow field. During the simulations, it was observed that the MRF results exhibited oscillatory residual con-vergence. This is often associated to non-stationary areas in the flow. Although the simulation attempts to find a steady state result, no such result exists in reality and the solver solution oscillates between possible solutions - this can be observed by visualizing flow structures during iteration of the steady state problem (not shown here). Better correlation could possibly be achieved by averaging a number of pro-files that are sampled (extracted) while the solver is iterating - this was not done for the present comparisons.

Figure G.9: *Effect of mesh density on tangential velocity profiles (top) and turbulent kinetic energy profiles (bottom).*
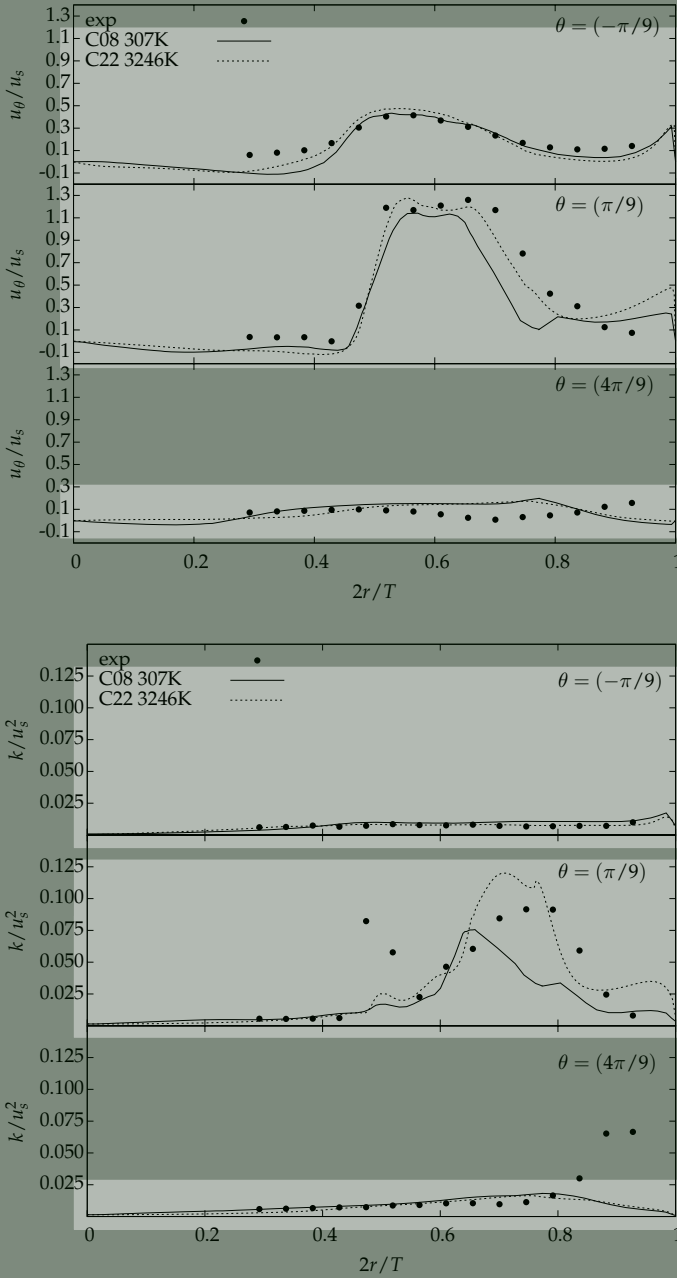
Figure G.10: *Effect of mesh density on tangential velocity profiles (top) and turbulent kinetic energy profiles (bottom).*
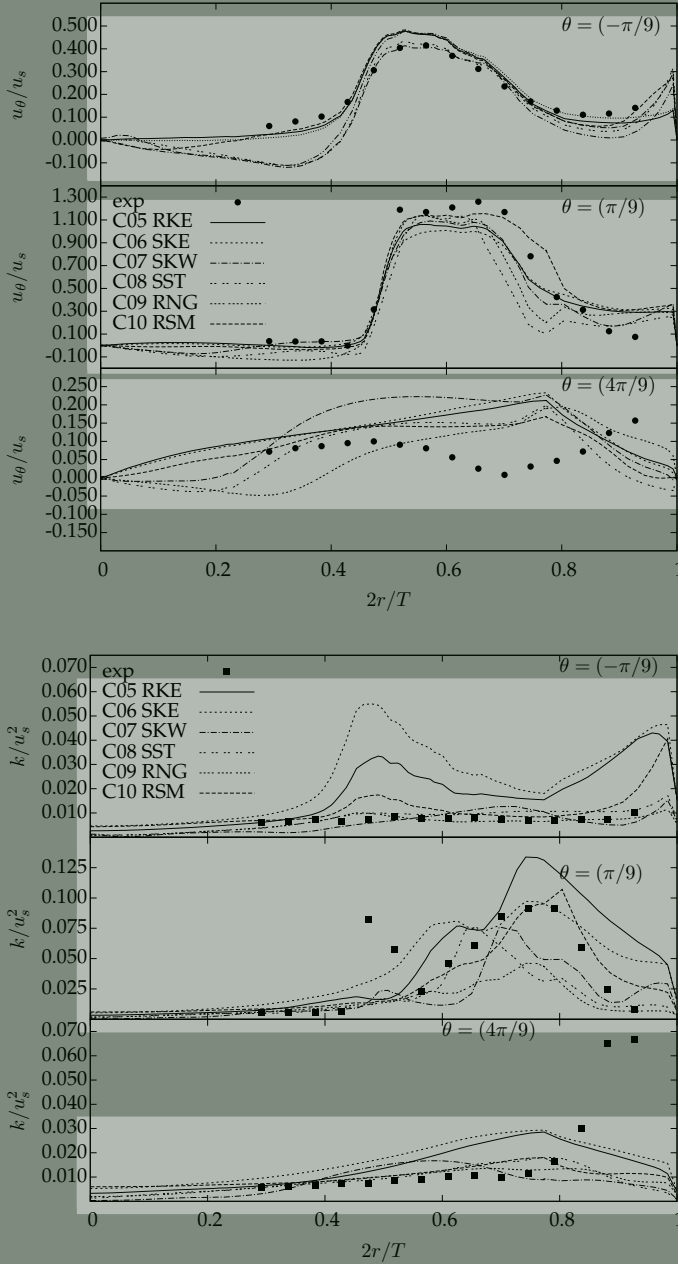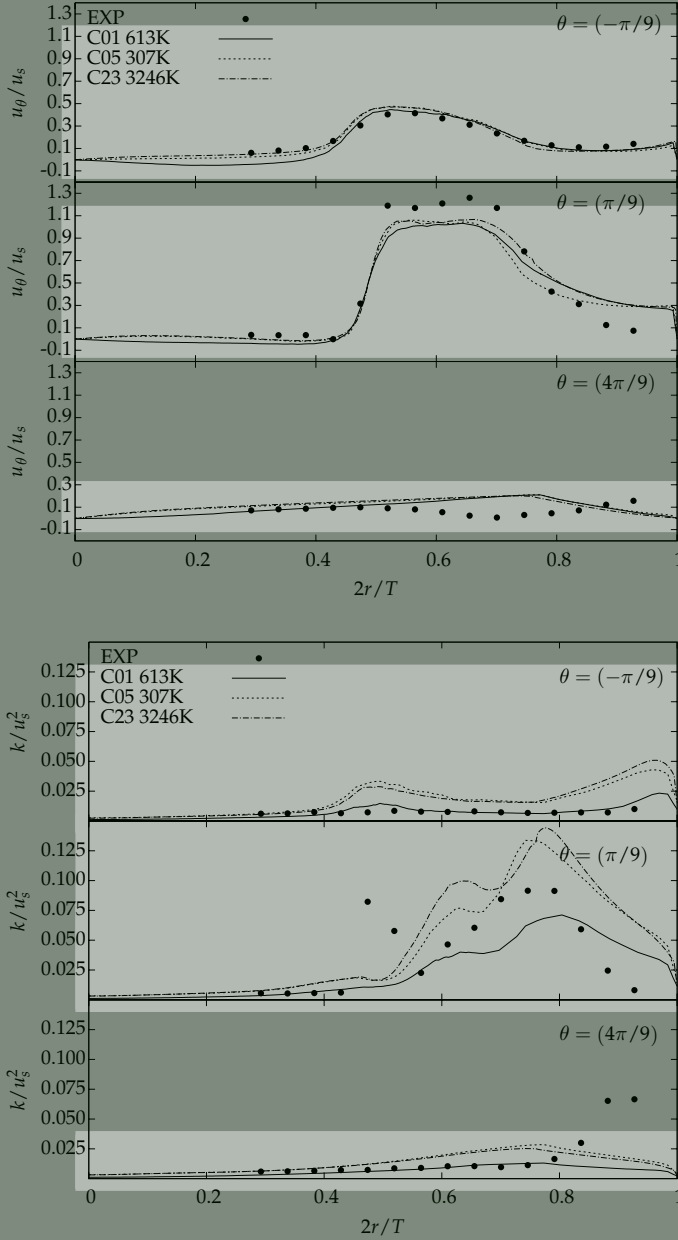
Table G.5: *Influence of stirrer leading edge geometry on the power number results for the MSR.*

Case	Mesh	MOV	EDGE	SURF.	TURB.	TANK	CELLS	N_P
C01	M1	MRF	sharp	LID	RKE	B2	613k	0.87
C29	M5	MRF	chamfer	LID	RKE	B2	547k	0.77
C05	M2	MRF	sharp	LID	RKE	B2	307k	0.89
C33	M6	MRF	chamfer	LID	RKE	B2	292k	0.76
C17	M2	SMM	sharp	LID	RKE	B2	307k	0.86
C40	M6	SMM	chamfer	LID	RKE	B2	292k	0.76
C18	M3	SMM	sharp	LID	SST-KW	B1	3246k	0.91
C56	M9	SMM	chamfer	LID	SST-KW	B1	2926k	0.78

G.2.5   Stirrer leading edge geometry

The monolith holder was initially modeled with a sharp leading edge. This was later modified to a chamfered edge as in the actual experiments (see figure 5.2). Table G.5 shows the comparison for four pairs of CFD data. The chamfered edge clearly results in a reduced value of N_P. This can be confirmed by a simple axi-symmetric CFD simulation of the sharp and chamfered profiles ($C_{d,sharp} = 1.06$, $C_{d,chamfer} = 0.61$).

The effect of the leading edge on the flow profiles are presented in figures G.11, G.12, G.13, and G.14. Tangential velocity profiles are similar - this can be expected due to the bluff nature of the stirrer blade which dominates the flow field. The edge effect is more distinct in the k/u_s^2 profiles. However, there is no clear trend as the fine mesh result with SMM (figure G.14) show very similar profiles for k/u_s^2.

Figure G.11: *Effect of stirrer leading edge geometry on tangential velocity profiles (top) and turbulent kinetic energy profiles (bottom).*
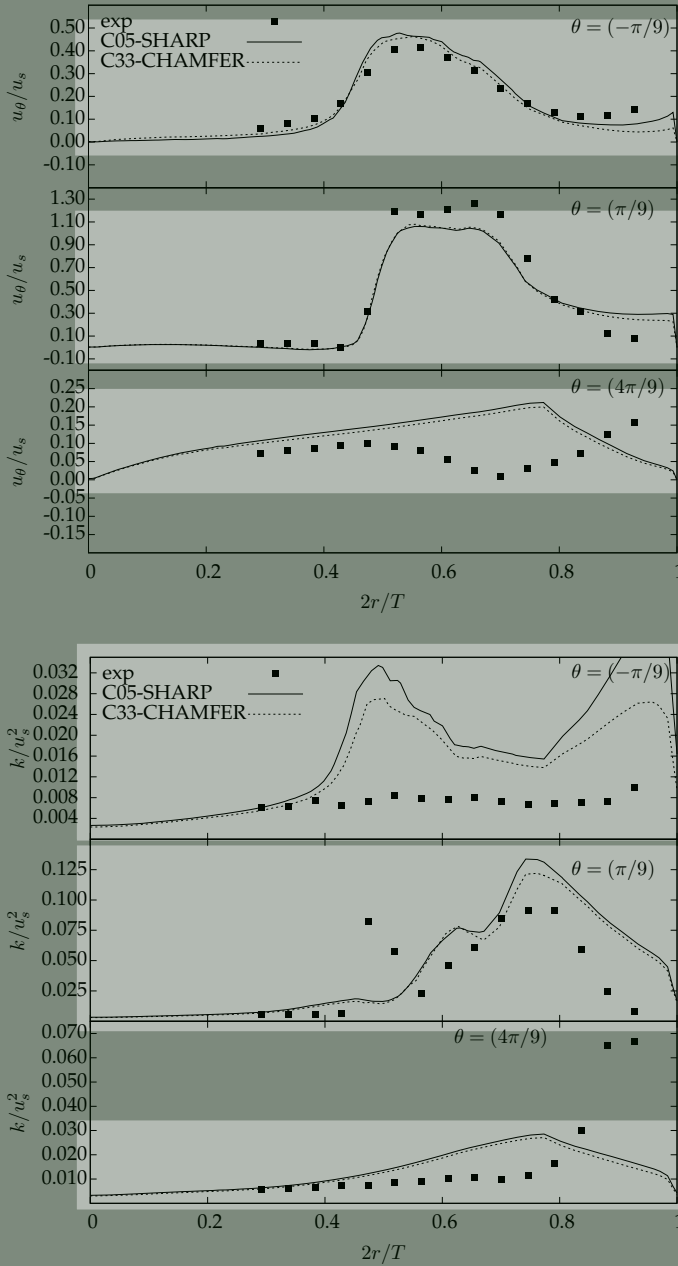
Figure G.12: *Effect of stirrer leading edge geometry on tangential velocity profiles (top) and turbulent kinetic energy profiles (bottom).*
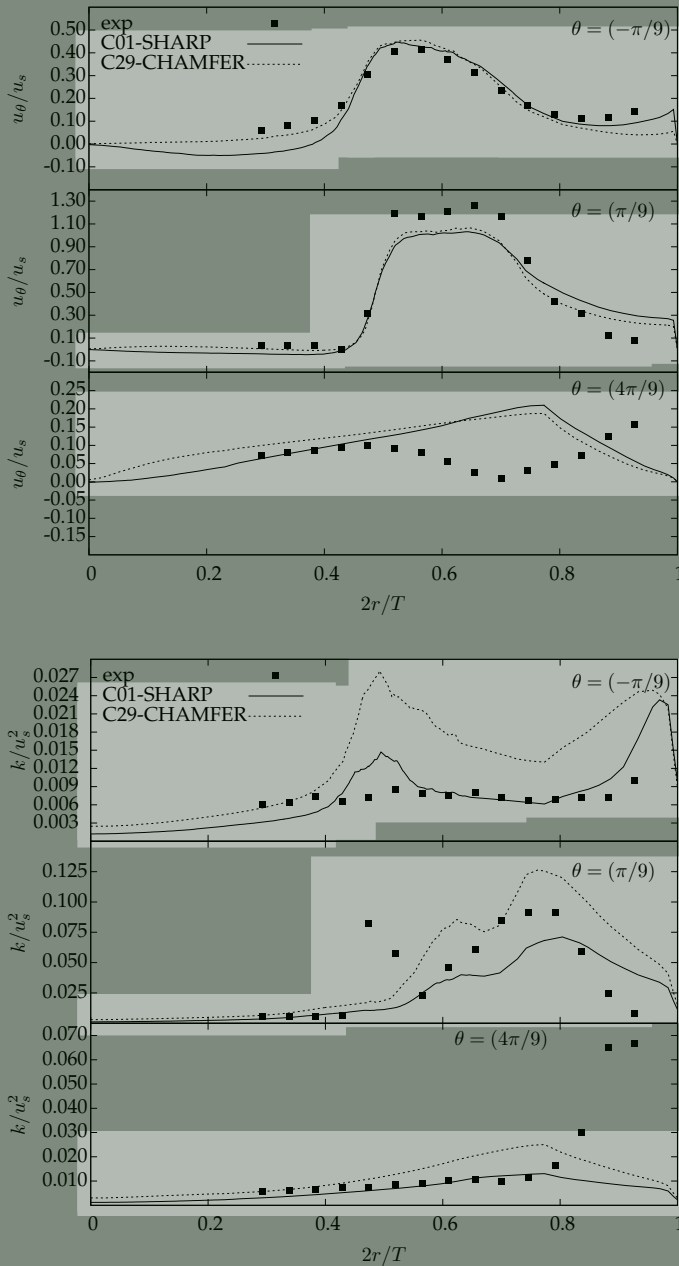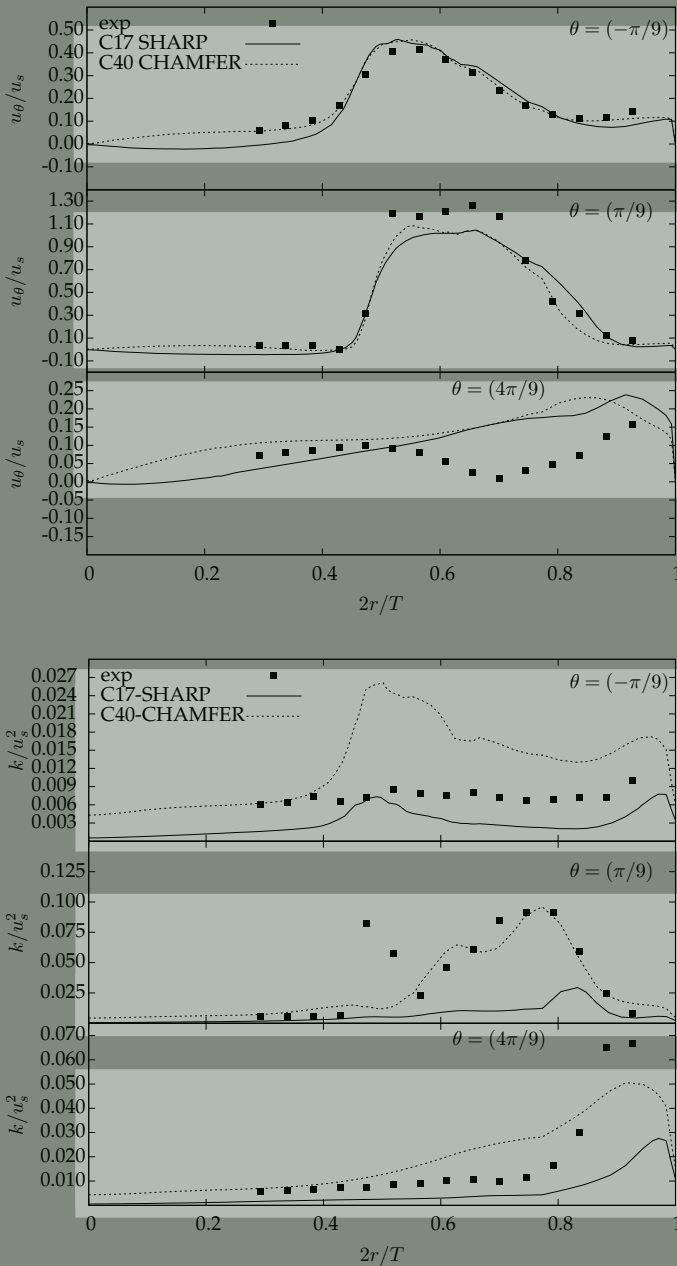
Figure G.13: *Effect of stirrer leading edge geometry on tangential velocity profiles (top) and turbulent kinetic energy profiles (bottom).*
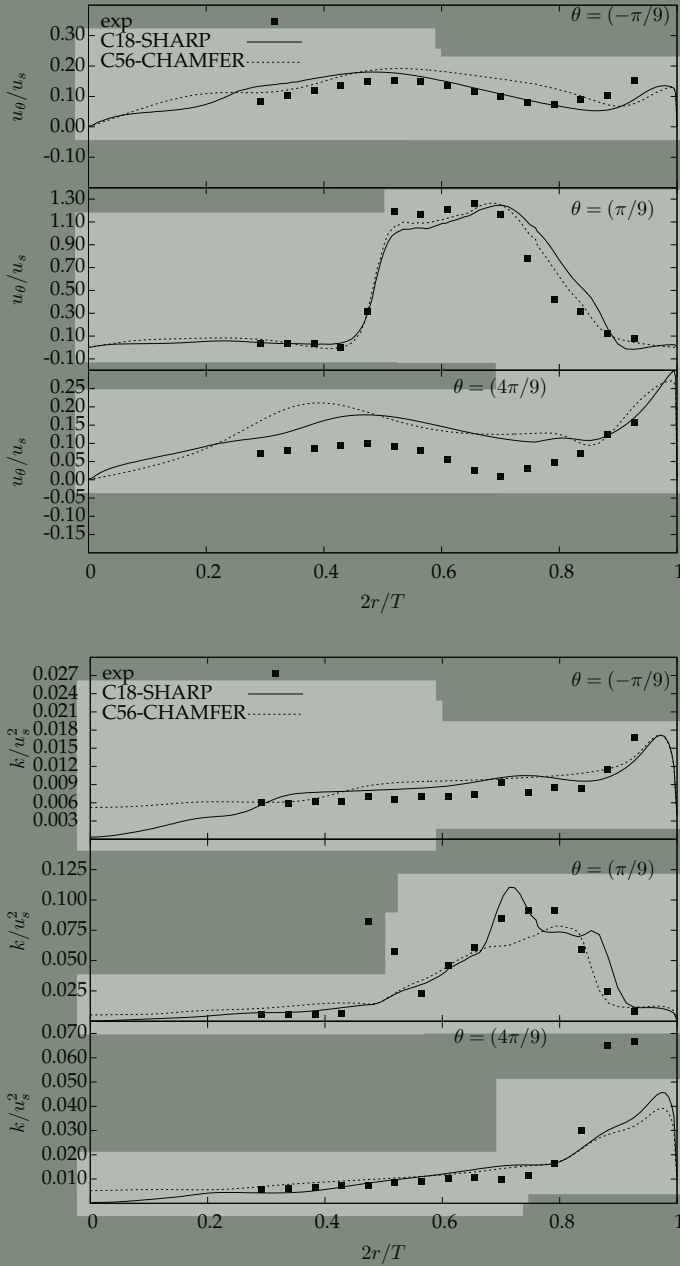
Figure G.14: *Effect of stirrer leading edge geometry on tangential velocity profiles (top) and turbulent kinetic energy profiles (bottom).*

G.3 Conclusions from sensitivity study

The geometry of the monolith holder leading edge was found to have the biggest impact on the CFD results for N_P. This was followed by the inclusion of a free-surface for the top of the tank, which also reduced the predicted values of N_P. Turbulence models, mesh density and impeller movement model did not significantly influence the N_P results.

Flow field results show fair agreement with the experimental data for u_θ/u_s in the vicinity of the blade. In the wake of the blade the agreement was best for the fine mesh, SMM model with a chamfered leading edge. The inclusion of the free-surface did not influence flow profiles significantly.

The MRF model profiles show a clear influence of the mesh interface between the rotating and stationary mesh zones - this effect is most visible away from the blade in areas with low values of u_θ/u_s and k/u_s^2.

Based on this study, an economic choice for the production runs of the MSR would be: steady-state simulations (MRF stirrer model and no free-surface), standard mesh resolution and either the RKE or SST-KW turbulence models (commonly available).

Appendix H

MSR simulation register

H.1 Overview

This appendix includes a table of the CFD simulations that were performed for chapter 5. It is included as a reference that contain all the information for a specific CFD case, referred to by the case number (given as Cnn, where nn is the specific case numbers). The information included for each case include: case number, geometry and mesh, stirrer angles (for MRF cases), stirrer speed, monolith holder edge geometry, top surface modeling option, turbulence model, tank configuration and the amount of computational cells (a key to the abbreviated table headers are included at the end of the table). The CFD data from a Fluent simulation is stored as a set of at least two files: a case file (.cas extension) with the information on the mesh, physics and boundary conditions, and a data file (.dat extension) that holds the data for each solver variable at each cell center. Each MRF case has three data sets (one for each impeller angle), while the SMM cases have several data sets that represent a time history of the stirrer rotation.

Table H.1: *Register of CFD cases for Chapter 5.5.1*

Case	MSH	MOV	ANGLES	RPM	BLADE	EDGE	SURFACE	TURBMOD	TANK	CELLS
C01	M1	MRF	I20P,I00P,I20N	60	BLK	sharp	LID	RKE	B2	613155
C02	M2	MRF	I20P,I00P,I20N	15	BLK	sharp	LID	RKE	B2	306818
C03	M2	MRF	I20P,I00P,I20N	30	BLK	sharp	LID	RKE	B2	306818
C04	M2	MRF	I20P,I00P,I20N	45	BLK	sharp	LID	RKE	B2	306818
C05	M2	MRF	I20P,I00P,I20N	60	BLK	sharp	LID	RKE	B2	306818
C06	M2	MRF	I20P,I00P,I20N	60	BLK	sharp	LID	SKE	B2	306818
C07	M2	MRF	I20P,I00P,I20N	60	BLK	sharp	LID	SKW	B2	306818
C08	M2	MRF	I20P,I00P,I20N	60	BLK	sharp	LID	SST-KW	B2	306818
C09	M2	MRF	I20P,I00P,I20N	60	BLK	sharp	LID	RNG-KE	B2	306818
C10	M2	MRF	I20P,I00P,I20N	60	BLK	sharp	LID	RSM	B2	306818
C11	M2	MRF	I20P,I00P,I20N	75	BLK	sharp	LID	RKE	B2	306818
C12	M2	MRF	I20P,I00P,I20N	90	BLK	sharp	LID	RKE	B2	306818
C13	M2	MRF	I20P,I00P,I20N	105	BLK	sharp	LID	RKE	B2	306818
C14	M2	MRF	I20P,I00P,I20N	120	BLK	sharp	LID	RKE	B2	306818
C15	M2	MRF	I20P,I00P,I20N	135	BLK	sharp	LID	RKE	B2	306818
C16	M2	MRF	I20P,I00P,I20N	150	BLK	sharp	LID	RKE	B2	306818
C17	M2	SMM	all	60	BLK	sharp	LID	RKE	B2	306818
C18	M3	SMM	all	60	BLK	sharp	LID	SST-KW	B1	3245753
C19	M3	MRF	I20P,I00P,I20N	15	BLK	sharp	LID	SST-KW	B1	3245753
C20	M3	MRF	I20P,I00P,I20N	30	BLK	sharp	LID	SST-KW	B1	3245753
C21	M3	MRF	I20P,I00P,I20N	45	BLK	sharp	LID	SST-KW	B1	3245753
C22	M3	MRF	I20P,I00P,I20N	60	BLK	sharp	LID	SST-KW	B1	3245753
C23	M3	MRF	I20P,I00P,I20N	60	BLK	sharp	LID	RKE	B1	3245753
C24	M3	MRF	I20P,I00P,I20N	90	BLK	sharp	LID	SST-KW	B1	3245753
C25	M3	MRF	I20P,I00P,I20N	120	BLK	sharp	LID	SST-KW	B1	3245753
C26	M3	MRF	I20P,I00P,I20N	150	BLK	sharp	LID	SST-KW	B1	3245753

Table H.1 – continued from previous page

Case	MSH	MOV	ANGLES	RPM	BLADE	EDGE	SURFACE	TURBMOD	TANK	CELLS
C27	M4	SMM	all	60	BLK	sharp	VOF	SST-KW	B1	8835355
C28	M4b	SMM	all	60	M400	sharp	LID	SST-KW	B1	3346939
C29	M5	MRF	120P,100P,120N	60	BLK	chamfer	LID	RKE	B2	546844
C30	M6	MRF	120P,100P,120N	15	BLK	chamfer	LID	RKE	B2	292182
C31	M6	MRF	120P,100P,120N	30	BLK	chamfer	LID	RKE	B2	292182
C32	M6	MRF	120P,100P,120N	45	BLK	chamfer	LID	RKE	B2	292182
C33	M6	MRF	120P,100P,120N	60	BLK	chamfer	LID	RKE	B2	292182
C34	M6	MRF	120P,100P,120N	75	BLK	chamfer	LID	RKE	B2	292182
C35	M6	MRF	120P,100P,120N	90	BLK	chamfer	LID	RKE	B2	292182
C36	M6	MRF	120P,100P,120N	105	BLK	chamfer	LID	RKE	B2	292182
C37	M6	MRF	120P,100P,120N	120	BLK	chamfer	LID	RKE	B2	292182
C38	M6	MRF	120P,100P,120N	135	BLK	chamfer	LID	RKE	B2	292182
C39	M6	MRF	120P,100P,120N	150	BLK	chamfer	LID	RKE	B2	292182
C40	M6	SMM	all	60	BLK	chamfer	LID	RKE	B2	292182
C41	M7	MRF	120P,100P,120N	15	M400	chamfer	LID	RKE	B2	306818
C42	M7	MRF	120P,100P,120N	30	M400	chamfer	LID	RKE	B2	306818
C43	M7	MRF	120P,100P,120N	45	M400	chamfer	LID	RKE	B2	306818
C44	M7	MRF	120P,100P,120N	60	M400	chamfer	LID	RKE	B2	306818
C45	M7	MRF	120P,100P,120N	75	M400	chamfer	LID	RKE	B2	306818
C46	M7	MRF	120P,100P,120N	90	M400	chamfer	LID	RKE	B2	306818
C47	M7	MRF	120P,100P,120N	105	M400	chamfer	LID	RKE	B2	306818
C48	M7	MRF	120P,100P,120N	120	M400	chamfer	LID	RKE	B2	306818
C49	M7	MRF	120P,100P,120N	135	M400	chamfer	LID	RKE	B2	306818
C50	M7	MRF	120P,100P,120N	150	M400	chamfer	LID	RKE	B2	306818
C51	M7	MRF	120P,100P,120N	60	M200	chamfer	LID	RKE	B2	306818
C52	M7	MRF	120P,100P,120N	60	M100	chamfer	LID	RKE	B2	306818
C53	M7	MRF	120P,100P,120N	60	M050	chamfer	LID	RKE	B2	306818

Table H.1 – continued from previous page

Case	MSH	MOV	ANGLES	RPM	BLADE	EDGE	SURFACE	TURBMOD	TANK	CELLS
C54	M7	SMM	all	60	M400	chamfer	LID	RKE	B2	306818
C55	M8	SMM	all	60	BLK	chamfer	VOF	RKE	B2	382580
C56	M9	SMM	all	60	BLK	chamfer	LID	SST-KW	B1	2925760
C57	M10	SMM	all	60	M400	chamfer	LID	RKE	B1	3147170
C58	M10	MRF	I20P,I00P,I20N	15	M400	chamfer	LID	RKE	B1	3147170
C59	M10	MRF	I20P,I00P,I20N	60	M400	chamfer	LID	RKE	B1	3147170
C60	M10	MRF	I20P,I00P,I20N	120	M400	chamfer	LID	RKE	B1	3147170

Key to table header

Case	Case reference number for the simulation
MSH	Stirrer geometry and mesh combination (see appendix E)
MOV	Stirrer movement model: MRF or SMM
ANGLES	Stirrer angles relative to the LDA plane in simulation: I20N - $\theta=-\pi/9$; I00P - $\theta=0$; I20P - $\theta=\pi/9$
RPM	Stirrer speed in revolutions per minute
BLADE	Type of blade used in simulation
EDGE	Stirrer holder leading edge configuration: sharp of chamfered
SURFACE	Tank surface model option: LID is fixed, VOF is free surface
TURBMOD	Turbulence model applied
TANK	Symmetry plane orientation and mesh density for outer part of geometry
CELLS	Cell count

Bibliography

ABSIL, L. H. J. 1995 Analysis of the laser doppler measurement technique for application in turbulent flows. Ph.d. thesis, Faculty of Aerospace Engineering, Delft University of Technology, Delft, The Netherlands.

AGRICOLA, G. 1556 *De re metallica*. unknown.

AIAA 1998 AIAA guide for the verification and validation of Computational Fluid Dynamics simulations. *Tech. Rep.* G-077-1998. American Institute of Aeronautics and Astronautics.

ALBRECHT, H. E., DAMASCHKE, N., BORYS, M. & TROPEA, C. 2003 *Laser Doppler and Phase Doppler Measurement Techniques*. Berlin, Germany: Springer-Verlag.

ANSYS 2009 *ANSYS FLUENT 12.0 User's Guide*. ANSYS, Inc., Canonsburg, Pennsylvania, U.S.A., available at http://www1.ansys.com/customer.

ASCANIO, G., CASTRO, B. & GALINDO, E. 2004 Measurement of power consumption in stirred vessels – a review. *Transactions of the Institution of Chemical Engineers, Part A: Chemical Engineering Research and Design* **82**, 1282–1290.

BADAMI, M., MILLO, F., ZUARINI, A. & GAMBAROTTO, M. 2003 Cfd analysis and experimental validation of the inlet flow distribution in close coupled catalytic converters. *SAE Paper* **2003-01-3072**, 12 pages.

BAKKER, A. 1992 Hydrodynamics of stirred gas-liquid dispersions. Ph.d. thesis, Kramers Laboratorium voor Fysiche Technologie, Delft University of Technology, Delft, The Netherlands.

BAVIERE, R. & AYELA, F. 2004 Micromachined strain gauges for the determination of liquid flow friction coefficients in microchannels. *Measurement Science and Technology* **15**, 377–383.

BENEDICT, L. H. & GOULD, R. D. 1996 Uncertainty estimates for any turbulence statistic. In *8th International Symposium on Applications of Laser Techniques to Fluid Mechanics*. Lisbon, Portugal, paper 36.1.

BENEDICT, R. P., CARLUCCI, N. A. & SWETZ, S. D. 1966 Flow losses in abrupt enlargements and contractions. *Journal of Engineering for Power, Transactions of ASME* pp. 73–81.

BENJAMIN, S. F., CLARKSON, R. J., HAIMAD, N. & GIRGIS, N. S. 1996 An experimental and predictive study of the flow field in axisymmetric automative exhaust catalyst systems. *SAE Paper* **961208**, 1008–1019.

BENJAMIN, S. F., HAIMAD, N., ROBERTS, C. A. & WOLLIN, J. 2001 Modelling the flow distribution through automotive catalytic converters. *Proceedings of the Institution of Mechanical Engineers, Part C: Journal of mechanical engineering science* **215**, 379–383.

BENJAMIN, S. F., ZHAO, H. & ARIAS-GARCIA, A. 2003 Prediciting the flow field inside a close-coupled catalyst - the effect of entrance losses. *Proceedings of the Institution of Mechanical Engineers, Part C: Journal of mechanical engineering science* **217**, 283–288.

BENNET, C. J., KOLACZKOWSKI, S. T. & THOMAS, W. J. 1991 Determination of heterogeneous reaction kinetics and reaction rates under mass transfer controlled conditions for a monolith reactor. *Transactions of the Institution of Chemical Engineers, Part B: Process Safety and Environmental Protection* **69**, 209–220.

BÖRGER, G. G. 1973 Optimierung von Windkanaldüsen für den Unterschallbereich. Ph.d. thesis, Ruhr University, Bochum, Germany.

BOUSSINESQ, J. 1887 Essai sur la théorie des eaux courantes. In *Mémoires présentés par divers savants à l'Académie royale des sciences de l'Institut de France*, *Sciences mathématiques et physiques*, vol. 23, pp. 46–50. Original available at `http://gallica.bnf.fr/digitallibrary`.

BRUCATO, A., CIOFALO, M., GRISAFI, F. & MICALE, G. 1998 Numerical prediction of flow fields in baffled stirred vessels: A comparison of alternative modelling approaches. *Chemical Engineering Science* **53**, 3653–3684.

CALVERT, J. R. 1967 Experiments on the low-speed flow past cones. *Journal of Fluid Mechanics* **27**, 273–294.

CAMPOLO, M., SBRIZZAI, F. & SOLDATI, A. 2003 Time-dependant flow structures and lagrangian mixing in rushton-impeller baffled-tank reactor. *Chemical Engineering Science* **58**, 1615–1629.

CARMODY, T. 1964 Establishment of the wake behind a disc. *Transaction of ASME part D: Journal of Basic Engineering* **86**, 797–882.

CASEY, M. & WINTERGERSTE, T., ed. 2000 *Best Practices Guidelines*, 1st edn. ER-COFTAC Special Interest Group on Quality and Trust in Industrial CFD.

CHAPPLE, D., KRESTA, S. M., WALL, A. & AFACAN, A. 2002 The effect of impeller and tank geometry on power number for a pitched blade turbine. *Transactions of the Institution of Chemical Engineers, Part A: Chemical Engineering Research and Design* **80**, 364–372.

CHEN, H. C. & PATEL, V. C. 1988 Near-wall turbulence models for complex flows including separation. *AIAA Journal* **26**, 641–648.

CHOUDHARY, V. R. & DORAISWAMY, L. K. 1972 Development of continuous-stirred gas-solid reactors for studies in kinetics and catalyst evaluation. *Industrial & Engineering Chemistry Process Design and Development* **11** (3), 420–427.

DACLES-MARIANI, J., ZILLIAC, G. G., CHOW, J. S. & BRADSHAW, P. 1995 Numerical/experimental study of a wingtip vortex in the near field. *AIAA Journal* **33** (9), 1561–1568.

DALY, B. J. & HARLOW, F. H. 1970 Transport equations in turbulence. *Physics of Fluids* **13**, 2634–2649.

DAVIDSON, P. 2004 *Turbulence. An Introduction for Scientists and Engineers*. Oxford University Press.

DE GRAAFF, D. B. 1999 Reynolds number scaling of the turbulent boundary layer on a flat plate and on swept and unswept bumps. Ph.d. thesis, Department of Mechanical Engineering, Stanford University, Stanford, U.S.A.

DEELDER, B. 2001 Measurements on the turbulent flow around and through monoliths for application in a monolithic stirred reactor. Master's thesis, Delft University of Technology, Kramers Laboratorium voor Fysische Technologie.

DERKSEN, J. & VAN DEN AKKER, H. E. A. 1999 Large eddy simulations on the flow driven by a rushton turbine. *AIChE Journal* **45** (2), 209–221.

DERKSEN, J. J., DOELMAN, M. S. & VAN DEN AKKER, H. E. A. 1999 Three-dimensional LDA measurements in the impeller region of a turbulently stirred tank. *Experiments in Fluids* **27**, 522–532.

DI FELICE, R., GIBILARO, L. G. & FOSCOLO, P. U. 1995 On the hindered settling of spheres in the inertial flow regime. *Chemical Engineering Science* **50** (18), 3005–3006.

DORSMAN, R. 2001 Piv measurements and numerical simulations of laminar flow in a Kenics static mixer. Master's thesis, Delft University of Technology, Kramers Laboratorium voor Fysische Technologie.

DRAIN, L. E. 1980 *The Laser Doppler Technique*. John Wiley & Sons, New York, U.S.A.

DURBIN, P. A. 1996 On the k-ϵ stagnation point anomaly. *International Journal of Heat and Fluid Flow* **17**, 89–90.

DURBIN, P. A. & PETTERSON REIFF, B. A. 2001 *Statistical theory and modeling for turbulent flows*. John Wiley & Sons Ltd.

DURST, F., JOVANOVIC, J. & SENDER, J. 1995 LDA measurements in the near-wall region of a turbulent pipe flow. *Journal of Fluid Mechanics* **295**, 305–335.

DURST, F., MELLING, A. & WHITELAW, J. H. 1981 *Principles and Practice of Laser Doppler Anemometry*, 2nd edn. Academic Press, London, UK.

EDVINSSON-ALBERS, R. K., HOUTERMAN, M. J. J., VERGUNST, T., GROLMAN, E. & MOULIJN, J. A. 1998 Novel monolithic stirred reactor. *AIChE Journal* **44**, 2459–2464.

EDWARDS, R. V. 1987 Report of the special panel on statistical bias problems in laser anemometry. *Journal of Fluids Engineering* **109**, 89–93.

EIFFEL, G. 1907 *Recherches experimentales sur la résistance de l'air exécutées a la tour Eiffel*. Maretheuse, Paris.

EKSTRÖM, F. & ANDERSSON, B. 2002 Pressure drop of monolithic catalytic converters: Experiments and modeling. In *SAE 2002 World Congress, SAE Paper 2002-01-1010*, , vol. 424-2, p. 9 pages. Warrendale, USA: SAE International.

ERTEM-MÜLLER, S. 2003 Numerical efficiency of implicit and explicit methods with multigrid for large eddy simulation in complex geometries. Ph.d. thesis, Numerische Berechnungsverfahren im Maschinenbau, Technische Universitt Darmstadt, Darmstadt, Germany.

ESCUDIÉ, R. & LINÉ, A. 2003 Experimental analysis of hydrodynamics in a radially agitated tank. *AIChE Journal* **49** (3), 585–603.

FERZIGER, J. H. & PERIĆ, M. 2002 *Computational Methods for Fluid Dynamics*, 3rd edn. Berlin, Germany: Springer-Verlag.

FU, S., LAUNDER, B. E. & LESCHZINER, M. A. 1988 Modeling strongly swirling recirculating jet flow with reynolds-stress transport closures. In *Sixth Symposium on Turbulent Shear Flows*. Toulouse, France.

GIBSON, M. M. & LAUNDER, B. E. 1978 Ground effects on pressure fluctuations in the atmospheric boundary layer. *Journal of Fluid Mechanics* **86**, 491–511.

GIROUX, T., HWANG, S., LIU, Y., RUETTINGER, W. & SHORE, L. 2005 Monolithic structures as alternatives to particulate catalysts for the reforming of hydrocarbons for hydrogen generation. *Applied Catalysis B: Environmental* **56**, 95–110.

GROEN, J. S. 2004 Scales and structures in bubble flows. Ph.d. thesis, Kramers Laboratorium voor Fysiche Technologie, Delft University of Technology, Delft, The Netherlands.

HAIMAD, N. 1997 A theoretical and experimental investigation of the flow performance of automotive catalytic converters. Ph.d. thesis, Coventry University, Coventry, U.K.

HARTEVELD, W. 2005 Detailed simulations of liquid and solid-liquid mixing. Ph.d. thesis, Kramers Laboratorium voor Fysiche Technologie, Delft University of Technology, Delft, The Netherlands.

HARTMANN, H., DERKSEN, J. J. & VAN DEN AKKER, H. E. A. 2006 Mixing times in a turbulent stirred tank by means of les. *AIChE Journal* **52** (11), 3696–3706.

HARTMANN, H., DERKSEN, J. J., MONTAVON, C., PEARSON, J., HAMILL, I. S. & VAN DEN AKKER, H. E. A. 2004 Assessment of large eddy and rans stirred tank simulations by means of LDA. *Chemical Engineering Science* **59**, 2419–2432.

HARVEY, P. S. & GREAVES, M. 1982*a* Turbulent flow in an agitated vessel part i: A predictive model. *Transactions of the Institution of Chemical Engineers, Part A: Chemical Engineering Research and Design* **60**, 195–200.

HARVEY, P. S. & GREAVES, M. 1982*b* Turbulent flow in an agitated vessel part ii: Numerical solution and model predictions. *Transactions of the Institution of Chemical Engineers, Part A: Chemical Engineering Research and Design* **60**, 201–210.

HAWTHORN, R. D. 1974 Afterburner catalysts - Effects of heat and mass transfer between gas and catalyst surface. *AIChE Symposium Series* **70** (137), 428–438.

HECK, R. M., GULATI, S. & FARRAUTO., R. J. 2001 The application of monoliths for gas phase catalytic reactions. *Chemical Engineering Journal* **82**, 149–156.

HIGUCHI, H., SAWADA, H. & KATO, H. 2008 Sting-free measurements on a magnetically supported right circular cylinder aligned with the free stream. *Journal of Fluid Mechanics* **596**, 49–72.

HILL, D. F., SHARP, K. V. & ADRIAN, R. J. 2000 Stereoscopic particle image velocimetry measurements of the flow around a rushton turbine. *Experiments in Fluids* **29**, 478–485.

HOEK, I. 2004 Towards the catalytic application of a monolithic stirrer reactor. Ph.d. thesis, Reactor & Catalysis Engineering, Delft University of Technology, Delft, The Netherlands.

HOERNER, S. F. 1965 *Fluid-dynamic drag*, 2nd edn. Hoerner Fluid Dynamics, Vancouver, WA 98665.

HOLMGREN, A. 1998 Catalysts for car exhaust: Oxygen storage in platinum/ceria and mass transfer in monoliths. Ph.d. thesis, Chemical Reaction Engineering, Chalmers University of Technology, SE-412 96 Göteborg, Sweden.

HOUTERMAN, M. J. J. 1997 Monolithic Catalyst Stirrer Reactor. Master's thesis, Delft University of Technology, Chemical Process Technology: Industrial Catalysis.

HUANG, P., BRADSHAW, P. & COAKLEY, T. 1993 Skin friction and velocity profile family for compressible turbulent boundary layers. *AIAA Journal* **31** (9), 1600–1604.

HUANG, R. F., CHEN, C. F., LIN, C. L. & BEAR, G. M. 1994 Smoke-wire visualization of the near-wake region behind a circular disc at low reynolds numbers. *Experiments in Fluids* **17**, 259–266.

HUNT, J. C. R., WRAY, A. A. & MOIN, P. 1988 Eddies, streams, and convergence zones in turbulent flows. In *Studying Turbulence Using Numerical Simulation Databases, 2. Proceedings of the Summer Program 1988*, pp. 193–208. NASA Ames Research Center, U.S.A.: Center for Turbulence Research.

JASAK, H. 1996 Error analysis and estimation for the finite volume method with applications to fluid flows. Ph.d. thesis, Department of Mechanical Engineering, Imperial College of Science, Technology and Medicine, London, UK.

JOHNSON, W. J., ed. 1998 *The Handbook of Fluid Dynamics*. CRC Press, Florida, U.S.A.

JONGEN, T. 1999 Simulation and modeling of turbulent incompressible flows. Ph.d. thesis, Ecole Polytechniques fédérales de Lausanne, Lausanne, Switzerland.

KADER, B. 1981 Temperature and concentration profiles in fully turbulent boundary layers. *International Journal of Heat and Mass Transfer* **24**, 1541–1544.

KAPTEIJN, F., HEISZWOLF, J. J., NIJHUIS, T. A. & MOULIJN, J. A. 1999 Monoliths in multiphase catalytic processes - aspects and prospects. *Cattech* **3** (1), 24–41.

KAYS, W. M. & LONDON, L. A. 1964 *Compact Heat Exchangers*, 2nd edn. McGraw-Hill, New York.

KIM, J. Y., LAI, M. C., LI, P. & CHUI, G. K. 1995 Flow distribution and pressure drop in diffuser-monolith flows. *Journal of Fluids Engineering* **117**, 362–368.

KOLTSAKIS, G. C. & STAMATELOS, A. M. 1997 Catalytic automotive exhaust aftertreatment. *Progress in Energy and Combustion Science* **23**, 1–39.

KOLTSAKIS, G. C. & STAMATELOS, A. M. 2000 Thermal response of automotive hydrocarbon adsorber systems. *Journal of Engineering for Gas Turbines and Power* **122**, 112–118.

KRAMERS, H., BAARS, G. M. & KNOLL, W. H. 1958 A comparative study on the rate of mixing in stirred tanks. *Chemical Engineering Science* **2**, 35–42.

KRAUME, M. & ZEHNER, P. 2001 Experience with experimental standards for measurements of various parameters in stirred tanks: A comparative test. *Transactions of the Institution of Chemical Engineers, Part A: Chemical Engineering Research and Design* **79**, 811–818.

KREUTZER, M. T. 2003 Hydrodynamics of taylor flow in capillaries and monolith reactors. Ph.d. thesis, Reactor & Catalysis Engineering, Delft University of Technology, Delft, The Netherlands.

KRITZINGER, H. P., DERKSEN, J. J. & VAN DEN AKKER, H. E. A. 2001 Simulation and measurement of the turbulent flow in a monolithic stirred tank. In *Proceedings of the ASME-PVP "3rd International Symposium on Computational Technologies for Fluid/Thermal/Chemical Systems with Industrial Applications"* (ed. C. R. Kleijn & V. V. Kudriavtsev), , vol. 424-2, pp. 27–34. The American Society of Mechanical Engineers, New York, USA.

KRITZINGER, H. P., KLEIJN, C. R. & VAN DEN AKKER, H. E. A. 2004 Drag on a confined cylinder in axial flow. In *Proceedings of the ASME-PVP "5th International Symposium on Computational Technologies for Fluid/Thermal/Chemical Systems with Industrial Applications"* (ed. C. R. Kleijn & V. V. Kudriavtsev), , vol. 491-1, pp. 125–131. New York, USA: The American Society of Mechanical Engineers.

LAI, M. C., LEE, T. & KIM, J. Y. 1992 Numerical and experimental characterizations of automotive catalytic converter internal flows. *Journal of Fluids and Structures* **6**, 451–470.

LARACHI, F., CHAOUKI, J., KENNEDY, G. & DUDUKOVIC, M. P. 1997 Radioactive particle tracking in multiphase reactors: Principles and applications. In *Noninvasive monitoring of multiphase flows*, , vol. 11. Amsterdam: Elsevier.

LAUNDER, B. E. 1989*a* Second-moment closure and its use in modeling turbulent industrial flows. *International Journal for Numerical Methods in Fluids* **9**, 963–985.

LAUNDER, B. E. 1989*b* Second-moment closure: Present... and future? *International Journal of Heat and Fluid Flow* **10**, 282–300.

LAUNDER, B. E., REECE, G. J. & RODI, W. 1975 Progress in the development of a reynolds-stress turbulence closure. *Journal of Fluid Mechanics* **68**, 537–566.

LAUNDER, B. E. & SHIMA, N. 1989 Second-moment closure for the near-wall sublayer: Development and application. *AIAA Journal* **27**, 1319–1325.

LAUNDER, B. E. & SPALDING, D. B. 1974 The numerical computation of turbulent flows. *Computer Methods in Applied Mechanics and Engineering* **3**, 269–289.

LIAKOPOULOS, C., POULOPOULOS, S. & PHILIPPOPOULOS, C. 2001 Kinetic studies of acetaldehyde oxidation over pt/rh and pd monolithic catalysts in a spinning-basket flow reactor. *Industrial and Engineering Chemistry Research* **40**, 1476–1481.

LIEN, F. S. & LESCHZINER, M. A. 1994 Assessment of turbulent transport models including non-linear rng eddy-viscosity formulation and second-moment closure. *Computers and Fluids* **23** (8), 983–1004.

LUO, J. Y., GOSMAN, A. D. & ISSA, R. I. 1994 Prediction of impeller-induced flows in mixing vessels using multiple frames of reference. In *8th European Conference on Mixing, September 21-23, 1994, IChemE Symposium Series No. 136*, pp. 549–556. Cambridge, U.K.

MCLAUGHLIN, D. K. & TIEDERMAN, W. G. 1973 Biasing correction for individual realisation of laser anemometer measurements in turbulent flows. *Physics of Fluids* **16**, 2082–2088.

MENTER, F. 2002 CFD best practice guidelines for cfd code validation for reactor-safety applications. *Tech. Rep.* EVOL-ECORA-D1. European Commission, 5th EURATOM Framework Programme.

MENTER, F. R. 1994 Two-equation eddy-viscosity turbulence models for engineering applications. *AIAA Journal* **32** (8), 269–289.

MEYERS, J. F. 1991 Biasing errors and corrections. *Tech. Rep.*. Lecture Series: Laser Velocimetry June 10 - 14, 1991, Biasing Errors and Corrections, Von Karman Institute, Sint-Genesius-Rode, Belgium.

MICHELET, S., KEMOUN, A., MALLET, J. & MAHOUAST, M. 1997 Space-time velocity correlations in the impeller stream of a rushton turbine. *Experiments in Fluids* **23**, 418–426.

MIDDLETON, J. C., PIERCE, F. & LYNCH, P. M. 1986 Computations of flow fields and complex reaction yield in turbulent stirred reactors, and comparison with experimental data. *Transactions of the Institution of Chemical Engineers, Part A: Chemical Engineering Research and Design* **64**, 18–22.

MÜHLE, J. 1972 Berechnung des trockenen Druckverlustes von Lochböden. *Chemie-Ingenieur-Technik* **44**, 72–79.

MUTO, S. & UENO, H. 1976 Report on JARI's full-scale automobile wind tunnel. *Tech. Rep.* 56. Japan Automobile Research Institute, Technical memo.

NAKAYAMA, A. 1985 Measurements of separating boundary layer and wake of an airfoil using laser doppler velocimetry. In *23rd Aerospace Sciences Meeting, Paper AIAA-1985-181*. Reston, Virginia, U.S.A.: American Institute of Aeronautics and Astronautics.

NERE, N. K., PATWARDHAN, A. W. & JOSHI, J. B. 2003 Liquid-phase mixing in stirred vessels: Turbulent flow regime. *Industrial and Engineering Chemistry Research* **42**, 2661–2698.

NEWTON, I. 1687 Principia. In *Book II*, *Prop. XXXIX* Theor. XXXI. King George.

NIENOW, A. W. & WISDOM, D. J. 1974 Flow over disc turbine blades. *Chemical Engineering Science* **29**, 1994–1997.

OBERKAMPF, W. L. & TRUCANO, T. G. 2002 Verification and validation in Computational Fluid Dynamics. *Tech. Rep.* SAND2002-059. Sandia National Laboratory.

ODA, N. & HOSHINO, T. 1974 Three-dimensional airflow visualization by smoke tunnel. *SAE paper* **741029**.

ORSZAG, S. A., YAKHOT, V., FLANNERY, W. S., BOYSAN, F., CHOUDHURY, D., MARUZEWSKI, J. & PATEL, B. 1993 Renormalization group modeling and turbulence simulations. In *Near-Wall Turbulent Flows. Proceedings of the International Conference on Near-Wall Turbulent Flows* (ed. R. M. C. So & C. G. Speziale). Tempe, Arizona, U.S.A.

PATANKAR, S. V. 1980 *Numerical Heat Transfer and Fluid Flow*. Hemisphere Publishing Corporation, New York, U.S.A.

ROACH, P. J. 1976 *Computational Fluid Dynamics*, 2nd edn. Hermosa Publishers, Albuquerque, New Mexico, U.S.A.

ROACH, P. J. 1998 *Verification and Validation in Computational Science and Engineering*. Hermosa Publishers, New Mexico, U.S.A.

ROY, S., BAUER, T., AL-DAHHAN, M., LEHNER, P. & TUREK, T. 2004 Monoliths as Multiphase Reactors: A Review. *AIChE Journal* **50** (11), 2918–2938.

RUDD, M. J. 1969 A new theoretical model for the laser dopplermeter. *Journal of Physics E: Scientific Instruments* **2**, 55–58.

RUMSEY, C. 2009 The wilcox k-omega turbulence model, NASA Langley Research Center. `http://turbmodels.larc.nasa.gov/wilcox.html`, *last accessed:* 15 August 2010.

RUSHTON, J. H., COSTICH, E. W. & EVERRETT, H. J. 1950 Power characteristics of mixing impellers, part i. *Chemical Engineering Progress* **46** (8), 395–404.

SHAH, R. K. 1978 A correlation for laminar hydrodynamic entry length solutions for circular and non-circular ducts. *Journal of Fluids Engineering* **100**, 177–179.

SHIH, T. H., LIOU, W. W., SHABBIR, A., YANG, Z. & ZHU, J. 1995 A new k-ϵ eddy-viscosity model for high reynolds number turbulent flows - model development and validation. *Computers and Fluids* **24** (3), 227–238.

SOHANKAR, A., DAVIDSON, L. & NORBERG, C. 2000 Large eddy simulation of flow past a square cylinder: Comparison of different subgrid models. *Journal of Fluids Engineering* **122**, 39–47.

SOMMERFELD, M. & DECKER, S. 2004 State of the art and future trends in CFD simulation of stirred vessel hydrodynamics. *Chemical Engineering & Technology* **27** (3), 215–223.

SPEE, M. P. R. 1999 Liquid-phase semihydrogenation of alkynes with supported palladium-copper catalysts. Ph.d. thesis, Debye Institute, Utrecht University, Utrecht, The Netherlands.

STOOTS, C. M. & CALABRESE, R. V. 1995 Mean velocity field relative to a rushton turbine blade. *AIChE Journal* **41** (1), 1–11.

TUMMERS, M. J. 1999 Investigation of a turbulent wake in an adverse pressure gradient using laser doppler anemometry. Ph.d. thesis, Faculty of Aerospace Engineering, Delft University of Technology, Delft, The Netherlands.

VAN MAANEN, H. R. E. 1999 Retrieval of turbulence and turbulence properties from randomly sampled laser-doppler anemometry data with noise. Ph.d. thesis, Kramers Laboratorium voor Fysiche Technologie, Delft University of Technology, Delft, The Netherlands.

VAN'T RIET, K. & SMITH, J. M. 1973 The behaviour of gasliquid mixtures near rushton turbine blades. *Chemical Engineering Science* **28**, 1031–1037.

VERDIER, O. 2004 Benchmark of Femlab, Fluent and Ansys. In *Preprints in Mathematical Sciences*, p. 22. Sweden: Centre for Mathematical Sciences, Lund University.

VERSTEEG, H. K. & MALALASEKERA, W., ed. 1995 *An introduction to Computational fluid dynamics: The finite volume method.*. Longman Group Ltd.

VERSTEEG, H. K. & MALALASEKERA, W., ed. 2007 *An introduction to Computational fluid dynamics: The finite volume method.*, 3rd edn. Longman Group Ltd.

VILLERMAUX, J. & SCHWEICH, D. 2004 Is the catalytic monolithic reactor well suited to environmentally benign processing. *Industrial and Engineering Chemistry Research* **33** (12), 3025–3030.

VOTRUBA, J., MIKUŠ, O., HLAVÁČEK, V. & SKŘIVÁNEK, J. 1974 A note on pressure drop in monolithic catalysts. *Chemical Engineering Science* **29**, 2128–2130.

VOTRUBA, J., NGUEN, K., MIKUŠ, O., HLAVÁČEK, V. & SKŘIVÁNEK, J. 1975 Heat and mass transfer in honeycomb catalysts–ii. *Chemical Engineering Science* **30**, 201–206.

WENDLAND, D. W. & MATTHES, W. R. 1986 Visualization of automotive catalytic converter internal flows. *SAE Paper* **861554**, 6.729–6.742.

WENDLAND, D. W., SORREL, P. L. & KREUCHER, J. E. 1991 Sources of monolith catalytic converter pressure loss. *SAE Paper* **912372**, 1008–1019.

WEST, G. S. & APELT, C. J. 1982 The effects of tunnel blockage and aspect ratio on the mean flow past a circular cylinder with reynolds numbers between 10^4 and 10^5. *Journal of Fluid Mechanics* **114**, 361–377.

WHITE, F. M. 1988 *Fluid Mechanics*, 2nd edn. McGraw-Hill, Singapore.

WHITE, F. M. 1991 *Viscous Fluid Flow*, 2nd edn. McGraw-Hill Education.

WHITE, F. M. & CHRISTOPH, G. H. 1971 A simple new analysis of compressible turbulent skin friction under arbitrary conditions. *Tech. Rep.* AFFDL-TR-70-133. Air Force Flight Dynamics Laboratory, Wright-Patterson Air Force Base, Ohio, U.S.A.

WIKIPEDIA 2009 Pliny the elder. `http://en.wikipedia.org/wiki/Pliny_the_Elder`, *last accessed:* 10 January 2009.

WILCOX, D. C. 1998 *Turbulence Modeling for CFD*. La Canada, California: DCW Industries, Inc.

WOLFSTEIN, M. 1969 The velocity and temperature distribution of one-dimensional flow with turbulence augmentation and pressure gradient. *International Journal of Heat and Mass Transfer* **12**, 301–318.

WS ATKINS CONSULTANTS 2002 Best practices guidelines for marine applications of CFD. *Tech. Rep.* MARNET-CFD Report. European Commission, Thematic network MARNET.

YEH, Y. & CUMMINS, H. Z. 1964 Localized fluid flow measurement with a He-Ne laser spectrometer. *Applied Physics Letters* **4** (10), 176–178.

YIANNESKIS, M., POPIOLEK, Z. & WHITELAW, J. H. 1987 An experimental study of the steady and unsteady flow characteristics of stirred reactors. *Journal of Fluid Mechanics* **175**, 537–555.

YOON, H. S., BALACHANDAR, S., HA, M. Y. & KAR, K. 2003 Large eddy simulation of flow in a stirred tank. *Journal of Fluids Engineering* **125**, 486–499.

YOUNGS, D. L. 1982 Time-dependent multi-material flow with large fluid distortion. In *Numerical Methods for Fluid Dynamics* (ed. K. W. Morton & M. J. Baines), pp. 273–286. London, United Kingdom: Academic Press.

ZHANG, Z. 2002 Velocity bias in LDA measurements and its dependence on the flow turbulence. *Flow Measurement and Instrumentation* **13**, 63–68.

ZHANG, Z. & EISELE, K. 1998 Further considerations of the astigmatism error associated with off-axis alignment of an LDA-probe. *Experiments in Fluids* **24**, 83–89.

Summary

Hydrodynamics of Monolithic Stirrer Reactors

The Monolithic Stirrer Reactor (MSR) is a novel concept for heterogeneously catalyzed reactors and is presented as an alternative device to slurry reactors. It uses a modified stirrer on which structured catalyst supports (monoliths) are fixed to form permeable blades. The monoliths consist of small square parallel channels on which a layer of catalytic material can be applied. The stirrer now has both a catalytic and a mixing function. The main advantage of this reactor type is the ease of the catalyst handling, since the catalyst is easily separated from the reaction mixture and can be re-used.

Chapter 1 introduces the goal of this work which is to study the hydrodynamic operation of the MSR and develop engineering models for its design. In particular, to evaluate the two main functions of the stirrer (i) mixing of the bulk fluid, and (ii) pumping fluid through the monolith to allow the catalytic reaction to take place. The amount of flow through the monolith, i.e., the fluid velocity in the monolith channels, determines the mass transfer rate inside the monolith - this is an important design parameter for the reactor. In addition to detailed three-dimensional computational fluid dynamics simulations with the CFD code Fluent, we performed experimental measurements of velocities in the bulk and in the monolith channels, of mixing and of power consumption in the MSR. Building on detailed CFD and experimental data, we developed a simple engineering model to predict the flow through the monolith channels.

In chapter 2, the hydrodynamics of the monolith is investigated for flow through and around a monolith placed in the streamwise direction in a duct. The experimental results show that the pressure drop characteristics of the monolith can be modeled accurately if the contribution of the developing flow in the inlet of the channels is taken into account - the correlation of Hawthorn (1974) was found to provide such a pressure drop model. The pressure drop correlation was imple-

mented in a user defined function (UDF) in Fluent to enable modeling of the monolith without resolving individual channels. The agreement between the CFD and experimental pressure drop results, as well as flow velocity results upstream from the monolith, were confirmed for a range of flow rates and different monolith geometries. Comparison of the flow field downstream from the monolith showed that the UDF is unable to replace the actual monolith if an exact prediction of the flow field in the vicinity of the monolith is required. It was shown that downstream velocities can be predicted accurately when performing a simulation which fully resolves the individual monolith channels. This, however, is not feasible for a full MSR simulation. The pressure drop prediction and the qualitative prediction of the flow field are satisfactory for the purposes required from the present modeling effort.

In chapter 3, with the now known monolith characteristics, an engineering model for the rapid calculation of the monolith channel velocity has been developed. As part of the model development the drag coefficient of an axial cylinder configuration in duct flow was investigated. The results show that the model can accurately predict the behavior of different monolith configurations in a confined duct without the need for fitting of correlations.

Chapter 4 describes experiments inside a prototype MSR to characterize MSR hydrodynamics. Using, amongst other techniques, phase resolved Laser Doppler Anemometry, the bulk flow, channel velocities, power draw and mixing characteristics were determined for a range of stirrer speeds and different stirrer configurations. The mean velocity of the fluid in the monolith channels ranged from 15 to 60% of the stirrer tip velocity. The magnitude of the channel velocity is a coupled function of the stirrer speed (driving force) and channel characteristics (loss coefficient) as captured in the engineering model. Typical power numbers of 0.40-0.65 were found, but these results were shown to be highly dependent on the geometry. The present data will therefore only apply to geometrically similar configurations. The same applies to the observed mixing times, which ranged from 10 to 24 impeller revolution times. Since there is a strong correlation between the power input and mixing times for stirred tanks, the present mixing results should also not be used for cases with different geometric configurations.

In chapter 5, the experimentally studied MSR reactor configurations are studied by CFD simulations, and a comparison is made between experimental data, CFD data and predictions from the proposed simple engineering model. All CFD results were obtained by employing our user-defined function in Fluent for simulation of the overall monolith. A sensitivity study was performed to investigate the influence of various modeling options - such as various turbulence models, sliding mesh versus Multiple Reference Frame approaches to model the impeller, the inclusion of a free surface, grid refinement and near wall resolution - on the results of the CFD simulations. This study showed that good results, in close agreement with experimental data on bulk and monolith channel velocities, power consumption and mixing times, could be obtained with a simple modeling approach, combining our UDF routine for modeling the pressure drop over the monolith with steady-

state simulations using the Multiple Reference Frame stirrer model, no free liquid surface, and standard turbulence models. The combination of our UDF routine for overall monolith behavior and the steady-state Multiple Reference Frame approach to model the rotating impeller allows for significant reductions in grid size and overall CPU time, enabling the relatively straightforward and accurate prediction of the hydrodynamics of single phase MSR reactors. The simple engineering model, which was developed for easy prediction of liquid velocities through the monolith channels as a function of monolith geometry and impeller speed, proved to be relatively robust and compared well with both the experimental and the CFD data. The model was deliberately kept very simple, but the predicting capability might be improved by considering additional effects, such as the influence of the angle at which the flow enters the monolith channels. With the model, it would be possible to predict the performance of monolith stirrer reactors.

In general, this work confirmed that the MSR concept could be of practical use in the process industry. Significant flow velocities can be obtained through the monolith, and mixing times and power consumption do not compare unfavourable with standard stirred tank reactors. We proposed a relatively simple, industrially feasible, yet accurate approach to computational fluid dynamics simulations of MSR reactors using a commercial CFD code, and we developed a simple engineering model capable of predicting liquid flows through monoliths in MSRs.

Samenvatting

De hydrodynamica van monolithische roerder reactoren

De monolithische roerder reactor (Monolithic Stirrer Reactor, MSR) is een nieuw concept voor heterogeen gekatalyseerde reactoren, dat wordt ontwikkeld als een alternatief voor slurry reactoren. Een MSR is een geroerde tankreactor, waarin gebruik wordt gemaakt van een roerder waarvan de bladen zijn vervangen door blokken monolietmateriaal. Deze bestaan uit vele dunne, vierkante, parallelle kanaaltjes, die aan de binnenkant zijn gecoat met katalytisch materiaal. De roerder van een MSR heeft een dubbele functie: Het mengen van de vloeistof in de tank, en die vloeistof intensief in contact brengen met de katalysator. Het belangrijkste voordeel van het MSR concept ligt in de eenvoud waarmee het katalysatormateriaal kan worden gescheiden van de reactorvloeistof en kan worden hergebruikt.

Hoofdstuk 1 introduceert het doel van dit werk: Het bestuderen van de hydrodynamische werking van de monolithische roerder reactor en het opstellen van modellen voor het ontwerp ervan. In het bijzonder was het doel om de twee belangrijkste functies van de roerder te evalueren: (i) het mengen van de bulkvloeistoffen, en (ii) het verpompen van vloeistof door de monoliet om de katalytische reactie te laten plaatsvinden. Het debiet van de stroom door de monoliet, dat wil zeggen, de vloeistofsnelheid in de monolietkanalen, bepaalt het stoftransport in de monoliet - dit is een belangrijke parameter voor het ontwerp van de reactor. Naast gedetailleerde driedimensionale computational fluid dynamics simulaties met de CFD code Fluent, zijn experimentele metingen gedaan aan de vloeistofsnelheden in de tank en in de monolietkanalen, de menging, en het vermogensverbruik. Op basis van de gedetailleerde CFD resultaten en experimentele data is een eenvoudig model ontwikkeld om vloeistofsnelheden in de monolietkanaaltjes te kunnen voorspellen.

In hoofdstuk 2 wordt een onderzoek beschreven naar de stroming rondom en door een monoliet geplaatst in een rechte buis met de monolietkanaaltjes in de

stromingsrichting. De experimentele resultaten tonen aan dat de drukval over de monoliet nauwkeurig gemodelleerd kan worden als de bijdrage van de zich ontwikkelende stroming in de inlaat van de kanalen in aanmerking wordt genomen. Een correlatie zoals voorgesteld door Hawthorn (1974) bleek hiervoor een geschikt model te zijn. Deze drukvalcorrelatie werd in een door de gebruiker gedefinieerde functie (UDF) in Fluent geïmplementeerd, zodat hiermee het grootschalige gedrag van stroming kan worden gemodelleerd zonder de stroming in de individuele monolietkanaaltjes uit te rekenen. Er werd een goede overeenkomst gevonden tussen de CFD- en de experimentele resultaten voor wat betreft de drukval over en de stroomsnelheden stroomopwaarts van de monoliet, voor een reeks van vloeistofdebieten door de buis en verschillende soorten monolieten. Het model bleek niet in staat om de stroming direct stroomafwaarts van de monoliet nauwkeurig te voorspellen. Hiervoor bleek het noodzakelijk om de stroming in de individuele monolietkanaaltjes mee te nemen in de simulaties, hetgeen niet haalbaar is voor een volledige MSR simulatie. De voorspelling van de drukval over de monoliet en de gemiddelde stroming door en rondom de monoliet zijn echter bevredigend voor het huidige doel van de modellering.

In hoofdstuk 3 wordt, op basis van de nu bekende kenmerken van de monoliet, een engineering model voor de snelle berekening van het vloeistofdebiet door de kanaaltjes van een monoliet in een MSR ontwikkeld. Als onderdeel van de ontwikkeling van dit model werd onderzoek gedaan naar de weerstandscoëfficiënt van een axiale cilinder in een buisstroming. Het ontwikkelde engineering model bleek in staat om het gedrag van verschillende monoliet-configuraties geplaatst in een rechte buis nauwkeurig te voorspellen, zonder gebruik van enige fitconstante.

Hoofdstuk 4 beschrijft experimenten in een prototype MSR om de hydrodynamica van zo'n reactor te karakteriseren. Gebruik makend van, onder andere, faseopgeloste Laser Doppler snelheidsmetingen, werden de bulkstroming, monoliet kanaalsnelheden, vermogensverbruik en mengtijden bepaald voor een scala van verschillende roerdersnelheden en -configuraties. De gemiddelde kanaalsnelheid varieerde van 15 tot 60% van de roerdertipsnelheid. Deze kanaalsnelheid is een functie van zowel de roerdersnelheid (drijvende kracht) als de eigenschappen van de monolietkanaaltjes (verliescoëfficiënt), beschreven door het engineering model. Typische vermogenskentallen van 0.40-0.65 werden gevonden voor de MSR, maar dit getal bleek sterk afhankelijk te zijn van de geometrie. De gevonden waarden zijn daarom alleen van toepassing op geometrisch vergelijkbare configuraties. Dat geldt ook voor de gevonden mengtijden, die lagen tussen 10 en 24 roerderomwentelingen. Aangezien er in geroerde vaten een sterke correlatie bestaat tussen het roerdervermogen en de mengtijd, zijn ook de in dit onderzoek gevonden mengtijden niet toepasbaar voor andere geometrische configuraties.

Hoofdstuk 5 beschrijft CFD simulaties van de experimenteel bestudeerde MSR reactorconfiguraties uit hoofdstuk 4. Er wordt een vergelijking gemaakt tussen experimentele data, CFD simulaties en voorspellingen van het ontwikkelde engineering model. Alle CFD resultaten voor de MSR zijn verkregen met gebruik van de ontwikkelde Fluent gebruikersfunctie (UDF) voor het modelleren van het hydro-

dynamische gedrag van de monolieten. Er werd een uitgebreide gevoeligheidsanalyse gedaan om de invloed van verschillende modelopties - zoals verschillende turbulentiemodellen, verschillende manieren om de draaiende roerder te modelleren, het al dan niet meenemen van het vrije vloeistofoppervlak, de roosterfijnheid en de manier waarop de stroming vlak bij wanden werd gemodelleerd - op de resultaten van de CFD simulaties te onderzoeken. Hieruit bleek dat CFD resultaten die goed overeenkomen met experimentele data - voor wat betreft bulk vloeistofsnelheden, vloeistofsnelheden door de monolietkanalen, mengtijden en vermogensconsumptie - kunnen worden verkregen met relatief eenvoudige CFD simulaties, waarin de UDF model voor het overall gedrag van de monoliet wordt gecombineerd met een tijdsonafhankelijke Multiple Reference Frame modellering van de draaiende roerder, standaard turbulentiemodellen, en een niet-bewegend vloeistofoppervlak. Door gebruik te maken van de UDF monolietmodel en de MRF modellering van de draaiende roerder kan aanzienlijk bezuinigd worden op de benodigde computercapaciteit en kan de hydrodynamica van een MSR relatief eenvoudig worden gemodelleerd. Vloeistofsnelheden in de monolietkanaaltjes zoals voorspeld met het ontwikkelde engineering model waren in goede overeenstemming met zowel de CFD voorspellingen als de experimentele data. Het model werd bewust zeer eenvoudig gehouden, maar het voorspellen van het vloeistofdebiet door de monoliet zou kunnen worden verbeterd door het meenemen van effecten zoals de vloeistof instroomhoek in de monolietkanaaltjes. Met het model zou het mogelijk zijn om de werking van monolithische roerder reactoren te voorspellen.

Samenvattend heeft dit onderzoek aangetoond dat het concept van een MSR van praktisch nut kan zijn in de procesindustrie. De geroerde vloeistof stroomt met aanzienlijke snelheden door de monolietkanaaltjes, en vermogensconsumptie en mengtijden steken niet ongunstig af bij die van meer conventionele geroerde vat reactoren. Met een relatief eenvoudige aanpak en gebruik makend van een commerciële code, kunnen, op een in de industriële praktijk haalbare wijze, nauwkeurige CFD simulaties worden uitgevoerd van MSRs. Het voorgestelde engineering model kan op eenvoudige wijze gebruikt worden om de vloeistofsnelheden door de monolietkanaaltjes te voorspellen.

Acknowledgements

We have been fortunate in meeting some of the nicest people on the planet during our stay in the Netherlands. We have spent many enjoyable encounters with Wilbert and Elise – I still love *boterkoek*. Michal and Ewelina have shown us around Poland and we were able to reciprocate by showing them around South Africa. Marcos and Carla have been an important part of our last year in the Netherlands – I owe Marcos a braai with South African beef. The Bouman family in Haarlem has been a shelter and family away from home. I want to thank them for their support and kindness during our stay in the Netherlands.

The final touches to the work were completed as a result of constant encouragement from my colleague Ken Craig. I want to thank him for convincing me that it is finally finished.

Jac and Febe have the dubious honor of having been on the PhD journey since its inception. We have enjoyed many beers, red wine and braais in Rotterdam – now we can continue doing so again in Pretoria. Despite me lagging a bit, the quartet is now complete.

My parents allowed me follow my own head. I am very grateful for the love and stability they have provided to me and my sisters over many years. My parents-in-law supported this work in many ways: sharing their house with us upon the return from abroad, entertaining my family on weekends when I was working and dragging me into the Drakensberg that first time long ago.

This book exists because Carien, Peter and Anke spent many weekends away from home to let "Daddy work on his thesis". I look forward to the next phase of our life together – thesis-less.

Pretoria,   *HP Kritzinger*
November 2010

Curriculum Vitae

HP Kritzinger was born on 11 October 1972 in Ceres, South Africa. He matriculated from the *Hoërskool Paarl Gimnasium* in 1990 and started at the Department of Mechanical Engineering of the University of Stellenbosch in 1991. In 1994 her graduated with the degree B.Eng (Meg.) and chose to continue with further studies. In 1999 he obtained the degree M.Sc.Eng (Mechanical) under the guidance of Prof. D.G. Kröger.

In 1998, after a brief stay as junior engineer at the Northam Platinum Mine, he started working as a CFD engineer at MegChem in Secunda. In June 2000 he left South Africa to start research on his PhD at the Delft University of Technology in the Netherlands. The results of this research are presented in this book.

At the end of 2005 he returned to South Africa. After a brief period with the Council for Scientific and Industrial Research, he joined the Pebble Bed Modular Reactor company where he was employed as Senior Engineering Specialist: CFD. In 2010 he joined Westinghouse Electric South Africa as a Principal Engineer.